

# Measurements and Predictions of Turbulent Flow Structures in Simulated Rod Bundles

by

Xiaohua Wu

A Thesis Presented to  
The University of Manitoba  
in Partial Fulfillment of the Requirements of the Degree of  
**Doctor of Philosophy**  
in Mechanical Engineering

Winnipeg, Manitoba, CANADA

September, 1993



National Library  
of Canada

Bibliothèque nationale  
du Canada

Acquisitions and  
Bibliographic Services Branch

Direction des acquisitions et  
des services bibliographiques

395 Wellington Street  
Ottawa, Ontario  
K1A 0N4

395, rue Wellington  
Ottawa (Ontario)  
K1A 0N4

*Your file* *Votre référence*

*Our file* *Notre référence*

The author has granted an irrevocable non-exclusive licence allowing the National Library of Canada to reproduce, loan, distribute or sell copies of his/her thesis by any means and in any form or format, making this thesis available to interested persons.

L'auteur a accordé une licence irrévocable et non exclusive permettant à la Bibliothèque nationale du Canada de reproduire, prêter, distribuer ou vendre des copies de sa thèse de quelque manière et sous quelque forme que ce soit pour mettre des exemplaires de cette thèse à la disposition des personnes intéressées.

The author retains ownership of the copyright in his/her thesis. Neither the thesis nor substantial extracts from it may be printed or otherwise reproduced without his/her permission.

L'auteur conserve la propriété du droit d'auteur qui protège sa thèse. Ni la thèse ni des extraits substantiels de celle-ci ne doivent être imprimés ou autrement reproduits sans son autorisation.

ISBN 0-315-86081-2

Canada

Name Xiaohua Wu

Dissertation Abstracts International is arranged by broad, general subject categories. Please select the one subject which most nearly describes the content of your dissertation. Enter the corresponding four-digit code in the spaces provided.

Heat and Thermodynamics

SUBJECT TERM

0348

SUBJECT CODE

U·M·I

**Subject Categories**

**THE HUMANITIES AND SOCIAL SCIENCES**

**COMMUNICATIONS AND THE ARTS**

Architecture ..... 0729  
 Art History ..... 0377  
 Cinema ..... 0900  
 Dance ..... 0378  
 Fine Arts ..... 0357  
 Information Science ..... 0723  
 Journalism ..... 0391  
 Library Science ..... 0399  
 Mass Communications ..... 0708  
 Music ..... 0413  
 Speech Communication ..... 0459  
 Theater ..... 0465

**EDUCATION**

General ..... 0515  
 Administration ..... 0514  
 Adult and Continuing ..... 0516  
 Agricultural ..... 0517  
 Art ..... 0273  
 Bilingual and Multicultural ..... 0282  
 Business ..... 0688  
 Community College ..... 0275  
 Curriculum and Instruction ..... 0727  
 Early Childhood ..... 0518  
 Elementary ..... 0524  
 Finance ..... 0277  
 Guidance and Counseling ..... 0519  
 Health ..... 0680  
 Higher ..... 0745  
 History of ..... 0520  
 Home Economics ..... 0278  
 Industrial ..... 0521  
 Language and Literature ..... 0279  
 Mathematics ..... 0280  
 Music ..... 0522  
 Philosophy of ..... 0998  
 Physical ..... 0523

Psychology ..... 0525  
 Reading ..... 0535  
 Religious ..... 0527  
 Sciences ..... 0714  
 Secondary ..... 0533  
 Social Sciences ..... 0534  
 Sociology of ..... 0340  
 Special ..... 0529  
 Teacher Training ..... 0530  
 Technology ..... 0710  
 Tests and Measurements ..... 0288  
 Vocational ..... 0747

**LANGUAGE, LITERATURE AND LINGUISTICS**

Language  
 General ..... 0679  
 Ancient ..... 0289  
 Linguistics ..... 0290  
 Modern ..... 0291  
 Literature  
 General ..... 0401  
 Classical ..... 0294  
 Comparative ..... 0295  
 Medieval ..... 0297  
 Modern ..... 0298  
 African ..... 0316  
 American ..... 0591  
 Asian ..... 0305  
 Canadian (English) ..... 0352  
 Canadian (French) ..... 0355  
 English ..... 0593  
 Germanic ..... 0311  
 Latin American ..... 0312  
 Middle Eastern ..... 0315  
 Romance ..... 0313  
 Slavic and East European ..... 0314

**PHILOSOPHY, RELIGION AND THEOLOGY**

Philosophy ..... 0422  
 Religion  
 General ..... 0318  
 Biblical Studies ..... 0321  
 Clergy ..... 0319  
 History of ..... 0320  
 Philosophy of ..... 0322  
 Theology ..... 0469

**SOCIAL SCIENCES**

American Studies ..... 0323  
 Anthropology  
 Archaeology ..... 0324  
 Cultural ..... 0326  
 Physical ..... 0327  
 Business Administration  
 General ..... 0310  
 Accounting ..... 0272  
 Banking ..... 0770  
 Management ..... 0454  
 Marketing ..... 0338  
 Canadian Studies ..... 0385  
 Economics  
 General ..... 0501  
 Agricultural ..... 0503  
 Commerce-Business ..... 0505  
 Finance ..... 0508  
 History ..... 0509  
 Labor ..... 0510  
 Theory ..... 0511  
 Folklore ..... 0358  
 Geography ..... 0366  
 Gerontology ..... 0351  
 History  
 General ..... 0578

Ancient ..... 0579  
 Medieval ..... 0581  
 Modern ..... 0582  
 Black ..... 0328  
 African ..... 0331  
 Asia, Australia and Oceania ..... 0332  
 Canadian ..... 0334  
 European ..... 0335  
 Latin American ..... 0336  
 Middle Eastern ..... 0333  
 United States ..... 0337  
 History of Science ..... 0585  
 Law ..... 0398  
 Political Science  
 General ..... 0615  
 International Law and Relations ..... 0616  
 Public Administration ..... 0617  
 Recreation ..... 0814  
 Social Work ..... 0452  
 Sociology  
 General ..... 0626  
 Criminology and Penology ..... 0627  
 Demography ..... 0938  
 Ethnic and Racial Studies ..... 0631  
 Individual and Family Studies ..... 0628  
 Industrial and Labor Relations ..... 0629  
 Public and Social Welfare ..... 0630  
 Social Structure and Development ..... 0700  
 Theory and Methods ..... 0344  
 Transportation ..... 0709  
 Urban and Regional Planning ..... 0999  
 Women's Studies ..... 0453

**THE SCIENCES AND ENGINEERING**

**BIOLOGICAL SCIENCES**

Agriculture  
 General ..... 0473  
 Agronomy ..... 0285  
 Animal Culture and Nutrition ..... 0475  
 Animal Pathology ..... 0476  
 Food Science and Technology ..... 0359  
 Forestry and Wildlife ..... 0478  
 Plant Culture ..... 0479  
 Plant Pathology ..... 0480  
 Plant Physiology ..... 0817  
 Range Management ..... 0777  
 Wood Technology ..... 0746  
 Biology  
 General ..... 0306  
 Anatomy ..... 0287  
 Biostatistics ..... 0308  
 Botany ..... 0309  
 Cell ..... 0379  
 Ecology ..... 0329  
 Entomology ..... 0353  
 Genetics ..... 0369  
 Limnology ..... 0793  
 Microbiology ..... 0410  
 Molecular ..... 0307  
 Neuroscience ..... 0317  
 Oceanography ..... 0416  
 Physiology ..... 0433  
 Radiation ..... 0821  
 Veterinary Science ..... 0778  
 Zoology ..... 0472  
 Biophysics  
 General ..... 0786  
 Medical ..... 0760

Geodesy ..... 0370  
 Geology ..... 0372  
 Geophysics ..... 0373  
 Hydrology ..... 0388  
 Mineralogy ..... 0411  
 Paleobotany ..... 0345  
 Paleoecology ..... 0426  
 Paleontology ..... 0418  
 Paleozoology ..... 0985  
 Palynology ..... 0427  
 Physical Geography ..... 0368  
 Physical Oceanography ..... 0415

**HEALTH AND ENVIRONMENTAL SCIENCES**

Environmental Sciences ..... 0768  
 Health Sciences  
 General ..... 0566  
 Audiology ..... 0300  
 Chemotherapy ..... 0992  
 Dentistry ..... 0567  
 Education ..... 0350  
 Hospital Management ..... 0769  
 Human Development ..... 0758  
 Immunology ..... 0982  
 Medicine and Surgery ..... 0564  
 Mental Health ..... 0347  
 Nursing ..... 0569  
 Nutrition ..... 0570  
 Obstetrics and Gynecology ..... 0380  
 Occupational Health and Therapy ..... 0354  
 Ophthalmology ..... 0381  
 Pathology ..... 0571  
 Pharmacology ..... 0419  
 Pharmacy ..... 0572  
 Physical Therapy ..... 0382  
 Public Health ..... 0573  
 Radiology ..... 0574  
 Recreation ..... 0575

Speech Pathology ..... 0460  
 Toxicology ..... 0383  
 Home Economics ..... 0386

**PHYSICAL SCIENCES**

**Pure Sciences**  
 Chemistry  
 General ..... 0485  
 Agricultural ..... 0749  
 Analytical ..... 0486  
 Biochemistry ..... 0487  
 Inorganic ..... 0488  
 Nuclear ..... 0738  
 Organic ..... 0490  
 Pharmaceutical ..... 0491  
 Physical ..... 0494  
 Polymer ..... 0495  
 Radiation ..... 0754  
 Mathematics ..... 0405  
 Physics  
 General ..... 0605  
 Acoustics ..... 0986  
 Astronomy and Astrophysics ..... 0606  
 Atmospheric Science ..... 0608  
 Atomic ..... 0748  
 Electronics and Electricity ..... 0607  
 Elementary Particles and High Energy ..... 0798  
 Fluid and Plasma ..... 0759  
 Molecular ..... 0609  
 Nuclear ..... 0610  
 Optics ..... 0752  
 Radiation ..... 0756  
 Solid State ..... 0611  
 Statistics ..... 0463

**Applied Sciences**

Applied Mechanics ..... 0346  
 Computer Science ..... 0984

Engineering  
 General ..... 0537  
 Aerospace ..... 0538  
 Agricultural ..... 0539  
 Automotive ..... 0540  
 Biomedical ..... 0541  
 Chemical ..... 0542  
 Civil ..... 0543  
 Electronics and Electrical ..... 0544  
 Heat and Thermodynamics ..... 0348  
 Hydraulic ..... 0545  
 Industrial ..... 0546  
 Marine ..... 0547  
 Materials Science ..... 0794  
 Mechanical ..... 0548  
 Metallurgy ..... 0743  
 Mining ..... 0551  
 Nuclear ..... 0552  
 Packaging ..... 0549  
 Petroleum ..... 0765  
 Sanitary and Municipal ..... 0554  
 System Science ..... 0790  
 Geotechnology ..... 0428  
 Operations Research ..... 0796  
 Plastics Technology ..... 0795  
 Textile Technology ..... 0994

**PSYCHOLOGY**

General ..... 0621  
 Behavioral ..... 0384  
 Clinical ..... 0622  
 Developmental ..... 0620  
 Experimental ..... 0623  
 Industrial ..... 0624  
 Personality ..... 0625  
 Physiological ..... 0989  
 Psychobiology ..... 0349  
 Psychometrics ..... 0632  
 Social ..... 0451



MEASUREMENTS AND PREDICTIONS OF TURBULENT FLOW  
STRUCTURES IN SIMULATED ROD BUNDLES

BY

XIAOHUA WU

A Thesis submitted to the Faculty of Graduate Studies of the University of Manitoba in partial fulfillment of the requirements for the degree of

DOCTOR OF PHILOSOPHY

© 1993

Permission has been granted to the LIBRARY OF THE UNIVERSITY OF MANITOBA to lend or sell copies of this thesis, to the NATIONAL LIBRARY OF CANADA to microfilm this thesis and to lend or sell copies of the film, and UNIVERSITY MICROFILMS to publish an abstract of this thesis.

The author reserves other publications rights, and neither the thesis nor extensive extracts from it may be printed or otherwise reproduced without the author's permission.

# Abstract

This research provided a package of experimental and numerical results. The phenomenon of unusual turbulence intensity distributions in closely-spaced rod bundles was first experimentally studied. The structures of fully developed isothermal air turbulent flow through simulated rod bundles were measured with hot-wire anemometers and a Preston tube. The rod bundle was formed by a single rod regularly mounted in a trapezoidal duct, and the Reynolds number range was  $2.5 \times 10^4$  to  $5.5 \times 10^4$ . The existence of a high turbulence kinetic energy patch was identified in the rod-to-wall gap region when the gap-to-diameter ratio  $g/d$  was within the range of 0.10 to 0.03 approximately. Energy density spectrum measurements revealed that cross-gap large-scale eddy motion is the probable mechanism behind this phenomenon and this kind of eddy motion is characterized by a peak frequency which depends on the geometry and flow condition. Secondary velocities on the rod setting with  $g/d$  as 0.220 were measured with X-probe; the obtained flow pattern coincided well with the bulges of wall shear stress and turbulence kinetic energy distributions. The impact of subchannel symmetry was also experimentally investigated.

Following these experimental studies, numerical predictions featuring the use of anisotropy factor and coordinate system transformation were carried out based on the finite volume method. Simulations were performed on fully developed turbulent flow through simulated symmetric rod bundle subchannels formed by the rod-trapezoidal

duct. With a unique coordinate system transformation from orthogonal cylindrical system to non-orthogonal curvilinear system, the highly irregular flow passage of rod-trapezoidal duct was converted to a regular rectangle. An empirical anisotropic eddy viscosity distribution derived from existing experimental data was used in conjunction with the algebraic stress model to address the influence of coherent large-scale cross-gap eddy motion, whose existence in closely spaced rod bundle subchannels has been substantiated by the extensive hot-wire measurements. Results of the calculation compared favourably with experimental data, with emphasis on secondary flow and turbulence kinetic energy. The credibility of this numerical scheme was established through a series of numerical tests on simple geometry flows.

Further numerical prediction on fully developed turbulent flow through simulated asymmetric rod bundle subchannels was carried out using the finite element method and standard two-equation turbulence model. Preliminary results indicated a large single vortex circulating around the rod which might explain the high mixing factors for asymmetric rod-to-wall gaps.

# Acknowledgements

The author wishes to express his heartfelt appreciation and gratitude to his advisor, Dr. A. C. Trupp, for his guidance and advice throughout this study. It is he who introduced the author into this challenging research area and his serious attitude on science has been and will always be a mirror for the author in his professional life. Words go short in expressing the author's indebtedness towards him.

Thanks are due to Dr. G. E. Sims and Dr. A. H. Shah who served as members of the author's advisory committee. Their valuable suggestions in this study are sincerely appreciated. Special thanks are extended to Dr. H. M. Soliman, who provided constant inspiration through his special interest in this research.

The funding provided by the Natural Sciences and Engineering Research Council of Canada through a grant to Dr. A. C. Trupp is gratefully acknowledged. During his program, the author held a University of Manitoba Graduate Student Fellowship, this support is also acknowledged.

The permission to access the finite element codes ANSYS 5.0 and FLOTRAN 2.1a by Wardrop Engineering Inc. is acknowledged.

# Nomenclature

$a_E, a_W, a_N, a_S, a_P$	coefficients of discretized linear equation (4.30)
$A( P )$	defined by Eq. (4.33)
$b$	half width of the trapezoidal duct bottom wall, also source term in Eq. (4.31)
$B$	bandwidth of digitization
$C_2, C_3, C_4$	related model coefficients in Eq. (4.4)
$C_{\epsilon_1}, C_{\epsilon_2}$	empirical constants in $k - \epsilon$ turbulence model, Eq. (4.6)
$c_p$	specific heat under constant pressure
$d$	rod diameter
$D_h$	hydraulic diameter
$D_n, D_s, D_e, D_w$	conductance defined by Eq. (4.32)
$\vec{e}_r, \vec{e}_\theta, \vec{e}_z$	unit vectors in cylindrical system
$E$	linearized hot-wire output
$E_{v_z'^2}, E_{v_{az}'^2}$	energy-density spectrum of axial and azimuthal component
$f$	frequency in energy spectrum, also Moody friction coefficient
$F_i$	source vector
$f_p$	peak frequency in energy spectrum
$F_n, F_s, F_e, F_w$	flow rates defined by Eq.(4.27)
$g$	gap spacing
$G$	production term for turbulence kinetic energy, Eq. (4.7)
$h$	height of the trapezoidal duct
$k$	mean turbulence kinetic energy, $(v_z'^2 + v_x'^2 + v_y'^2)/2$
$K$	calibration constant
$K_{ij}$	coefficient matrix
$l_t, l_i$	top and side wall lengths of the trapezoidal duct
$m'_{ij}$	mass flow rate between subchannels $i$ and $j$
$n(r, \theta)$	anisotropic eddy viscosity factor, Eq.(4.13)
$p$	pitch (distance between adjacent rod centers)
$q_{ij}$	heat transport between subchannels $i$ and $j$ , Eq. (3.3)
$r$	radial coordinate

$r_a, r_b(\theta)$	radii of inner and outer computational boundaries
$r_P$	radial coordinate of the the main grid point P
Re	Reynolds number (based on average axial velocity)
s	spacing between rod bottom and trapezoidal top surfaces
$S_{\Phi}(r, \theta)$	original source terms defined by Eqs.(4.1) to (4.3) and Eqs. (4.5) and (4.6)
$S_{\Phi}(\eta, \xi)$	transformed original source terms $S_{\Phi}(r, \theta)$
$S'_{\Phi}$	extra terms resulting from transformation, Eq.(4.23)
$S''$	extra term of the transformed continuity equation, Eq. (4.26)
$S'''$	defined by Eq.(4.34)
$Str_{\tau}$	Strouhal number ( $= fd/v^*$ )
$T_i, T_j$	bulk temperatures of two adjacent subchannels
$V_{eff}$	effective cooling velocity
$\bar{V}_z, \bar{V}_{z,b}$	local and bulk mean axial velocities
$\bar{V}_x, \bar{V}_y$	mean secondary velocities in horizontal and vertical directions
$\bar{V}_r, \bar{V}_{\theta}$	mean secondary velocities in radial and peripheral directions
$v'_z, v'_x, v'_y$	r.m.s. value of fluctuating velocities
$\overline{v_x v_y}, \overline{v_x v_z}, \overline{v_y v_z}$	tangential Reynolds stresses in Cartesian system
$\overline{v_r v_{\theta}}, \overline{v_r v_z}, \overline{v_{\theta} v_z}$	tangential Reynolds stresses in cylindrical system
$\overline{v_{\theta}^2}, \overline{v_r^2}$	normal Reynolds stresses in cylindrical system
$\overline{v_x^2}, \overline{v_y^2}$	normal Reynolds stresses in Cartesian system
$v^*$	average friction velocity [ $= (\bar{\tau}_w/\rho)^{1/2}$ ]
$\bar{v}^*$	average friction velocity derived from pressure drop
$v_{loc}^*$	local friction velocity, m/s
W	weighting function
$w_{eff}$	effective mean mixing velocity, Eq. (3.6)
x,y,z	Cartesian coordinates
Y	mixing factor defined by Eq. (3.10)

## Greek Symbols

$\alpha$	angle between wire normal and z-axis
$\epsilon$	rate of turbulence kinetic energy dissipation
$\bar{\epsilon}$	reference eddy viscosity
$\eta, \xi, \zeta$	curvilinear non-orthogonal coordinates
$\zeta^*$	nondimensional wall distance
$\gamma_w$	rotation angle of the wire around the z-axis

$\Gamma_{\Phi}$	effective transport coefficients
$\Gamma_r, \Gamma_{\theta}$	transport coefficients in radial and peripheral directions
$\delta_P^*$	non-dimensional wall distance, Eq. (4.14)
$\nu$	kinematic viscosity
$\mu$	dynamic viscosity
$\mu_t$	eddy viscosity
$\Phi$	general dependent variable
$\rho$	density
$\tau_w$	local wall shear stress
$\bar{\tau}_w$	average wall shear stress
$\theta$	angular coordinate, degree

### Subscripts

<i>az</i>	azimuthal component
<i>bottom</i>	bottom rod-to-wall gap or bottom duct wall
<i>incl</i>	inclined duct wall
<i>inlet</i>	inlet of the flow domain
<i>max</i>	maximum value
<i>pin</i>	in the presence of the support pin
<i>rod</i>	rod surface
<i>side</i>	side rod-to wall gap
<i>top</i>	top rod-to-wall gap, or top duct wall

# Contents

Abstract	i
Acknowledgements	iii
Nomenclature	iv
List of Figures	xi
List of Tables	xiii
<b>1 Introduction</b>	<b>1</b>
1.1 Rod Bundle Subchannel Flow .....	1
1.2 Simulated Rod Bundles and Motivation .....	2
1.3 Objectives .....	3
1.4 Layout of the Dissertation .....	4
<b>2 Review of Literature</b>	<b>5</b>
2.1 Scope of the Review .....	5
2.2 Experimental Investigations .....	6
2.3 Computational Simulation .....	16
2.4 Remarks .....	19
<b>3 Measurements of Turbulence Structures in Simulated Rod Bundles</b>	<b>21</b>

3.1	Experimental Apparatus .....	22
3.1.1	Wind Tunnel and Test Section .....	22
3.1.2	Instrumentation .....	26
3.1.3	Secondary Flow and Experimental Errors .....	28
3.2	Preliminary Results .....	29
3.2.1	Existence of Log-law .....	29
3.2.2	Proof of Developed Flow .....	31
3.2.3	Flow Symmetry .....	33
3.2.4	Support Pin Disturbance .....	35
3.3	Experimental Results .....	37
3.3.1	Turbulence Intensities .....	38
3.3.2	Turbulence Kinetic Energy .....	48
3.3.3	Reynolds Shear Stresses .....	53
3.3.4	Local Wall Shear Stress .....	54
3.3.5	Secondary Flow .....	57
3.4	Spectral Measurements and Mixing Correlation .....	61
3.4.1	Results of Power Spectral Density .....	62
3.4.2	Mixing Correlations .....	70
<b>4</b>	<b>Predictions of Turbulence Structures in Simulated Symmetric</b>	
	<b>Rod Bundles: Finite Volume Method</b> .....	<b>75</b>
4.1	Mathematical Formulations .....	76
4.1.1	Momentum Equations .....	76
4.1.2	Turbulence Model .....	78
4.1.3	Boundary Conditions .....	82
4.1.4	Coordinate System Transformation .....	85

4.2	Numerical Scheme .....	86
4.2.1	Discretization Procedure .....	86
4.2.2	Solution Procedure .....	91
4.3	Credibility Studies .....	93
4.3.1	Laminar Square Duct Flow .....	93
4.3.2	Turbulent Trapezoidal Duct Flow .....	94
4.3.3	Triangular Array Rod Bundles .....	96
4.4	Numerical Results .....	99
4.4.1	Friction Factors .....	99
4.4.2	Mean Axial Velocities .....	101
4.4.3	Secondary Velocities .....	104
4.4.4	Wall Shear Stresses .....	107
4.4.5	Turbulence Kinetic Energy .....	109
<b>5</b>	<b>Predictions of Turbulence Structures in Simulated Asymmetric Rod Bundles: Finite Element Method</b> .....	<b>112</b>
5.1	Mathematical Formulations .....	113
5.1.1	Momentum Equations .....	113
5.1.2	Turbulence Model .....	114
5.1.3	Boundary Conditions .....	116
5.2	Numerical Scheme .....	116
5.2.1	Discretization Procedure .....	117
5.2.2	Solution Procedure .....	120
5.3	Numerical Results .....	123
5.3.1	Mean Axial Velocities .....	123
5.3.2	Secondary Velocities .....	123

5.3.3	Turbulence Kinetic Energy .....	124
<b>6</b>	<b>Concluding Remarks</b>	<b>130</b>
6.1	Experimental Studies .....	130
6.2	Numerical Studies .....	132
6.3	Recommendations .....	134
	<b>References</b>	<b>136</b>
<b>Appendix A</b>	<b>Error Analysis of Secondary Velocity Measurements</b>	<b>142</b>
<b>Appendix B</b>	<b>Computer Code To Predict Real and Simulated Rod Bundle Subchannel Flows</b>	<b>159</b>

# List of Figures

Figure 3-1	Layout of the wind tunnel for rod bundle turbulence studies	23
Figure 3-2	Cross-section of the test rig	24
Figure 3-3	Check of linearized normal-wire calibration	27
Figure 3-4	Check of existence of the log-law of wall	30
Figure 3-5	Check of symmetry via local wall shear stress (a) left; (b) right	34
Figure 3-6	Contours of axial turbulence intensity $v'_z/v^*$ (a) Case A; (b) Case B; (c) Case C; (d) Case D; (e) Case F	40
Figure 3-7	Distribution of horizontal turbulence intensity $v'_x/v^*$ (a) Case A; (b) Case B; (c) Case C; (d) Case D; (e) Case F	44
Figure 3-8	Distribution of vertical turbulence intensity $v'_y/v^*$ (a) Case A; (b) Case B; (c) Case C; (d) Case D; (e) Case F	46
Figure 3-9	Contours of turbulence kinetic energy $k/v^{*2}$ (a) Case A; (b) Case B; (c) Case C; (d) Case D; (e) Case E; (f) Case F	50
Figure 3-10	Contours of tangential Reynolds shear stresses for Case B (a) $\overline{v_z v_x}$ ; (b) $\overline{v_z v_y}$	52
Figure 3-11	Distribution of local wall shear stress (a) Case A; (b) Case B; (c) Case C; (d) Case D; (e) Case F	55
Figure 3-12	Measured secondary velocity vectors for Case A	60
Figure 3-13	Energy density spectra for Case a1 (a) axial; (b) horizontal	66
Figure 3-14	Linear-log plots of energy density spectra for Case a2 (a) axial; (b) horizontal	67
Figure 3-15	Linear-log plots of energy density spectra for Case d2 (a) axial; (b) azimuthal	68
Figure 3-16	Correlation of Strouhal number and nondimensional gap size	69
Figure 3-17	Correlation of mixing factor and nondimensional gap size	74

Figure 4-1	Cross-section of general flow passage in numerical studies	77
Figure 4-2	Anisotropic factor $n(r, \theta)$ distributions (a) Case A ; (b) Case C	81
Figure 4-3	Control volume and staggered grids in transformed computational plane	88
Figure 4-4	Comparison of predicted and measured secondary flows in the trapezoidal duct	95
Figure 4-5	Comparison of predicted and measured wall shear stress in the trapezoidal duct	95
Figure 4-6	Comparison of predicted and measured turbulence kinetic energy in the trapezoidal duct	95
Figure 4-7	Cross-section of the triangular array rod bundle subchannel	98
Figure 4-8	Comparison of predicted and measured secondary flows in the triangular array rod bundle subchannel	98
Figure 4-9	Comparison of predicted and measured local wall shear stresses in the triangular array rod bundle subchannel	98
Figure 4-10	Friction factor dependence on Reynolds number	100
Figure 4-11	Comparison of predicted and measured mean axial velocities (a) Case A, prediction; (b) Case A, measurement; (c) Case C, prediction; (d) Case C, measurement; (e) Case D, prediction, (f) Case D, measurement	102
Figure 4-12	Predicted secondary velocity vectors in rod-trapezoidal duct (a) Case A; (b) Case C; (c) Case D	105
Figure 4-13	Comparison of predicted and measured local wall shear $\tau_w/\bar{\tau}_w$ in the rod-trapezoidal duct (a) Case A; (b) Case C; (c) Case D	108
Figure 4-14	Comparison of predicted and measured turbulence kinetic energy $k/v^2$ in the rod-trapezoidal duct (a) Case A; (b) Case C; (c) Case D	111
Figure 5-1	The cross section of the test rig for Case F	115
Figure 5-2	Solution flow chart by finite element method	124
Figure 5-3	Comparison between predicted and measured axial velocity for Case F (a) prediction; (b) measurement	125
Figure 5-4	Predicted secondary velocities for Case F (a) velocity vectors; (b) velocity magnitude	126
Figure 5-5	Predicted turbulence kinetic energy for Case F	129

# List of Tables

Table 3-1:	Dimensions of the rod-trapezoidal duct	25
Table 3-2:	Summary of experimental errors	29
Table 3-3:	Sample near-wall axial velocity distributions	31
Table 3-4:	Check of flow development and end blockage	33
Table 3-5:	Check of support pin disturbance	36
Table 3-6:	Summary of experimental conditions	37
Table 3-7:	Experimental conditions for spectrum analysis	62
Table 3-8:	Peak frequencies of rod-to-wall gaps	65
Table 3-9:	Summary of mixing velocity and mixing factor ( $Re = 52,000$ )	70
Table 4-1:	Comparison of numerical and analytical results for fully developed laminar square duct flow	94
Table 4-2:	Summary of numerically studied cases	99
Table 5-1:	Flow and geometric conditions of Case F	123
Table A-1:	Calibration position for secondary velocity measurements ( $s/d = 1.220$ )	149
Table A-2:	Systematic error constituents in secondary flow measurements	150
Table A-3:	Recapitulation of systematic error	156
Table A-4:	Directional response of X-wire via calibrator	157

# Chapter 1

## Introduction

During the past twenty years continued research efforts have been devoted to the field of axially developed turbulent flow through rod bundles due to its wide application in the nuclear energy industry. While such endeavours have resulted in solutions to many questions raised by the engineering sector, uncertainties still remain and new flow phenomena emerge from experimental observations. Among those are the roles of secondary flow and large-scale cross-gap eddy motion in rod bundle subchannel flows, which have recently received increasing attention.

### 1.1 Rod Bundle Subchannel Flow

Nuclear reactor fuel channels generally consist of a cluster of fuel rods arranged in a flow tube with the coolant moving axially through the subchannels formed between neighbouring fuel rods and between the peripheral fuel rods and the flow tube. The necessity to predict the bulk coolant temperature distribution among the various subchannels of the fuel bundle in reactor core design calls for knowledge about coolant mixing rates between homogeneous or heterogeneous subchannels. Under normal operational conditions in which coolant flow state is fully developed turbulence, three

different component mechanisms contribute to the overall mixing process; namely, turbulent diffusion, turbulent convection and convection by mean motion. Turbulent diffusion is of conventional gradient-type and is caused by small-scale turbulence of the order of magnitude of the dissipation scale or the integral scale. Turbulence convection originates from the large-scale motions of eddies comparable in size to the geometric characteristic length and is of non-gradient-type. Convection by mean motion denotes the transport by secondary flow of the second kind which in turn is caused by non-uniformities in wall turbulence and appear in channels which do not possess axial symmetry. The combined effect of these individual transport phenomena markedly modifies the temperature and velocity fields in the fuel channel transversal plane and hence influences the subchannel mixing process.

## 1.2 Simulated Rod Bundles and Motivation

The cross-section of a typical fuel bundle channel consists of various numbers of triangular array and square array interior subchannels plus some irregular wall subchannels. Direct measurements and simulations on coolant flow through these subchannels generated much useful information but was unable to unveil peculiarities of the three transport mechanisms. Imperfections of the geometry tend to swamp the sensitive and weak identities of turbulence and mean convection. In comparison, simulated rod bundles are more suitable for basic mechanism study due to their better construction tolerance. A number of such subchannels appeared in the course of researches conducted in this area; for instance, a duct consisting of a single row of rods between two flat walls. In this study, effort was spent on fully developed turbulent flow through a duct formed by a single rod regularly housed by a trapezoidal duct. This rod-trapezoidal-duct belongs to the family of simulated rod bundles. Such

flow was found to be of interest after a computer literature survey was conducted at the beginning of the research. Specifically, the important facts may be stated as follows:

1. Four subchannels are formed in the rod-trapezoidal duct which are interconnected via four rod-to-wall gaps. The top and bottom gaps provide linkages between two pairs of homogeneous subchannels and the two side gaps bridge two heterogeneous subchannels, respectively.
2. Alteration of the rod setting will bring about the change in four gap sizes, which would facilitate the study of the impact of the gap size on transport mechanisms.
3. Certain similarities exist in geometric shape between such subchannels and those in real fuel bundle subchannels, especially in the hexagonal duct bounded wall subchannels.

It is these considerations that motivated the present research.

### **1.3 Objectives**

The research involved two components; viz. , an experimental investigation of fully developed isothermal turbulent air flow through the rod-trapezoidal duct, and a numerical study on the same flow. The main objectives were as follows:

- A) To study experimentally the existence and effect of the large-scale turbulence convection, and to investigate the effect of gap size on such eddy motions.
- B) To correlate the turbulence convection with geometry and flow characteristics via spectrum analysis.

- C) To study experimentally the existence and effect of secondary flow convection.
- D) To correctly predict the main flow identities such as the turbulence convection effect and secondary velocity.

## 1.4 Layout of the Dissertation

This dissertation is composed of six chapters. An extensive review of the literature is supplied in Chap. 2. Full particulars of the experimental study are documented in Chap. 3 which include experimental setup, equipment, and preliminary and final results. Objectives A, B and C are dealt with in this chapter. Chapter 4 contains details of the numerical study on symmetric rod bundle subchannels by the finite volume method; the governing equations, coordinate system transformation, numerical scheme, test results and final outcomes are presented. Chapter 5 documents the finite element analysis on flow through asymmetric rod bundle subchannels. Finally, conclusions and recommendations are given in Chapter 6. Regarding the credibility of the experimental data, Appendix A presents the error analysis associated with the measurements of secondary velocity. The computer code employed in the numerical study reported in Chapter 4 is given in Appendix B.

# Chapter 2

## Review of Literature

Throughout the literature, information on the thermal-fluid aspects of nuclear reactor fuel channel design technology is widely scattered. Thus, this review is intended to gather the relevant contributions and to draw a clear picture of the background for the present research.

### 2.1 Scope of the Review

This review is limited to fully developed turbulent flow structure through real and simulated rod bundle subchannels. To highlight the previous studies, the review is organized in terms of experimental investigations and computational simulations. The experimental or numerical methodology and rod bundle geometry in each selected paper were addressed, with special emphasis on the results with direct relevance to the three major transport mechanisms governing subchannel mixing, i. e. turbulent diffusion, and turbulent and mean convection. In the experimental category, limited attention is given to empirical correlation studies about mass and heat subchannel mixing except for those providing direct linkage between coolant mixing and turbulence structure. In the numerical part, papers only concerning general model

development or computational schemes are excluded.

## 2.2 Experimental Investigations

Experimental research on fully developed flow through rod bundles can be traced back to as early as the 1950s. The early experimental studies concentrated on the overall flow properties such as flow resistance and pressure drop along the mainflow direction while the crossflow mixing was resolved by various empirical correlations. Among the numerous correlations of interest are those with implications concerning the effect of turbulence and mean convections on coolant flow mixing. Galbraith and Knudsen (1971) performed careful mixing experiments in a square array rod bundle with water over a wide range of pitch-to-diameter ratio ( $p/d$ ) from 1.228 to 1.011. They observed a negative dependence of the mixing rate upon rod gap size; surprisingly high mixing rates were found for very small gaps. Such mixing-rate and gap-size relationship suggested the presence of some transport mechanism(s) other than the conventional turbulence diffusion.

Having sensed the lack of information on local fluid flow, some measurements at the time-mean axial velocity level were carried out in the 1960s. Palmer and Swanson (1961) investigated the mean axial velocity distribution and the flow resistance of a triangular array rod bundle with  $p/d = 1.015$ . The velocity measurements were performed in air at a Reynolds number of  $2 \times 10^4$  using Pitot and Kiel probes. Excessively large flow resistances were reported for such a tightly packed rod bundle. The friction factors determined over a Reynolds number range of  $3 \times 10^3$  to  $3 \times 10^4$  were approximately 5% larger than those for smooth pipes. Eifler and Nijsing (1967) systematically studied the axial velocity fields and hydraulic resistance of triangular array rod bundles in fully developed turbulent flows. The velocity distributions

were obtained for  $p/d = 1.0, 1.025, 1.05, 1.1, 1.15$  in the Reynolds number range from  $1.3 \times 10^4$  to  $5.4 \times 10^4$ . Good agreement was reported between measured velocity profiles normal to the walls with Reichardt's velocity law. For the  $p/d = 1.15$  case, the friction coefficients after correction for test section wall effects were 15% higher than the corresponding values for smooth pipes. Subbotin et al (1971) used triangular array bundles with  $p/d = 1.05, 1.10, 1.20$  for air flow at Reynolds numbers around  $4 \times 10^4$ . Velocity and wall shear stress measurements were made using Pitot and Preston tubes, respectively. Axial velocity profiles normal to the walls showed good agreement with Nikuradse's law of the wall. For the case of  $p/d = 1.05$ , the isovels and the wall shear stress distribution showed distinct curvature suggesting the presence of secondary flows.

The turning point, marking the beginning of investigations on subtle turbulence structure influences on crossflow mixing process, did not occur until Kjellström (1971) reported his comprehensive study of fully developed turbulent air flows through a six-rod bundle of triangular array with  $p/d = 1.217$  using hot-wire anemometer. The experiments included measurements of friction factors, the distributions of axial and secondary flow velocities, Reynolds stresses and wall shear stresses in the Reynolds number range from  $5 \times 10^4$  to  $4 \times 10^5$ . The wall shear stresses showed a relatively flat distribution with a maximum of 3% variation around the average value. However, the skewness of the wall shear stress distribution suggesting the presence of secondary flows. Attempts to measure secondary flow velocities were mostly unsuccessful. The secondary velocities were less than one percent of the axial velocity with considerable scatter in the data. Turbulence intensity profiles normal to the walls were found to be in fair agreement with the data of pipe flow, but the axial velocity distribution normal to the walls did not show complete agreement with Nikuradse's universal velocity law.

Measured Reynolds stresses and velocity gradients were used to compute local eddy diffusivities. The results showed that momentum diffusivity is strongly anisotropic with circumferential diffusivity typically exceeding its radial counterpart by a factor of 5 near the walls. The core flow was found nearly isotropic.

Rowe et al (1974) systemized the argument that macroscopic turbulence structure influences the transport processes in rod bundle flow , especially in gap regions. LDA was used to resolve the mean-velocity distribution and two components of the Reynolds stresses, for developed flow of water through a square-pitch array with  $p/d = 1.125$  and  $1.250$ . Their Reynolds stress data showed that both the axial intensity and the intensity parallel to the walls were higher than in circular tubes. The turbulence intensities in the axial direction had a relative maximum on the centerline between subchannel centers and the rod gap, at about  $15^\circ$  to  $20^\circ$  from the gap. This relative maximum increased considerably with decreasing relative gap width or pitch-to-diameter ratio. The conclusion drawn was that macroscopic flow processes exist adjacent to the rod gap, including secondary flows and flow pulsations characterized by increased scale and dominant frequency with decreasing rod gap spacing. Their measured autocorrelation functions for the axial velocity component confirmed the existence of significant periodic flow pulsations in the gap regions. However, in some strongly asymmetric wall and corner subchannels, the axial intensity data did not show an increase but a decrease for the reduced gap spacing, suggesting the distinct effect of geometric symmetry on intersubchannel mixing. Secondary-flow cells were proposed for wall and corner subchannels, based on the distortions of the axial turbulence intensity. Such distortions, however, did not occur in interior subchannels.

Trupp and Azad (1975) performed a detailed study of fully developed turbulent

air flow through triangular array rod bundles with  $p/d = 1.2, 1.35$  and  $1.5$  over a Reynolds number range of  $1.2 \times 10^4$  to  $8.4 \times 10^4$ . Their data include friction factors, local wall shear stresses and the distributions of mean axial velocity, Reynolds stresses and eddy viscosities. Local values of the wall shear stress around the rods were measured using a flush-mounted hot-film probe and a Preston tube. The results showed a maximum of 3% variation about the average wall shear stress in the case of  $P/D = 1.20$ . Secondary flows were inferred from the skewed wall shear stress and the axial turbulence intensity distributions. Their Reynolds stress data, when scaled by the local friction velocity, established similarities with the data of circular tubes. The eddy viscosity parallel to the walls exceeded the eddy viscosity normal to the wall by a factor of at least 2 or 3. Attempts to measure secondary velocities using X-array probes in triangular-array rod bundles were unsuccessful and problems due to geometric imperfections were reported. Also, the velocity profile normal to the walls showed poor agreement with Nikuradse's universal law for pipe flow.

Carajilescov and Todreas (1976) investigated the problem of turbulent water flow through the interior subchannel of a triangular rod array with  $p/d = 1.123$  using LDA. Measurements of the distributions of axial velocity, turbulent kinetic energy and Reynolds stresses were performed in the Reynolds number range from  $9 \times 10^3$  to  $6.5 \times 10^4$ . Their Reynolds stress data showed the turbulence intensities for flow through rod bundles to be similar to the data of circular tubes, if scaled by the local wall friction velocity. They used the same technique as that of Rowe et al (1974), but experimental error precluded identification of secondary velocities having a magnitude less than 0.67% of the bulk velocity. This work was extended by Bartzis and Todreas (1979) and the importance of anisotropic viscosities in rod arrays was stressed.

The Reynolds stress data of Kohav et al (1976) showed that both the axial inten-

sity and the intensity parallel to the walls were higher than in circular tubes. This applied particularly to regions close to the gaps between the rods, and between the rods and channel walls. They observed a relative maximum of the turbulence intensities in the axial direction on the centerline between subchannel centers and the rod gap, at about  $30^\circ$  from the gap which confirmed the results of Rowe et al. (1974).

Fakory and Todreas (1979) measured the wall shear stresses and computed friction factors in the Reynolds number range from  $4 \times 10^3$  to  $3.6 \times 10^4$ . The experiments were performed with air and the wall shear stresses were measured by a Preston tube. Wall shear stress was found to increase monotonically from a minimum value at the rod gap ( $\theta = 0$ ) to a maximum value at the largest flow area ( $\theta = \pi/6$ ) which implied that secondary flows exerted little influence on the wall shear stress distribution. They also showed that, for fully turbulent flows with Reynolds numbers above  $9 \times 10^3$ , the normalized wall shear distributions were essentially independent of the Reynolds number. The friction factors computed using the average wall shear stresses were practically indistinguishable from smooth pipe friction factors at the same Reynolds number.

Rehme (1978, 1980, 1982, 1987a) reported a series of hot-wire experiments yielding detailed information on turbulent flow structure for wall and corner subchannels using four rods arranged in line with  $p/d = 1.036$  to 1.4. The experiments were performed with air flow at Reynolds numbers in the range from  $6 \times 10^4$  to  $2 \times 10^5$ . Most attention was directed to cases of closely-spaced rod arrays. The mean axial velocity and wall shear stress distributions showed little effect of secondary flows. An energetic and almost periodic azimuthal turbulent-velocity component directed through the gap governed the transport processes. The azimuthal turbulent-velocity component was found not to be associated with mean-secondary-flow velocities driven by Reynolds-

stress gradients, but rather generated by an incompressible-flow parallel-channel instability. Structural analyses were also performed for certain geometric configurations. The measured large length scales of the axial and azimuthal turbulent-velocity components relative to the gap width, emphasized the anisotropy of the turbulent transport processes in the gaps of rod bundles.

Chieng and Lin (1979) performed local velocity measurements in the outer subchannels of a CANDU type 19 rod bundle placed inside a smooth pipe using LDA at a Reynolds number of  $1.89 \times 10^5$  in water. Their results showed higher average and peak velocities as well as steeper velocity gradients in wall channels facing triangular subchannels as compared to geometrically similar ones facing square subchannels. It was also claimed that secondary flow velocities were measured and found to be negligibly small, but no data are presented in the paper.

Eichhorn et al. (1980) measured the wall shear stress distribution around the central rod of a 9 rod square array bundle using a flush-mounted hot-film sensor. The pitch to diameter ratio was 1.4 and the Reynolds numbers in water ranged from  $1.22 \times 10^4$  to  $3.15 \times 10^4$ . In all cases, the wall shear stress distributions were nearly sinusoidal in shape with the maxima and minima occurring at the maximum and minimum subchannel spacings, respectively. Hence, there was no discernible presence of secondary flows. Their data when normalized with respect to the average wall shear stress, showed a Reynolds number dependence which contradicted the results of Fakory and Todreas (1979). This discrepancy was attributed to the fouling of the hot-film by naturally occurring contaminants in water.

For the purpose to determine the effect of the displacement of one rod in a regular rod bundle on the field of local time-averaged hydrodynamic quantities, Hejna and Mantilk (1982) used a triangular array of 19 rods arranged with  $p/d = 1.17$  inside

a hexagonal flow channel, performed velocity and wall shear stress measurements in the Reynolds number range from  $3 \times 10^4$  to  $1.6 \times 10^5$ . Compared with the regular rod bundle, a more pronounced effect of the secondary flow was inferred from a number of anomalies in the wall shear stress distribution. The most typical effects include the marked local minima of the wall shear stress in wide parts of the channel and, conversely, local maxima in narrow parts of the channel and shifts of the maximum velocity lines. The normalised wall shear stress profiles were insensitive to Reynolds number variation and were skewed suggesting the presence of secondary flows. The distributions of axial velocity normal to the walls showed satisfactory agreement with Nikuradse's universal law of the wall.

Seale (1982) reported detailed measurements of mean axial and secondary flow velocities as well as Reynolds stresses at a Reynolds number  $2 \times 10^5$  in a duct that simulated the two interconnected subchannels of a rod bundle with a  $p/d = 1.20$ . Distributions of the principal Reynolds stresses normal to the duct wall were similar to those observed in axisymmetric pipe flow. The maximum secondary-flow velocities obtained by the cells circulating in the square corners of the duct were 1.5% of the bulk axial velocity. The maximum level in the single open rod-gap area was less, being approximately 0.5% of the bulk axial velocity. The presence of the secondary flow cells were also apparent from the wall shear stress distribution and from the distorted axial velocity and turbulent kinetic energy contours. Although particular emphasis was placed on the maintenance of the dimensional accuracy of the test section, such a channel does not occur in practical rod bundles and the secondary flow data were strongly affected by the corner of the test section, hence decisive conclusion for rod bundles should not be developed based on Seale's secondary flow data.

Hooper (1980) and Hooper and Wood (1984) used square-pitched and six-rod bun-

dles with  $p/d$  ratios of 1.107 and 1.194. Measurements of the mean axial velocities, wall shear stresses and Reynolds stresses were carried out using Pitot and Preston tubes, and hot-wire anemometry. They were the first to measure all components of the Reynolds stresses. Their results for the smaller gap  $p/d = 1.107$  showed that the shear stress  $\overline{\rho v'_r v'_\theta}$  may become significant in the gap region for small gaps. The departure of the turbulent flow structure from axisymmetric pipe flow was found to depend strongly on the  $p/d$  ratio, particularly in the rod gap regions. For the same  $p/d$  ratio, the normalized wall shear stress distributions around the rods showed only a weak dependence on Reynolds number. In the case of the  $p/d = 1.194$  bundle, the wall shear stress distributon attained a peak value at  $32^\circ$  (well before the  $45^\circ$  symmetry line) but this type of behaviour was not observed in the other channel. The secondary flow velocities could not be measured accurately, however, their attempted observation together with the turbulent kinetic energy profiles indicated their existence. Maximum axial turbulence intensity was found between  $15^\circ$  to  $20^\circ$  from the gap and was almost independent of the position normal to the wall. The azimuthal turbulence intensity had its maximum value directly in the gap. Moreover, the shear stress in the direction parallel to the wall showed the maximum values between  $15^\circ$  to  $20^\circ$  from the gap.

Hooper and Rehme (1984) confirmed the presence of an energetic large-scale and almost periodic momentum exchange process through the gap between rods through cross-correlation measurements. Both the axial and azimuthal turbulent velocity components were found to be significantly correlated for a considerable distance from the gap between the rods. The cyclic momentum exchange process generated by a pulsating flow between subchannels was claimed to be responsible for the increased levels of axial and azimuthal turbulence intensities in the open gap areas of rod-bundle

flow.

Vonka et al (1988), using LDA, successfully resolved secondary flow vortices in two regular subchannels of a triangularly arranged bare rod bundle with pitch-to-diameter ratio  $p/d = 1.3$  under the Reynolds number conditions  $6.0 \times 10^4$  and  $1.75 \times 10^5$ . One single secondary vortex, having the average tangential velocity slightly less than 0.1% of the mean bulk velocity, was resolved per minimum symmetry sector of the bundle geometry. The secondary vortex velocities, when normalized by the mean friction velocity, turned out to be independent of Reynolds number. Also the secondary velocity profiles showed a similar form for both Reynolds numbers. Comparing with the numerous conclusions inferred from the distortions of mean axial velocity and other turbulence quantities, their secondary flow data are among the few direct reliable proofs which support the existence of secondary flows in real rod bundle subchannels.

Renksizbulut and Hadaller (1986) performed experimental investigation of the distributions of wall shear stress, mean axial velocity and turbulence intensity in fully developed turbulent water flow through a six rod bundle ( $p/d = 1.15, s/d = 0.62$ ) at a Reynolds number of  $5 \times 10^5$ . Calibrated Preston tubes were used for the measurement of wall shear stresses. The results showed very large wall shear stress variations reaching  $\pm 40\%$  of the mean values around the rods. Although the secondary flow velocities were not measured directly, the skewed wall shear stress profiles together with the deformed isovels suggest their presence in the corner subchannels. However, their effects appeared to be minimal in the wall and central subchannels. Mean axial velocity and turbulence intensity measurements from laser-Doppler velocimetry indicated that the core flow in the central subchannel was similar to pipe flow, but much higher turbulence intensities were encountered in the gap regions. The data

suggested that, compared to triangular array bundles of nearly equal  $p/d$  ratios, square array rod clusters produce higher turbulence intensities at the gaps. Also, their results indirectly supported previous observations that turbulent mixing rate between adjacent subchannels was rather insensitive to gap size.

Experimental investigations on the turbulence structure of the flow through two asymmetric rod bundles were undertaken by Rehme (1987b). The rod bundles were arranged at  $p/d = 1.148$  and  $s/d$  ratios between 1.045 and 1.252. The narrow rod-to-wall gap connecting two symmetric subchannels whereas the wide rod-to-rod gap connecting two asymmetric subchannels. The experimental results showed that a strong momentum transport existed between the two asymmetric subchannels. The highest mean axial velocity of the narrow subchannel was found in the gap between the rods, rather than at the position of largest extent of the cross section of the subchannel. The rod wall shear stress distribution exhibited similar behaviour. The average wall shear stress in the narrow subchannel was smaller than that in the wide subchannel. The axial turbulence intensity reached high levels on the line of maximum normal distance from the walls at about  $30^\circ$  from the gap between the rod and channel walls in the narrow subchannels. The axial intensity increased with decreasing  $w/d$  ratio or decreasing gap width. The turbulence intensity parallel to the walls also increased with decreasing  $w/d$  ratio along the line of maximum normal distance from the walls in the region of the rod-to-wall gap. However, the highest values were found directly in the gap. High turbulence intensities in the symmetric gap were attributed to a periodic flow pulsation across the gaps between neighbouring two symmetric subchannels whereas those in the asymmetric gap were attributed to momentum transport between two asymmetric subchannels. No evidence of secondary flow was mentioned.

Möller (1991) investigated the macroscopic flow pulsations systematically using the same wall-bounded rod array as Rehme (1987a). Data via hot-wire measurements were evaluated to obtain energy spectra as well as autocorrelations and cross correlations. The dominant frequency of the flow pulsation was found to be a function of gap spacing and Reynolds number. Strong flow pulsations were found to persist for a rod gap with  $p/d$  value as low as 1.007. This work was recently analysed by Rehme (1992) and a simple correlation of mixing factor which claimed to be applicable for any gap geometry was developed.

## 2.3 Computational Simulation

The evolutionary nature of numerical studies conducted in the area of fully developed turbulent flow through rod bundle subchannels, like its experimental counterpart, has seen a progressive move towards the modelling of the combined effect of the three major transport mechanisms. The first generation of predictions in general involved many simplifications including ignoring cross-plane flows or allowing indirectly in some way for their effects. Bender and Switick (1968) presented a method to determine the two-dimensional axial velocity distribution for an infinite triangular array rod bundle. In this method, turbulent momentum transport was directly calculated via a mixing length theory based on actual flow geometry. The velocity solution was determined by iteration between the momentum equation and the definition of turbulent momentum diffusivity. This method did not allow for secondary flows and hence predicted the local wall shear stress to monotonically increase from the gap to the position facing the subchannel axial centerline.

The first simulations of the full three-dimensional flow field including secondary flow for rod bundle geometry are those of Carajilescov and Todreas (1976). Two

equilateral triangular arrays with  $p/d = 1.217$  and  $1.123$  were examined. They essentially applied the stream function and vorticity formulation and algebraic stress model proposed by Launder and Ying (1973). The vorticity production due to shear stresses was neglected and their own empirically derived length scale was used. A polar cylindrical mesh was employed in the calculation with special boundary cells at non-orthogonal intersections. Two cells of secondary flow were predicted in each subchannel. Predicted axial velocity were compared with LDA measurements. The distortions of axial velocity contours and wall shear stress distribution were attributed to secondary flow.

Trupp and Aly (1979) conducted a thorough numerical study on the secondary flow fields and other turbulence quantities for infinite equilateral triangular arrays having  $p/d$  range from 1.35 to 1.12. Again, the stream function/vorticity scheme and one equation Launder and Ying model was adopted with the inclusion of both normal and shear stress contributions to vorticity production. For all the cases, the secondary flow was found to be a single cell of circulation for each primary flow cell of a subchannel. The strength of the secondary flow increased with Reynolds number but decreased with rod spacing. The predicted wall shear stress variations and axial velocity and turbulence kinetic energy distributions offered good comparisons with existing experimental data. An important step was taken on investigating the effects of anisotropic eddy viscosities on turbulence structures through which they concluded that the effects of anisotropic eddy viscosities on the wall shear stress distributions were very similar to the effects provided by secondary flow.

Continued efforts on the prediction of secondary flow in infinite equilateral triangular array and finite seven rod cluster were made by Bartzis and Todreas (1979) and Benodeker and Date (1979), respectively. In both cases the  $k - \epsilon$  two equation

turbulence model and the Launder and Ying model were used, together with polar cylindrical meshes. Predicted secondary flow patterns appeared to be far from those expected, with up to three circulation cells in a subchannel for the geometry of Bartzis and Todreas (1979). Seale (1982) studied the secondary flow and other turbulence structures in a simulated rod bundle. A fairly coarse Cartesian mesh with step approximation on curved walls and empirical stress distributions based on his measurements were used, together with simulated turbulence kinetic energy profiles instead of the Launder and Ying stress model. The predictions obtained compared favourably with the measurements. In an effort to avoid any geometric compromise on subchannel boundaries, Rapley and Gosman (1986) used an orthogonal curvilinear mesh based SIMPLE method to study secondary flows in infinite triangular array rod bundles with three different gap spacings,  $p/d = 1.2, 1.123$  and  $1.06$ . Launder and Ying algebraic stress model and the  $k - \epsilon$  differential equation turbulence model were employed. Their predictions for different rod spacings agreed with existing experimental findings. A single circulation of secondary flow was predicted for both  $p/d = 1.06$  and  $1.123$ . In comparison, an additional minor swirl near the gap was predicted for the case of  $p/d = 1.20$ , and its influence was claimed to be trivial. The simulated rod bundle geometry of Seale (1982) was reexamined by Demuren (1991) using his algebraic stress model derived by simplifying model transport equations for the individual Reynolds stress. A non-orthogonal grid based SIMPLE numerical scheme was employed. Results essentially the same as those of Seale (1982) were obtained.

While numerous numerical studies have been conducted in the simulation of turbulent diffusion by small scale eddies and mean convection by secondary flow in rod bundle subchannels, progress in the modelling of the transport effect by large-scale

cross-gap eddy motion, i.e. turbulent convection which was experimentally studied by Hooper and Rehme (1984) is very limited. The only known attempt so far is that due to Lemos (1988). He tried to describe turbulence transport across closely-spaced rod bundle subchannel boundaries through an algebraic stress model which involves an approximation of the full transport equation for individual stress component. The coupling between the axial and lateral stresses at the gap region was suggested to be a function of the turbulence production and dissipation through the modelling of the wall correction to the pressure-strain correlation. The full system of equations were not solved (including equations for  $k$  and  $\epsilon$ ). Prediction was achieved through the prescription of ratio of turbulence production and dissipation. Comparisons between predictions and the experiments of Hooper and Rehme (1984) were only fairly good.

## 2.4 Remarks

Experimental and numerical researches on fully developed turbulent flow through rod bundle subchannels are now at the stage that while sufficient routine measurements and simulations have been done, a consensus still remains to be reached regarding the transport by turbulence and mean convection in gap regions. Controversies seem to be centered around several points,

1. Regarding the existence of the flow pulsation induced large-scale cross-gap eddy motion, recent experimental evidence was almost exclusively collected from the simulated rod-bundle subchannels at the Karlsruhe Nuclear Research Center (Rehme (1982), Hooper and Rehme (1984) and Möller (1991)). Further experimental corroboration from other laboratories is desirable.
2. The author believes that there must exist two threshold gap size values within

which turbulence kinetic energy will vary with gap spacing. Beyond the upper limit, subchannel mixing is governed by gradient-type turbulent diffusion. Below the lower limit mixing is dominated by laminar diffusion. In other words, the occurrence of large-scale cross-gap eddy motion, if it indeed truly exists as such, is confined to a specific range of gaps.

3. Regarding symmetric (homogeneous) versus asymmetric (heterogeneous) subchannels, to what extent is turbulence convection (by large eddies) influenced by the absence or presence of net mean convection by secondary flows? On the other hand, do secondary flows significantly penetrate the asymmetric boundary of two adjacent heterogeneous channels?
4. Since the majority of the existing turbulence models are constructed on the basis that transport is gradient-type diffusion, the inclusion of the non-gradient-type turbulence convection in the numerical simulation poses a challenging problem.

It is hopeful that this research will contribute towards clarifying these issues.

## Chapter 3

# Measurements of Turbulence Structures in Simulated Rod Bundles

The experiments described in this chapter were designed to examine fully developed turbulence structures in the simulated rod bundles formed by a rod-trapezoidal duct. Particular emphasis was placed on the study of the dependence of large-scale cross-gap eddy motion on rod-to-wall gap spacing. Some attention was also given to the examination of the variation of secondary flow in different rod orientations. With a single rod symmetrically mounted in a trapezoidal duct to simultaneously achieve a small bottom rod-to-wall gap and a correspondingly larger top one, it was expected that axial turbulence intensity would exhibit unconventional boundary layer behavior in the bottom gap region provided this gap spacing was small enough to fulfil some kind of geometric requirement. Then, when the rod was systematically moved vertically upward, the distinct region was expected to transfer accordingly from the bottom to the top region. With progressive rod movement upward, the trend could be tested until extremely small top gaps made any large-scale eddy motion between adjacent subchannels impossible. It was also intended to gain knowledge on the impact of subchannel homogeneity on the existence of turbulence convection by measuring

the turbulence structure for asymmetric rod setting with respect to the duct symmetry line. Other objectives were to correlate spectrum measurement results with flow and geometric conditions as well as providing reliable secondary flow pattern for the present simulated rod bundle subchannels (rod-trapezoidal-duct).

## 3.1 Experimental Apparatus

### 3.1.1 Wind Tunnel and Test Section

The wind tunnel, up to the test section of the current work, was that used previously by Trupp (1973) and later modified by Gerrard (1976). Construction details of this open circuit mode wind tunnel were fully described by Aly (1977). Isothermal atmospheric air was blown through the tunnel and discharged to atmosphere at the exit of the test-section. As already mentioned, the present simulated rod bundle was basically achieved by mounting a rod into an existing trapezoidal duct to simultaneously produce four subchannels bridged by top, bottom and two side gaps. The duct, which had been used by Khalifa and Trupp (1988), consists of a wooden entrance length ( $2.40 \text{ m} \pm 1.0 \text{ mm}$ ) and a final precision acrylic section ( $2.44 \text{ m} \pm 0.25 \text{ mm}$ ). Actually, this trapezoidal duct was obtained from an equilateral triangular duct (Aly et al. 1978) by installing an isosceles fillet at the upper vertex of the triangle. Layout of the wind tunnel, as well as the wooden entrance and test sections are illustrated in Fig. 3-1. The acrylic rod was made up of three sections with outside diameter of  $50.8 \text{ mm} \pm 0.2 \text{ mm}$ . The top and bottom duct wall lengths were  $50.8 \text{ mm}$  and  $127.0 \text{ mm}$ , and the inclined duct wall length was  $76.2 \text{ mm}$ . Variations in the side-wall lengths were less than  $\pm 0.25 \text{ mm}$  and  $\pm 0.10 \text{ mm}$  for the acrylic and wooden sections, respectively. Equivalent hydraulic diameter  $D_h$  of the cross-section was  $31.4 \text{ mm}$ . The cross-section of the simulated rod bundle is schematically shown in Fig. 3-2

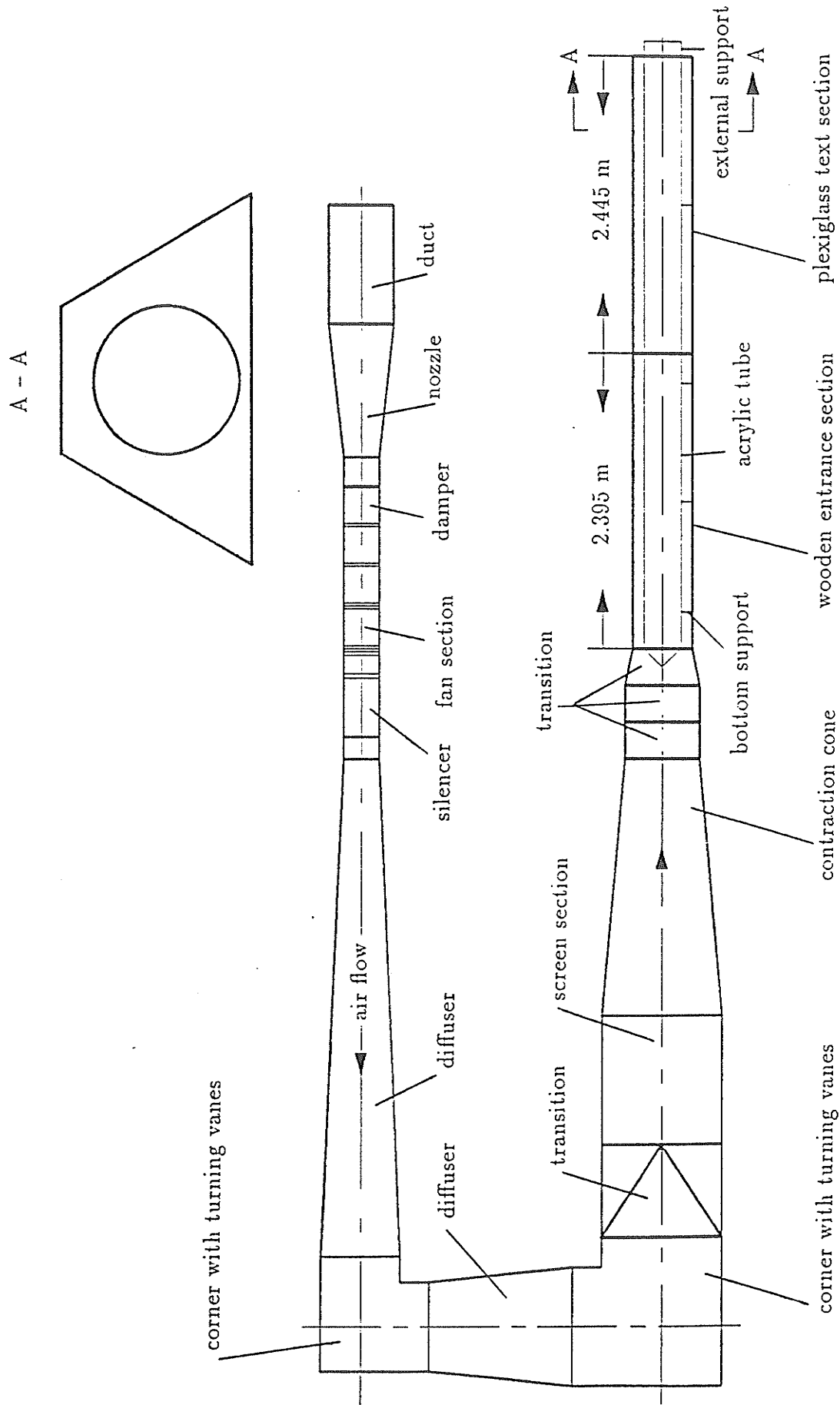


Figure 3-1 Layout of the wind tunnel for rod bundle turbulence studies

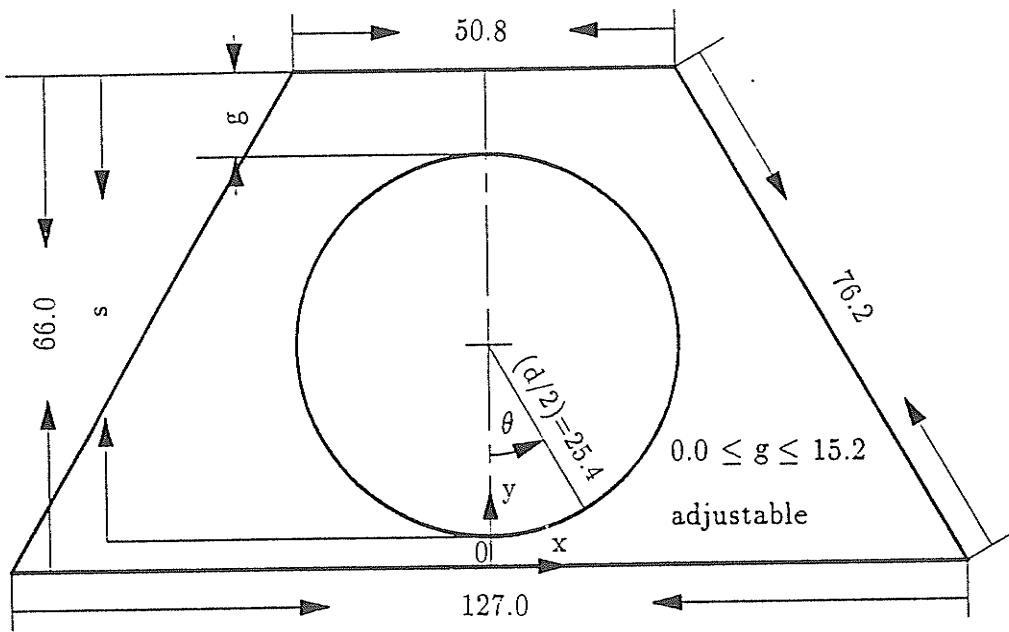


Figure 3-2 Cross-section of the test rig

and detailed dimensions and other geometric properties of the rod-trapezoidal duct are listed in Table 3-1.

Table 3-1: Dimensions of the Rod-trapezoidal Duct

rod outside diameter	50.8 mm	top duct wall	50.8 mm
bottom duct wall	127.0 mm	inclined duct wall	76.2 mm
top gap size range	0.0 ~ 15.2 mm	area	3844.1 mm <sup>2</sup>
perimeter	489.8 mm	hydraulic diameter	31.4 mm

In order to provide the longest possible entrance length and easy access, the measuring station was located 20.0 mm upstream from the open end of the duct. This location corresponded to a distance of about  $154.0 D_h$  from the test section inlet and  $77.6 D_h$  from the beginning of the acrylic duct. The rod position was attained and held using screws in a three-jaw-chuck arrangement in the wooden entrance section and in the acrylic test section a single vertical support pin which was located  $41.2 D_h$  upstream of the measuring station. The diameter of each support pin was 1.50 mm. Possible blockage effect by the rod support/spacer structure was investigated and results are documented in Section 3.2.4.

Provision for axial pressure gradient measurements was made by locating static taps at 152.4 mm intervals along the duct length. Taps in the wooden section consisted of 0.8 mm holes drilled midway across the base. In the plastic section, piezometric rings were formed by joining 0.6 mm square edge holes located in the middle of each wall. Connectors for the manometer tubing were epoxied in 8 mm holes drilled behind the small diameter holes.

### 3.1.2 Instrumentation

A Pitot tube with outside diameter of 1.07 mm and having inside to outside diameter ratio of 0.714 was used to calibrate the hot wire system. Pressure readings were taken using a Betz Projection Manometer which had a range of 0 ~ 400 mm H<sub>2</sub>O and an accuracy of  $\pm 0.05$  mm H<sub>2</sub>O. Reynolds number was evaluated from the mean axial velocity obtained by integrating the Pitot tube data. Turbulence measurements were made with linearized constant temperature hot-wire anemometer(DANTEC 55M01). This system was operated in conjunction with a DISA 55P11 single wire and a DISA 55P61 X-probe. The ancillary equipment consisted of DISA 55D35 rms voltmeter, DISA 55D31 digital voltmeter and DISA 55 turbulence processor. Data reduction from hot-wire experiments was performed according to Lawn (1969) and Vagt (1979). For spectral analysis, a KROHN-HITE model 3700 band-pass filter with cutoff frequency accuracy of 5 per cent was used. All hot wire probes were calibrated in situ against the Pitot tube located at the subchannel geometric central region with maximum axial velocity. A static calibration for the DANTEC 55M01 system with the DISA 55D10 linearizers consisted of multipoints over a narrow range. A set of typical calibration results is presented in Fig.3-3 for the DISA 55P61 X-probe.

Overall average friction velocity was obtained by averaging the local wall shear stresses from a Preston tube. The proper use of a Preston tube to determine wall shear stress, involves two nominal prerequisites; viz, the existence of a log law region and a probe size sufficiently small so as to be totally (or at least, largely) immersed in the log law region. The current Preston tube was small: 1.07 mm O. D. with 0.714 radius ratio. Measured near-wall mean axial velocity distributions (in directions normal to the duct wall or the rod), presented in Section 3.2.1, were found to be log law. Also since secondary flows were expected to be small, the wall shear stress direction always

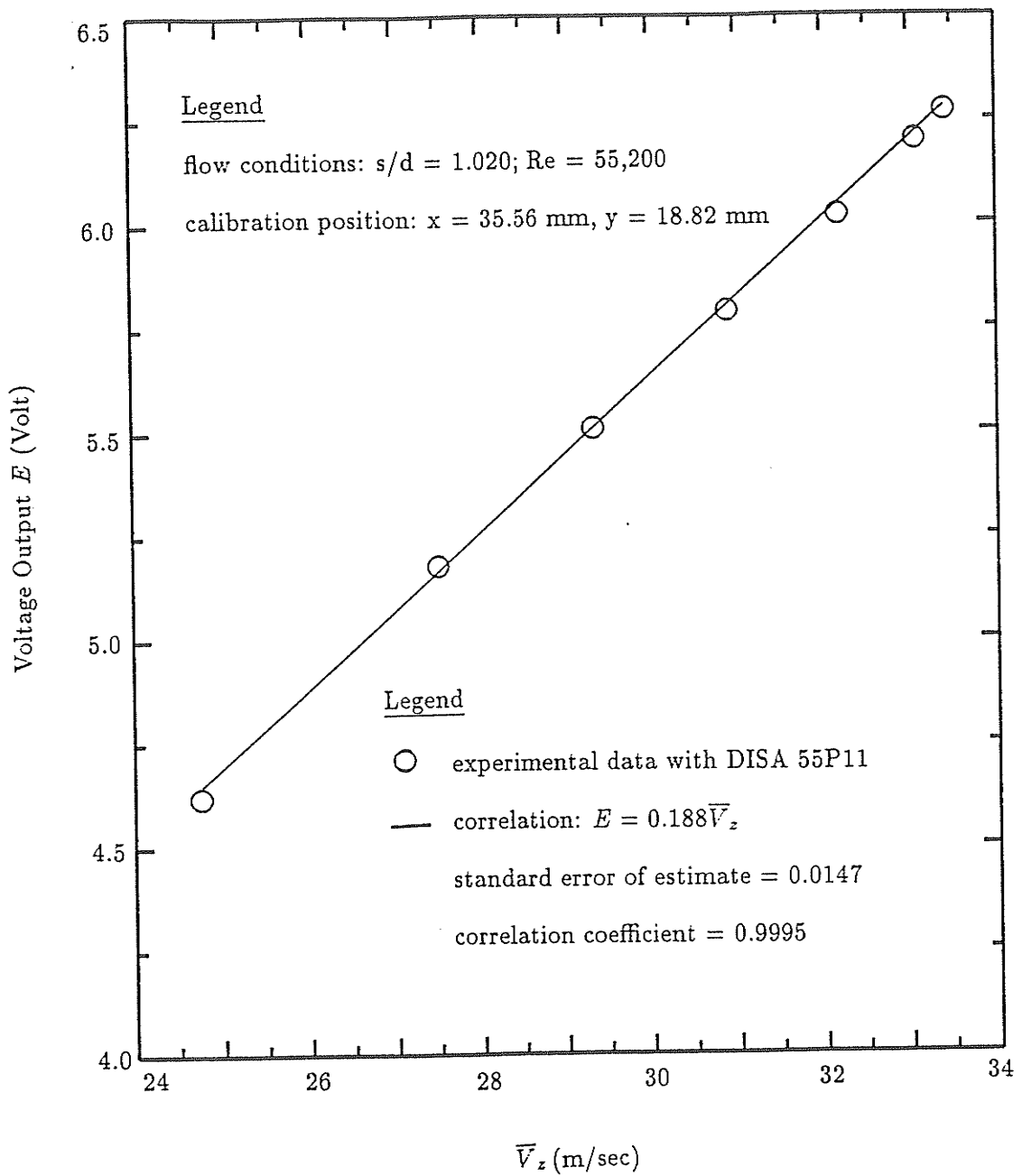


Figure 3-3 Check of linearized normal-wire calibration

essentially coincides with the axial ( $z$ ) direction. Overall, the use of the Preston tube was considered appropriate in this study.

Measurements were conducted on the basis of a Cartesian coordinate system (Fig. 3-2). Accurate relative positioning of either a Pitot tube or a hot-wire probe was achieved using a traversing mechanism having resolutions of 0.01 mm in both horizontal ( $x$ ) and vertical ( $y$ ) direction. Further details of the traversing mechanism were documented by Aly (1977).

### **3.1.3 Secondary Flow and Experimental Uncertainties**

Measurements of secondary flow by miniature DISA 55P61 X-probe followed the basic procedures followed by Aly et al. (1978) and by Khalifa and Trupp (1988) for the equilateral triangular duct and trapezoidal duct, respectively. However, in view of the comparative smallness of the present geometry and hence the associated steep mean velocity gradients, a compensation technique was applied to the secondary flow measurement. After measurements were completed with one of the two wires for one traverse, the X-probe was moved the (measured) wire-separation distance so as to locate the second wire to the same position as the first wire for the subsequent repeating traverse. More details about the secondary flow measurement technique can be found in Appendix A.

Given the fact that hot wire measurement is such a sensitive and intricate technique, it is quite natural that one inherent problem always associated with the application of hot wire anemometry is the estimation of experimental error. In this research, experimental errors were estimated using the method of Yavuzkurt (1984) and Vagt (1979). Such estimations were exemplified by a thorough error analysis on the measurement of secondary velocities that is documented in Appendix A. Certain doubt may arise on the applicability of the small signal assumption related to the

linearization of the hot-wire response to turbulence fluctuation. According to Hinze (1975), even though the truly correct measurement of turbulence of high intensity is nearly impossible, it is still permissible to use the linear relations to measure flows with a turbulence intensity of up to 20 or 25 per cent if errors of 10 per cent are acceptable, which is the case of the present experiment. Table 3-2 summarizes all the error estimations for measured quantities in this research.

Table 3-2: Summary of Experimental Uncertainties

Measured quantity	Uncertainty estimate
$E_{v_z'^2}, E_{v_x'^2}$	$\pm 16\%$
$f$	$\pm 5\%$
$\tau_w$	$\pm 2\%$
$V_{z,b}$	$\pm 1\%$
$\bar{V}_x, \bar{V}_y$	$\pm 47\%$ *
$v_z'$	$\pm 6\%$
$v_x', v_y'$	$\pm 12\%$
$k$	$\pm 12\%$
$\overline{v_z v_x}, \overline{v_z v_y}$	$\pm 22\%$
$z$	$\pm 0.1$ mm
$x, y$	$\pm 0.01$ mm

\* at the  $(0.01V_{z,b})$  level

## 3.2 Preliminary Results

Prior to undertaking detailed turbulence structure measurements, the apparatus was investigated for existence of log-law near wall axial velocity distribution, establishment of fully-developed flow conditions, disturbance of rod support pin and flow symmetry. All the preliminary tests were conducted at both the mean velocity and turbulence levels and by checking the local wall shear stress over the entire duct and rod perimeter.

### 3.2.1 Existence of Log-law

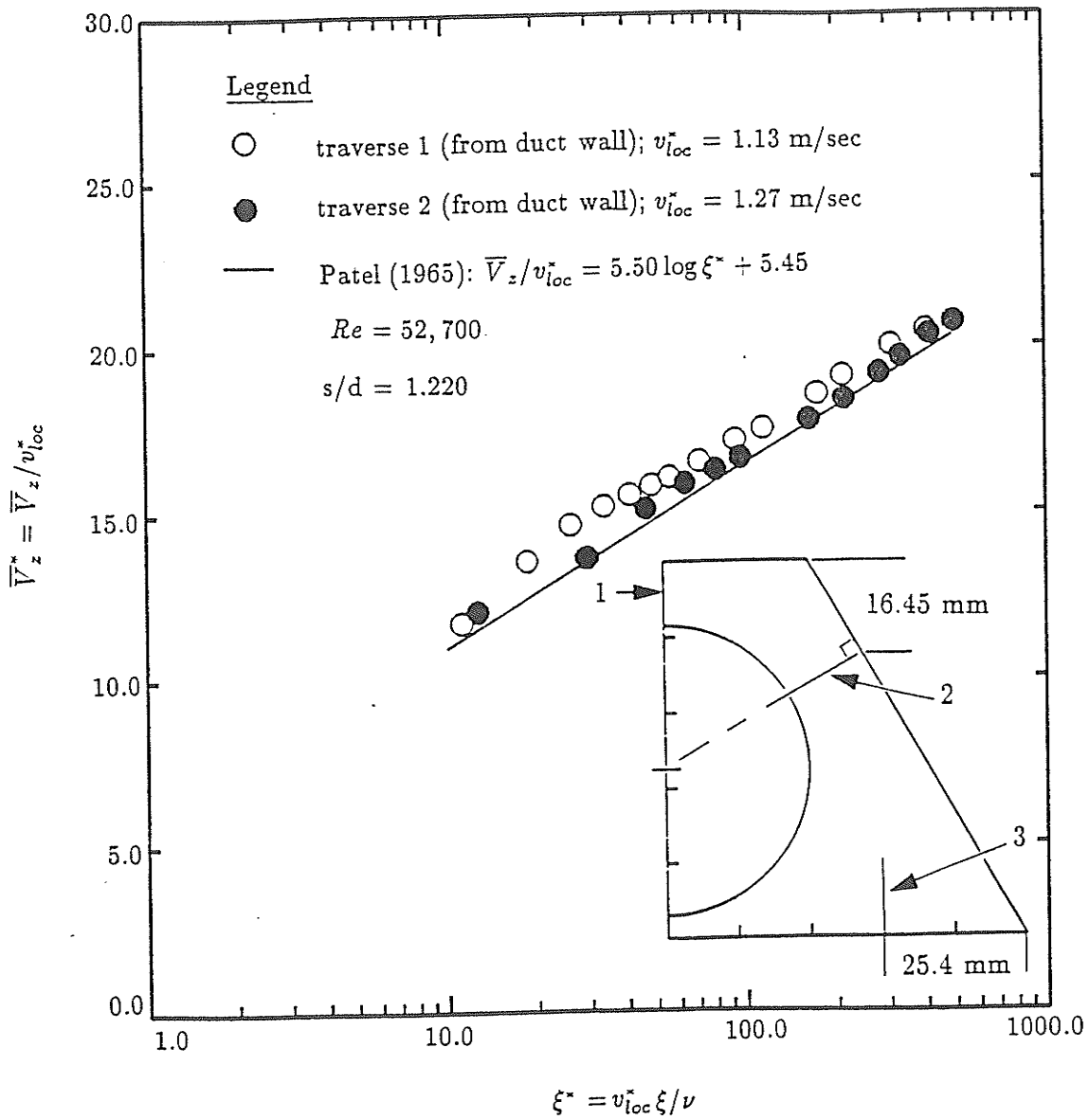


Figure 3-4 Check of existence of the log-law of wall

One of the prerequisites for the proper use of a Preston tube to measure wall shear stress is the existence of the log-law for the near-wall axial velocity distribution; such semi-empirical formula is also an essential boundary condition for the numerical simulation which follows later. In view of these necessities, in this research, near-wall axial velocity measurements were conducted with a flat-nosed Pitot tube which was capable of approaching to 0.15 mm from the wall. Fig. 3-4 compares the log-law obtained by Patel (1965) (which has been widely used to calibrate Preston tubes) with the present measurements along top and side gap traverses. Table 3-3 summarizes five correlation results based on data collected from three representative traverses which are schematically shown in the descriptive figure associated with Fig. 3-4. It was found that Patel's correlation ( $A = 5.50$  and  $B = 5.45$ ) offered a reasonably good average approximation for all the present correlations (maximum deviation 10% occurring at top gap), hence it was later used in the calibration of the Preston tube and in the description of wall functions for numerical studies.

Table 3-3: Sample Near-wall Axial Velocity Distributions  
 Form:  $\bar{V}_z/v_{loc}^* = A \log \xi^* + B$   
 $s/d = 1.220$ ,  $Re = 52,700$

Traverse Number	Wall	Rod	A	B	Max. $\xi^*$ in range	No. of data pts.	Std.Dev. (%) <sup>+</sup>
1	×		6.75	5.29	377	47	1.83
1		×	7.51	4.66	150	20	1.13
2	×		5.71	5.52	603	35	1.50
2		×	5.85	5.49	170	31	2.01
3	×		5.53	5.10	500	15	0.98

<sup>+</sup> Measured vs least-squares-fit ( $\bar{V}_z/v_{loc}^*$ ); expressed as a percentage of the average ( $\bar{V}_z/v_{loc}^*$ ) in the range

### 3.2.2 Proof of Developed Flow

As stated, the measuring station was located  $154.0 D_h$  from the test section inlet,  $77.6 D_h$  from the beginning of the acrylic duct and about 20.0 mm from the discharged

end of the test section. The entrance length required for fully developed conditions depends on the geometry and entrance conditions. Trupp and Azad (1975) reported that rod bundle geometries tend to require a short entrance length to reach fully developed state ( $16 D_h$  for their triangular array rod bundle). In the preliminary tests, mean axial velocity ( $\overline{V}_z$ ) and the normal and shear stresses,  $\overline{v_z^2}$  and  $\overline{v_z v_x}$ , were measured along different streamwise positions to check the axial gradient vanishments of these variables ( $\partial\Phi/\partial z = 0$ ). Longitudinally, probes were initially positioned at the duct exit ( $z = 0.0$ ) and after measurements on the point corresponding to the calibration position were performed, they were moved axially upstream to another cross section. Test results summarized in Table 3-4 clearly indicate that the flow at the measuring station was essentially fully developed. This conclusion was reinforced by the perfect linearity of the axial pressure gradient ( $\partial\overline{P}/\partial z = \text{const}$ ) starting as early as the beginning of the acrylic duct. Comparison between the data at the duct exit and at the measuring station revealed and there was negligible influence from any possible end-blockage effect.

Table 3-4: Check of Flow Development and End Blockage  
 $s/d = 1.220$ ,  $Re = 52,700$   
 $x = 35.56$  mm,  $y = 18.82$  mm

$z/D_h$	$\bar{V}_z/v^*$	$v'_z/v^*$	$\overline{v_z v_x}/v^{*2}$
0.00	24.85	1.14	0.005
0.08	24.85	1.14	0.005
0.16	24.85	1.14	0.005
0.24	24.85	1.15	0.006
0.32	24.85	1.14	0.005
0.40	24.85	1.14	0.005
0.48	24.85	1.14	0.004
0.56	24.85	1.14	0.005
0.64 <sup>+</sup>	24.85	1.14	0.006
0.88	24.85	1.14	0.005
1.20	24.85	1.13	0.004
1.60	24.85	1.14	0.005
2.00	24.85	1.14	0.005
2.40	24.85	1.15	0.005
2.80	24.85	1.14	0.003
3.20	24.85	1.14	0.005
3.60	24.85	1.13	0.006
4.00	24.85	1.14	0.005

<sup>+</sup> Measuring station

### 3.2.3 Flow Symmetry

The simulated rod bundle was formed by mounting a rod symmetrically (only in one case asymmetrically) with respect to the trapezoidal duct axis. Symmetries of flows in adjacent homogeneous subchannels were investigated in each rod setting case by checking the values of mean axial velocity, local wall shear stress and axial turbulence intensity between symmetric points. Fig. 3-5(a,b) compares the local wall shear stress distributions on the duct wall and rod surfaces for the rod setting  $s/d = 1.220$ . Maximum point deviation (1.2%) from symmetry occurred on the inclined duct wall where local maxima were attained. It was also found that differences

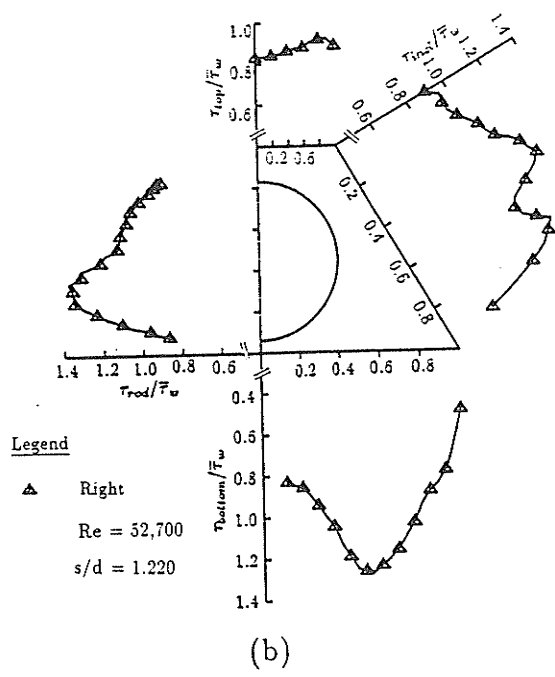
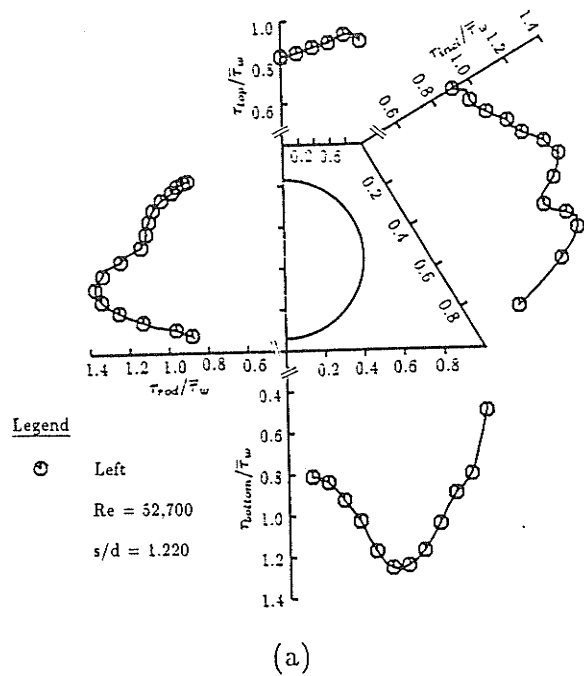


Figure 3-5 Check of symmetry via local wall shear stress  
 (a) left; (b) right

in mean axial velocity and axial turbulence intensity were less than 1.0% and 2.1%, respectively. Results for other geometric settings showed the same order of deviations with a slight tendency of higher asymmetry towards small  $s/d$  ratio settings.

### 3.2.4 Support Pin Disturbance

Attainment of a desired rod position in the trapezoidal duct was achieved by using screws in a three-jaw-chuck arrangement in the wooden entrance section and a single vertical support pin in the acrylic section. The last rod support pin was located  $41.2 D_h$  upstream of the measuring station. Possible disturbance from the support pin was investigated by inserting a test pin between the measuring station and the actual support pin. This extra test pin had the same diameter as the support pin (1.50 mm O. D. ) and its distance was  $24.8 D_h$  upstream of the measuring station. Measurements on axial velocity, wall shear and axial turbulence intensity were conducted before and after the installation of the test pin. Table 3-5 presents data to allow comparisons of bottom duct wall shear stresses and axial turbulence intensities. It was found that the differences for  $\tau_w$  and  $v'_z$  were within 0.5% and 1.0%, respectively. No measurable difference could be detected for  $\bar{V}_z$ .

Table 3-5: Check of Support Pin Disturbance

$s/d = 1.220$ ,  $Re = 52,700$

$\tau_w$  : bottom

$v'_z$ :  $x/b = 0.0$ ,  $y/h = 0.03$

$x/b$	$\tau_w/\bar{\tau}$	$\tau_{w,pin}/\bar{\tau}$	$v'_z/v^*$	$v'_{z,pin}/v^*$
0.00	—	—	—	—
0.04	—	—	1.65	1.65
0.08	—	—	1.66	1.66
0.12	0.84	0.84	1.71	1.72
0.16	0.86	0.86	1.78	1.78
0.20	0.90	0.89	1.83	1.84
0.24	0.95	0.95	1.91	1.91
0.28	0.99	0.99	1.94	1.94
0.32	1.04	1.05	1.98	1.98
0.36	1.11	1.11	2.01	2.02
0.40	1.17	1.18	2.01	2.02
0.44	1.23	1.23	1.98	1.98
0.48	1.27	1.27	1.98	1.98
0.52	1.28	1.29	1.97	1.97
0.56	1.26	1.26	1.98	1.98
0.60	1.23	1.24	2.02	2.04
0.64	1.19	1.19	2.09	2.10
0.68	1.14	1.15	2.11	2.12
0.72	1.07	1.07	2.07	2.08
0.76	0.99	1.00	1.94	1.94
0.80	0.92	0.92	1.82	1.82
0.84	0.87	0.87	1.72	1.72
0.88	0.83	0.83	1.63	1.63
0.92	0.75	0.75	1.48	1.48
0.96	0.58	0.58	—	—
1.00	0.49	0.49	—	—

### 3.3 Experimental Results

Five rod settings, (four symmetric with respect to the duct axis), were chosen in this research for the purpose of studying turbulence convection in different rod-to-wall gap regions of various dimensions. It is conventional to express rod-to-wall gap spacing in terms of a nondimensional ratio  $s/d$  named as the wall-to-diameter ratio as illustrated in Fig. 3-2. The geometric parameters corresponding to the five settings, together with Reynolds number and average friction velocities, are tabulated in Table 3-6. For the sake of consistency, all wall-to-diameter ratios,  $s/d$ , were deduced with reference to the top gap, hence it should be noted that a large  $s/d$  represents a small bottom gap and vice versa. In the case of the asymmetric rod setting with respect to the duct axis, the bottom and left-side gaps have the same dimension, 4.0 mm. Both the typical vertical and horizontal distances between neighbouring measuring positions on the test section are 1.0 mm.

Table 3-6: Summary of Experimental Conditions

Case	$g$ (mm)	$s$ (mm)	$s/d$	$v_z^*$ (m/s)	Re	$g/2v_{z,loc}^*/\nu^a$
A	11.2	62.0	1.220	1.24	52,700	412
B	4.0	54.8	1.078	1.30	55,200	161
C	3.0	53.8	1.059	1.26	54,200	117
D	1.0	51.8	1.020	1.26	55,200	21 <sup>b</sup>
E	11.2	62.0	1.220	0.55	21,300	183
F <sup>c</sup>	11.2	62.0	1.220	0.64	26,300	60 <sup>d</sup>

a: based on measured local wall (not rod) shear stress

b: estimated local wall shear stress

c: asymmetric, bottom gap size equals to left-side gap size,  $g = 4.0$  mm

d: evaluated for the left-side gap

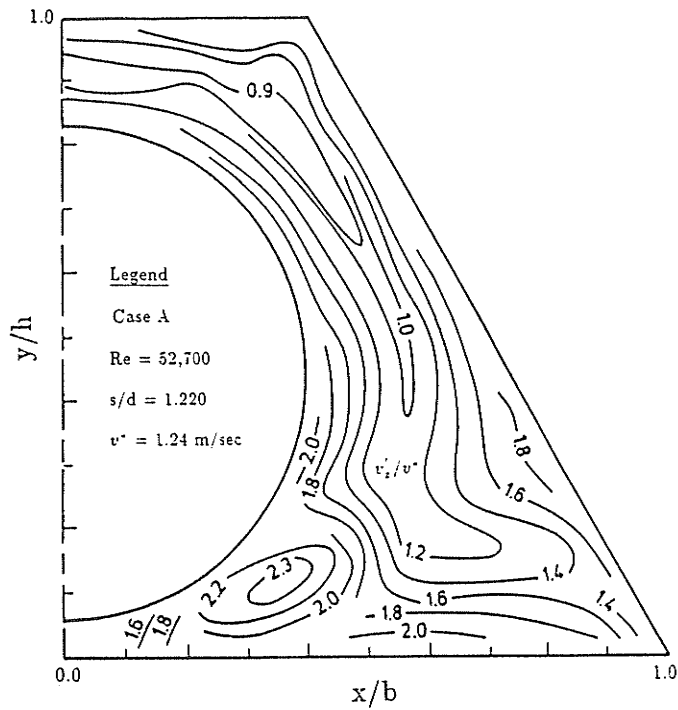
Experiments performed in cases A to D were aimed at examining the variation of turbulence convection with the change of gap size. It should be noted that the top

and bottom gap sizes in case A were interchanged in case B. The extremely small top gap in case D was used as a trial value for the critical gap size below which possible coherent relationship between adjacent subchannels was cut off. The study of Reynolds number dependence was made possible through the comparison between case A and E.

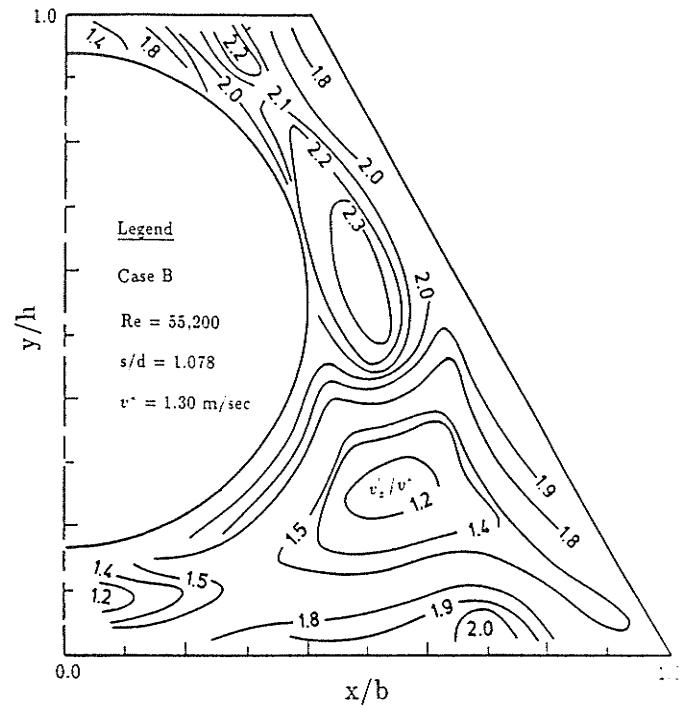
### 3.3.1 Turbulence Intensities

The turbulent velocity component in the longitudinal z-direction was measured with a normal hot-wire and the results were double checked with X-probe. The two sets of data gave identical trends and any quantitative discrepancies between them were within 1.5%. The existence of a distinctive patch of high axial turbulence intensity, and its migration in the cross-section with change in wall-to-diameter ratio  $s/d$ , is clearly illustrated in the nondimensional contour plots of  $v'_z/v^*$  shown in Fig. 3-6(a)-(d). For the case of a small bottom gap ( $s/d = 1.220$ , Case A),  $v'_z/v^*$  distributions are fairly normal, (apart from obvious distortions caused by secondary flow convection) with one major exception. A region with unusual  $v'_z/v^*$  distribution can easily be discerned near the small bottom gap between  $\theta = 30^\circ$  and  $60^\circ$ . In this distinctive area,  $v'_z/v^*$  increases radially from the vicinity of the rod surface up to approximately the subchannel center corresponding to this radial direction. The peak magnitude of  $v'_z/v^*$  in this spot region surpasses those in any other regions of the whole flow cross-section (except, of course, for perhaps very near walls where measurements could not be made). It should also be noted that when normalization is made using local friction velocities  $v_{loc}^*$  instead of the overall average values  $v^*$ , the resulting contour plots preserve the basic patterns as in Fig. 3-6 with only slight changes in magnitude. The dependence of the unusual axial turbulence intensity distribution on rod-to-wall gap spacing is illustrated by comparing Fig. 3-6(a) and

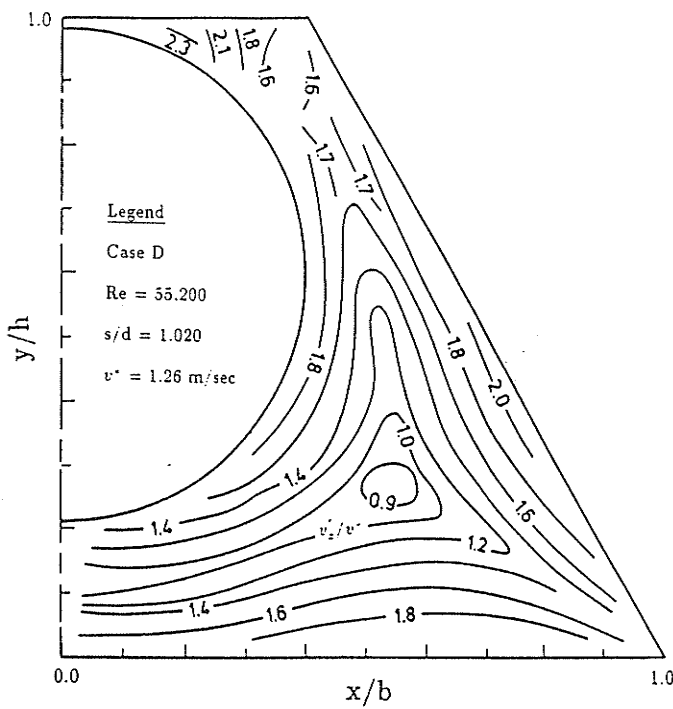
Fig. 3-6(b), noting that the bottom gap spacing in Fig. 3-6(a) is equal to the top gap spacing in Fig. 3-6(b) (both 4.0mm). The shift of the high-intensity region from between  $\theta = 30^\circ$  and  $60^\circ$  to  $\theta = 80^\circ$  and  $130^\circ$  indicates that its existence is tightly related to relative gap size. Two other notable features are the relative invariance of the peak magnitudes of  $v'_z/v^*$  in these two cases and the larger area of the distinctive region in the latter case. Also whereas turbulence intensities are fairly similar in the regions immediately adjacent to the two (small) 4 mm gaps, turbulence intensities are quite different in the vicinity of the two (large) 11.2 mm gaps. These differences in overall structure for the larger gaps indicate a strong effect of the channel walls which are different in both cases. A comparison of Figs. 3-6(b) and 3-6(c) indicates that there is an increase in magnitude of the axial turbulence intensity  $v'_z/v^*$  with decreasing rod-to-wall spacings. A slight decrease in rod-to-wall gap spacing (from 4.0 mm to 3.0 mm) markedly enhanced the level of  $v'_z/v^*$ , especially in the peak region. This trend is in agreement with those reported by Rowe et al (1974), and by Hooper and Rehme (1984). More importantly, the question as to whether or not the above trend continues to extremely small gaps, is answered by comparing Fig. 3-6(c) and 3-6(d). Whereas Fig. 3-6(c) ( $g = 3.0$  mm) has an obvious atypical axial turbulence intensity distribution, no unusual distribution of  $v'_z/v^*$  can be discerned in Fig. 3-6(d) ( $g = 1.0$  mm). According to Hinze (1975), for moderate flow velocities (not much greater than 100 m/s), the smallest space scale or eddy will be hardly less than 1 mm, i.e. the gap size for Fig. 3-6(d). This implies that the small gap for Fig. 3-6(d) renders the coherent connection between the two adjacent subchannels practically infeasible. At the same time, it appears very possible that the existence of the unusual  $v'_z/v^*$  distribution is related to cross-gap eddy motion which applies only to cases of moderately small gaps.



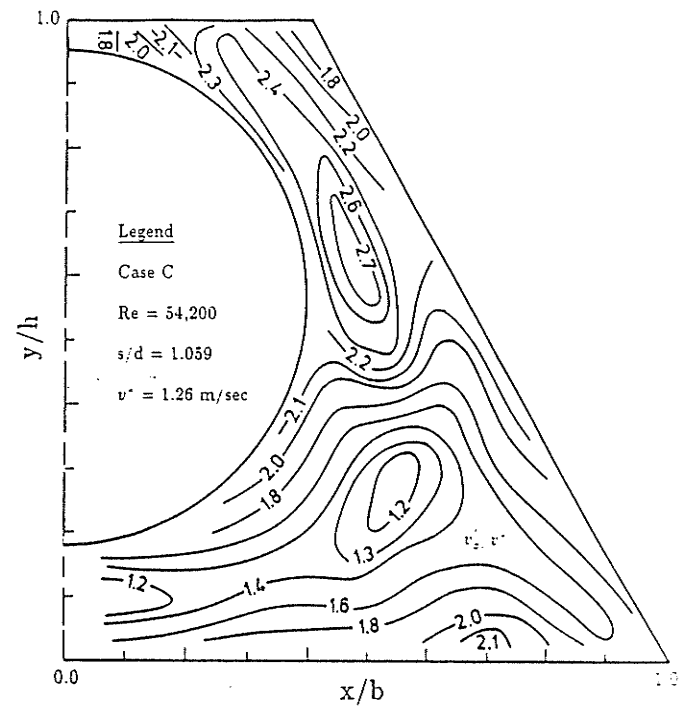
(a)



(b)

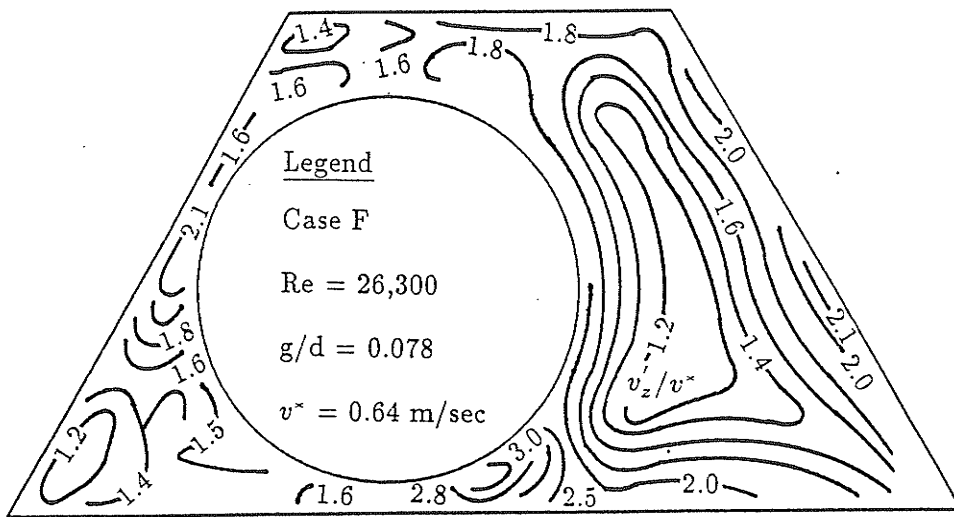


(d)



(c)

Figure 3-6 Contours of axial turbulence intensity  $v'_z/v^*$   
 (a) Case A; (b) Case B; (c) Case C; (d) Case D; (e) Case F



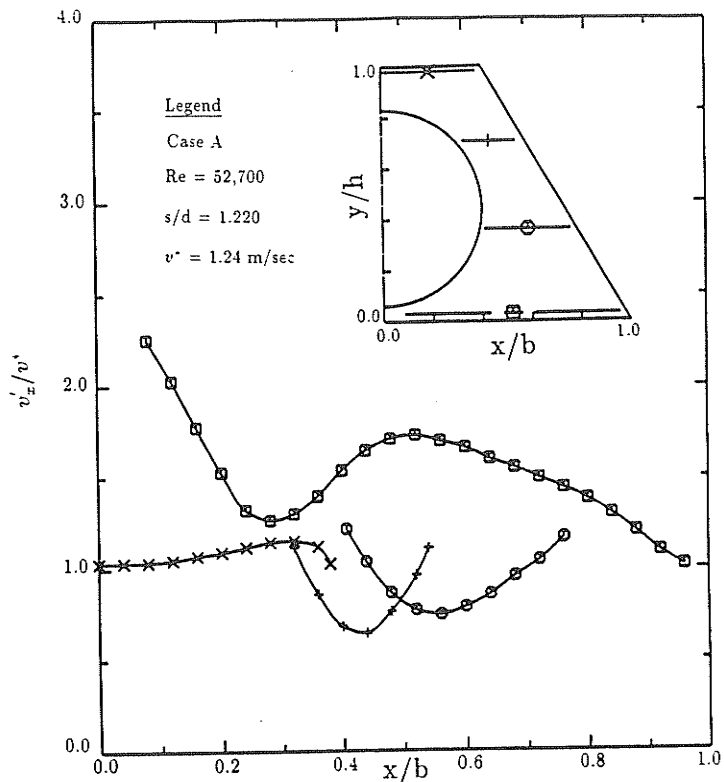
(e)

Figure 3-6 Contours of axial turbulence intensity  $v'_z/v^*$   
 (a) Case A; (b) Case B; (c) Case C; (d) Case D; (e) Case F

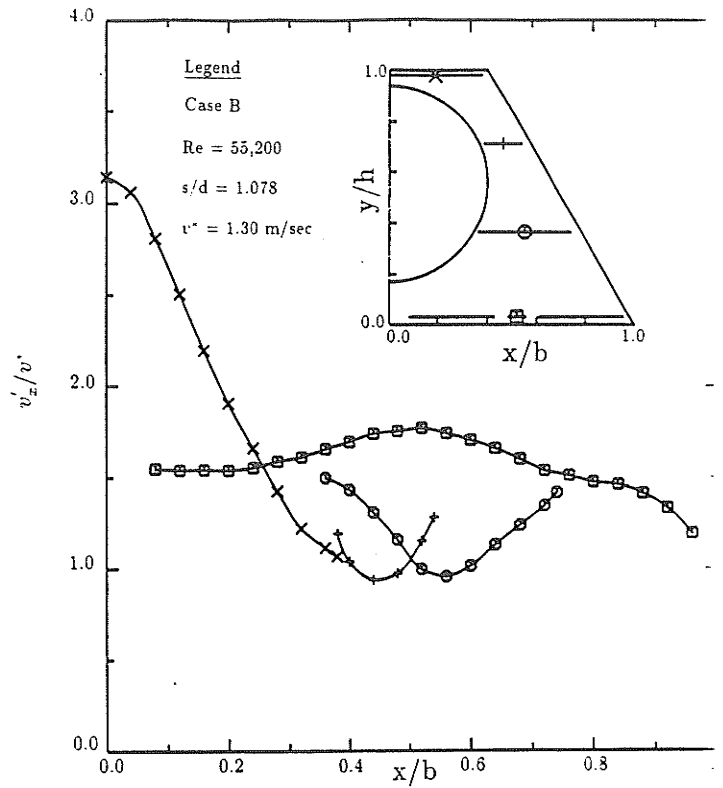
Fig. 3-6(e) gives the contour plots of  $v'_z/v^*$  for the asymmetric rod setting (Case F,  $g = 4.0$  mm, bottom and left-side). The distortions in the contours of the right-half of the flow cross-section are similar to those in Fig. 3-6(a) which has the same bottom gap size (4.0 mm), suggesting similar secondary flow patterns. Quite obvious is the difference between the two sides of the bottom gap in Fig. 3-6(e) where  $v'_z/v^*$  in the right (with the large subchannel size) shows an unconventional distribution, but in the left (with small subchannel size) the axial turbulence intensity distribution is quite conventional. In the left-side gap area, the local subchannel maximum of  $v'_z/v^*$  value of (2.1) occurs not right in the gap but slightly aside from it towards the bottom corner subchannel which is relatively large in size compared to the top subchannel. This suggests the possible influence of cross-gap eddy motion. Comparison of Fig. 3-6(a) and (e) (same  $g/d$ ) only offers a gray picture regarding the dependence of axial turbulence intensity on subchannel/symmetry.

Normalized turbulent velocity components in the horizontal ( $x$ ) direction  $v'_x/v^*$  are given in Fig. 3-7(a)-(e). It is noted that the direction of this component is tangential to the top and bottom gaps, therefore, the term azimuthal intensity is occasionally used to denote  $v'_x$  in a broad sense. For cases A to D, results along four representative traverses are shown in Fig. 3-7(a)-(d), and for asymmetric case F, contour plots are presented. The most notable feature in Fig. 3-7(a), where  $s/d = 1.220$ , are the high levels of  $v'_x/v^*$  that are attained in the bottom gap. Here  $v'_x/v^*$  levels reached as high as 2.3, exceeding those for  $v'_z/v^*$  (less than 1.6) in Fig. 3-6(a); This experimental evidence is a strong indication of the existence of an energetic cross-gap eddy motion. Hooper and Rehme (1984) reported, for a rod-to-wall gap with similar size to Case B ( $g/d = 0.071$  instead of 0.078), that  $v'_x/v^*$  reached about 2.0 right in the gap, which also exceeding their  $v'_z/v^*$  about (1.7) at the same place. However, the results

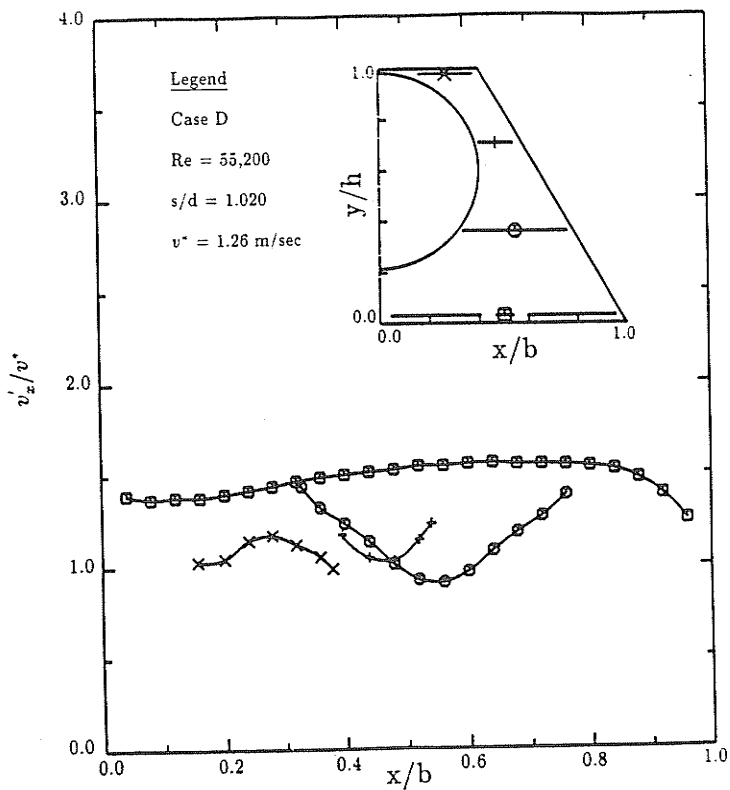
for the other three traverses for Cases A and B are more typical of non-circular duct flows. The large bulge in the central part of the bottom traverse for Case B is partly due to the large flow cross area it occupies and to the transport by secondary flow. The parabola-shaped  $v'_x/v^*$  distributions along the two central traverses are essentially similar to that of pipe flow where turbulence is mainly generated adjacent to the duct wall, causing turbulence intensity to decrease monotonously from wall to subchannel center. For Case A on the top traverse, the nearly-flat distribution indicates the influence of secondary flow is trivial. Next, comparing Figs. 3-7(a) and (b), similar to the variation of  $v'_z/v^*$  with  $s/d$  discussed earlier, there is a shift of the high peak of the azimuthal turbulence intensity from the bottom gap to the top gap which corresponds to the decrease of the top rod-to-wall gap spacing from 11.2 mm to 4.0 mm. Peak values (when normalized by  $v^*$ ) are higher in Fig. 3-7(b); about 3.2 compared to about 2.3 in Fig.3-7(a). The quantitative dependence of the azimuthal turbulence intensity on wall-to-diameter ratio is further illustrated in Fig. 3-7(b) versus Fig. 3-7(c). With a slight decrease in top gap size from 4.0 mm to 3.0 mm, the distribution of  $v'_x/v^*$  becomes markedly steeper and the peak value jumps from about 3.2 to 3.6. Such an increase suggests that the magnitude of the energetic cross-gap eddy motion can be enhanced by decreasing gap size, provided that the gap size falls within a certain medium-small range. But the sizeable increase in  $v'_x/v^*$  with decreasing  $s/d$  holds only true for a narrow gap range since data from the other three traverses stay at about their original levels. Finally, a comparison of Fig. 3(c) (medium-small top gap,  $g = 3.0$  mm) to Fig. 3(d) (extremely small top gap  $g = 1.0$  mm) shows a dramatic change in the  $v'_x/v^*$  distributions around the top gap. Along the top traverse, horizontal turbulence intensity falls from its previous peak value of about 3.6 to 1.0, implying the disappearance of energetic cross-gap eddy motion.



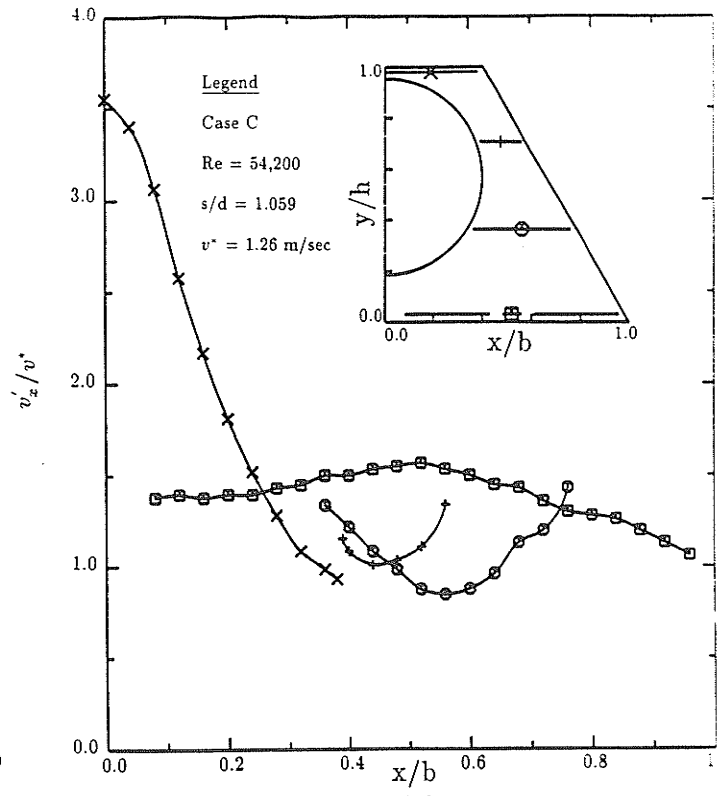
(a)



(b)



(d)



(c)

Figure 3-7 Distribution of horizontal turbulence intensity  $v'_x/v^*$   
(a) Case A; (b) Case B; (c) Case C; (d) Case D; (e) Case F

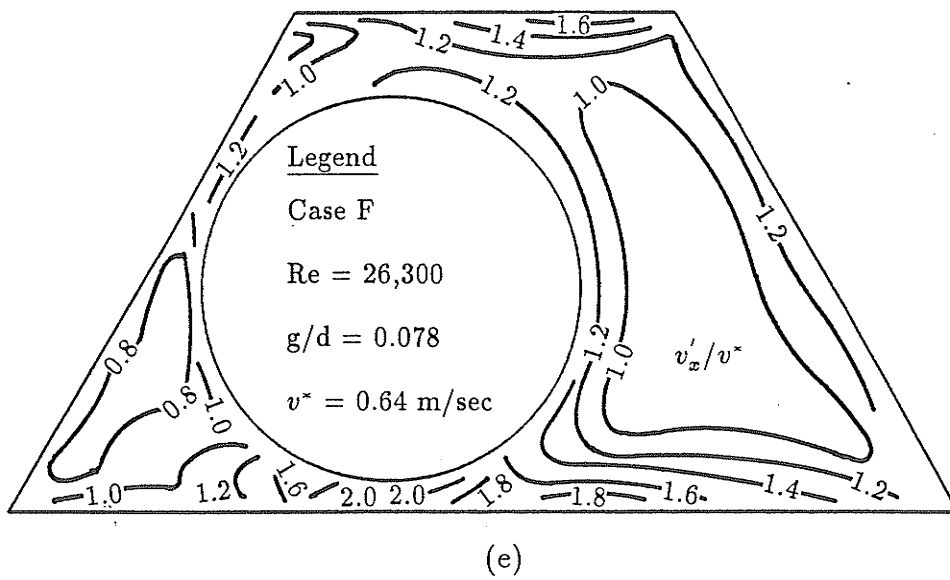


Figure 3-7 Distribution of horizontal turbulence intensity  $v'_x/v^*$   
 (a) Case A; (b) Case B; (c) Case C; (d) Case D; (e) Case F

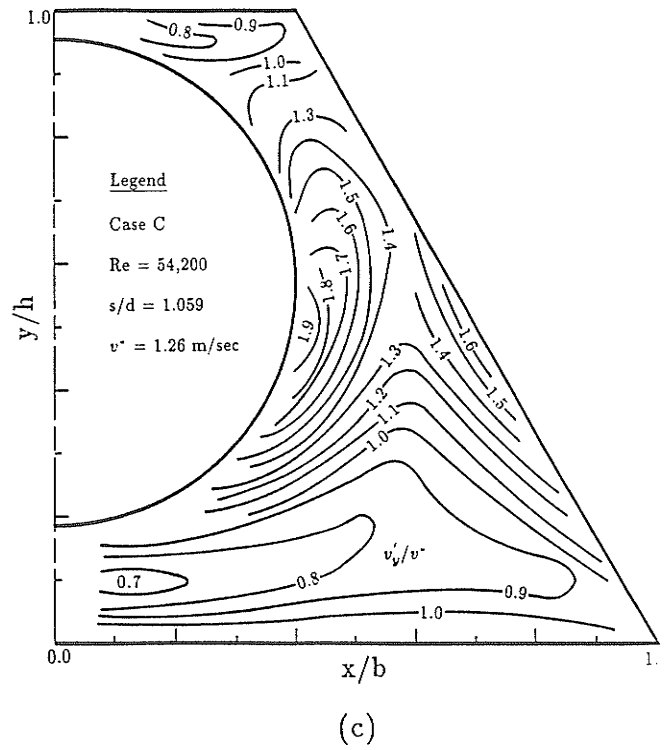
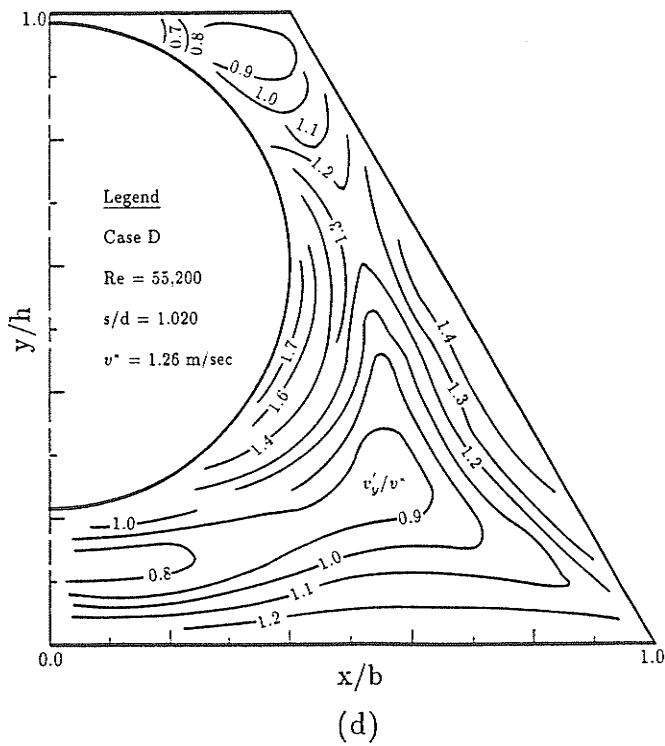
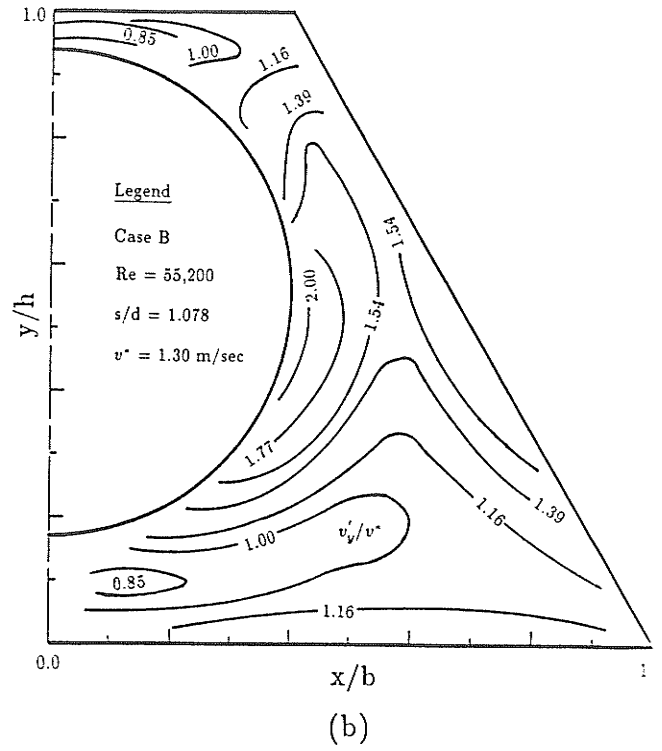
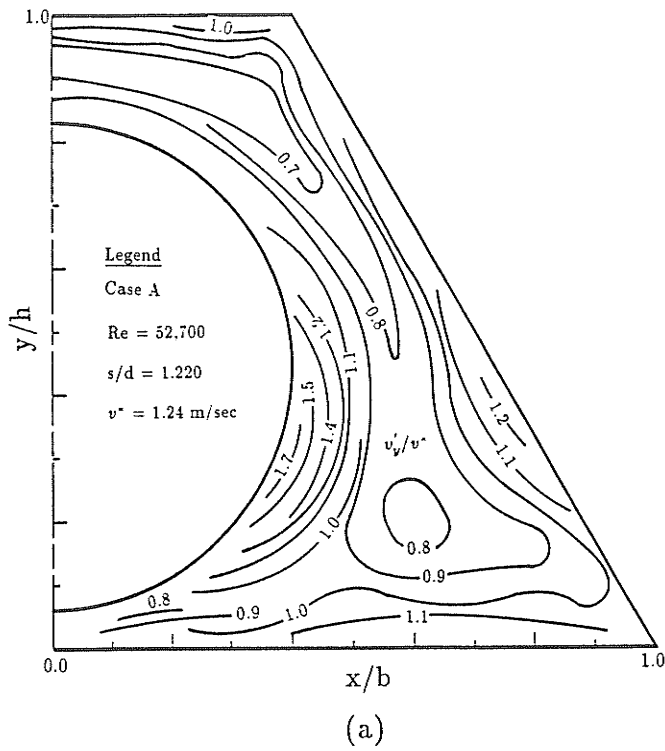


Figure 3-8 Distribution of vertical turbulence intensity  $v'_y/v^*$   
(a) Case A; (b) Case B; (c) Case C; (d) Case D; (e) Case F

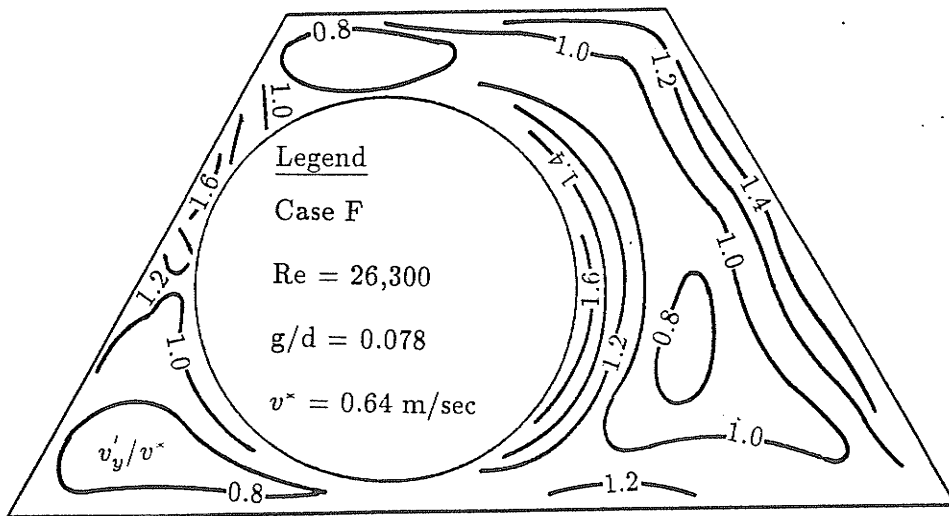


Figure 3-8 Distribution of vertical turbulence intensity  $v'_y/v^*$   
 (a) Case A; (b) Case B; (c) Case C; (d) Case D; (e) Case F

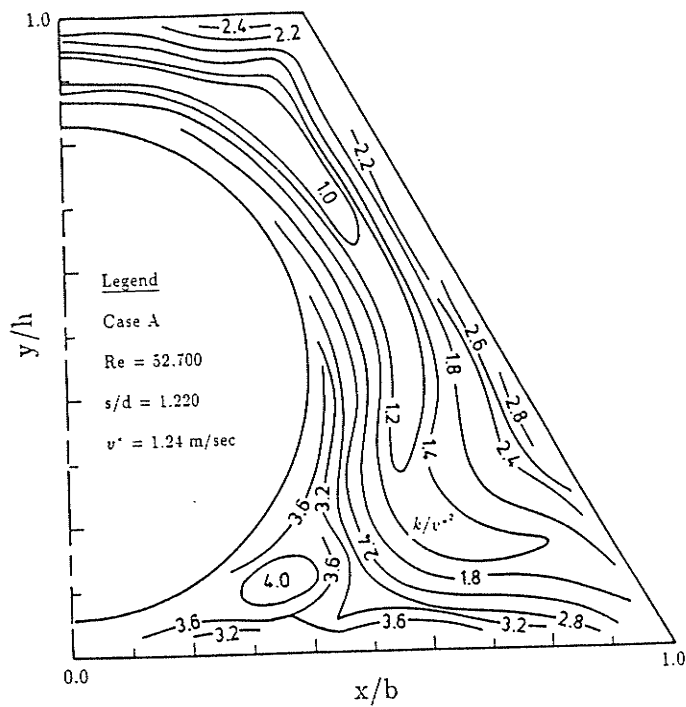
This finding indicates that cross-gap eddy motions only exist in medium-small gaps. For the asymmetric case F, Fig.3-7(e) shows that high  $v'_x/v^*$  values were achieved in the two small gap regions (2.0 for the 4.0 mm bottom gap and 1.2 for the 4.0 left-side gap).

Contours of turbulence velocity component in the vertical direction  $v'_y/v^*$  are given in Fig. 3-8(a)-(e). For the four symmetric rod setting cases (A to D), the global peak values of  $v'_y/v^*$  were consistently located at the near-rod surface region where  $\theta \approx 70^\circ$  to  $90^\circ$ , where the direction of the velocity component is more or less parallel to the wall. Quantitatively, the maxima are from about 1.7 to 2.0, smaller than those of the axial and horizontal turbulence velocity components. Apart from the small gap regions where cross-gap eddy motions are believed to be present, the contours of  $v'_y/v^*$  for the most part of the whole flow cross-section, resemble in shape those of  $v'_x/v^*$  and of  $v'_z/v^*$ , with numerical levels also quite close, for example, see Fig. 3-6(a) and Fig. 3-8(a). The similarity of the contour shapes and closeness of the magnitudes suggest that in the central subchannel regions where large-scale cross-gap eddy motion is absent, local isotropy is a good approximation. For the asymmetric Case F, Fig. 3-8(e) shows two peak values in the distribution at a level of about 1.6. One of the maxima occurs right in the left-side gap, which is an indication of the activity of a cross-gap eddy motion, since the vertical velocity component projects a large portion of the resultant in a direction which is azimuthal to the side gap. The other peak value is close to the rod surface at  $\theta \approx 60^\circ$  to  $90^\circ$ , and here it is typical of non-circular duct behavior as discussed above. Comparison of Fig. 3-7(e) and Fig. 3-8(e) also suggests, for the right half of the flow cross-section, that local isotropy approximately holds true in the central subchannel region.

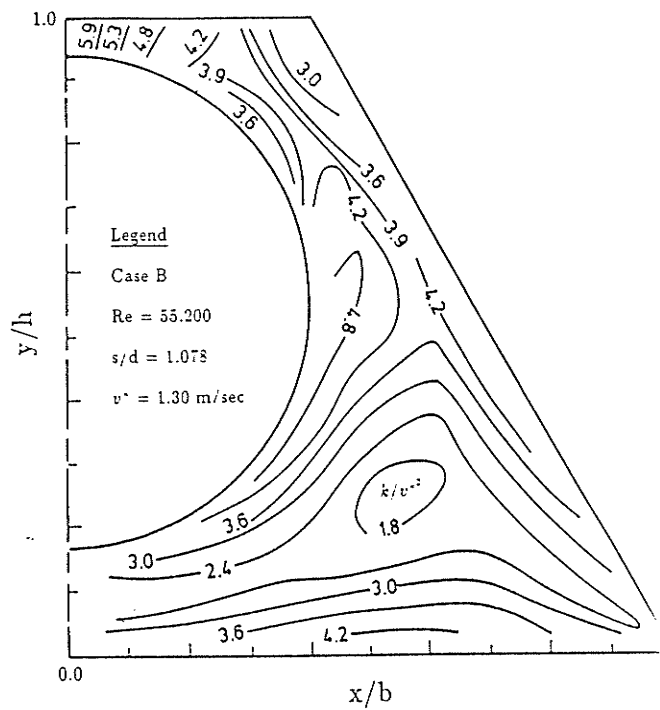
### 3.3.2 Turbulence Kinetic Energy

In studies of non-circular duct flows, the distributions of turbulence kinetic energy usually receive special attention because it is regarded as a transferable quantity which reflects the effect of mean convection, and also perhaps the effect of large scale turbulent convection. From the view point of analogy, the distribution of turbulence kinetic energy is also significant in the sense that the transport of heat is believed to be an intermediate process between the transport of turbulence kinetic energy and of axial flow momentum, particularly at the large scale turbulent transport level when a non-gradient type of transport is brought into the picture. Consistent with the contour plots of axial turbulence intensity given in Fig. 3-6, there are also patches of high turbulence kinetic energy as shown in Fig. 3-9. In Case A, the highest turbulence kinetic energy in the cross-section is found in a patch which overlaps that for  $v'_z/v^*$ . The radial increase of  $k/v^{*2}$  in this special region clearly indicates that a generation mechanism other than wall-turbulence is present. Otherwise, the distortions of the  $k/v^{*2}$  contours towards the corners and away from the inclined duct wall can be attributed to transport by secondary flow. For Figs. 3-9(b) and (c), global peak values of  $k/v^{*2}$  do not occur in these patches but rather in the small top gap which is due to the high peak values of  $v'_x/v^*$  located there as described earlier. The local maximum in the patch region is about 4.8 for Case B and about 5.6 for Case C, which is another indication that decreasing gap size is capable of enhancing cross-gap eddy motion. In Case D, the distinctive patch ceases to exist and the global maximum of  $k/v^{*2}$  is found right near the rod surface at  $\theta \approx 70^\circ$  to  $90^\circ$  instead of in the gap region. The marked transition between cases C and D is obvious in comparing Figs. 3-9(c) and (d).

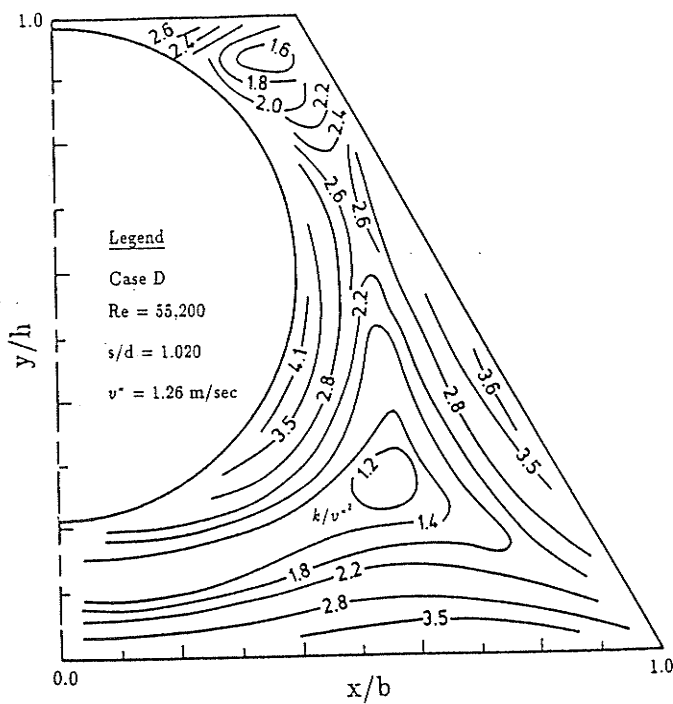
The hypothesis of Reynolds number similarity in rod bundle subchannel flows has been confirmed by the experimental data of Trupp and Azad (1975), and Hooper and



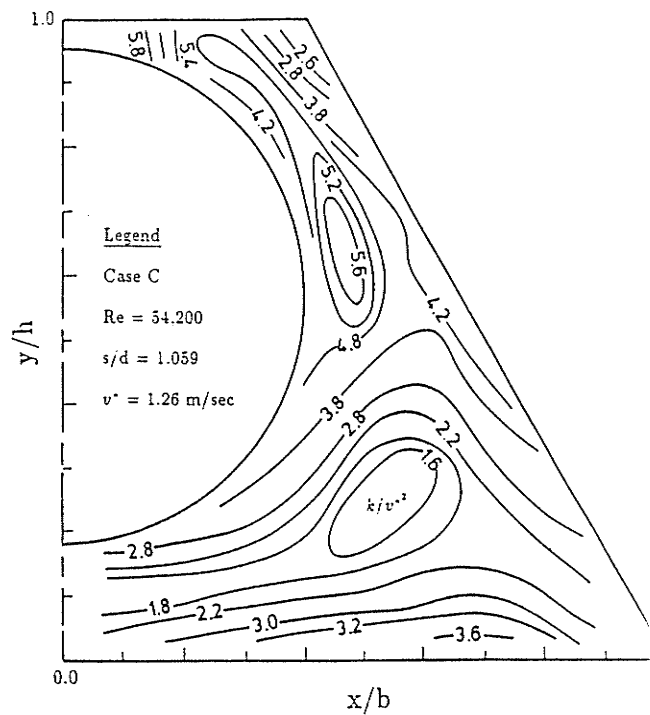
(a)



(b)

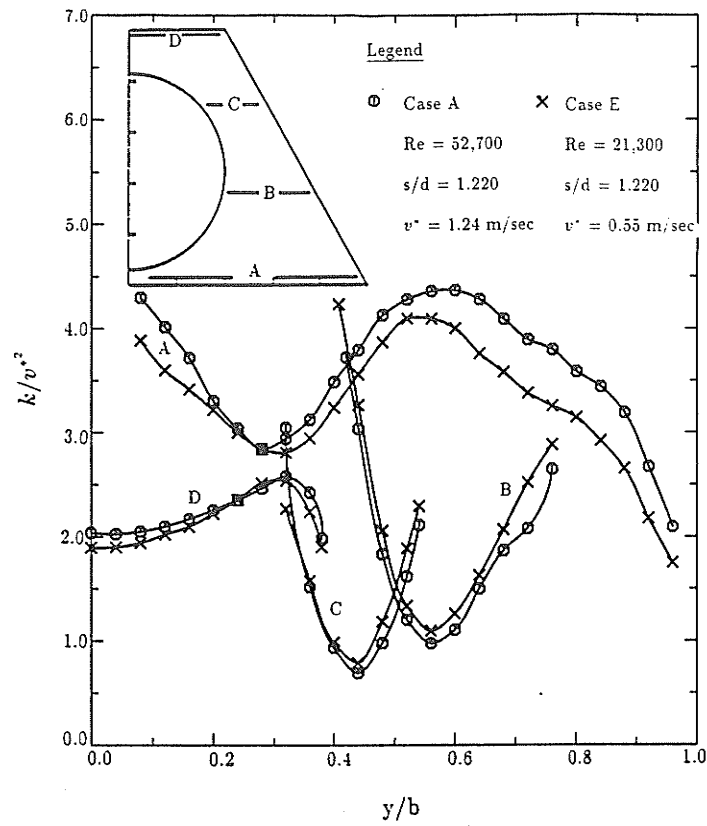


(d)

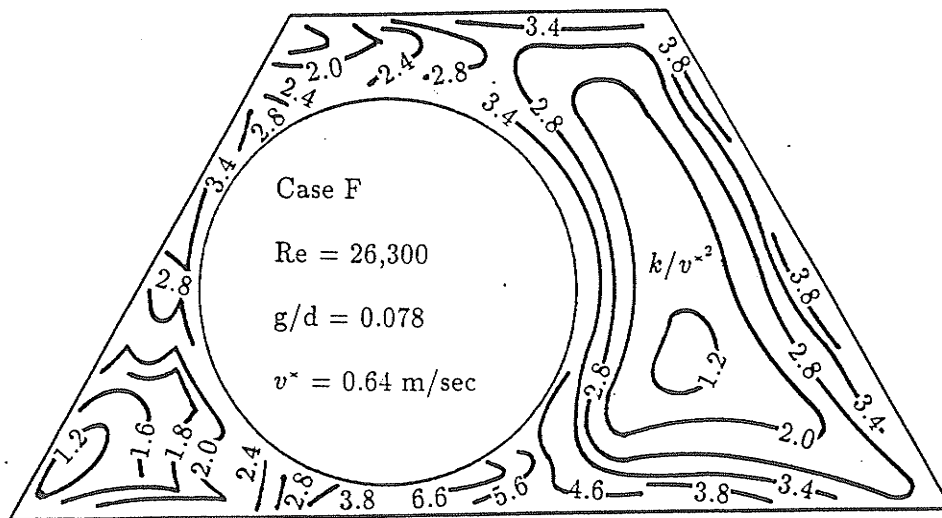


(c)

Figure 3-9 Contours of turbulence kinetic energy  $k/v^2$   
(a) Case A; (b) Case B; (c) Case C; (d) Case D; (e) Case E; (f) Case F



(e)



(f)

Figure 3-9 Contours of turbulence kinetic energy  $k/v^2$   
 (a) Case A; (b) Case B; (c) Case C; (d) Case D; (e) Case E; (f) Case F

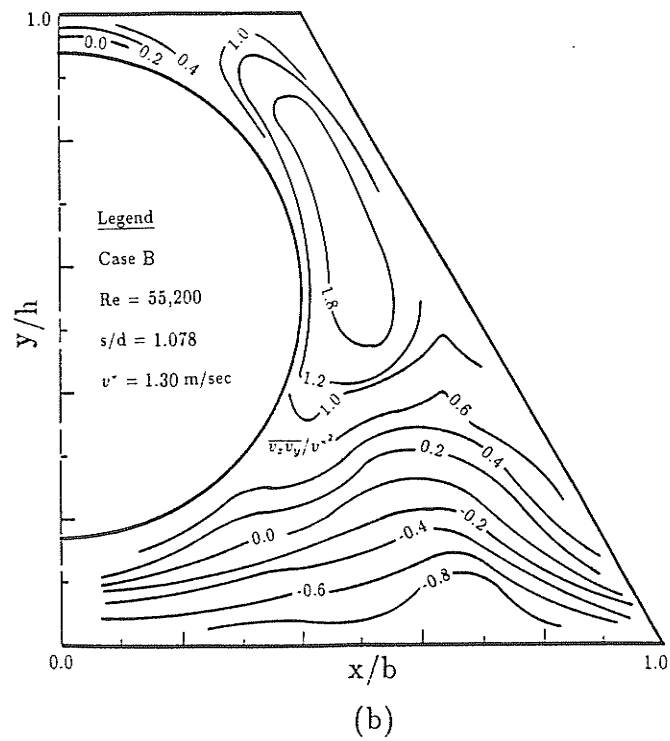
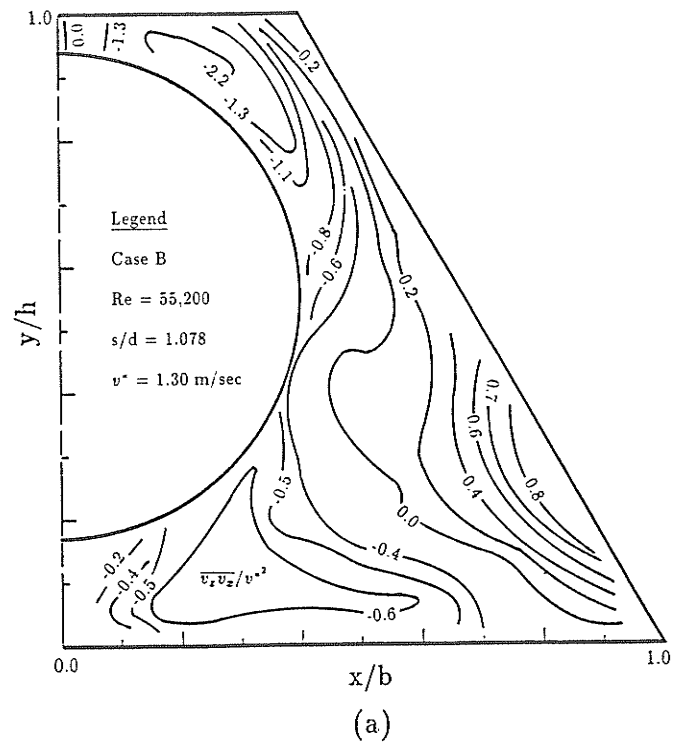


Figure 3-10 Contours of tangential Reynolds shear stresses for Case B  
(a)  $\bar{v}_z \bar{v}_x$ ; (b)  $\bar{v}_z \bar{v}_y$

Rehme (1984). The present data shown in Fig. 3-9(e) also support this fundamental condition. On the other hand, it is worth pointing out that this same principle will not hold true unconditionally, because the underlying concept in the similarity hypothesis is that the flow is dominated by large scales, which remain unaffected with increasing  $Re$ , that can only affect the fine scales. For the asymmetric Case F, local maxima of  $k/v^{*2}$  reach about 6.6 for the bottom 4.0 mm gap and about 3.4 for the left-side 4.0 mm gap (see Fig. 3-9(e)). Difference may be partly attributed to subchannel geometry, noting that the left-side gap is associated with subchannels that involve relatively small flow rates.

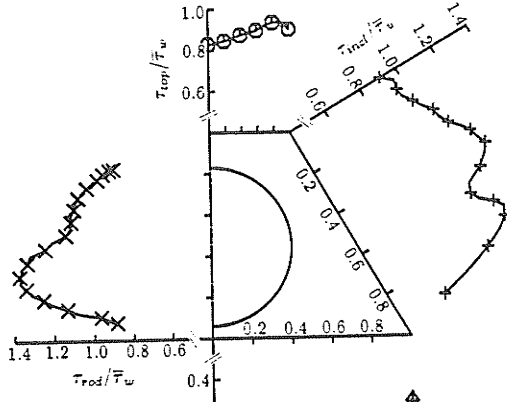
### 3.3.3 Reynolds Shear Stresses

Two of the three Reynolds shear stresses were measured with X-wire probe. The contours of  $\overline{v_z v_x}$  and  $\overline{v_z v_y}$  for case B are given in Fig. 3-10(a) and (b), respectively. Three nil- $\overline{v_z v_x}$  lines are discernible in Fig. 3-10(a). The two nil- $\overline{v_z v_x}$  lines in the top and bottom (not shown) gaps demonstrate the simulated rod bundle geometry has good symmetry with respect to the duct axis. Deviations from zero of  $\overline{v_z v_x}$  right at the top gap are within  $\pm 0.1$ . The central zero shear stress line divides the flow cross-section into two parts with opposite signs: negative left half and positive right half. In the top gap region,  $\overline{v_z v_x}$  increases rapidly from the zero line to a global maximum of about 2.2, thus creating a region with unusually high azimuthal shear stress. This trend of steep gradient of azimuthal shear stress also occurs in Fig. 3-10(b) where a high  $\overline{v_z v_y}$  region with a global maximum of about 1.8 overlaps the high  $k/v^{*2}$  patch. Within this distinctive region,  $\overline{v_z v_y}$  increases rapidly in the radial direction from the rod surface into the subchannel central region, establishing a reverse trend in comparison with ordinary non-circular duct flow. Apparently the large azimuthal shear stress field is directly related to the large-scale cross-gap eddy

motion, however the precise connection is not clear. Nonetheless, certain deductions concerning numerical computation can be made from here. Since the turbulence kinetic energy patch caused by cross-gap eddy motion is always accompanied by large azimuthal shear stress such as shown in the top gap region in Fig. 3-10(a) for  $\overline{v_z v_x}$  and in Fig. 3-10(b) for  $\overline{v_z v_y}$ , an empirical approach to simulate the resulting high  $k$  patch is to simulate  $k$ -production in these regions. Distributions of  $\overline{v_z v_x}$  and  $\overline{v_z v_y}$  for all other cases demonstrated essentially the same behaviour as Case B.

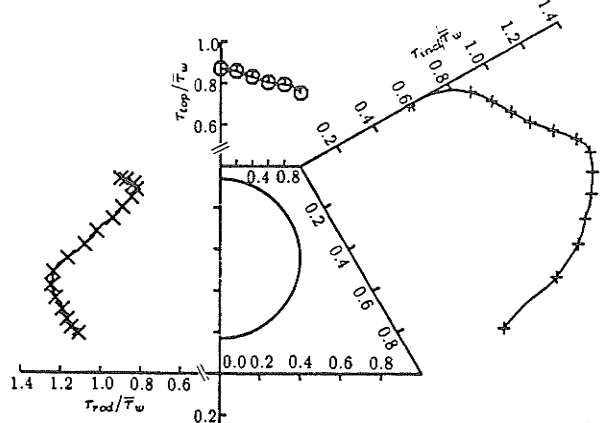
### 3.3.4. Local Wall Shear Stress

Local wall shear stresses  $\tau_w$  were measured along all the duct walls and rod surface by Preston tube using the appropriate correlation of Patel (1965). For each case, the overall average wall shear stress  $\bar{\tau}_w$  was determined by numerical integration over the tube surface and all duct walls (after corner shaping) of the measured values of the axial component of local wall shear stress. The  $\tau_w$  values derived in this manner via Preston tube were found to be within 2% of the duct average values  $\bar{\tau}$  corresponding to the measured axial pressure gradients ( $D_h/4\partial\bar{P}/\partial z$ ). The distributions of local wall shear stress (normalized by  $\bar{\tau}_w$ ) are shown in Fig. 3-11(a)-(f). For all five symmetric rod settings, global maxima of  $\tau_w/\bar{\tau}_w$  are constantly found on the rod surface where  $\theta \approx 60^\circ$  to  $80^\circ$  with values between 1.3 to 1.4, while global measured minima are generally located in the  $60^\circ$  trapezoidal duct sharp corner at a level of about 0.3. Of interest in the distributions are signs containing implications of the transport roles of secondary flow and turbulence convection. For case A, attention is drawn to the dual peaks along the inclined wall. The dip between the two peaks represents about a 10 percent decrease in comparison with the lower peak value of about  $1.1\tau_w/\bar{\tau}_w$ . Such a wavy wall shear stress distribution is a typical effect caused by secondary flow transport. In general, returning secondary flow tends to direct momentum away from



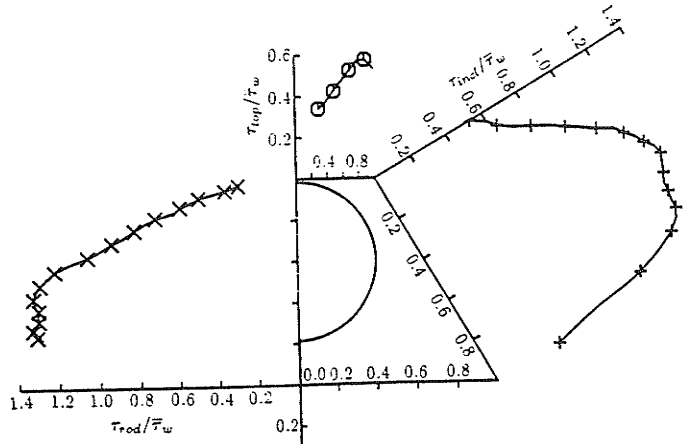
**Legend**  
 Case A  
 Re = 52,700  
 s/d = 1.220  
 v\* = 1.24 m/sec

(a)



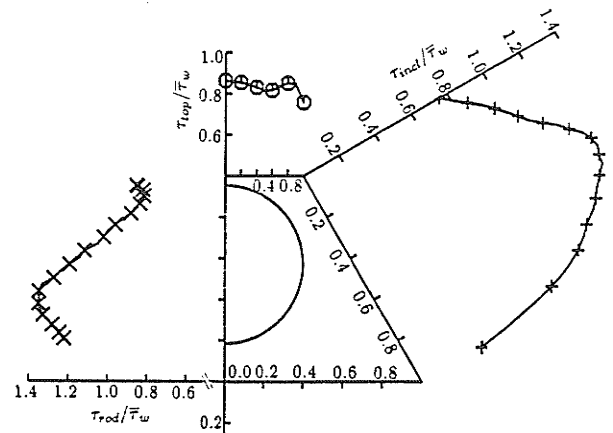
**Legend**  
 Case B  
 Re = 55,200  
 s/d = 1.078  
 v\* = 1.30 m/sec

(b)



**Legend**  
 Case D  
 Re = 55,200  
 s/d = 1.020  
 v\* = 1.26 m/sec

(d)



**Legend**  
 Case C  
 Re = 54,200  
 s/d = 1.059  
 v\* = 1.26 m/s

(c)

Figure 3-11 Distribution of local wall shear stress  
 (a) Case A; (b) Case B; (c) Case C; (d) Case D; (e) Case F

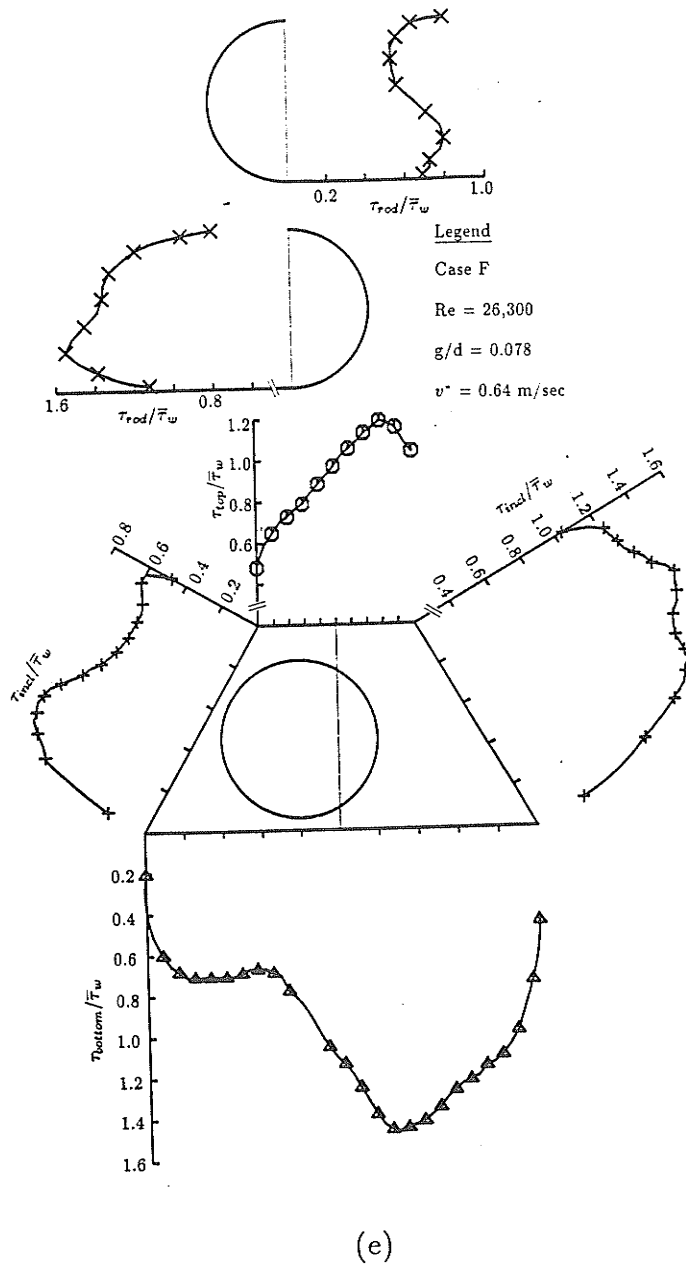


Figure 3-11 Distribution of local wall shear stress  
 (a) Case A; (b) Case B; (c) Case C; (d) Case D; (e) Case F

the wall, thus lowering the local wall shear stress. Since the returning secondary flows always occur near the wall bisector where the local mass flow rate is large and so is the local wall shear stress, the resultant effect is an equalization of wall shear around the flow passage perimeter. In this particular case, the returning secondary flow from the sharp  $60^\circ$  duct corner was so strong that a large dip was formed. This point is pursued further in conjunction with the experimental secondary flow data.

For case B, peculiarities can be found in the top gap region. As discussed, large-scale cross-gap eddy motion was apparently active in this area; this activity was also reflected in wall shear stress distributions. Due to the momentum transported by eddies, top wall shear stress  $\tau_{top}/\bar{\tau}_w$  increased starting from the obtuse duct corner to the center of the top gap, the total variation being from about 0.75 to 0.87. Rod wall shear stress from  $\theta \approx 150^\circ$  to  $180^\circ$  established the same trend, with a total variation of  $\tau_{rod}/\bar{\tau}_w$  from about 0.8 to 0.92. Such distributions were preserved in case C whose gap size was close to that in case B. But for case D, both the top wall and rod surface shear stress decreased monotonically approaching the center of the top rod-to-wall gap. Near the top gap, both  $\tau_{top}/\bar{\tau}_w$  and  $\tau_{rod}/\bar{\tau}_w$  were around 0.3. It is quite obvious that the cutoff of the coherent interrelation between the two homogeneous subchannels is responsible for the reversion of the wall shear stress trends.

For case F, it is noted that the local maximum of the bottom wall shear stress was displaced from the position corresponding to the largest flow rate, suggesting the presence of secondary flow transport. The two peaks of the almost sinusoidal distribution of  $\tau_{rod}/\bar{\tau}_w$  on the left half of the rod surface are corresponding to the centroids of the two adjacent subchannels connected by the small left-side gap. Due to the relatively large size of the right-side gap, peaks in the wall shear distribution on the right half of the rod surface are less distinctive.

### 3.3.5 Secondary Flow

The secondary flow results for  $s/d = 1.220$  are presented in Fig. 3-12. Three counter-rotating secondary flow cells were discerned from the X-probe measurements and the pattern is shown in the inset to Fig. 3-12. The magnitude of secondary flow in most places was around the level of  $1\% \bar{V}_{z,b}$ , with a maximum of about  $3.4\% \bar{V}_{z,b}$  located near the rod surface where  $\theta \approx 90^\circ$ . Note that measurement location corresponds to the tail of each arrow, and that secondary velocities with magnitudes less than 0.5 per cent of the bulk velocity  $V_{z,b}$  were disregarded owing to the limitation of the present technique. Due to this limitation, the present measured three-cell pattern does not exclude more subtle circulations of secondary flow within the framework presented in Fig. 3-12. For example, detailed secondary flow patterns in the top and bottom gaps were unable to be discerned from present X-probe measurements. It is noted that the large central circulation cell confined itself within the subchannel bounded by the side and bottom gaps, suggesting that even for heterogeneous subchannels, penetration of secondary flow through gaps is minimal. On the other hand, the enhancement role of secondary flow to the interchange of energy between subchannels is not weakened by such inability to penetrate subchannel boundary, since mixing can be strengthened by moving high momentum and energy from subchannel center to gap region as done by secondary flow. While the presented flow pattern fails to convey any definite message related to the high- $k$  (or high- $v'_z$ ) patch, it does well account for the dip of the wall shear stress distribution along the duct inclined wall which is shown in Fig. 3-11(a) and the obvious bulges of turbulence kinetic energy distribution in the same area (Fig. 3-9(a)), in addition to bulges into both corners. Had there not been the modification by secondary flow, the wall shear stress along the inclined wall would have established a single peak approximately opposite to the

maximum flow rate region. Thus although secondary flow does not appear to be the main mechanism behind the coherent relations between two adjacent subchannels, it still plays a significant role in the transport processes within a given subchannel.

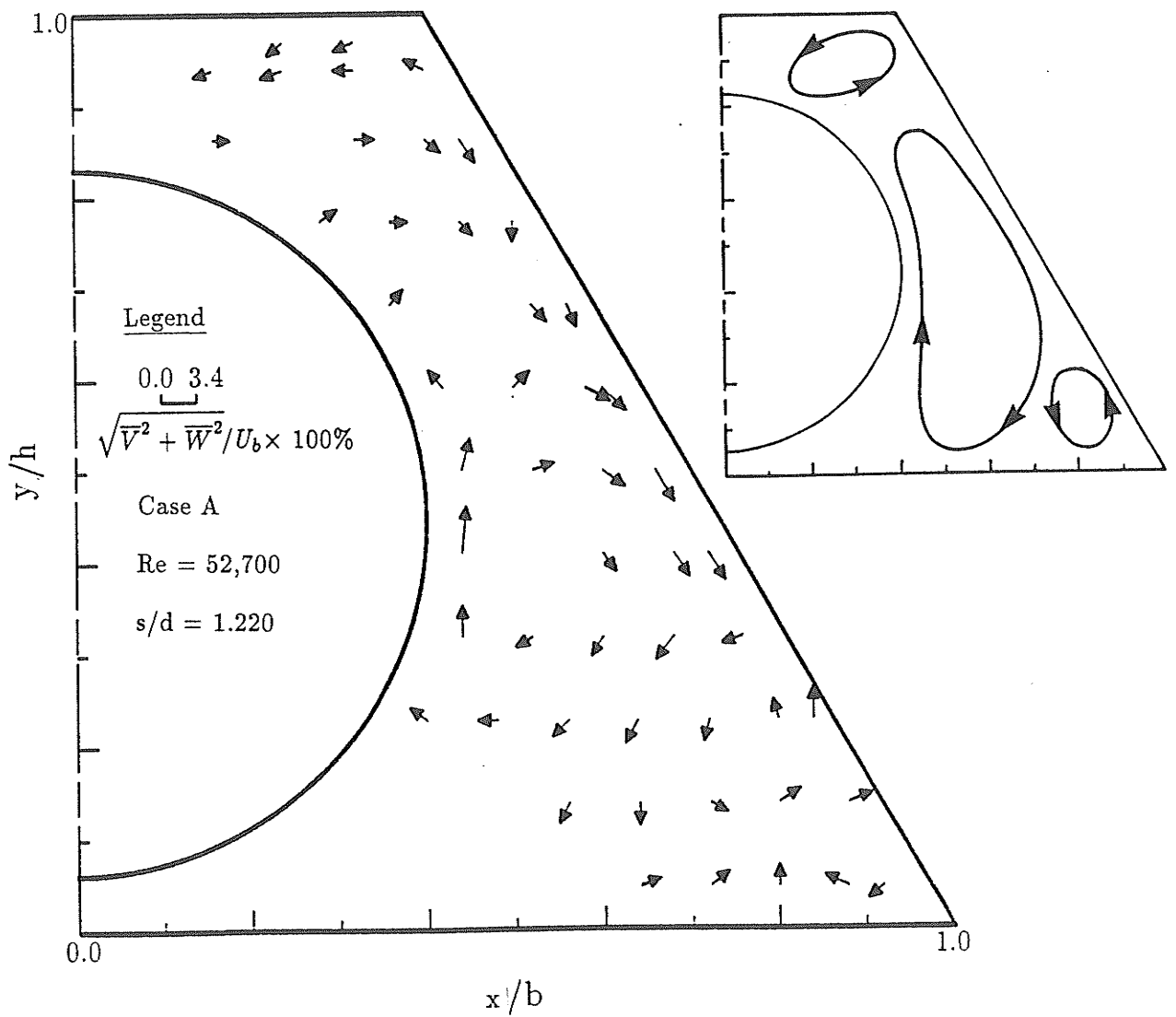


Figure 3-12 Measured secondary velocity vectors for Case A

### 3.4 Spectral Measurements and Mixing Correlation

To this point, the experimental evidence presented from Figs. 3-6 to 3-12 defines an atypical character of turbulent flow structure in the simulated rod bundle subchannels. The abnormality of this flow is represented by a gap-size dependent large-scale cross-gap eddy motion whose existence was first directly studied by Rowe et al (1974) and its importance later stressed by Hooper and Rehme (1984). The presented experimental findings confirm the universality of this phenomenon in the sense of its weak subchannel shape dependence, which was first suggested by Rowe et al (1974). More importantly, the occurrence, augmentation and disappearance of the high  $k$  patch with the variation of gap size reported in this experimental work settled an outstanding issue for one special case (rod-trapezoidal duct), as raised by Rogers and Todreas (1968), "no information is available on the critical gap to diameter ratio below which the mixing rate decreases". As a continuation of the turbulence structure studies, further experimental work on power spectrum was conducted in this research following the approaches of Hooper and Rehme (1984), and Möller (1992), aiming at revealing the dependence of a possible dominant frequency of the cross-gap eddy motion on flow conditions and the implications of this cyclic motion on subchannel mixing. Six rod settings were chosen (each with two different Reynolds numbers) in the spectrum studies and they were generally different from those used in the structural studies as summarized in Table 3-6. The geometric characters of the total twelve test cases, together with Reynolds numbers and overall friction velocities, are tabulated in Table 3-7, noting that they are categorized into two groups according to the symmetry of the rod with respect to duct axis.

Table 3-7: Experimental Conditions for Spectrum Analysis

Case	$g_{bottom}$ (mm)	$g_{bottom}/d$	$\bar{v}_z$ (m/sec)	Re
symmetric setting				
a1	4.0	0.078	1.24	52,700
a2	4.0	0.078	0.55	21,300
b1	3.0	0.059	1.21	52,000
b2	3.0	0.059	0.64	26,000
c1	2.0	0.039	1.20	52,000
c2	2.0	0.039	0.63	26,000
asymmetric setting <sup>+</sup>				
d1	4.0	0.079	1.18	52,000
d2	4.0	0.079	0.64	26,300
e1	3.0	0.059	1.16	52,000
e2	3.0	0.059	0.61	26,000
f1	2.0	0.039	1.12	52,000
f2	2.0	0.039	0.59	26,000

<sup>+</sup>  $g_{bottom} = g_{left-side}$

### 3.4.1 Results of Power Spectral Density

Power spectral data were obtained for axial and azimuthal fluctuating velocities via a KROHN-HITE model 3700 band-pass filter (cutoff frequency accuracy of 5 per cent). In the symmetric setting cases (from a1 to c2), spectra were taken at the top and bottom gaps and at two near-bottom gap locations, which are schematically defined in the insets to Figs. 3-13 and 3-14. In the asymmetric rod setting cases (d1 to f2), spectrum measurements were made at the centers of the top, bottom and left-side gaps as shown in Fig. 3-15. For measurements conducted in the left-side gaps, the X-wire probe was oriented perpendicular to the gap center line between the duct wall and rod surface, this orientation facilitated the collection of azimuthal turbulent velocity power spectral information. Selected power density results are graphically presented in Figs. 3-13 to 3-15. For each energy spectrum of the axial component  $E_{v_z}(f)$  in Fig. 3-13(a), only that in the high-intensity region establishes a discernible peak frequency whereas in Fig. 3-13(b) all three energy density spectra

of the azimuthal component for the bottom gap  $E_{v_z'}(f)$  are related to the same peak frequency ( $\sim 150$  Hz). The spectrum at the wide top gap [Fig.3-13(b)] also has a weak peak of somewhat lower frequency ( $\sim 90$  Hz). Similar results for case a2 are given in Fig. 3-14, but in a linear-log form to accentuate the energy-containing frequency bands. Peaks centered around the lower frequency (65 Hz) in Fig. 3-14(b) and in the upper part of Fig. 3-14(a) represents a strong disturbance originated from the bottom gap, whereas peaks in the higher frequency ranges are typical of the behavior of wall turbulence (Bremhorst and Walker (1973)). It is known that a peak in a spectrum (frequency domain) reflects the presence of a strong periodic component. Therefore it seems reasonable to speculate that the physical picture behind this is a strong energy-containing large eddy motion along the azimuthal direction from the small rod-to-wall gap which interchanges its energy with the axial component as it moves to the subchannel central area, maintaining the same characteristic frequency.

Fig. 3-15(a) gives the axial spectral data for the asymmetric setting case d2 (same bottom gap size 4.0 mm as in case a2). In the bottom gap area, the high peak of  $E_{v_z'}(f)$  centres around 60 Hz which is close to the 65 Hz found in the symmetric setting a2. However, for the left-side gap which also has the same gap size as case a2 (4.0 mm), the peak frequency is only about 40 Hz. The difference in peak frequency suggests that while the phenomenon of large-scale cross-gap eddy motion is universal with respect to subchannel shape as suggested by Rowe (1974) and Rehme (1992), the periodicity of the cyclic eddy motion is subchannel geometry dependent. An important observation can also be made by comparing Fig. 3-14 (b) and Fig. 3-15(b). In the symmetric setting case of Fig. 3-14(b), the  $fE_{v_z'}/v^{*2} - f$  plot does not bear a visible peak in the top gap area, implying the absence of large-scale cyclic eddy motion. On the other hand, in the asymmetric setting case such eddy motion through

the top gap is clearly shown in Fig. 3-15(b). In the top gap region, experimental data constantly show the existence of eddy motion in the asymmetric rod setting cases with little indication of such motion in symmetric rod setting cases.

So far, it is fairly certain that the coherent cross-gap eddy motion contributes significantly to the enhancement of transport by turbulence convection and probably also influences the local turbulence production. What remains unclear is the precise description of the periodicity in terms of the known quantities and the proportion of contribution to the total kinetic energy by the eddy motion characterized by the peak frequency. Hooper and Rehme (1984) first suggested that the dominant frequency varies linearly with Reynolds number based on the mean subchannel velocity and the hydraulic diameter of the subchannel. Möller (1991) found that peak frequencies could be correlated in terms of Strouhal number ( $Str = f_p d / v^*$ ) and nondimensional gap size, as follows,

$$Str^{-1} = 0.808g/d + 0.056 \quad (3.1)$$

Deviation as high as fifteen per cent occurred when Eq. (3.1) was used to correlate the data of Möller (1991). Table 3-8 tabulates the peak frequencies obtained in this research, together with the predicted Strouhal number according to Eq. (3.1). Since results from the asymmetric side gaps apparently differ from those from top and bottom gaps, they are given in a separate entry in Table 3-8. Fig. 3-16 offers graphical comparison of the present data with Möller's correlation Eq. (3.1), excluding results from left-side gaps. The present data seem to offer a correlation which has the approximate same slope as Eq. (3.1) but a higher intercept,

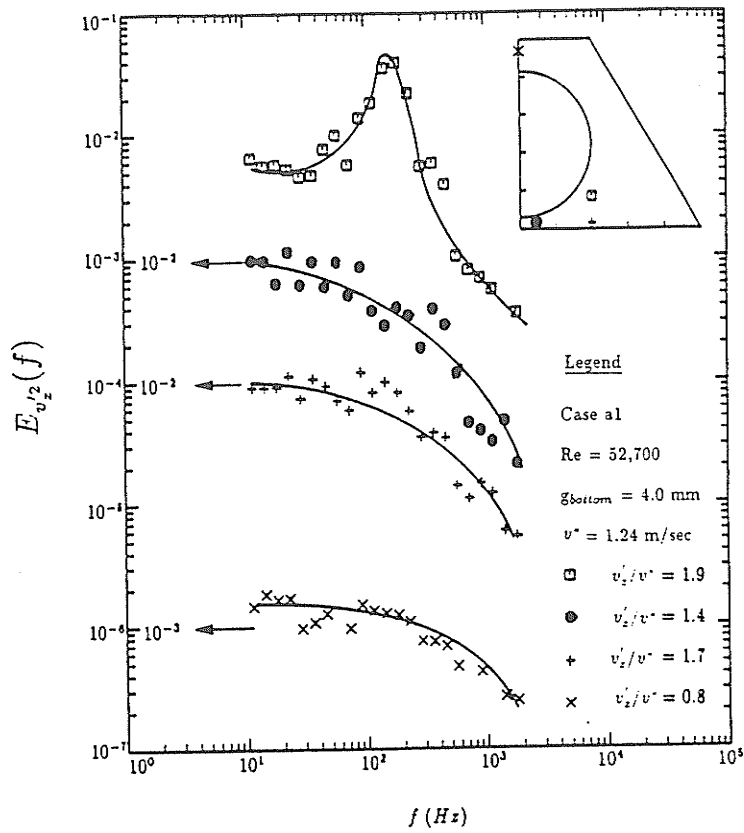
$$Str^{-1} = 0.822g/d + 0.144 \quad (3.2)$$

The standard error estimate associated with Eq. (3.2) is 0.07378. Overall, when grouped into the inverse of Strouhal number and nondimensional gap size, the present

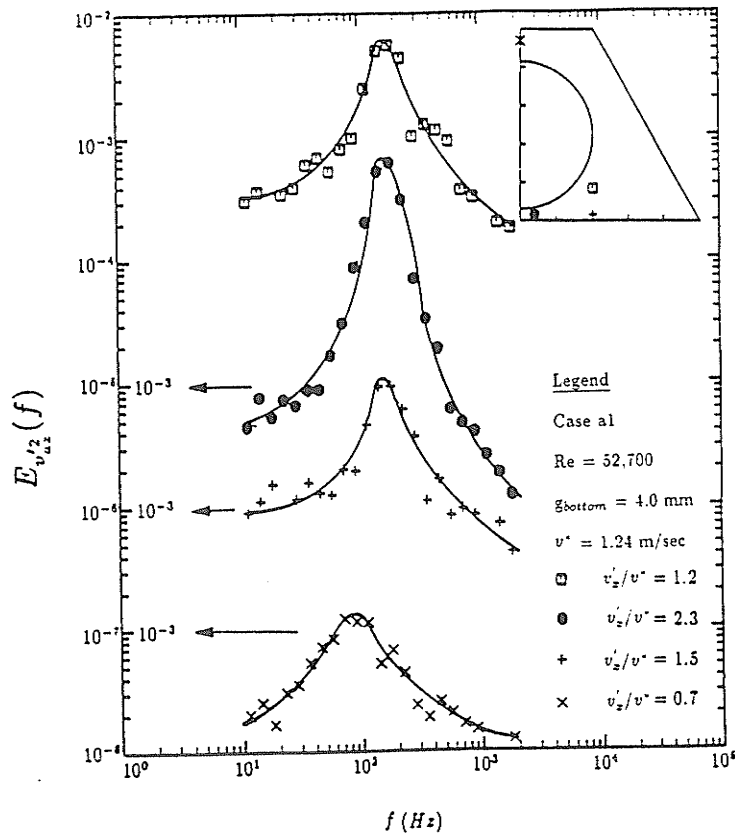
date lie above the correlation of Möller (1991). This difference emphasises the fact that although the existence of large-scale cross-gap eddy motion has weak subchannel shape dependence, the quantitative description of such motion is still geometry dependent.

Table 3-8: Peak Frequencies of Rod-to-wall Gaps

gap	g (mm)	$f_p$ (Hz)	$v^*$ (m/s)	$(f_p d/v^*)^{-1}$	Eq. (3.1)	g/d
symmetric gaps						
bottom	4.0	150	1.24	0.1627	0.1196	0.0787
top	11.2	90	1.24	0.2712	0.2341	0.2204
bottom	4.0	65	0.55	0.1666	0.1196	0.0787
top	11.2	45	0.55	0.2406	0.2341	0.2204
bottom	3.0	130	1.21	0.1832	0.1037	0.0591
top	12.2	60	1.21	0.3970	0.2500	0.2402
bottom	3.0	60	0.64	0.2100	0.1037	0.0591
top	12.2	30	0.64	0.4200	0.2505	0.2402
bottom	2.0	130	1.20	0.1817	0.0878	0.0394
top	13.2	85	1.20	0.2779	0.2660	0.2598
bottom	2.0	57	0.63	0.2176	0.0878	0.0394
asymmetric gaps						
bottom	4.0	120	1.18	0.1936	0.1196	0.0787
top	11.2	70	1.18	0.3318	0.2341	0.2204
bottom	4.0	69	0.64	0.1826	0.1196	0.0787
top	11.2	34	0.64	0.3705	0.2341	0.2204
bottom	3.0	130	1.16	0.1757	0.1037	0.0591
top	12.2	70	1.16	0.3262	0.2500	0.2402
bottom	3.0	53	0.61	0.2266	0.1037	0.0591
top	12.2	21	0.61	0.5718	0.2500	0.2402
bottom	2.0	120	1.12	0.1837	0.0878	0.0394
top	13.2	100	1.12	0.2205	0.2660	0.2598
bottom	2.0	58	0.59	0.2002	0.0878	0.0394
left-side gaps						
side	4.0	60	1.18	0.3871	0.1196	0.0787
side	4.0	33	0.64	0.3817	0.1196	0.0787
side	3.0	50	1.16	0.4567	0.1037	0.0591
side	3.0	21	0.61	0.5718	0.1037	0.0591
side	2.0	90	1.12	0.2450	0.0878	0.0394
side	2.0	60	0.59	0.1936	0.0878	0.0394



(a)



(b)

Figure 3-13 Energy density spectra for Case a1  
 (a) axial; (b) horizontal

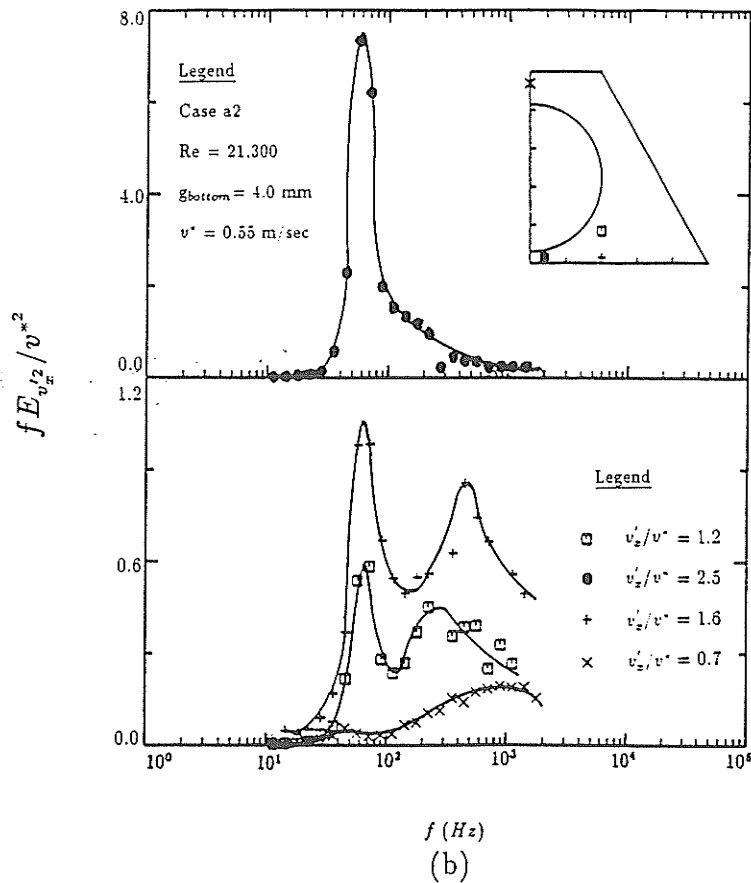
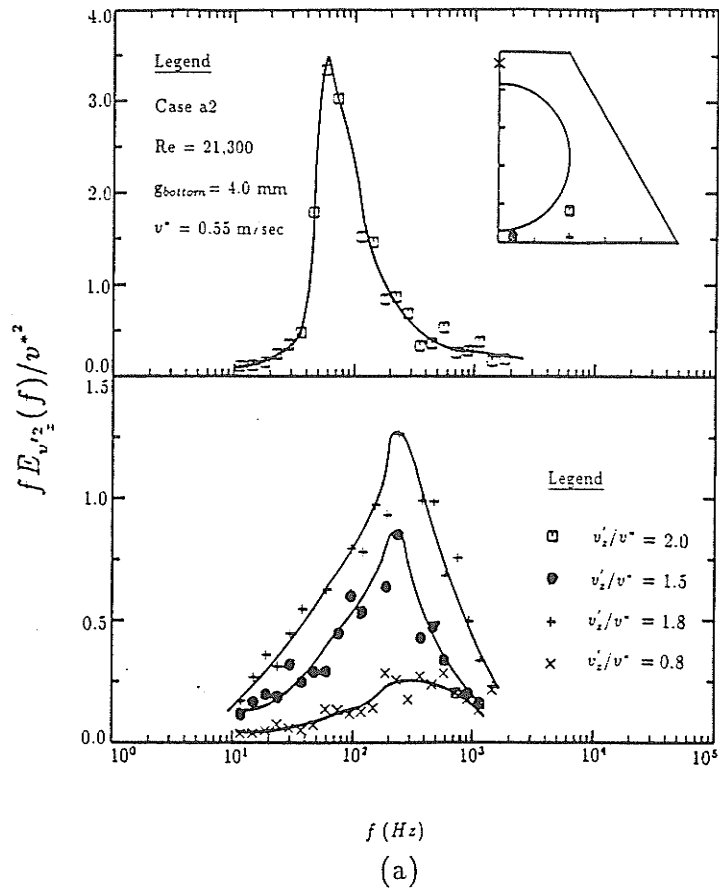


Figure 3-14 Linear-log plots of energy density spectra for Case a2  
(a) axial; (b) horizontal

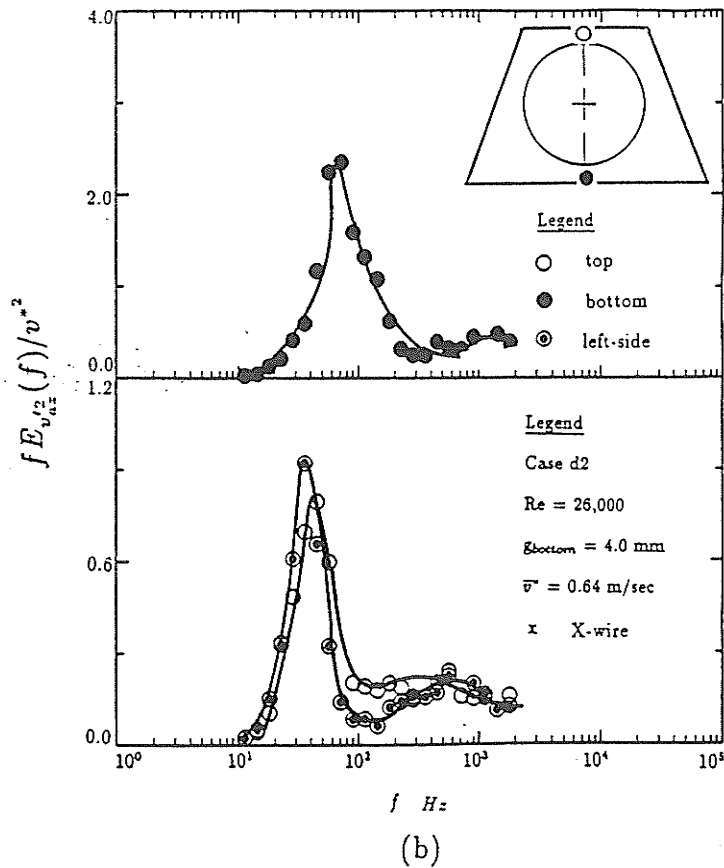
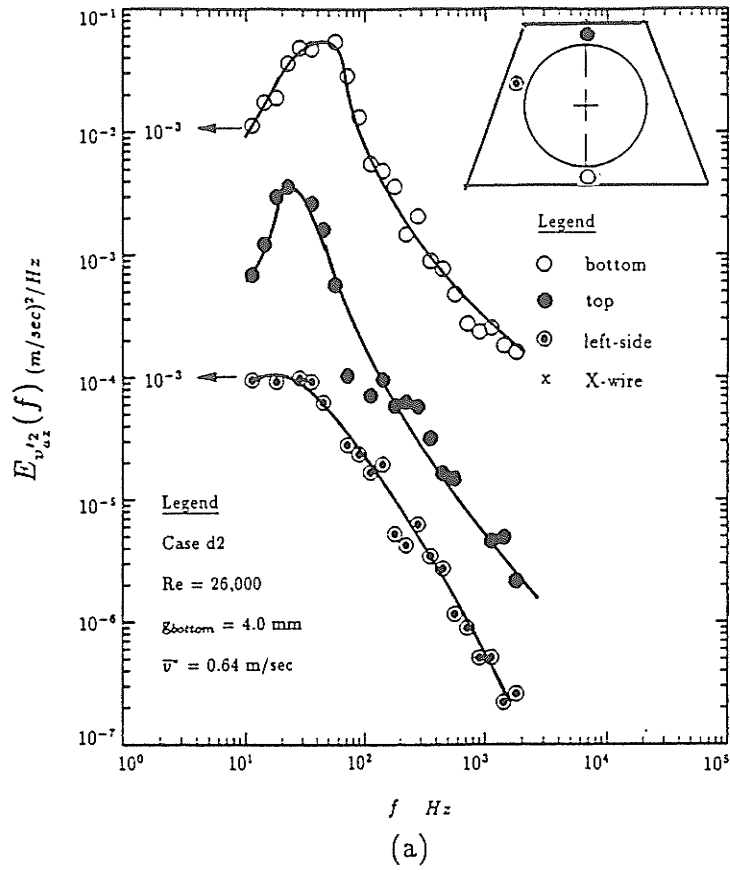


Figure 3-15 Linear-log plots of energy density spectra for Case d2  
 (a) axial; (b) azimuthal

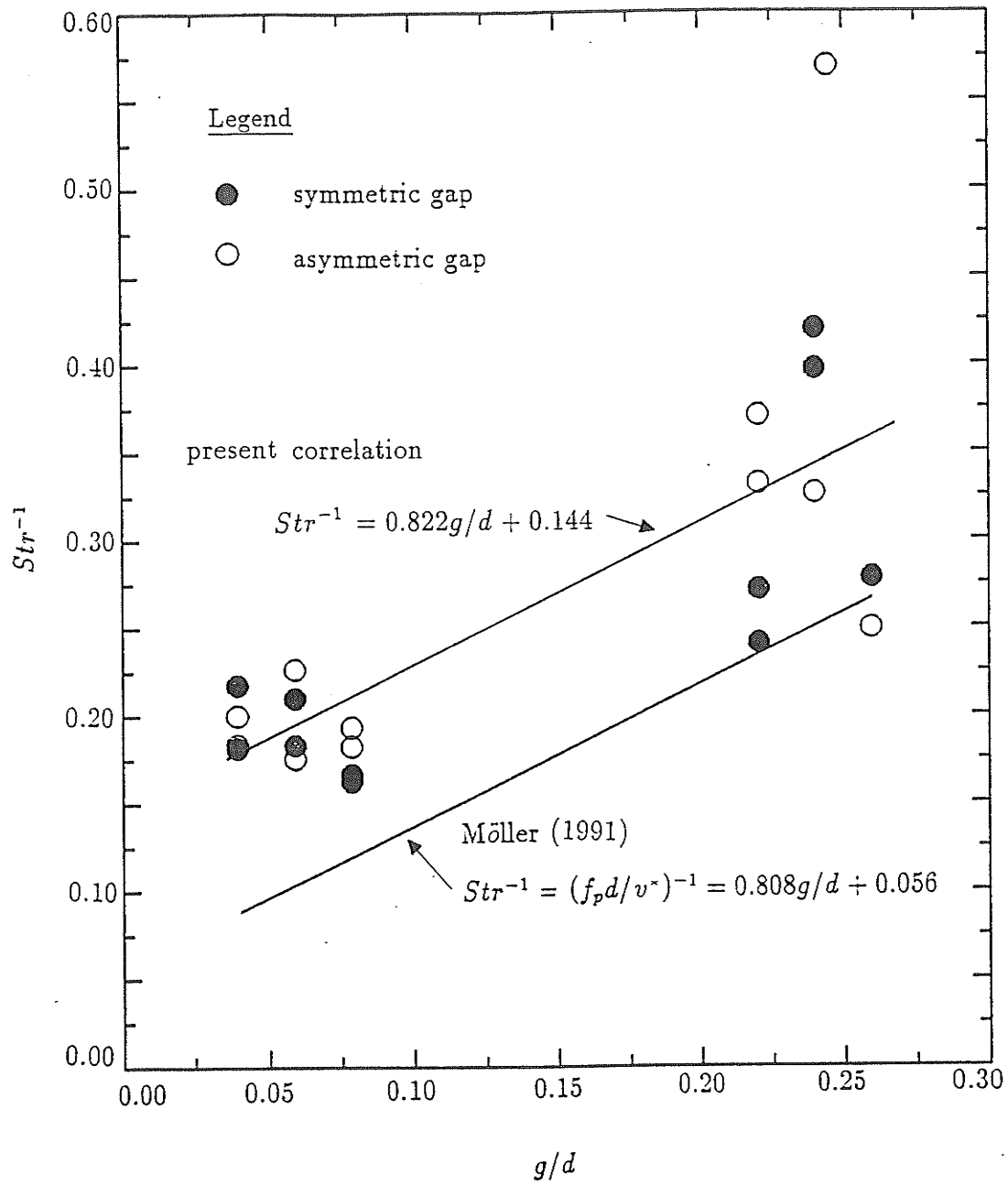


Figure 3-16 Correlation of Strouhal number and nondimensional gap size

### 3.4.2 Mixing Correlations

Admitting that the large-scale cross-gap eddy motion is one of the major mechanisms in rod bundle subchannel mixing process, and perhaps the dominant one for a range of medium-small gaps, it is possible to derive a semi-empirical quantitative description about the mixing process based on the existing experimental information, on power spectral densities. In doing so, the approach of Möller (1992) and Rehme (1992) were followed in this research.

Table 3-9: Summary of Mixing Velocity and Mixing Factor ( $Re = 52,000$ )

case	gap	g/d	$\delta_{ij}$	$w_{eff}$ (m/sec)	$Y = w_{eff}\delta_{ij}/\bar{\epsilon}$	Eq.(3.11)
symmetric gaps						
a1	bottom	0.078	0.090	0.34	15.4	9.40
a1	top	0.220	0.042	0.22	4.6	3.47
a2	bottom	0.078	0.090	0.46	20.7	9.40
b1	bottom	0.059	0.096	0.38	18.2	12.29
b2	bottom	0.059	0.096	0.56	27.6	12.29
c1	bottom	0.039	0.098	0.33	16.4	18.29
c2	bottom	0.039	0.098	0.40	19.4	18.29
asymmetric gaps						
d1	bottom	0.078	0.087	0.49	21.2	9.40
d1	top	0.220	0.038	0.77	14.6	3.47
d2	bottom	0.078	0.087	0.42	18.3	9.40
d2	top	0.220	0.038	0.87	16.5	3.47
e1	bottom	0.059	0.085	0.65	27.6	12.29
e1	top	0.240	0.037	0.53	9.9	3.20
e2	bottom	0.059	0.085	0.67	28.5	12.29
e2	top	0.240	0.037	0.61	7.6	3.20
f1	bottom	0.039	0.083	0.73	30.3	18.29
f1	top	0.240	0.036	0.50	9.0	2.96
f2	bottom	0.039	0.083	0.64	26.4	18.29
f2	top	0.240	0.036	0.41	7.3	2.96

Assuming  $T_i$  and  $T_j$  are the bulk temperatures of two adjacent subchannels  $i$  and  $j$ , the heat transported through the gap per unit length by the effective subchannel

mixing mechanism is

$$q_{ij} = m'_{ij} c_p (T_i - T_j) \quad (3.3)$$

where  $m'_{ij}$  is the instantaneous mass flow rate per unit length between subchannels  $i$  and  $j$  and can be expressed as

$$m'_{ij} = \rho w_{eff} g \quad (3.4)$$

where  $w_{eff}$  is the effective mean mixing velocity. It should be noted that for homogeneous subchannels, that  $\overline{m'_{ij}} = 0$ . Based on the occurrence and disappearance of the high turbulence kinetic energy patch with the variation of  $g/d$  as reported in Section 3.3.2, and the data of Hooper and Rehme (1984), it is judged that turbulence convection, manifested itself as periodic cross-gap eddy motion, is the dominant mixing mechanism in the following gap range (at least applicable for rod-trapezoidal duct)

$$0.020 \leq g/d \leq 0.100 \quad (3.5)$$

Since such cross-gap eddy motion is characterized by a peak in the spectral density function of azimuthal turbulence velocity, it is possible to express the effective mixing velocity in terms of the spectral data. Möller (1992) calculated the mixing velocity  $w_{eff}$  to be

$$w_{eff} = \sqrt{E_{v'_{az}}(f)B} \quad (3.6)$$

where  $E_{v'_{az}}(f)$  is the power spectral density of the azimuthal fluctuating velocity in the gap center and  $B$  is the bandwidth of the digitalization. Eq. (3.6) implies that only the bandwidth of the peak frequency contributes to the mixing velocity. As pointed out by Rehme (1992), such handling is doubtful since the cross-gap eddy motions are not caused by large-scale eddies of one size at a certain frequency but by a spectrum of eddies of different sizes. In this research, the mixing velocity is defined

as

$$w_{eff} = \sqrt{\int_{f_p - f_p/4}^{f_p + f_p/4} E_{v'_{az}}(f) df} \quad (3.7)$$

In order to facilitate comparison among different mixing results, Möller (1992) followed the definition of intersubchannel heat mixing proposed by Ingesson and Hedberg (1970),

$$q_{ij} = \rho c_p \bar{\epsilon} g Y \frac{T_i - T_j}{\delta_{ij}} \quad (3.8)$$

where  $\delta_{ij}$  is the mixing distance which is assumed to be the centroid distance between the subchannels  $i$  and  $j$ , and the mixing factor  $Y$  accounts for the increase of the effective viscosity compared to the reference eddy viscosity  $\bar{\epsilon}$  which is often taken as the mean value of pipe flow

$$\bar{\epsilon} = \nu \frac{Re}{20} \sqrt{\frac{f}{8}} \quad (3.9)$$

where  $f$  is the Moody friction factor.

A comparison between Eq. (3.2) and (3.7) gives the expression of mixing factor in terms of mixing velocity

$$Y = \frac{w_{eff} \delta_{ij}}{\bar{\epsilon}} \quad (3.10)$$

Table 3-9 summarizes the derived mixing velocities  $w_{eff}$  and mixing factors  $Y$ . All data were converted to a single Reynolds number  $Re = 52,000$  assuming that  $w_{eff}$  is proportional to  $Re^{0.9}$  as suggested by Rehme (1992). For all the rod settings, the four subchannel centroids were defined as the intersections between the MVL (maximum mean axial velocity line) and the lines connecting the rod center and duct corners. The distance between adjacent subchannel centers were then taken as the MVL length connecting the two centroids. Rehme (1992) proposed a correlation between mixing factor  $Y$  and nondimensional gap size  $g/d$ ,

$$Y = 0.812(g/d)^{-0.96}, \quad \text{universal in subchannel shape} \quad (3.11)$$

It is noted that the mixing factor  $Y$  in Eq. (3-11) was multiplied by a factor 0.85 to account for a profile of the mixing velocity. Fig. 3-16 compares the present derived mixing factors with the those predicted by Eq. (3-11). While the present symmetric gap data exhibit good correlation with Eq. (3-11), large deviations occur for asymmetric gap data. One possible explanation to this is that secondary flows may not be bounded by the highly asymmetric subchannel boundaries in these cases, causing the enhancement of mixing between adjacent subchannels, hence large mixing factors. This point is explained further in Chapter 5 in conjunction with predicted secondary flow pattern by finite-element method.

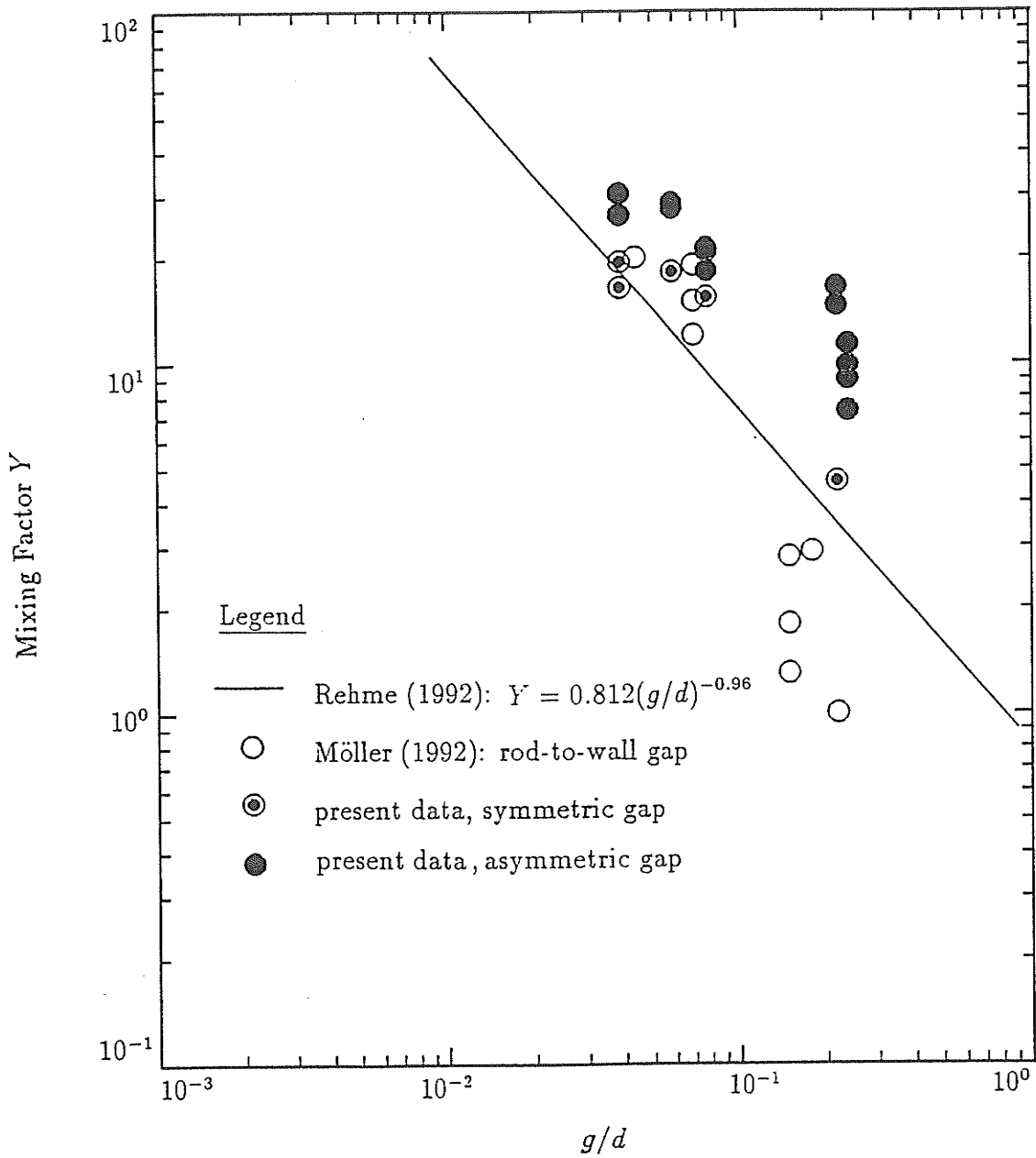


Figure 3-17 Correlation of mixing factor and nondimensional gap size

## Chapter 4

# Predictions of Turbulence Structures in Simulated Symmetric Rod Bundles: Finite Volume Method

The goal-oriented numerical research presented in this chapter serves as a natural continuation and supplementation to the extensive experimental work reported in the preceding chapter. This study was aimed at simulating fully developed turbulence structures in simulated symmetric rod bundles formed by the rod-trapezoidal duct. Special attention was devoted to the predictions of secondary flows, since the subtle secondary velocity picture was not clearly depicted by X-probe measurements due to various limitations. Efforts were also made to the reproductions of turbulence kinetic energy and wall shear stress distributions in medium-small rod-to-wall gaps, which were found experimentally to bear strong traces of the influence of coherent large-scale cross-gap eddy motion. Other parameters of interest included axial velocity distribution and the dependence of friction factor on Reynolds number.

The methodology adopted in the numerical study described in this chapter, was a combination of curvilinear non-orthogonal grids and primitive variables. With a simple coordinate system transformation from an orthogonal cylindrical system to a non-orthogonal curvilinear system, the highly irregular flow passage of the rod-

trapezoidal duct was converted to a regular rectangle. Since this transformation is applicable to other geometries formed by a rod enclosed by an arbitrary noncircular duct, a series of numerical tests were performed on several simple geometries for which experimental data were available for comparison to the predicted results. The purpose here was to develop the method and then to establish credibility by demonstrating accuracy and versatility. The algebraic stress model developed by Launder & Ying (1973) along with the two-equation ( $k$  and  $\epsilon$ ) model was employed for the prediction of normal fully developed turbulent flows. An empirical anisotropic eddy viscosity distribution based on the present experimental data was then used in conjunction with the above turbulence model to address the influence of coherent large-scale cross-gap eddy motion, whenever the rod-to-wall gap size fell within the experimentally determined range given by Eq. (3-5).

This chapter is organized in accordance with the natural course of the implementation of the present numerical study. The mathematical formulations, including governing equations, turbulence model, boundary conditions, and details of the coordinate transformation, are given first, followed by the descriptions of the numerical scheme. The full documentation of the comparisons between the predictions and experimental data for the rod-trapezoidal duct is preceded by the results of a number of numerical test cases. The computer code used in this study can be found in Appendix B.

## 4.1 Mathematical Formulations

### 4.1.1 Momentum Equations

Consider a general passage formed by a rod and an arbitrary duct such as shown in Fig. 4-1 with primary flow ( $\bar{V}_z$ ) parallel to the rod. Note that the radius of the

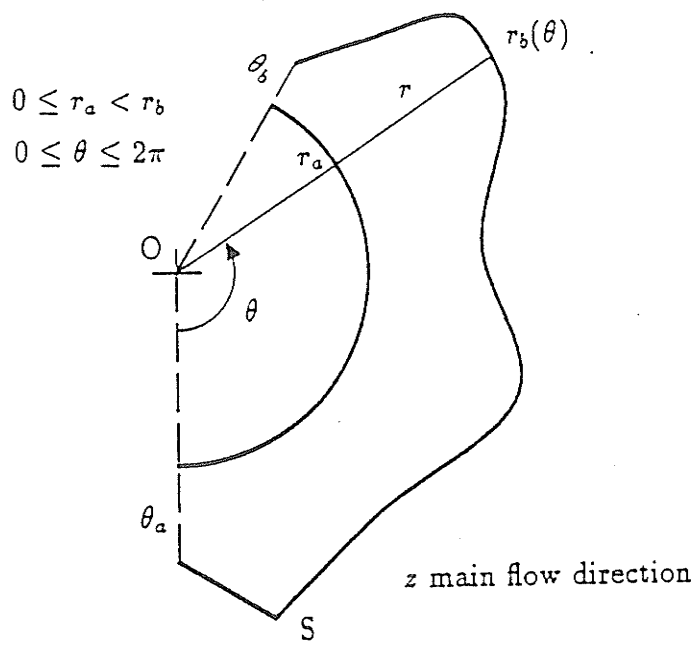


Figure 4-1 Cross-section of general flow passage in numerical studies

rod may vanish and that "corner" point(s) S may exist along the duct wall. For fully developed turbulent flow of a constant properties fluid, in a cylindrical coordinate system  $(r, \theta, z)$ , the Reynolds equations are (Trupp and Aly (1979)):

Reynolds equation for the radial direction,

$$\frac{1}{r} \frac{\partial}{\partial r} (\rho r \bar{V}_r \bar{V}_r) + \frac{1}{r} \frac{\partial}{\partial \theta} (\rho \bar{V}_\theta \bar{V}_r) = \frac{1}{r} \frac{\partial}{\partial r} (\mu r \frac{\partial \bar{V}_r}{\partial r}) + \frac{1}{r^2} \frac{\partial}{\partial \theta} (\mu \frac{\partial \bar{V}_r}{\partial \theta}) + S_{\bar{V}_r} \quad (4.1)$$

$$S_{\bar{V}_r} = -\mu \left[ \frac{\bar{V}_r}{r^2} + \frac{2}{r^2} \frac{\partial \bar{V}_\theta}{\partial \theta} \right] - \rho \left[ \frac{1}{r} \frac{\partial}{\partial r} (r \overline{v_r^2}) + \frac{1}{r} \frac{\partial \overline{v_r v_\theta}}{\partial \theta} - \frac{\overline{v_\theta^2}}{r} \right] + \rho \frac{\bar{V}_\theta^2}{r} - \frac{\partial \bar{P}}{\partial r}$$

Reynolds equation for the peripheral direction,

$$\frac{1}{r} \frac{\partial}{\partial r} (\rho r \bar{V}_r \bar{V}_\theta) + \frac{1}{r} \frac{\partial}{\partial \theta} (\rho \bar{V}_\theta \bar{V}_\theta) = \frac{1}{r} \frac{\partial}{\partial r} (\mu r \frac{\partial \bar{V}_\theta}{\partial r}) + \frac{1}{r^2} \frac{\partial}{\partial \theta} (\mu \frac{\partial \bar{V}_\theta}{\partial \theta}) + S_{\bar{V}_\theta} \quad (4.2)$$

$$S_{\bar{V}_\theta} = \mu \left[ \frac{2}{r^2} \frac{\partial \bar{V}_r}{\partial \theta} - \frac{\bar{V}_\theta}{r^2} \right] - \rho \left[ \frac{\partial}{\partial r} \overline{v_r v_\theta} + \frac{1}{r} \frac{\partial \overline{v_\theta^2}}{\partial \theta} + \frac{2 \overline{v_r v_\theta}}{r} \right] + \frac{\rho}{r} \bar{V}_r \bar{V}_\theta - \frac{1}{r} \frac{\partial \bar{P}}{\partial \theta}$$

Reynolds equation for the axial direction,

$$\frac{1}{r} \frac{\partial}{\partial r} (\rho r \bar{V}_r \bar{V}_z) + \frac{1}{r} \frac{\partial}{\partial \theta} (\rho \bar{V}_\theta \bar{V}_z) = \frac{1}{r} \frac{\partial}{\partial r} (\mu r \frac{\partial \bar{V}_z}{\partial r}) + \frac{1}{r^2} \frac{\partial}{\partial \theta} (\mu \frac{\partial \bar{V}_z}{\partial \theta}) + S_{\bar{V}_z} \quad (4.3)$$

$$S_{\bar{V}_z} = -\rho \left[ \frac{1}{r} \frac{\partial}{\partial r} (r \overline{v_r v_z}) + \frac{1}{r} \frac{\partial}{\partial \theta} \overline{v_\theta v_z} \right] - \frac{\partial \bar{P}}{\partial z}$$

#### 4.1.2 Turbulence Model

The algebraic stress model developed by Launder & Ying (1973) was employed by Nakayama et al (1983) along with the two-equation  $k$  and  $\epsilon$  model for predictions of fully developed turbulent flows in square, rectangular and trapezoidal ducts. In the

present research, this path was followed for flows without the presence of coherent cross-gap eddy motion. For such cases, turbulent stress tensor appearing in the Reynolds equations are expressed as follows,

$$\begin{aligned}
\overline{v_\theta^2} &= C_3 k - C_2 C_4 \frac{k^3}{\epsilon^2} \left( \frac{\partial \overline{V}_z}{r \partial \theta} \right)^2 \\
\overline{v_r^2} &= C_3 k - C_2 C_4 \frac{k^3}{\epsilon^2} \left( \frac{\partial \overline{V}_z}{\partial r} \right)^2 \\
\overline{v_r v_\theta} &= -C_2 C_4 \frac{k^3}{\epsilon^2} \frac{\partial \overline{V}_z}{\partial r} \frac{\partial \overline{V}_z}{r \partial \theta} \\
\overline{v_r v_z} &= -C_4 \frac{k^2}{\epsilon} \frac{\partial \overline{V}_z}{\partial r} \\
\overline{v_\theta v_z} &= -C_4 \frac{k^2}{\epsilon} \frac{\partial \overline{V}_z}{r \partial \theta}
\end{aligned} \tag{4.4}$$

where  $C_2 = 0.0185$ ,  $C_3 = 0.552$  and  $C_4 = 0.09$  are related model coefficients (Nakayama et al (1983)). It should be noted that these expressions imply the introduction of isotropic turbulent viscosity.

The transport equations for the turbulence kinetic energy  $k$  and the dissipation rate of turbulence kinetic energy  $\epsilon$  appearing in the turbulent stress tensor (Eq.(4.4)) are as follows,

$$\frac{1}{r} \frac{\partial}{\partial r} (r \rho \overline{V}_r k) + \frac{1}{r} \frac{\partial}{\partial \theta} (\rho \overline{V}_\theta k) = \frac{1}{r} \frac{\partial}{\partial r} \left( r \frac{\mu_t}{\sigma_k} \frac{\partial k}{\partial r} \right) + \frac{1}{r^2} \frac{\partial}{\partial \theta} \left( \frac{\mu_t}{\sigma_k} \frac{\partial k}{\partial \theta} \right) + S_k \tag{4.5}$$

$$S_k = G - \rho \epsilon$$

$$\frac{1}{r} \frac{\partial}{\partial r} (r \rho \overline{V}_r \epsilon) + \frac{1}{r} \frac{\partial}{\partial \theta} (\rho \overline{V}_\theta \epsilon) = \frac{1}{r} \frac{\partial}{\partial r} \left( r \frac{\mu_t}{\sigma_\epsilon} \frac{\partial \epsilon}{\partial r} \right) + \frac{1}{r^2} \frac{\partial}{\partial \theta} \left( \frac{\mu_t}{\sigma_\epsilon} \frac{\partial \epsilon}{\partial \theta} \right) + S_\epsilon \tag{4.6}$$

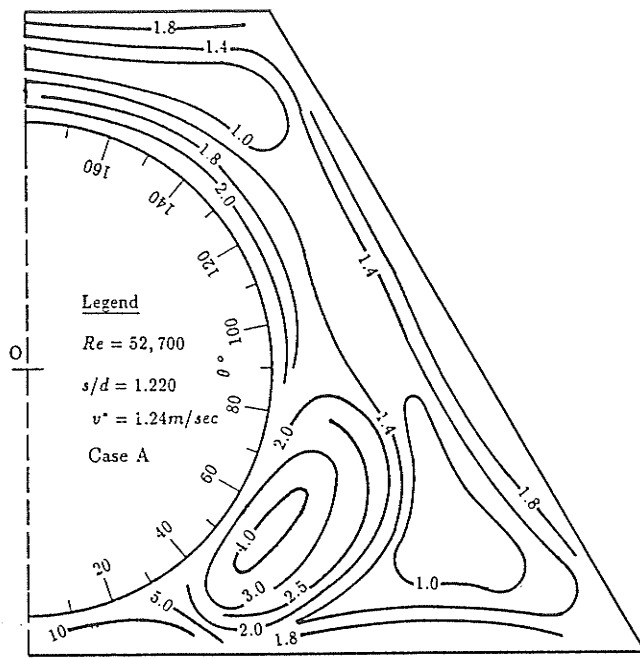
$$S_\epsilon = \epsilon \frac{(C_{\epsilon_1} G - C_{\epsilon_2} \rho \epsilon)}{k}$$

where  $\mu_t = C_4 k^2 / \epsilon$ ;  $\sigma_k = 0.9$  and  $\sigma_\epsilon = 1.3$  are turbulent Prandtl numbers for  $k$  and  $\epsilon$ , respectively;  $C_{\epsilon_1} = 1.55$  and  $C_{\epsilon_2} = 2.0$  are empirical constants and  $G$  represents the

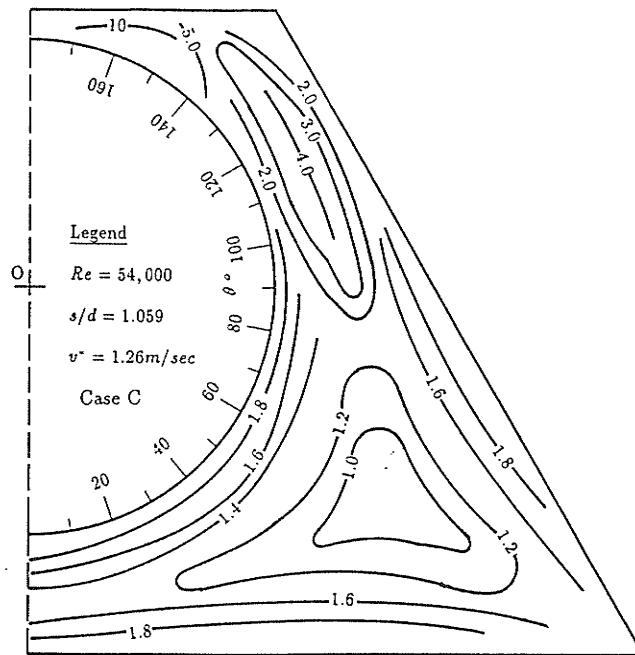
production rate of turbulence kinetic energy in which only gradients in axial velocity are retained,

$$G = -\rho \overline{v_r v_z} \frac{\partial \overline{V}_z}{\partial r} - \rho \overline{v_\theta v_z} \frac{\partial \overline{V}_z}{r \partial \theta} \quad (4.7)$$

Modelling of turbulence in the presence of coherent large-scale cross-gap eddy motion poses a challenging problem. Transport of momentum and turbulence energy by turbulence convection, unlike the conventional gradient-type turbulence diffusion, is not driven by the non-uniformity of the transferable quantity. Therefore, the existing turbulence models which are all constructed on Prandtl's fundamental philosophy (Hinze (1975)) that eddy-viscosity is directly related to integral length scale are inherently incapable of handling the non-gradient type transport by the cross-gap eddy motion. This is not to say that the so-far successful combination of algebraic stress model and two-equation  $k$  and  $\epsilon$  model suddenly becomes totally obsolete in the rod-trapezoidal duct case. On the contrary, experimental evidence presented in Chapter 3 and those of Hooper and Rehme (1984) suggest that the turbulence structures in simulated rod bundle subchannels follow the non-circular duct flow behaviors in general, with certain degrees of modification by large-scale turbulence convection in confined gap regions provided that the gap size falls within medium-small range as given by Eq. (3-5). In this regard, complete modelling of the rod-trapezoidal duct flow involves two necessary components, the prediction of typical non-circular duct flow behaviors for most of the flow passage and the simulation of non-gradient type transport in certain designated gap areas. It is therefore quite natural to use the model employed by Nakayama et al (1983) to handle the fully developed turbulence structures for passages not directly influenced by the coherent eddy motion, and this model was then superimposed with a certain experimental input to accommodate the presence of large-scale cross-gap eddy motion. Numerical modelling of this particular



(a)



(b)

Figure 4-2 Anisotropic factor  $n(r, \theta)$  distributions  
 (a) Case A ; (b) Case C

aspect is still in its adolescent stage.

Specific steps of the superposition was made possible by extending the consideration of the fact that at the time-average level the periodic large-scale cross-gap eddy motion manifests itself as a high turbulence kinetic energy patch in the near gap region. As pointed by Rehme (1992) and by Wu and Trupp (1993a), the source of the high turbulence kinetic energy comes from the extremely high turbulence shear stress  $\overline{v_z v_\theta}$  and  $\overline{v_\theta^2}$ . If correct reproduction of the turbulence kinetic energy is of primary concern, an approach based on the empirical input of the level of turbulence shear stresses seems plausible, admitting that the physics behind this coherent structure may not be truly depicted by such simplification. In practice, an anisotropic eddy viscosity factor was defined as

$$\overline{v_z v_\theta} = n(r, \theta) \mu_t \frac{\partial \overline{V}_z}{r \partial \theta} \quad (4.8)$$

$$\overline{v_z v_r} = \mu_t \frac{\partial \overline{V}_z}{\partial r} \quad (4.9)$$

or explicitly

$$n(r, \theta) = \frac{\overline{v_z v_\theta}}{\overline{v_z v_r}} \left( \frac{\partial \overline{V}_z}{\partial r} / \frac{\partial \overline{V}_z}{r \partial \theta} \right) \quad (4.10)$$

the right-hand side of Eq. (4-10) can be determined experimentally. The newly defined azimuthal turbulence shear stress  $\overline{v_z v_\theta}$  in Eq. (4-8) and azimuthal normal shear stress

$$\overline{v_\theta^2} = n(r, \theta) \left[ C_3 k - C_2 C_4 \frac{k^3}{\epsilon^2} \right] \quad (4.11)$$

are substituted into Eqs.(4-1) to (4-3) for all the rod settings where the existence of coherent eddy motion was detected by measurements. The derived anisotropic factor  $n(r, \theta)$  contours from available experimental information for cases of  $s/d = 1.220$  and  $1.059$  are shown in Fig. 4-2.

### 4.1.3 Boundary Conditions

The boundaries of the solution domain (Fig. 4-1) contain symmetric lines and solid walls. In the limiting case of zero rod radius, the imaginary rod surface is regarded as a symmetric line. Usually advantage is taken to arrange the starting and ending angular positions  $\theta = \theta_a$  and  $\theta = \theta_b$  to coincide with geometry symmetric lines. On a symmetric line, the velocity normal to this line is zero as are the normal gradients of the remaining velocity components and of all other variables.

The usual "non-slip" conditions apply at a wall. The various diffusive fluxes across the wall were calculated by use of "wall functions" (Antonopoulos (1986)), which are based on the assumptions that in the region very near the wall: (a) the flow behaves as an one-dimensional Couette flow with low streamwise pressure gradient, and (b) production of  $k$  is approximately equal to its dissipation. A brief outline of the relations employed is given below.

The nearest-to-the-wall grid node P, located at distance  $\delta_P$  from the wall, is considered to lie in the fully turbulent region of the Couette flow, if the value of quantity  $\delta_P^*$  at this point is defined as

$$\delta_P^* = \left[ \frac{\rho C_4^{1/4} k^{1/2} \delta_P}{\mu} \right]_P \quad (4.12)$$

is greater than 11.63, while for  $\delta_P^* \leq 11.63$  the point is taken to lie in the laminar sublayer.

Thus, for the momentum equations, the wall shear stress component in the axial  $z$ -direction at point P is calculated by use of the linear or the logarithmic law of the wall as

$$\tau_z = \left[ \mu \frac{\bar{V}_z}{\delta_P} \right]_P \quad \text{for } \delta_P^* \leq 11.63 \quad (4.13)$$

$$\tau_z = \left[ \frac{\rho C_4^{1/4} k^{1/2} \bar{V}_z}{5.50 \log(9.77 \delta_P^*)} \right]_P \quad \text{for } \delta_P^* > 11.63 \quad (4.14)$$

The values of the constants 5.50 and 9.77 are evaluated based on the logarithmic law obtained by Patel (1965) which serves as a good approximation to the measured near wall axial velocity distribution shown in Fig. 3-4.

For the  $k$ -transport equation, the value of  $k$  at the nearest-to-the-wall point P is calculated by use of the wall shear stress expressions given above,

$$k_P = \left[ \frac{\tau}{\rho C_4^{1/2}} \right]_P \quad (4.15)$$

For the  $\epsilon$ -transport equation, the value of  $\epsilon$  at the nearest to the wall point P is calculated as

$$\epsilon_P = \left[ \frac{C_4^{3/4} k^{3/2}}{5.50 \delta_P} \right]_P \quad (4.16)$$

#### 4.1.4 Coordinate System Transformation

The coordinate system transformation employed in this research was that first used by Markatos et al. (1978) to solve three dimensional turbulent boundary layers on a ship's hull. Following the same path, Nakayama et al (1983) successfully dealt with fully developed turbulent flows in various non-circular ducts. Recently, this methodology was reviewed thoroughly by Melaaen (1992). With reference to the general flow passage shown in Fig. 4-1, the elements of a new curvilinear non-orthogonal system  $(\eta, \xi, \zeta)$  are defined in terms of orthogonal, cylindrical coordinates  $(r, \theta, z)$  as follows:

$$\begin{aligned} \vec{\eta} &= \frac{r - r_a}{r_b(\theta) - r_a} \vec{e}_r \\ \vec{\xi} &= \frac{\theta - \theta_a}{\theta_b - \theta_a} \vec{e}_\theta \\ \vec{\zeta} &= z \vec{e}_z \end{aligned} \quad (4.17)$$

where  $r_a, r_b, \theta_a, \theta_b$  are diagrammatically shown in Fig. 4-1 and  $\vec{e}_r, \vec{e}_\theta, \vec{e}_z$  are unit vectors in the cylindrical system. It should be noted that the radius of the rod  $r_a$  is

constant and the radius of the outer boundary  $r_b$  is a function of angle  $\theta$ . Applying the chain rule of derivation to Eq. (4-18) yields the following transformation law for the first order derivatives

$$\frac{\partial}{\partial r} = \frac{1}{r_b - r_a} \frac{\partial}{\partial \eta} \quad (4.18)$$

$$\frac{\partial}{\partial \theta} = \frac{1}{\theta_b - \theta_a} \frac{\partial}{\partial \xi} - \frac{1}{r_b - r_a} \left[ \eta \frac{\partial r_b(\theta)}{\partial \theta} \right] \frac{\partial}{\partial \eta} \quad (4.19)$$

For a "corner" point S at which discontinuity of the first derivative occurs as shown in Fig. 4-1,  $\partial r_b(\theta)/\partial \theta$  is defined as the average of its left and right derivatives of the same order,

$$\left. \frac{\partial r_b(\theta)}{\partial \theta} \right|_S = \frac{1}{2} \left[ \left. \frac{\partial r_b(\theta)}{\partial \theta} \right|_{S-} + \left. \frac{\partial r_b(\theta)}{\partial \theta} \right|_{S+} \right] \quad (4.20)$$

With the transformation defined by Eq. (4-18) to (4-20), the whole length of the duct wall is transformed to  $\eta = 1$ , while the rod surface is transformed to  $\eta = 0$ . It is interesting to note that a noncircular duct flow can be considered as a special case of the rod-noncircular duct flow family by assigning  $r_a = 0$  and by correspondingly changing the boundary condition at  $r = r_a$ . Similarly, instead of considering  $r_b(\theta)$  as representing a solid duct wall, it is permissible to apply symmetric conditions on  $r_b(\theta)$ , which is the case of a rod-bundle subchannel flow. This generality can also be extended so as to impose different kinds of boundary conditions on various sections of the whole length of  $r_b(\theta)$ .

In a cylindrical coordinate system  $(r, \theta, z)$  the transport equations of momentum Eqs. (4-1) to (4-3) and of  $k$  and  $\epsilon$  Eqs. (4-5) and (4-6) conform to the following form,

$$\frac{1}{r} \frac{\partial}{\partial r} (\rho r \bar{V}_r \Phi) + \frac{1}{r} \frac{\partial}{\partial \theta} (\rho \bar{V}_\theta \Phi) = \frac{1}{r} \frac{\partial}{\partial r} (\Gamma_\Phi r \frac{\partial \Phi}{\partial r}) + \frac{1}{r^2} \frac{\partial}{\partial \theta} (\Gamma_\Phi \frac{\partial \Phi}{\partial \theta}) + S_\Phi(r, \theta) \quad (4.21)$$

where the general variable  $\Phi$  denote  $\bar{V}_z$ ,  $\bar{V}_r$ ,  $\bar{V}_\theta$ ,  $k$  and  $\epsilon$ . The effective transport

coefficient  $\Gamma_\Phi$  and the original source term  $S_\Phi(r, \theta)$  have already been defined in the corresponding transport equations.

By applying the transformation laws Eqs. (4-18) to (4-20) on Eqs. (4-22), we obtain the following general governing equation in the transformed  $(\xi, \eta, \zeta)$  system,

$$\begin{aligned} & \frac{1}{r} \frac{1}{r_b - r_a} \frac{\partial}{\partial \eta} \left[ \rho r \Phi (\bar{V}_r - \frac{\bar{V}_\theta}{r} (\eta \frac{\partial r_b}{\partial \theta})) \right] + \frac{1}{r} \frac{1}{\theta_b - \theta_a} \frac{\partial}{\partial \xi} (\rho \bar{V}_\theta \Phi) \\ = & \frac{1}{r} \frac{1}{(r_b - r_a)^2} \frac{\partial}{\partial \eta} \left\{ \frac{\partial \Phi}{\partial \eta} r [\Gamma_\Phi + \Gamma_\Phi \frac{\eta^2}{r^2} (\frac{\partial r_b}{\partial \theta})^2] \right\} + \frac{1}{r^2} \frac{1}{(\theta_b - \theta_a)^2} \frac{\partial}{\partial \xi} (\Gamma_\Phi \frac{\partial \Phi}{\partial \xi}) \\ & + S'_\Phi + S_\Phi(\eta, \xi) \end{aligned} \quad (4.22)$$

where  $S'_\Phi$  represents extra terms resulting from the coordinate transformation,

$$\begin{aligned} S'_\Phi = & -\frac{1}{r} \frac{1}{r_b - r_a} \frac{\partial r_b}{\partial \theta} \rho \bar{V}_\theta \Phi \\ & - \frac{1}{r^2} \frac{1}{\theta_b - \theta_a} \frac{1}{r_b - r_a} (\eta \frac{\partial r_b}{\partial \theta}) \frac{\partial}{\partial \eta} (\Gamma_\Phi \frac{\partial \Phi}{\partial \xi}) \\ & - \frac{1}{r^2} \frac{1}{\theta_b - \theta_a} \frac{\partial}{\partial \xi} (\Gamma_\Phi \frac{1}{r_b - r_a} \eta \frac{\partial r_b}{\partial \theta} \frac{\partial \Phi}{\partial \eta}) \\ & - \frac{1}{r} \frac{1}{(r_b - r_a)^2} \Gamma_\Phi \eta (\frac{\partial r_b}{\partial \theta})^2 \frac{\partial \Phi}{\partial \eta} \frac{\partial}{\partial \eta} (\frac{\eta}{r}) \end{aligned} \quad (4.23)$$

and  $S_\Phi(\eta, \xi)$  represents the original source terms  $S_\Phi(r, \theta)$  transformed from the cylindrical system which can be easily done by substituting all the derivatives with respect to  $r$  and  $\theta$  with the transformation rules given in Eq. (4-19) and (4-20).

Apart from the transformation of the general governing equations from Eq. (4-23) to Eq. (4-24), all auxiliary relations such as boundary conditions (except for Dirichlet boundary conditions) must also be similarly transformed. After this is done, computation can start with the regular computational  $(\eta, \xi)$  domain.

## 4.2 Numerical Scheme

### 4.2.1 Discretization Procedure

The first step in the development of a numerical scheme for solving the equations given in the previous section, is to obtain discretized equivalents of the partial differential equations (i.e. finite-difference equations). In the present section it is shown how the partial differential equations are discretized by integration over the control volumes which surround the nodes of the grid system.

The control volume surrounding a grid node, P, is indicated in Fig. 4-3, and is termed the main control volume. The grid spacings need not necessarily be uniform over the flow domain. The finite-difference grid is chosen after experimentation with finer and coarser grids so as to make the results of the computation substantially independent of the grid employed. All the scalar variables ( $p, k, \epsilon$ ) and the axial velocity  $\bar{V}_z$  are stored at nodal points while velocities  $\bar{V}_r$  and  $\bar{V}_\theta$  are stored at points midway between grid nodes in the  $\xi$  and  $\eta$  direction, respectively. As a result of such grid arrangements, control volumes appropriate to the  $\bar{V}_r$  and  $\bar{V}_\theta$  are staggered from the main control volumes.

The general transport equation Eq. (4.23) is integrated for each variable, over the appropriate control volume that encloses the specific variable. Taking one scalar variable  $\Phi$ , for instance, define

$$\begin{aligned}
 J_n &= \frac{1}{r_P} \frac{1}{r_b - r_a} \left[ \rho r \Phi (\bar{V}_r - \frac{\bar{V}_\theta}{r} (\eta \frac{\partial r_b}{\partial \theta})) \right]_n \Delta \xi \\
 &\quad - \frac{1}{r_P} \frac{1}{(r_b - r_a)^2} \left\{ \frac{\partial \Phi}{\partial \eta} r [\Gamma_{\Phi, r} + \Gamma_{\Phi, \theta} \frac{\eta^2}{r^2} (\frac{\partial r_b}{\partial \theta})^2] \right\}_n \Delta \xi \\
 J_s &= \frac{1}{r_P} \frac{1}{r_b - r_a} \left[ \rho r \Phi (\bar{V}_r - \frac{\bar{V}_\theta}{r} (\eta \frac{\partial r_b}{\partial \theta})) \right]_s \Delta \xi \\
 &\quad - \frac{1}{r_P} \frac{1}{(r_b - r_a)^2} \left\{ \frac{\partial \Phi}{\partial \eta} r [\Gamma_{\Phi, r} + \Gamma_{\Phi, \theta} \frac{\eta^2}{r^2} (\frac{\partial r_b}{\partial \theta})^2] \right\}_s \Delta \xi \quad (4.24) \\
 J_e &= \frac{1}{r_P} \frac{1}{\theta_b - \theta_a} (\rho \bar{V}_\theta \Phi)_e \Delta \eta - \frac{1}{r_P^2} \frac{1}{(\theta_b - \theta_a)^2} (\Gamma_{\Phi, \theta} \frac{\partial \Phi}{\partial \xi})_e \Delta \eta
 \end{aligned}$$

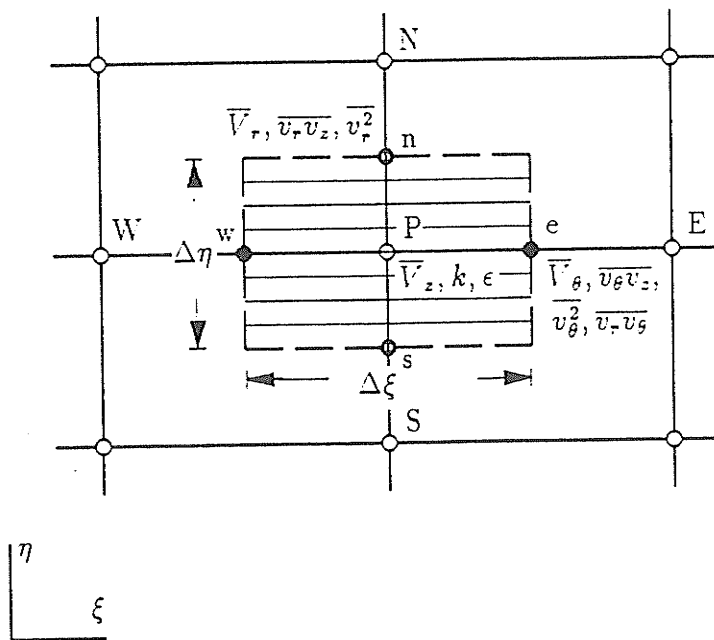


Figure 4-3 Control volume and staggered grids in transformed computational plane

$$J_w = \frac{1}{r_P} \frac{1}{\theta_b - \theta_a} (\rho \bar{V}_\theta \Phi)_w \Delta \eta - \frac{1}{r_P^2} \frac{1}{(\theta_b - \theta_a)^2} (\Gamma_{\Phi, \theta} \frac{\partial \Phi}{\partial \xi})_w \Delta \eta$$

Integration of the general governing equation for the scalar  $\Phi$  over the main control volume shown in Fig. 4-3 yields:

$$J_n - J_s + J_e - J_w = (S'_\Phi + S_\Phi)_P \Delta \xi \Delta \eta \quad (4.25)$$

In the  $\eta, \xi$  system, according to the transformation law, the continuity equation has the following form,

$$\frac{1}{r} \frac{1}{r_b - r_a} \frac{\partial}{\partial \eta} \left[ \rho r (\bar{V}_r - \frac{\bar{V}_\theta}{r} (\eta \frac{\partial r_b}{\partial \theta})) \right] + \frac{1}{r} \frac{1}{\theta_b - \theta_a} \frac{\partial}{\partial \xi} (\rho \bar{V}_\theta) = S'', \quad (4.26)$$

where  $S''_\Phi$  represents extra term as a result of the coordinate transformation,

$$S'' = -\frac{1}{r} \frac{1}{r_b - r_a} \frac{\partial r_b}{\partial \theta} \rho \bar{V}_\theta.$$

Define

$$\begin{aligned} F_n &= \frac{1}{r_P} \frac{1}{r_b - r_a} \left[ \rho r (\bar{V}_r - \frac{\bar{V}_\theta}{r} (\eta \frac{\partial r_b}{\partial \theta})) \right]_n \Delta \xi \\ F_s &= \frac{1}{r_P} \frac{1}{r_b - r_a} \left[ \rho r (\bar{V}_r - \frac{\bar{V}_\theta}{r} (\eta \frac{\partial r_b}{\partial \theta})) \right]_s \Delta \xi \\ F_e &= \frac{1}{r_P} \frac{1}{\theta_b - \theta_a} (\rho \bar{V}_\theta)_e \Delta \eta \\ F_w &= \frac{1}{r_P} \frac{1}{\theta_b - \theta_a} (\rho \bar{V}_\theta)_w \Delta \eta \end{aligned} \quad (4.27)$$

Integration of the continuity equation over the control volume yields

$$F_n - F_s + F_e - F_w = S''_\Phi)_P \Delta \xi \Delta \eta \quad (4.28)$$

If we now multiply the discretized continuity equation Eq. (4-29) by  $\Phi_P$  and subtract it from the discretized general governing equation Eq. (4-26), we obtain,

$$\begin{aligned} &(J_n - F_n \Phi_P) - (J_s - F_s \Phi_P) + (J_e - F_e \Phi_P) - (J_w - F_w \Phi_P) \\ &= (S'_\Phi + S_\Phi)_P \Delta \xi \Delta \eta - S''_\Phi)_P \Delta \xi \Delta \eta \Phi_P \end{aligned} \quad (4.29)$$

The discretization equation Eq. (4-30) can be rearranged to the following explicit form,

$$a_P \Phi_P = a_N \Phi_N + a_S \Phi_S + a_E \Phi_E + a_W \Phi_W + b \quad (4.30)$$

where

$$\begin{aligned} a_E &= D_e A(|P_e|) + \text{MAX}(-F_e, 0) \\ a_W &= D_w A(|P_w|) + \text{MAX}(F_w, 0) \\ a_N &= D_n A(|P_n|) + \text{MAX}(-F_n, 0) \\ a_S &= D_s A(|P_s|) + \text{MAX}(F_s, 0) \\ b &= (S_{\Phi}' + S_{\Phi})_P \Delta \xi \Delta \eta + S_{\Phi}'' \Phi_P \Delta \xi \Delta \eta \\ a_P &= a_E + a_W + a_N + a_S \end{aligned} \quad (4.31)$$

The flow rates  $F_n, F_s, F_e, F_w$  have been defined before, and the corresponding conductance are defined by

$$\begin{aligned} D_n &= \frac{1}{r_P} \frac{1}{(r_b - r_a)^2} \left\{ r [\Gamma_{\Phi, r} + \Gamma_{\Phi, \theta} \frac{\eta^2}{r^2} (\frac{\partial r_b}{\partial \theta})^2] \right\}_n \Delta \xi \frac{1}{\delta \eta_n} \\ D_s &= \frac{1}{r_P} \frac{1}{(r_b - r_a)^2} \left\{ r [\Gamma_{\Phi, r} + \Gamma_{\Phi, \theta} \frac{\eta^2}{r^2} (\frac{\partial r_b}{\partial \theta})^2] \right\}_s \Delta \xi \frac{1}{\delta \eta_s} \\ D_e &= \frac{1}{r_P^2} \frac{1}{(\theta_b - \theta_a)^2} (\Gamma_{\Phi, \theta})_e \Delta \eta \frac{1}{\delta \xi_e} \\ D_w &= \frac{1}{r_P^2} \frac{1}{(\theta_b - \theta_a)^2} (\Gamma_{\Phi, \theta})_w \Delta \eta \frac{1}{\delta \xi_w} \end{aligned} \quad (4.32)$$

The Peclet numbers:

$$P_e = \frac{F_e}{D_e} \quad P_w = \frac{F_w}{D_w} \quad P_n = \frac{F_n}{D_n} \quad P_s = \frac{F_s}{D_s}$$

The function  $A(|P|)$  is defined as:

$$A(|P|) = \text{MAX}(0, (1 - 0.1|P|)^5) \quad (4.33)$$

The discretized Eq. (4-30) is applicable to all the variables that are defined at the main grid point P, and in principal, applies to those defined in staggered grids provided that the definitions of flow rates and conductances are changed according to the position of the staggered control volume.

## 4.2.2 Solution Procedure

As stated, the present numerical scheme was constructed as a the combination of curvilinear non-orthogonal grids and the method of primitive variables. One fundamental prerequisite for the use of the matured SIMPLE algorithm is the construction of a pressure correction equation to generate a field of pressure perturbations which tend to drive the velocities towards the satisfaction of continuity. In this research, the pressure correction equation was derived from a modified form of the continuity equation Eq. (4-27). By moving the second term in the first bracket of Eq. (4-26) to the right-hand-side of the equation, we obtain

$$\begin{aligned} \frac{1}{r} \frac{1}{r_b - r_a} \frac{\partial}{\partial \eta} (\rho r \bar{V}_r) + \frac{1}{r} \frac{1}{\theta_b - \theta_a} \frac{\partial}{\partial \xi} (\rho \bar{V}_\theta) &= -\frac{1}{r} \frac{1}{r_b - r_a} \frac{\partial r_b}{\partial \theta} \rho \bar{V}_\theta + \frac{1}{r} \frac{1}{r_b - r_a} \frac{\partial}{\partial \eta} \left[ \rho \left( \eta \frac{\partial r_b}{\partial \theta} \right) \bar{V}_\theta \right] \\ &= S''' \end{aligned} \quad (4.34)$$

where the right hand side of Eq.(4-35),  $S'''$ , can be regarded as a virtual source for the continuity equation. By doing so, the pressure correction at point P (Fig. 4-3) is only related to the pressure corrections at its four nearest neighbours. Such practice entails the use of small under-relaxation coefficients.

Solution procedures followed the standard SIMPLE algorithm with wall shear stresses as the entry (Trupp and Aly (1979)). The pressure correction equation was solved by a point-by-point Gauss-Seidal method instead of the line-by-line iterative technique which was found inferior by Lei (1990). Typical under-relaxation numbers were 0.1 for  $\bar{V}_z$ ,  $k$  and  $\epsilon$ , and 0.05 for  $\bar{V}_r$ ,  $\bar{V}_\theta$  and pressure correction. Grid numbers

varied from  $12 \times 12$  for triangular array rod bundles to  $48 \times 24$  for other geometries. The validity of the use of these grid numbers was confirmed by grid refinement studies. Convergence was quite good and the criteria were set as

$$\left| \frac{\Phi_{new} - \Phi_{old}}{\Phi_{new}} \right|_{max} \leq 10^{-5} \quad (4.35)$$

and by checking the local residual of the pressure correction equation. It was found that by 1,600 iterations converged solutions to the flow in rod-trapezoidal ducts could be achieved.

## 4.3 Credibility Studies

Prior to performing the predictions of fully developed turbulent flow through rod-trapezoidal ducts, extensive test calculations were performed on various laminar and turbulent flow cases for which benchmark solutions (exact, experimental or numerical) existed. Test cases for fully developed laminar flows (e.g. square duct) were aimed at checking the numerical accuracy without the presence of ambiguity due to possible imperfection of the turbulence model. Further scrutiny on the numerical scheme and turbulence model was made possible by test calculations for fully developed turbulent flows through the trapezoidal duct of Khalifa and Trupp (1988), and for flows in infinite triangular array rod bundle subchannels. From an application point of view, these tests also demonstrated the generality of the adopted numerical approach, i.e. the combination of curvilinear non-orthogonal grids and primitive variables. More details about these test calculations other than here presented following can be found elsewhere (Wu and Trupp (1993b)).

### 4.3.1 Laminar Square Duct Flow

Calculations were performed for fully developed laminar flow through a square duct at  $Re = 996.6$ . Advantage was taken of the inherent symmetry of the duct so only one fourth of the duct was addressed. The inner rod in the generalized flow passage (Fig. 4-1)) was treated as a symmetrical line with zero radius ( $r_a = 0$ ). Three grid numbers were used to check the solution for grid independence, ( $21 \times 21$ ,  $25 \times 25$  and  $30 \times 30$ ). Secondary velocities  $\bar{V}_r$  and  $\bar{V}_\theta$  were known to be zero, so their governing equations were not solved. Converged solutions satisfying the criteria of Eq. (4-37) were achieved after 400 iterations with the under relaxation numbers

as 1.0. The predicted results were compared with the analytical solutions given by Shah and London (1978); the results are summarized in Table 4-1.

Table 4-1: Comparison of Numerical and Analytical Results For Fully Developed Laminar Square Duct Flow

Grids	Re	fRe	$V_{z,max}/\bar{V}_z$	dP/dz (Pa/m)
21 × 21	990.3	14.34	2.076	0.251
25 × 25	993.5	14.29	2.084	0.251
30 × 30	996.3	14.24	2.093	0.251
Exact	996.6	14.23	2.096	0.251

### 4.3.2 Turbulent Trapezoidal Duct Flow

The fully developed turbulent flow in the symmetric trapezoidal duct shown in Fig. 4-4 ( $l_t/2b = 0.4$ ,  $l_i/2b = 0.6$ ) was studied experimentally by Khalifa and Trupp (1988) using Pitot tube and hot-wire anemometry over a Reynolds number range of  $3.7 - 11.6 \times 10^4$ . This duct was constructed from the equilateral triangular duct used by Aly et al. (1978) and it turns out to be the bounding duct employed in the rod-trapezoidal duct subchannel study by the present author. Predictions for the trapezoidal duct flow were carried out for two Reynolds numbers ( $6.7$  and  $9.9 \times 10^4$ ) [corresponding to the data presented by Khalifa and Trupp (1988),] by locating the imaginary rod center (zero radius) at the symmetric center of the original equilateral triangular duct. Fig. 4-4 shows the predicted and measured resultant secondary flow in the symmetric half cross-section at  $Re = 9.9 \times 10^4$ . Each arrowhead and arrow-bar indicate the direction and the magnitude (see scale), respectively; location corresponds to the tail of the arrow. Both the numerical and experimental results display four discernible counter-rotating cells of secondary flow with the global maximum being located adjacent to the inclined wall. The predicted global maximum secondary velocity was twenty percent higher compared with the  $2.2\% \bar{V}_b$  value from measurements. Further discrepancies

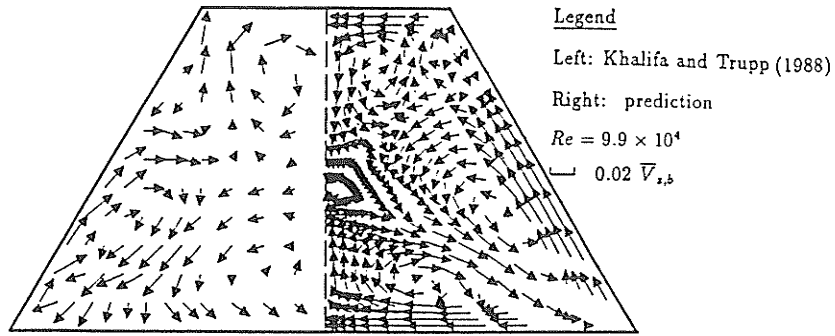


Figure 4-4 Comparison of predicted and measured secondary flows in the trapezoidal duct

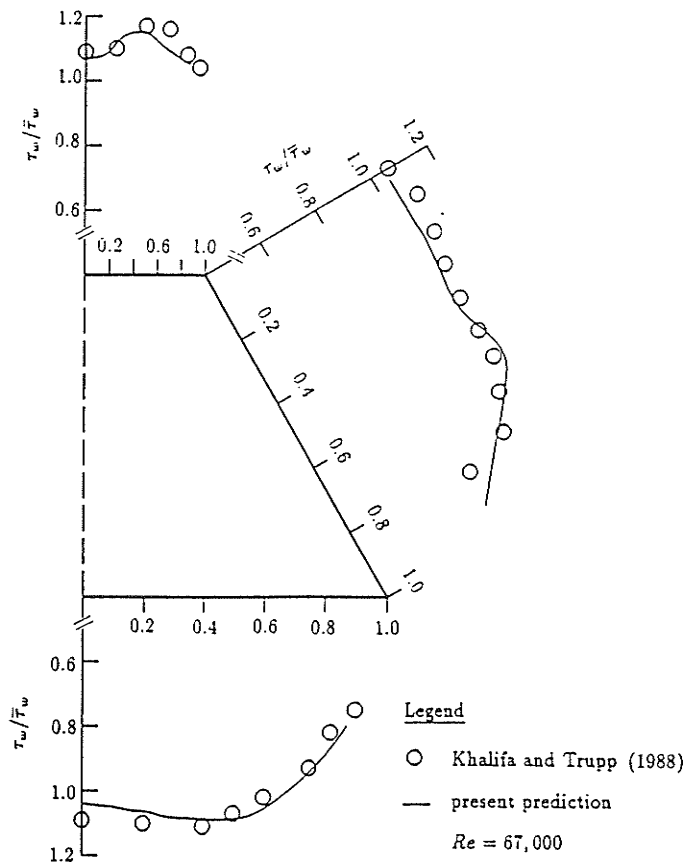


Figure 4-5 Comparison of predicted and measured wall shear stress in the trapezoidal duct

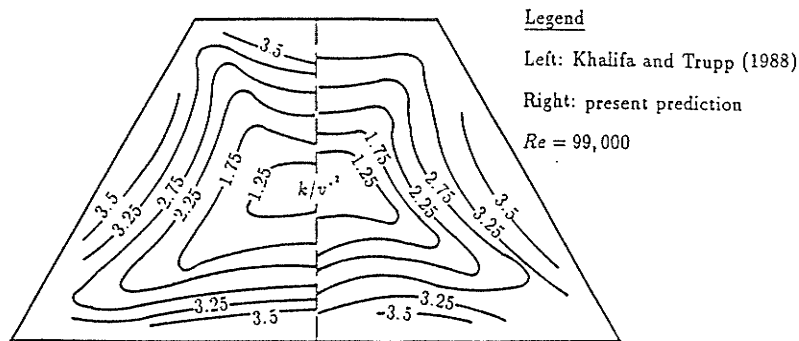


Figure 4-6 Comparison of predicted and measured turbulence kinetic energy in the trapezoidal duct

occur in the top and bottom wall areas in terms of both direction and magnitude; this is probably largely due to the fact that the X-probe generally registered too high near the top wall and too low near the bottom. Fig. 4-5 compares the computed and measured local wall shear stress (normalized by  $\bar{\tau}_w$ ) for  $Re = 6.7 \times 10^4$ . Generally, the correct trends have been predicted and the quantitative agreement between numerical and experimental data is fairly good with a maximum deviation of about 7%. Fig. 4-6 allows the comparison of the contours of turbulent kinetic energy at  $Re = 9.9 \times 10^4$ . Predicted strong distortions of the contours towards the  $60^\circ$  corner and bulges away from the inclined wall are in very good agreement with the experimental plot. However, bulges near the bottom wall are more pronounced than those from hot-wire measurements while bulges near the top wall display the reverse behavior. This is consistent with the differences in secondary flows shown in Fig. 4-4.

### 4.3.3 Triangular Array Rod Bundles

Trupp and Azad (1975) reported a wide-ranging experimental study on semi-infinite equilateral triangular rod bundle arrays having pitch-to-diameter ratios ( $p/d$ ) of 1.20 to 1.50 and Reynolds numbers in the range  $1.2 - 8.4 \times 10^4$ . Secondary flow was only inferred in their studies. Trupp and Aly (1979) later numerically studied secondary flows in such arrays with pitch-to-diameter ratios of 1.12–1.35. The present predictions were conducted for three combinations of  $p/d$  and Reynolds number, by assigning symmetric boundary conditions on the outer boundary  $r_b(\theta)$  (see Fig. 4-7). For  $p/d = 1.06$ , Fig. 4-8 compares the present predicted secondary flow and that predicted by Rapley and Gosman (1986) who used a curvilinear orthogonal grid. The single swirl of secondary flow from both predictions is in agreement with the measurements of Tahir and Rogers (1979). The global maximum secondary velocity in the current prediction is  $1.6\% \bar{V}_b$  compared to  $1.8\% \bar{V}_b$  of Rapley and Gosman

(1986); the present prediction also displays weaker secondary flow in the small gap region compared to that reported by the above authors. But this is consistent with the finding by Trupp and Aly (1979) that even for  $p/d = 1.123$ , secondary flow is unable to penetrate significantly into the gap region and such penetration decreases with decreasing  $p/d$ . Fig. 4-9 compares wall shear stress profiles for the cases of  $p/d = 1.10, Re = 3.6 \times 10^4$  and  $p/d = 1.20, Re = 3.5 \times 10^4$  and shows the predictions to be in good agreement with the measurements of Fakory and Todreas (1979) and of Trupp and Azad (1975). The discrepancies in comparison with the data of Fakory and Todreas (1979) lie in the neighbour of  $\theta = 0^\circ$  and  $\theta = 30^\circ$ . In the area around  $\theta = 30^\circ$ , prediction gives a shift in maximum value of  $\tau_w/\bar{\tau}_w$  towards small  $\theta$  direction; and in the area around  $\theta = 0^\circ$  the reverse shift is predicted. Considering the fact that the subchannel employed by Fakory and Todreas (1979) was not symmetrically bounded by its boundaries, which means cross-gap secondary flow in their subchannel would inevitably move maximum wall shear stress towards the geometric center, the above discrepancies are not surprising.

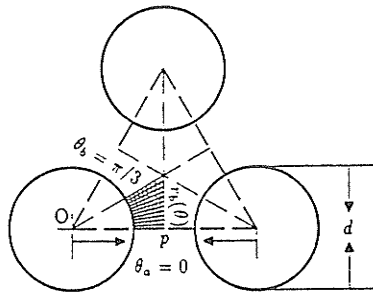


Figure 4-7 Cross-section of the triangular array rod bundle subchannel

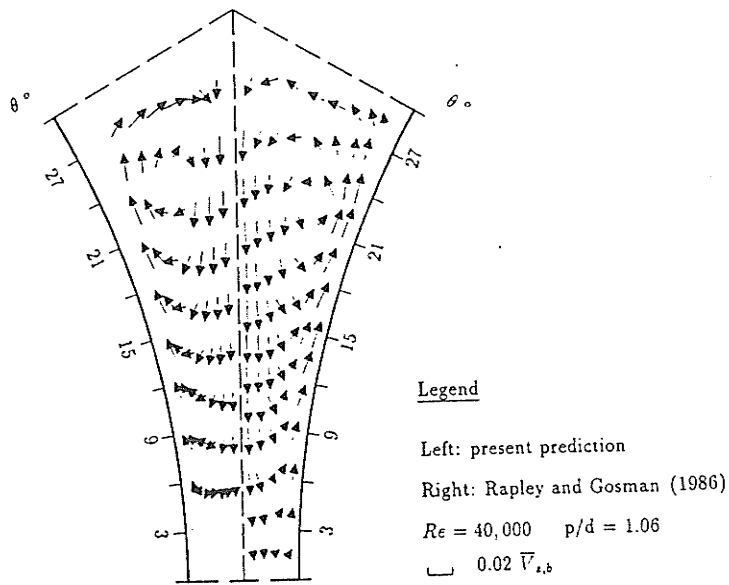


Figure 4-8 Comparison of predicted and measured secondary flows in the triangular array rod bundle subchannel

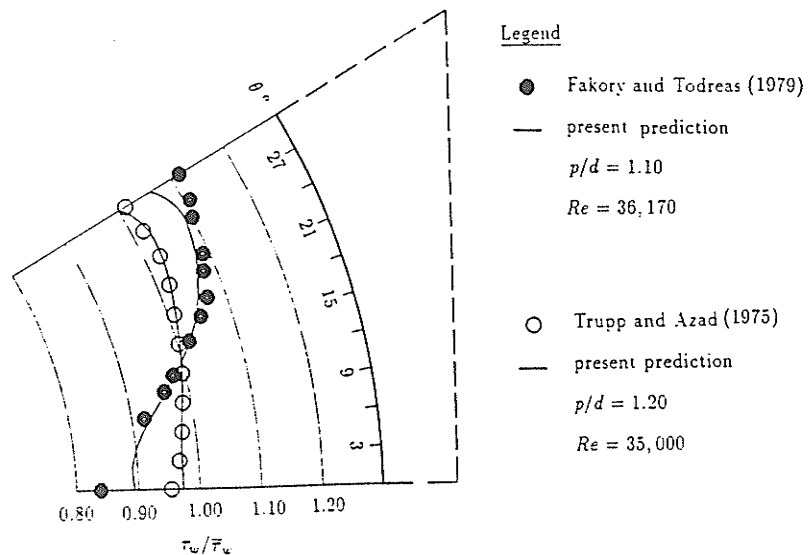


Figure 4-9 Comparison of predicted and measured local wall shear stresses in the triangular array rod bundle subchannel

## 4.4 Numerical Results

Three of the six experimental cases tabulated in Table 3-6 were investigated numerically, using the methodology outlined in the preceding subsections. The flow and geometric specifications of these three cases are retabulated in Table 4-2. For the sake of consistency, the sequential case numbers in Table 3-6 are retained.

Table 4-2: Summary of Numerically Studied Cases

Case	g (mm)	s (mm)	s/d	$v_z^*$ (m/s)	Re
A	11.2	62.0	1.220	1.24	52,700
C	3.0	53.8	1.059	1.26	54,200
D	1.0	51.8	1.020	1.26	55,200

For cases A and C in which coherent cross-gap eddy motions were detected by hot-wire measurements, the anisotropic eddy viscosity factor defined by Eqs.(4.8)-(4.13) were incorporated into the conventional algebraic stress model along with the  $k-\epsilon$  model given by Eqs.(4.4)-(4.7), whilst in case D where no large-scale cross-gap eddy motion was detected, only Eqs.(4.4)-(4.7) were called for in the turbulence model.

### 4.4.1 Friction Factors

Predicted friction factor characteristics are compared with experimental data in Fig. 4-10, where they are seen to lie slightly above the spread of the data. For  $s/d = 1.220$ , the predicted friction factor-Reynolds number correlation  $f = 0.173Re^{-0.203}$  is, on the average, about 3% higher than the experimental correlation  $f = 0.152Re^{-0.192}$ . Comparisons are extended to include the smooth pipe correlation  $f = 0.184Re^{-0.20}$  which closely fits the Kármán-Nikuradse equation and the trapezoidal duct correlation  $f = 0.198Re^{-0.214}$  by Khalifa and Trupp (1988). The numerically calculated friction factors for the current rod-trapezoidal duct are about 10% lower than the values for

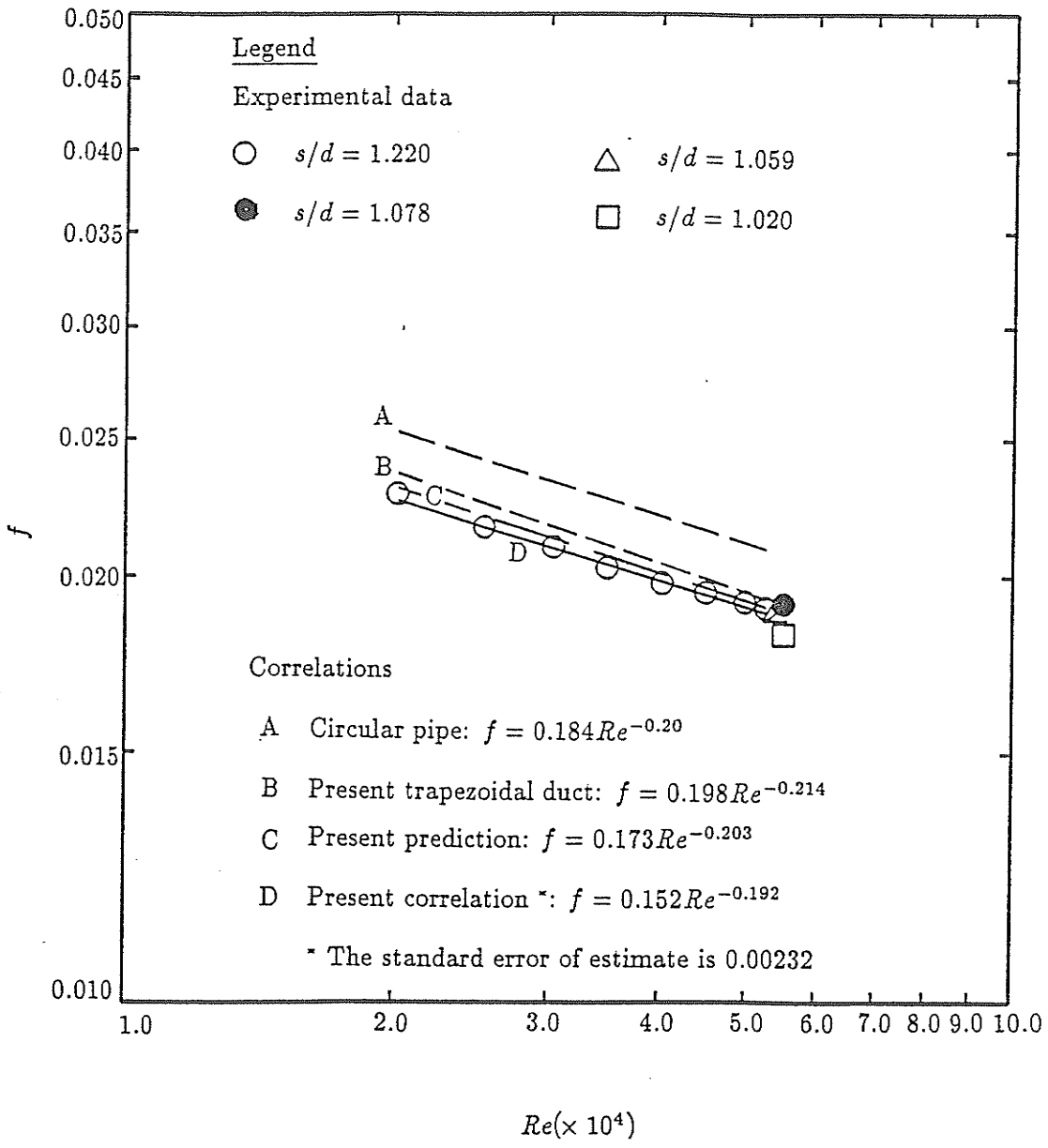
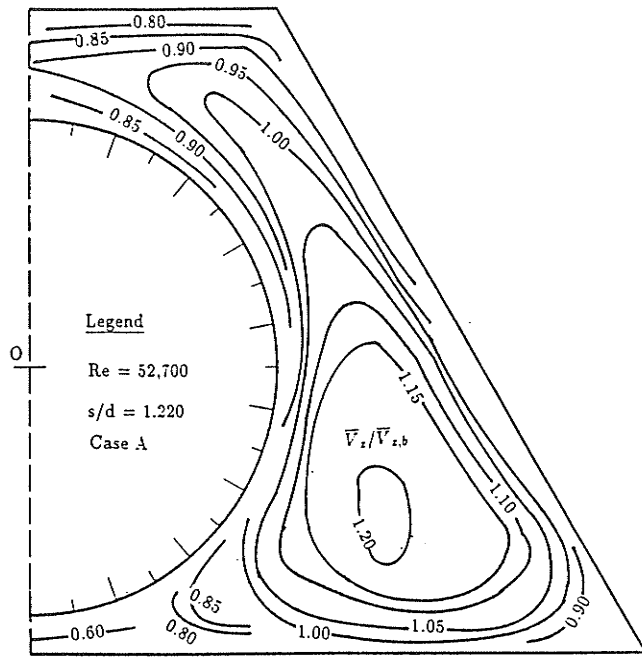


Figure 4-10 Friction factor dependence on Reynolds number

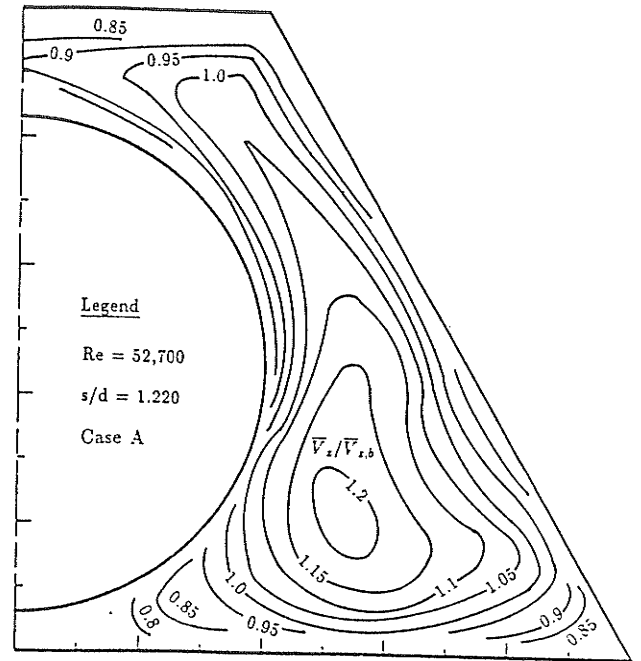
smooth pipe flow. Similar conclusion was drawn by Seale (1982), who found the friction factors for a rod-rectangular duct were 2% lower than the Kármán-Nikuradse correlation. Taking into account the finding by Trupp and Aly (1979), that in smooth triangular array rod bundles, friction factors are higher than those of pipe flow by 12% to 18% for the same Reynolds numbers, it can be inferred that the friction factors in simulated rod bundle subchannels are generally lower than pipe flow values.

#### 4.4.2 Mean Axial Velocities

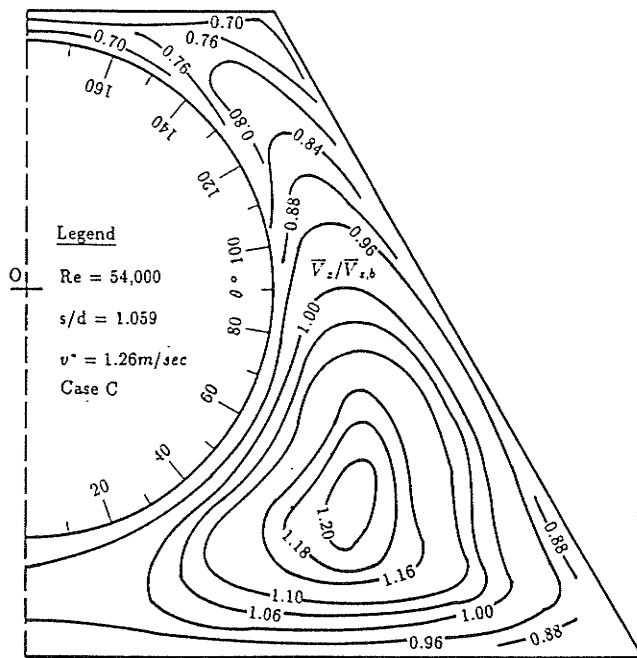
Isovels ( $\bar{V}_z/\bar{V}_{z,b}$ ) in rod-trapezoidal ducts for  $s/d = 1.220, 1.059$  and  $1.020$  are shown in Fig.4-11, where the predicted velocities are compared with the experimental data. As can be seen, contour shapes are very similar. The maximum deviation between the numerical and experimental data was about 1.5% in the subchannel central regions and about 3.0% in the corner and gap regions. Similar differences reported by Trupp and Aly (1979) in the gap region of triangular array rod bundle were attributed to incomplete flow development. In all three cases, the maximum axial velocities are about 20% higher than the subchannel average values. All the predicted and experimental isovels bear strong traces of the influence of secondary flow; most evident are the indentations away from the inclined wall in case A where at the same place Fig. 3-12 shows return secondary flows. Less obvious are the bulges of isovels towards the  $60^\circ$  and  $120^\circ$  duct corners. There is no indication that the mean axial velocity distribution is affected by the large scale turbulence cross-gap eddy motion. As already shown in Fig.3-4 and Table 3-3, near wall axial velocity distributions in the rod-trapezoidal duct conform to the log-law.



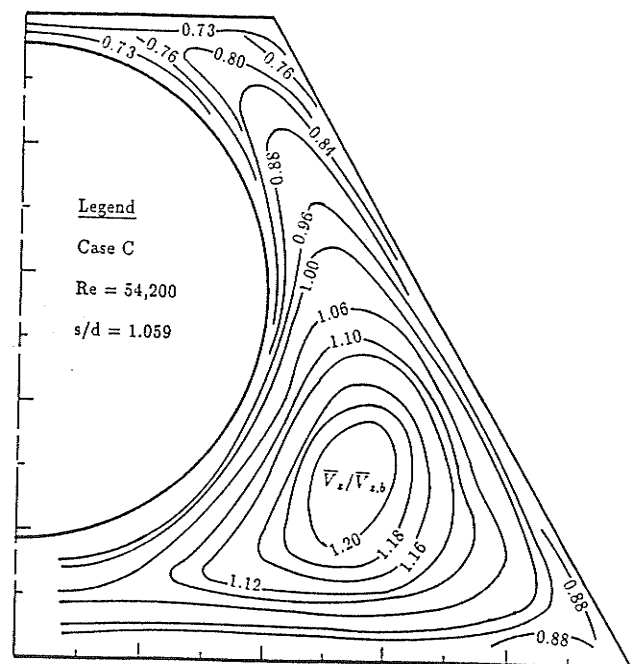
(a)



(b)

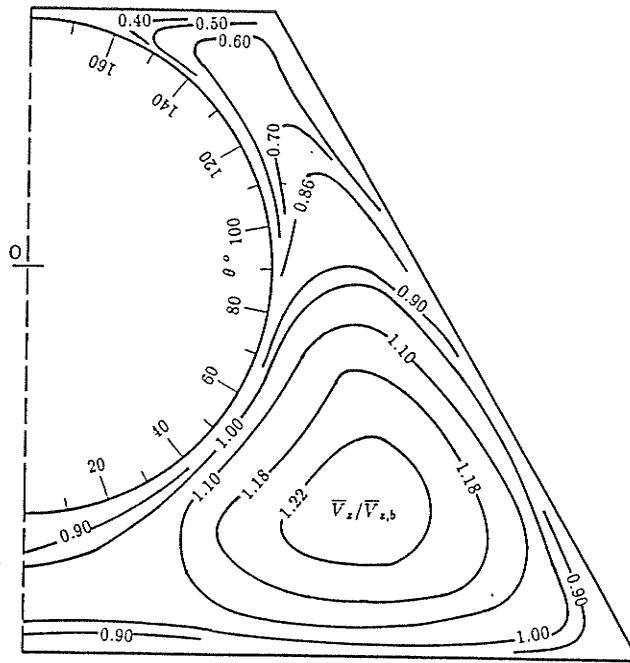


(c)

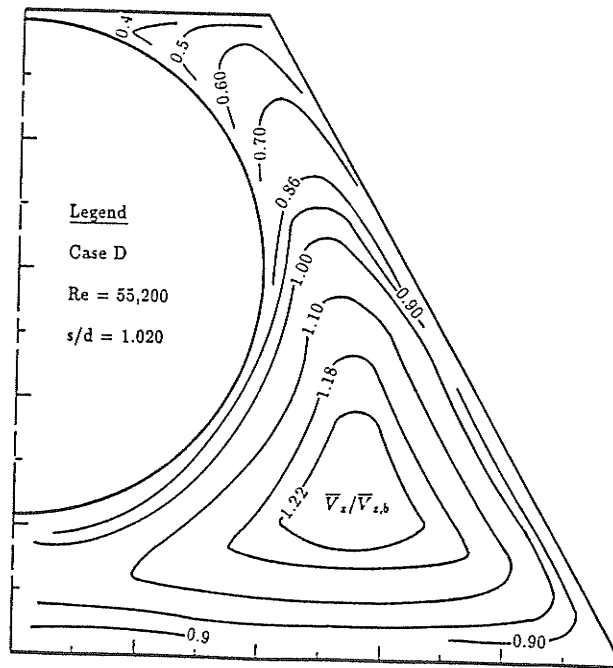


(d)

Figure 4-11 Comparison of predicted and measured mean axial velocities  
 (a) Case A, prediction; (b) Case A, measurement;  
 (c) Case C, prediction; (d) Case C, measurement;  
 (e) Case D, prediction, (f) Case D, measurement



(e)



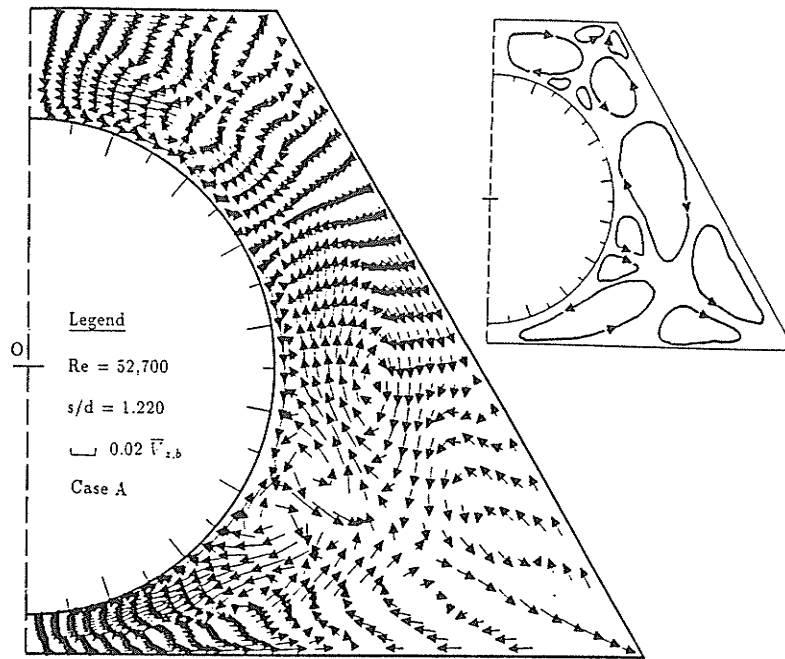
(f)

Figure 4-11 Comparison of predicted and measured mean axial velocities  
 (a) Case A, prediction; (b) Case A, measurement;  
 (c) Case C, prediction; (d) Case C, measurement;  
 (e) Case D, prediction, (f) Case D, measurement

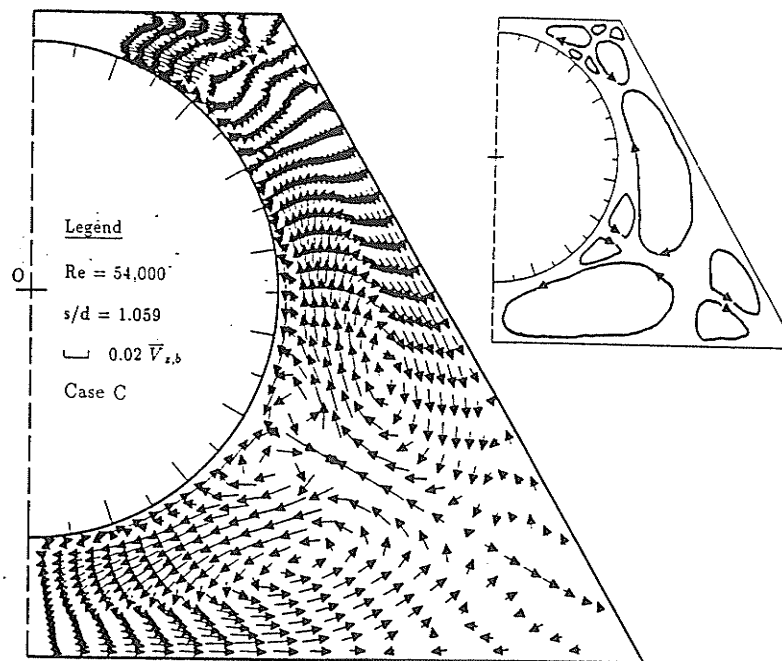
### 4.4.3 Secondary Velocities

Fig.4-12 (a-c) presents the predicted secondary velocity vectors for case A, C and D. As indicated by the inserted illustrative figures, the numerical calculations generate a large vortex and a small counter-rotating vortex for each of the three rod-to-wall gaps (top, bottom and inclined); and for each of the two duct corners ( $60^\circ$  and  $120^\circ$ ) there exist two counter-rotating cells coming from the central region towards the corner. These two pairs of counter-rotating cells in the duct corners will eventually become dominant when the radius of the central rod is reduced. The limiting case (trapezoidal duct) can be reached by considering a zero radius rod; in this situation the secondary flow pattern described in Fig. 4-4 would emerge. Consistent with the existing knowledge on the function of secondary flow in rod bundle subchannels, the main rotating secondary flow cells in rod-to-wall gap regions convect high momentum from the subchannel central regions to gap areas, facilitating intersubchannel mixing.

Comparison with experimental data can be made for case A whose X-probe measured secondary velocity vectors are documented in Fig.3-12. The predicted twelve-cell pattern partially encompass the measured rough three-cell secondary flow pattern, in the sense that the experimentally established large central cell and the returning corner cell are reproduced in the present prediction. Of particular importance is the consistent returning secondary flow from the  $60^\circ$  duct corner along the inclined duct wall. The strong distortions of the measured axial velocity, wall shear stress and turbulence kinetic energy in this region are believed to be an effect of such a secondary flow pattern. The magnitudes of the predicted secondary flows, like the experimental data, are within about 3.5% of the mean average axial velocity. It is of further interest to notice the obvious difference of the secondary flow pattern in case D from those in Case A and C. The larger occupation area of the two returning secondary flows



(a)



(b)

Figure 4-12 Predicted secondary velocity vectors in rod-trapezoidal duct  
 (a) Case A; (b) Case C; (c) Case D

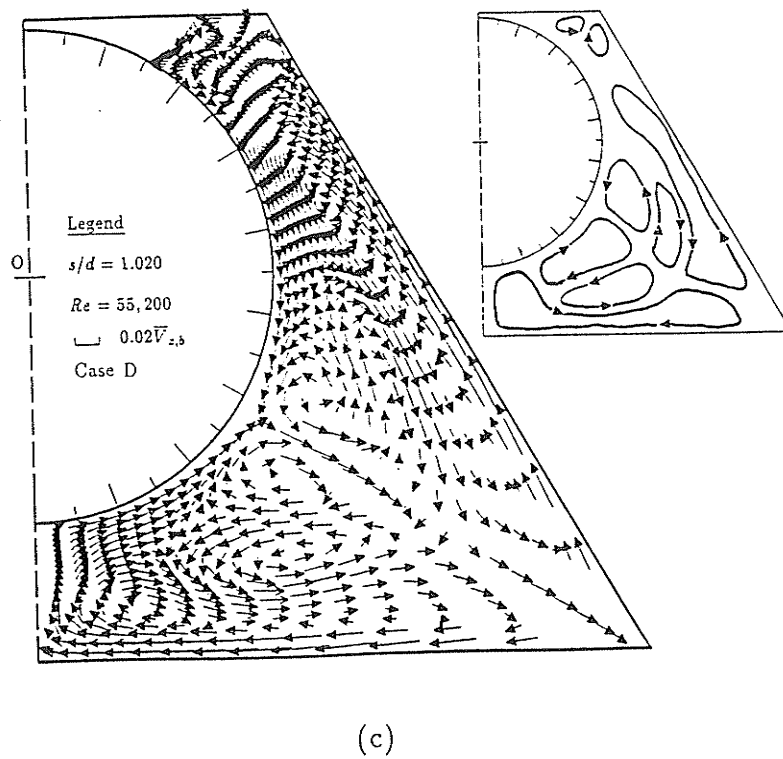


Figure 4-12 Predicted secondary velocity vectors in rod-trapezoidal duct  
 (a) Case A; (b) Case C; (c) Case D

from the  $60^\circ$  duct corner represent the gradually increasing dominance of the duct corner as the rod is brought up to the 1.0 mm small top gap. It is also another indication that eventually as the the rod diminishes the present secondary flow pattern will degenerate into that of the trapezoidal duct given in Fig. 4-4.

#### 4.4.4 Wall Shear Stresses

Comparisons between the predicted local wall shear stress distributions and those measured by Preston tube are afforded by Fig. 4-13(a-c). In the present numerical work, the local wall shear stresses are calculated from the turbulence field by Eqs. (4.15) and (4.16). From Fig. 4-13(a) for case A, it is evident that the present prediction was unable to reproduce the dip of wall shear stress on the inclined wall where a returning secondary flow was detected both experimentally and numerically. This may be attributed to the relatively weaker predicted returning secondary flow in this region. This dip region aside, the numerical prediction offers satisfactory comparison with the experimental data, follows the same trends and has a maximum difference of about 6% near the bottom gap region. Actually, the experimental data in the bottom gap region may be biased by the smallness of the gap.

For case C, the prediction is in general agreement with the measured wall shear stress. Deviations occur in the top gap region where measured data show an increasing trend towards the gap whereas the predicted wall shear exhibits the opposite trend. This difference boils down to the cross-gap eddy motion whose influence is shown by the experiment but is less pronounced by the present numerical model. In this case, the maximum quantitative difference is about 5% which occurs in the top gap region near the  $120^\circ$  duct corner.

For case D where only a conventional turbulence model was involved, the predicted wall shear stress offers very close fit to the experimental data. The maximum

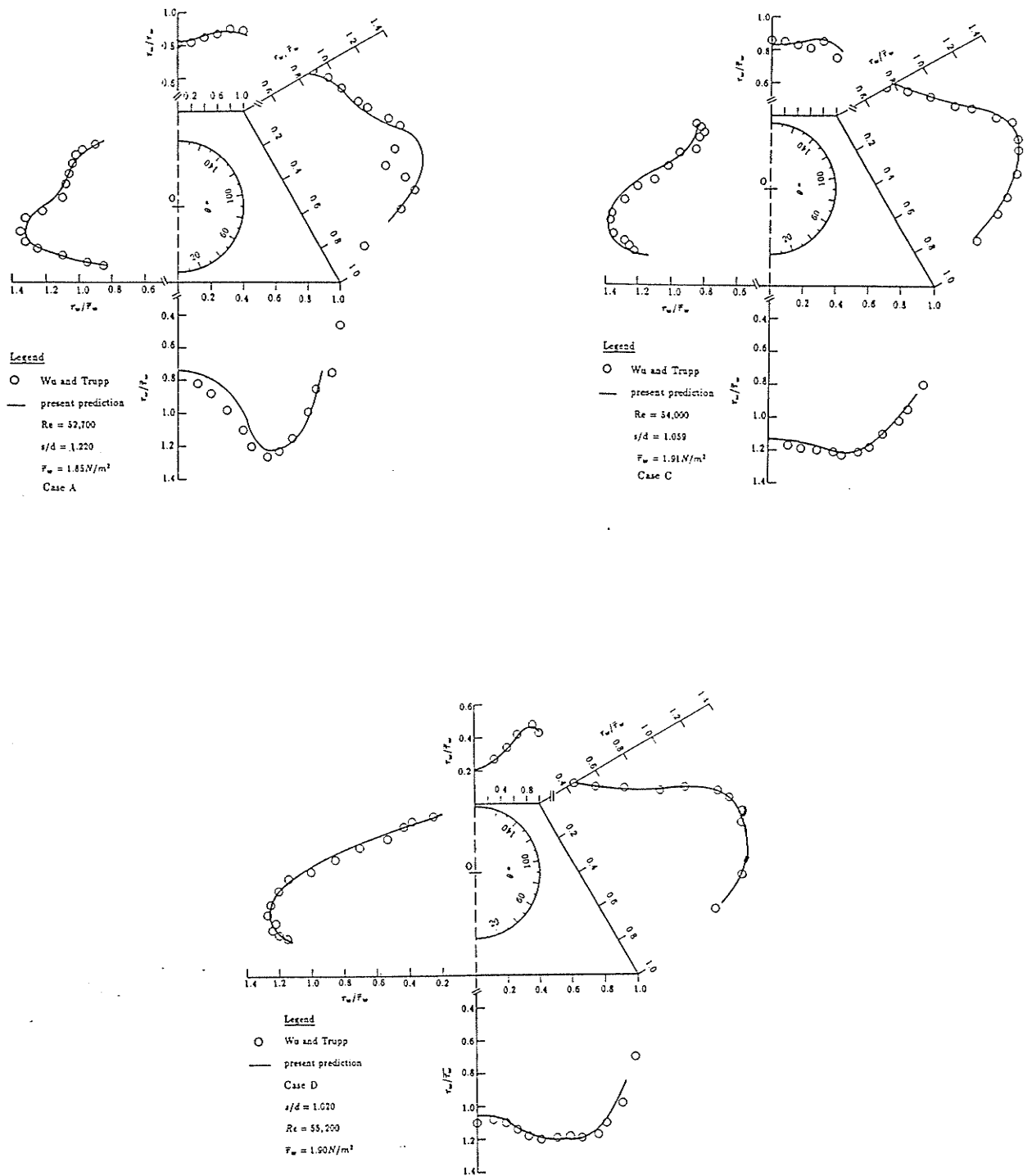


Figure 4-13 Comparison of predicted and measured local wall shear  $\tau_w/\bar{\tau}_w$  in the rod-trapezoidal duct (a) Case A; (b) Case C; (c) Case D

deviation of about 3% was located near the 60° trapezoidal duct corner.

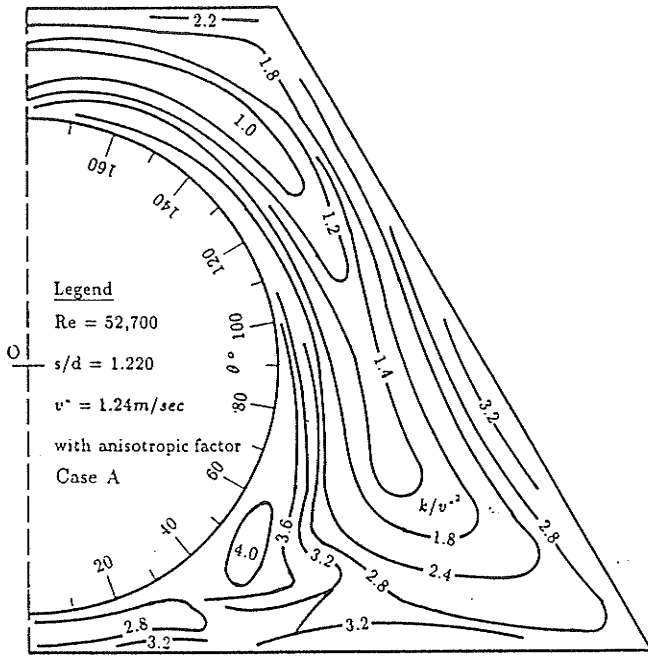
#### 4.4.5 Turbulence Kinetic Energy

The predicted normalized turbulence kinetic energy contours ( $k/v^{*2}$ ) are given in Fig. 4-14(a-c). Comparison of the calculated  $k$  distributions for the three cases with the experimental data shown in Figs. 3-9(a)(b) and (d) offers good overall agreement. For case A, the high  $k$  patch in Fig.3-9(a) resulting from the coherent cross-gap eddy motion is correctly predicted by the numerical calculation with about 10% quantitative difference (maximum about 30% in gap region). Since the anisotropic factor  $n(r, \theta)$  in the current turbulence model was derived from experimental results, it is quite understandable that prediction method should be able to generate the same quantitative turbulence kinetic energy distribution within certain numerical deviation. Consistent with the prediction on wall shear stress, the predicted  $k$  distribution exhibits a weakened dip (in comparison with measurements) in the near-inclined-wall region where returning secondary flow was measured.

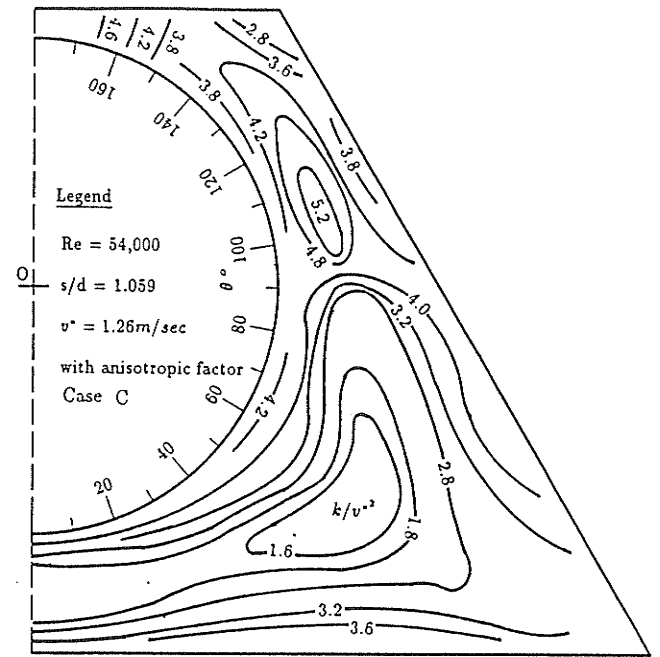
For case C, the predicted maximum turbulence kinetic energy is located in the center of the high  $k$  patch, rather than in the small top gap region as indicated by the experimental data shown in Fig.3-9(c). As depicted in Fig.4-14(b), the strong indentation of  $k/v^{*2}$  contours in the near rod surface region where  $\theta = 50^\circ \sim 70^\circ$  is the result of strong returning secondary flow from the rod surface towards the subchannel center. A similar indentation for case C is also shown in Fig. 4-16(c) with a strong bulge towards the 60° duct corner.

For case D, the maximum  $k/v^{*2}$  values are located near the rod and duct surfaces opposite to the largest flow cross-section. Here there is no cross-gap eddy motion to modify the turbulence kinetic energy contours, which is in agreement with the experimental data shown in Fig.3-9(d). In general, the present turbulence model

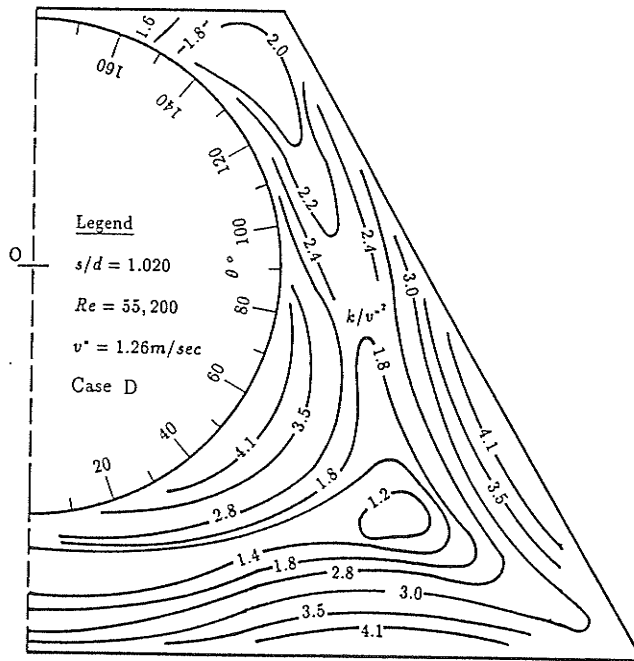
based on anisotropic eddy viscosity is capable of predicting the turbulence kinetic energy fields in closely-spaced rod bundle subchannels, provided that a description of anisotropic factor is available.



(a)



(b)



(c)

Figure 4-14 Comparison of predicted and measured turbulence kinetic energy  $k/v^{*2}$  in the rod-trapezoidal duct (a) Case A; (b) Case C; (c) Case D

## Chapter 5

# Predictions of Turbulence Structures in Simulated Asymmetric Rod Bundles: Finite Element Method

The numerical studies reported in this chapter serves a further continuation and supplementation to the extensive experimental work reported in Chapter 3. This study was aimed at simulating fully developed turbulence structures in simulated asymmetric rod bundles formed by the rod-trapezoidal duct. Special attention was devoted to the prediction of secondary flows. Efforts were also made to the reproduction of wall shear stress and axial velocity distributions. Predictions of turbulence kinetic energy and dissipation were also of interest.

The methodology adopted in the numerical study described in this chapter, was a combination of existing finite element code ANSYS 5.0 and FLOTRAN 2.1a. The calculations reported in Chapter 4 were performed using the finite volume method, whose power is embedded in two features: 1) only non-zero terms for each nodal equation are stored, and 2) the governing equations are solved sequentially using iterative matrix solution methods. Both of these features minimize the core storage requirements for the calculation. The present reported approach combines these robust features of SIMPLE algorithms with the geometric flexibility of the finite element method. With

the finite element model built by ANSYS, FLOTRAN solves the governing equations using the Galerkin weighted integral method, streamline upwinding, and a sequential solution algorithm. Modelling of turbulence is made possible by using the built-in  $k - \epsilon$  two-equation model, although this model has been proven to be not adequate for rod bundl flow.

This chapter is organized in accordance with the natural course of the implemeta-tion of the present numerical study. The mathematical formulations, including gov-erning equations, turbulence model, boundary conditions, and details of the finite element discretization procedures, will be first given. The documentation of the comparisons between the predictions and experimental data for the asymmetric rod-trapezoidal duct is preceded by the a description of the FLOTRAN sequential solution algorithm.

## 5.1 Mathematical Formulations

### 5.1.1 Momentum Equations

For fully developed turbulent flow of a constant properties fluid, in a Cartesian coordinate system  $(x, y, z)$ , the Reynolds equations are

Reynolds equation for x direction,

$$\frac{\partial}{\partial x}(\rho \bar{V}_x \bar{V}_x) + \frac{\partial}{\partial y}(\rho \bar{V}_y \bar{V}_x) = \frac{\partial}{\partial x}(\mu \frac{\partial \bar{V}_x}{\partial x}) + \frac{\partial}{\partial y}(\mu \frac{\partial \bar{V}_x}{\partial y}) + S_{\bar{V}_x} \quad (5.1)$$

$$S_{\bar{V}_x} = -\rho \left[ \frac{\partial}{\partial x}(\overline{v_x^2}) + \frac{\partial}{\partial y}(\overline{v_y v_x}) \right] - \frac{\partial \bar{P}}{\partial x}$$

Reynolds equation for y direction,

$$\frac{\partial}{\partial x}(\rho \bar{V}_x \bar{V}_y) + \frac{\partial}{\partial y}(\rho \bar{V}_y \bar{V}_y) = \frac{\partial}{\partial x}(\mu \frac{\partial \bar{V}_y}{\partial x}) + \frac{\partial}{\partial y}(\mu \frac{\partial \bar{V}_y}{\partial y}) + S_{\bar{V}_y} \quad (5.2)$$

$$S_{\bar{V}_y} = -\rho \left[ \frac{\partial}{\partial x} \overline{v_x v_y} + \frac{\partial}{\partial y} \overline{v_y^2} \right] - \frac{\partial \bar{P}}{\partial y}$$

Reynolds equation for the axial direction,

$$\frac{\partial}{\partial x} (\rho r \bar{V}_x \bar{V}_z) + \frac{\partial}{\partial y} (\rho \bar{V}_y \bar{V}_z) = \frac{\partial}{\partial x} \left( \mu \frac{\partial \bar{V}_z}{\partial x} \right) + \frac{\partial}{\partial y} \left( \mu \frac{\partial \bar{V}_z}{\partial y} \right) + S_{\bar{V}_z} \quad (5.3)$$

$$S_{\bar{V}_z} = -\rho \left[ \frac{\partial}{\partial x} (\overline{v_x v_z}) + \frac{\partial}{\partial y} (\overline{v_y v_z}) \right] - \frac{\partial \bar{P}}{\partial z}$$

### 5.1.2 Turbulence Model

Turbulent stress tensor appearing in the Reynolds equations are expressed as follows,

$$\begin{aligned} \overline{v_x^2} &= -\mu_t \frac{\partial \bar{V}_x}{\partial x} \\ \overline{v_y^2} &= -\mu_t \frac{\partial \bar{V}_y}{\partial y} \\ \overline{v_x v_y} &= -\mu_t \frac{\partial \bar{V}_y}{\partial x} \\ \overline{v_y v_x} &= -\mu_t \frac{\partial \bar{V}_x}{\partial y} \\ \overline{v_x v_z} &= -\mu_t \frac{\partial \bar{V}_z}{\partial x} \\ \overline{v_y v_z} &= -\mu_t \frac{\partial \bar{V}_z}{\partial y} \end{aligned} \quad (5.4)$$

The transport equations for the turbulence kinetic energy  $k$  and the dissipation rate of turbulence kinetic energy  $\epsilon$  appearing in the turbulent stress tensor (Eq.(5-4)) are as follows,

$$\rho \bar{V}_x \frac{\partial k}{\partial r} + \rho \bar{V}_y \frac{\partial k}{\partial y} = \frac{\partial}{\partial x} \left( \frac{\mu_t}{\sigma_k} \frac{\partial k}{\partial x} \right) + \frac{\partial}{\partial y} \left( \frac{\mu_t}{\sigma_k} \frac{\partial k}{\partial y} \right) + S_k \quad (5.5)$$

$$S_k = \mu_t G - \rho \epsilon$$

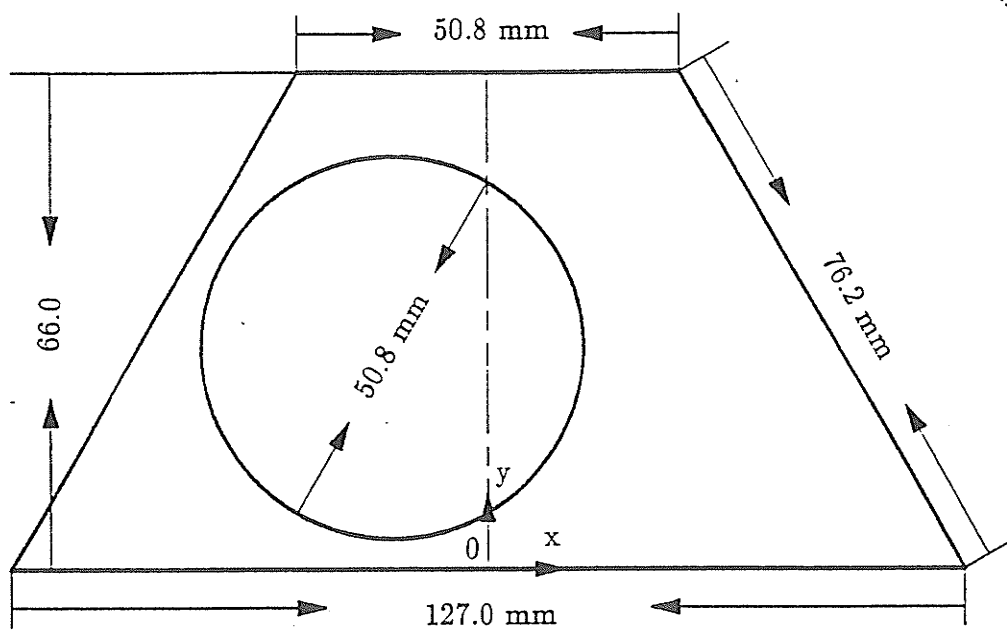


Figure 5-1 The cross section of the test rig for Case F

$$\rho \bar{V}_x \frac{\partial \epsilon}{\partial x} + \rho \bar{V}_y \frac{\partial \epsilon}{\partial y} = \frac{\partial}{\partial x} \left( \frac{\mu_t}{\sigma_\epsilon} \frac{\partial \epsilon}{\partial x} \right) + \frac{\partial}{\partial y} \left( \frac{\mu_t}{\sigma_\epsilon} \frac{\partial \epsilon}{\partial y} \right) + S_\epsilon \quad (5.6)$$

$$S_\epsilon = \epsilon \frac{(C_{\epsilon_1} \mu_t G - C_{\epsilon_2} \rho \epsilon)}{k}$$

where  $\mu_t = C_4 \rho k^2 / \epsilon$ ;  $\sigma_k = 1.0$  and  $\sigma_\epsilon = 1.3$  are turbulent Prandtl numbers for  $k$  and  $\epsilon$ , respectively;  $C_{\epsilon_1} = 1.44$ ,  $C_{\epsilon_2} = 1.92$  and  $C_4 = 0.09$  are empirical constants and  $G$  represents the production rate of turbulence kinetic energy in which only gradients in axial velocity are retained,

$$G = 2 \left[ \left( \frac{\partial \bar{V}_x}{\partial x} \right)^2 + \left( \frac{\partial \bar{V}_y}{\partial y} \right)^2 \right] + \left[ \frac{\partial \bar{V}_x}{\partial y} + \frac{\partial \bar{V}_y}{\partial x} \right]^2 \quad (5.7)$$

### 5.1.3 Boundary Conditions

There are three boundary condition types in the three dimensional flow domain shown in Fig. 5-1: inflow, outflow and no-slip wall.

At the inlet, velocities are specified as  $\bar{V}_x = 0$ ,  $\bar{V}_y = 0$ ,  $\bar{V}_z = \bar{V}_b$ . The turbulent kinetic energy is estimated at the inlet using the relation:  $k_{inlet} = 1.5(1\% \bar{V}_b)^2$ . The turbulence kinetic energy dissipation rate at the inlet is estimated as  $\epsilon_{inlet} = C_4 k_{inlet}^{1.5} / L$  where  $L$  is the characteristic length scale of the problem.

On solid walls, turbulence and mean axial velocity calculations in the vicinity of a wall are made possible using the law-of-the-wall.

Zero pressure are applied on the outlet plane with other quantities left unspecified.

## 5.2 Numerical Scheme

This section is divided into three parts. The first subsection discusses the discretization methods applied to Eqs. (5-1)-(5-3) and (5-5)-(5-6). The second part

deals with the aspect of velocity-pressure coupling. Finally, the third part describes the sequential FLOTRAN solution algorithm. Again, all equations are in Cartesian coordinates, unless noted otherwise.

### 5.2.1 Discretization Procedure

To facilitate understanding of the discretization methods, it is worthwhile to consider the following generalized transport equation that is similar in mathematical form to Eqs. (5-1)-(5-3) and (5-5)-(5-6).

$$\frac{\partial(\rho\bar{V}_x\Phi)}{\partial x} + \frac{\partial(\rho\bar{V}_y\Phi)}{\partial y} = \frac{\partial}{\partial x}\left(\Gamma_\Phi \frac{\partial\Phi}{\partial x}\right) + \frac{\partial}{\partial y}\left(\Gamma_\Phi \frac{\partial\Phi}{\partial y}\right) + S_\Phi \quad (5.8)$$

The left hand side of Eq. (5-8) governs advection of  $\Phi$ . On the right hand side, the second order terms represent diffusion of  $\Phi$  with  $\Gamma_\Phi$  as a generalized diffusion coefficient. Finally,  $S_\Phi$  is a generalized source term already defined in the individual transport equations.

The Galerkin method of weighted residuals is used to discretize the diffusion and source terms in the governing equations. Consider a steady state, diffusion dominated flow so that the advection terms in Eq. (5-8) are negligible, giving:

$$\frac{\partial}{\partial x}\left(\Gamma_\Phi \frac{\partial\Phi}{\partial x}\right) + \frac{\partial}{\partial y}\left(\Gamma_\Phi \frac{\partial\Phi}{\partial y}\right) + S_\Phi = 0 \quad (5.9)$$

The weak form of this equation is established by taking the weighted average of the scalar equation over the individual elements:

$$\int W \left[ \frac{\partial}{\partial x}\left(\Gamma_\Phi \frac{\partial\Phi}{\partial x}\right) + \frac{\partial}{\partial y}\left(\Gamma_\Phi \frac{\partial\Phi}{\partial y}\right) + S_\Phi \right] dA^e = 0 \quad (5.10)$$

where  $W$  is the weighting function which, for the Galerkin method, is the same as the element interpolation function. Superscript 'e' denotes integration over individual elements.

Since only linear interpolation functions are used to approximate the distribution of  $\Phi$  in the h-type elements, the second order derivative terms in Eq. (5-10) must be transformed to first order. This is achieved by simple integration by parts to give:

$$\int \Gamma_{\Phi} \left[ \frac{\partial W}{\partial x} \partial \Phi \partial x + \frac{\partial W}{\partial y} \partial \Phi \partial y \right] dA^e - \int W \Gamma_{\Phi} \left[ \frac{\partial \Phi}{\partial x} + \frac{\partial \Phi}{\partial y} \right] dS^e - \int W S_{\Phi} dA^e = 0 \quad (5.11)$$

The second integral is over the element surface  $S^e$ . The next step is to substitute the following approximations for  $\Phi$ ,  $S_{\Phi}$  and  $\Gamma_{\Phi}$  into Eq. (5-11):

$$\Phi = \sum_{i=1}^{N^n} W_i \Phi_i; S_{\Phi} = \sum_{i=1}^{N^n} W_i S_{\Phi,i}; \Gamma_{\Phi} = \sum_{i=1}^{N^n} W_i \Gamma_{\Phi,i} \quad (5.12)$$

where  $N^n$  is the number of nodes in the element. The resulting equation is:

$$\int \sum_{i,j,k=1}^{N^n} W_j \Gamma_{\Phi,j} \left[ \frac{\partial W_j}{\partial x} \frac{\partial W_k}{\partial x} \Phi_k + \frac{\partial W_j}{\partial y} \frac{\partial W_k}{\partial y} \Phi_k \right] dA^e - \int \sum_{i,j,k=1}^{N^n} W_i W_j \Gamma_{\Phi,j} \left[ \frac{\partial W_k}{\partial x} \Phi_k + \frac{\partial W_k}{\partial y} \Phi_k \right] dS^e - \int \sum_{i,j=1}^{N^n} W_i W_j S_{\Phi,j} dA^e = 0 \quad (5.13)$$

Rewriting Eq. (5-13) in matrix form:

$$\sum_{j=1}^{N^n} K_{ij}^e \Phi_j^e = F_j^e, i = 1, 2, 3, \dots, N^n \quad (5.14)$$

where

$$K_{ij}^e = \int \sum_{i,j,k=1}^{N^n} W_j \Gamma_{\Phi,j} \left[ \frac{\partial W_j}{\partial x} \frac{\partial W_k}{\partial x} \Phi_k + \frac{\partial W_j}{\partial y} \frac{\partial W_k}{\partial y} \Phi_k \right] dA^e - \int \sum_{i,j,k=1}^{N^n} W_i W_j \Gamma_{\Phi,j} \left[ \frac{\partial W_k}{\partial x} \Phi_k + \frac{\partial W_k}{\partial y} \Phi_k \right] dS^e \quad (5.15)$$

$$F_i^e = \int_{i,j=1}^{N^n} W_i W_j S_{\Phi,j} dA^e \quad (5.16)$$

The discretized equations (5-14) are formed on an element basis and assembled into global system in which coefficient matrix  $K_{ij}$  and source vector  $F_i$  are defined as

$$K_{ij} = \sum_{e=1}^{N^e} K_{ij}^e; F_i = \sum_{e=1}^{N^e} F_i^e \quad (5.17)$$

where  $N^e$  is the number of elements in the solution domain.

The elements used are the linear tetrahedral. The weighting/interpolation function has the following form for each element:

$$W_i = a_i + b_i x + c_i y \quad (5.18)$$

The monotone streamline upwind method is used to discretize the advection terms. The strength of this scheme is that upwinding occurs along a streamline, not necessarily a coordinate axis as is the case for conventional upwinding techniques. The intent is to minimize crosswind numerical diffusion that occurs when the flow runs diagonally across an element in which case the first order truncation errors associated with the upwinded advection terms are highest. The physical basis for the monotone streamline upwind method is that pure advection is a characteristic value problem in which the conserved quantity is transported along characteristic lines, the streamlines. Since characteristic value problems typically govern phenomena that are fundamentally discontinuous, then advective transport must also be considered a discontinuous process. Consequently, the monotone streamline upwind method represents the non-linear advection terms with discontinuous approximations.

Assume a completely inviscid flow with no source terms so that Eq. (5-8) reduces to

$$\frac{\partial(\rho \bar{V}_x \Phi)}{\partial x} + \frac{\partial(\rho \bar{V}_y \Phi)}{\partial y} = 0 \quad (5.19)$$

The expression represents pure advective transport of  $\Phi$  in conservative form. In streamwise coordinates, Eq. (5-19) can be written as:

$$\frac{\partial(\rho \bar{V}_s \Phi)}{\partial s} = 0 \quad (5.20)$$

Eq. (5-20) indicates that for pure advection flows,  $(\rho \bar{V}_s \Phi)$  is constant along a

streamline. This is implemented on an element basis by assuming

$$\left[ \frac{\partial(\rho\bar{V}_s\Phi)}{\partial s} \right]^e = \text{constant} \quad (5.21)$$

for the element. As a result, discretization of the advection terms becomes:

$$\int W \left[ \frac{\partial(\rho\bar{V}_x\Phi)}{\partial x} + \frac{\partial(\rho\bar{V}_y\Phi)}{\partial y} \right] dA^e = \left[ \frac{\partial(\rho\bar{V}_s\Phi)}{\partial s} \right]^e \int W dA^e \quad (5.22)$$

The gradient  $\partial(\rho\bar{V}_s\Phi)/\partial s$  is calculated using a backward difference:

$$\left[ \frac{\partial(\rho\bar{V}_s\Phi)}{\partial s} \right]^e = \frac{(\rho\bar{V}_s\Phi)_{N1} - (\rho\bar{V}_s\Phi)_{Ns}}{ds} \quad (5.23)$$

where  $N1$  is the downwind node and  $Ns$  the point of intersection between the upstream face and the streamline that coincides with the downstream node.

### 5.2.2 Solution Procedure

Similar to the SIMPLE method, a Poisson equation for pressure is derived for implementation in FLOTRAN by substituting an expression for velocity in terms of the pressure gradient derived from the momentum equation into the continuity equation. This permits the use of equal order interpolation functions for pressure and velocity since these variables both appear in second order terms in the pressure equation. There are two steps in the development of the solution algorithm for pressure. The first is a derivation of the expressions used to relate the velocity to pressure. These expressions are obtained from a rearrangement of the partially discretized momentum equations. The second step is to substitute the velocity-pressure relations into the continuity equation after it has been discretized using Galerkin's weighted integral method.

FLOTRAN solves the governing equations sequentially rather than as one large system. The flow chart in Fig. 5-2 illustrates the global iteration loop. The momentum equations are solved sequentially, as noted. So, when the x-momentum equation

is solved with TDMA solver for velocity  $\bar{V}_x$ , the variables,  $\bar{V}_y, \bar{V}_z, \bar{P}$  and the source terms are treated as known from the initial guess or the previous iteration. An analogous procedure is used for the  $y$ - and  $z$ - momentum equations and the pressure and turbulence equations.

Typical under-relaxation numbers were 0.5 for all the variables. Element numbers were 65 x 15 x 15 for the three dimensional computational domain shown in Fig. 5-1. Total node and element numbers were 16,640 and 18,525, respectively. An element spacing ratio of 1:10 was used in the  $z$ - main flow direction to account for the large gradient near the inlet region. Convergence was declared after all the primary variables satisfied the criterion:

$$\left| \frac{\Phi_{new} - \Phi_{old}}{\Phi_{new}} \right|_{max} \leq 10^{-5} \quad (5.24)$$

It was found that after 300 iterations, converged solutions to the flow of asymmetric rod-trapezoidal duct were achieved on a HP 725 Unix work-station with 43,200 CPU seconds.

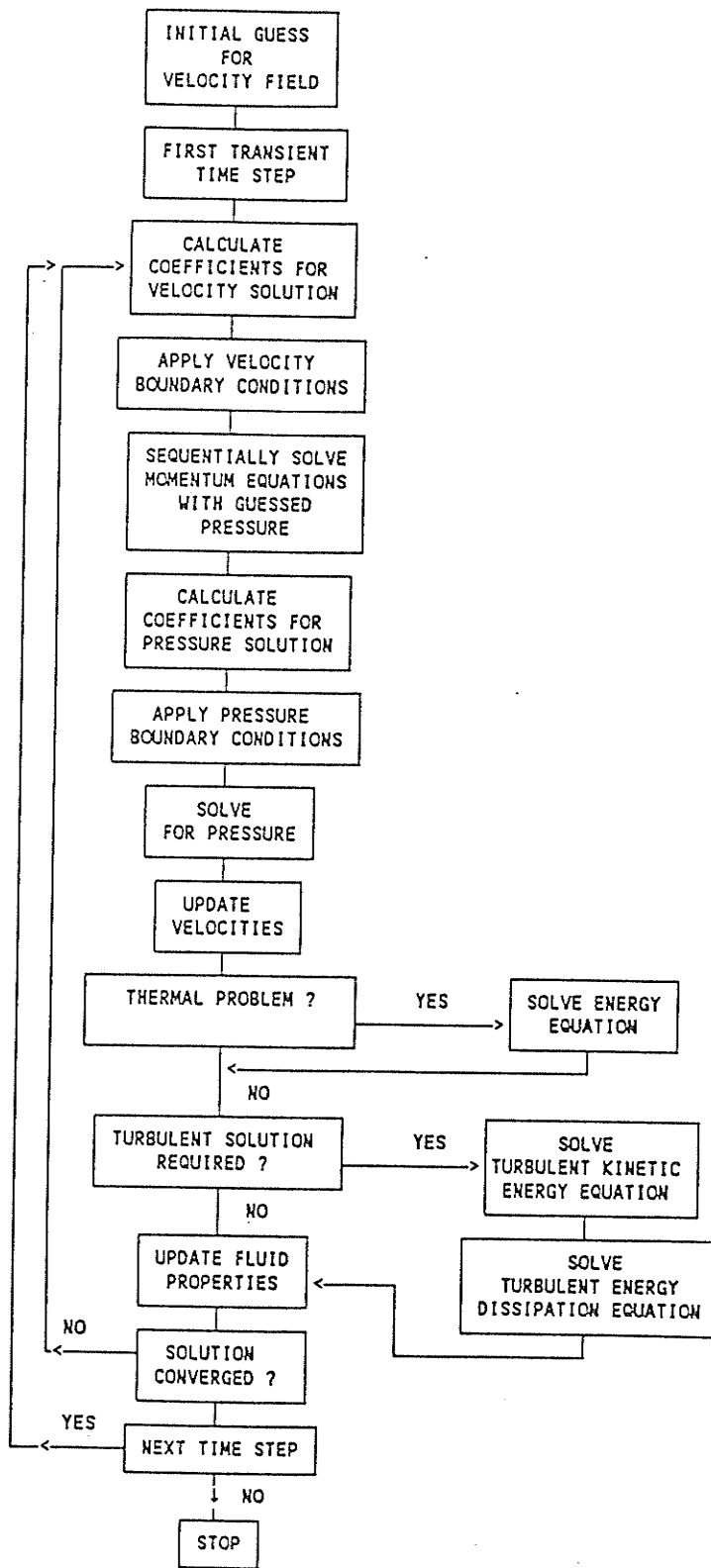


Figure 5-2 Solution flow chart by finite element method

## 5.3 Numerical Results

The asymmetric experimental case tabulated in Table 3-6 was investigated numerically, using the finite element method outlined in the preceding subsections. The flow and geometric specifications of this case are retabulated in Table 5-1. For the sake of consistence, the sequential case number in Table 3-6 is retained.

Table 5-1: Flow and Geometric Conditions of Case F

Case	g (mm)	s (mm)	s/d	$v_z^*$ (m/s)	Re
F <sup>a</sup>	11.2	62.0	1.220	0.64	26,300

a: asymmetric, bottom gap size equals to left-side gap size,  $g = 4.0$  mm

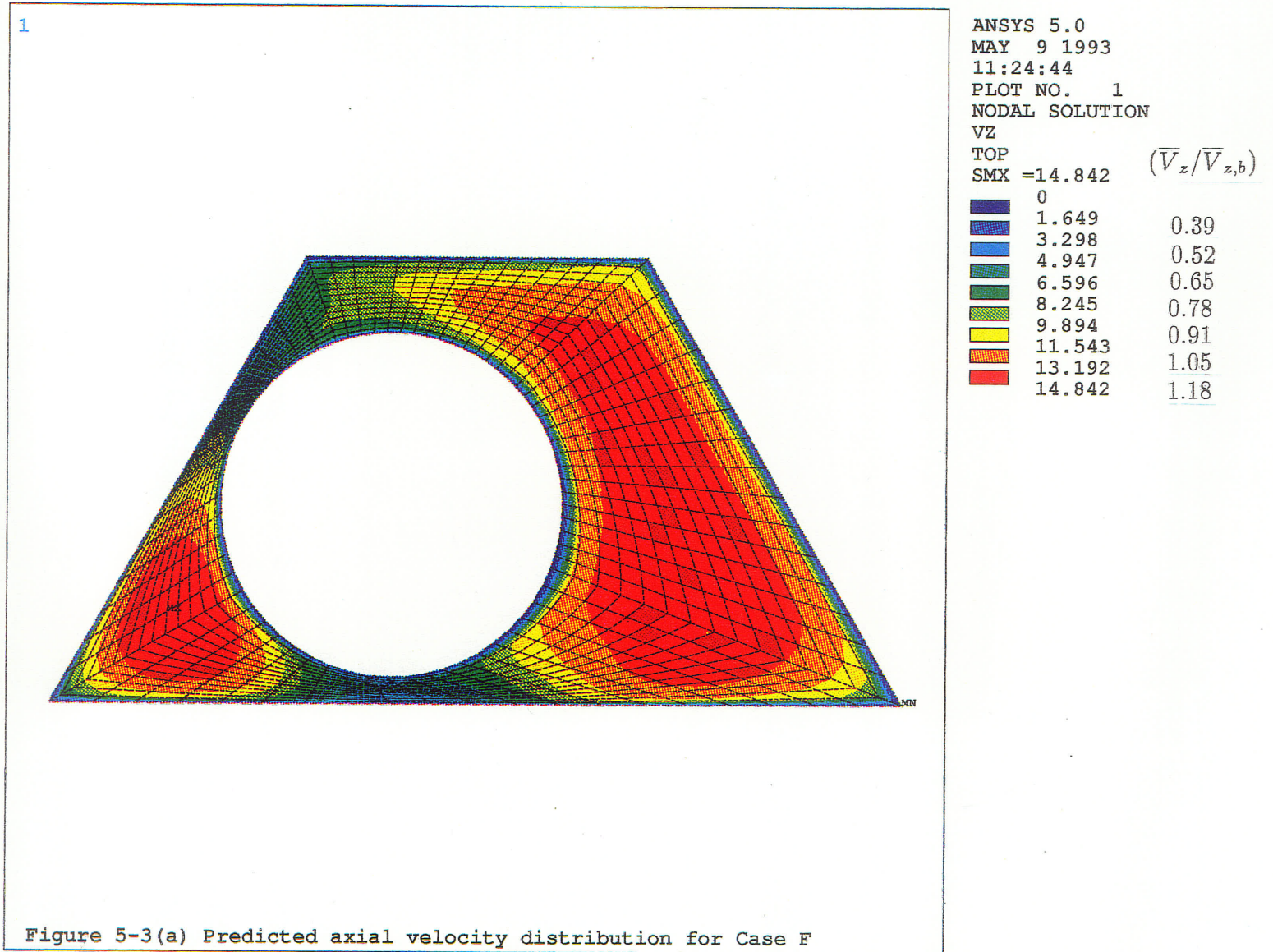
In the Cartesian coordinate system defined in Fig. 3-2, the axis of the rod is located at the line of (0.0126 mm, 0.0294 mm). The bulk axial velocity corresponding to the selected Reynolds number is 12.6 m/sec.

### 5.3.1 Mean Axial Velocities

Isovels ( $\bar{V}_z$ ) in the rod-trapezoidal duct for case F are shown in Fig.5-3, where the predicted velocity are compared with the experimental data. Contour shapes are very similar; the maximum deviation between the numerical and experimental data is about 3% in the subchannel central regions and higher in the corner and gap regions.

### 5.3.2 Secondary Velocities

Fig.5-4 (a-b) presents the predicted secondary velocities for case F. As indicated by the velocity vector plot in Fig. 5-4(a), the numerical calculations generate a large single vortex circulating around the rod. Thus secondary flows may not be bounded by artificial subchannel boundaries for highly asymmetric rod-bundle subchannels. Also being conveyed in this flow pattern, provided that the real flow was correctly



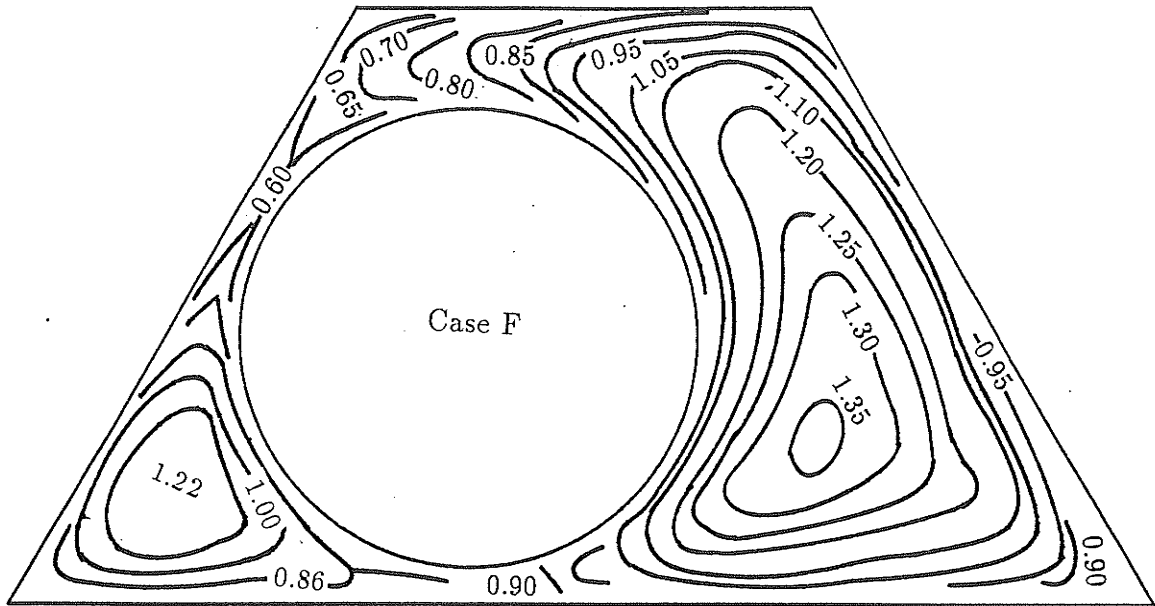
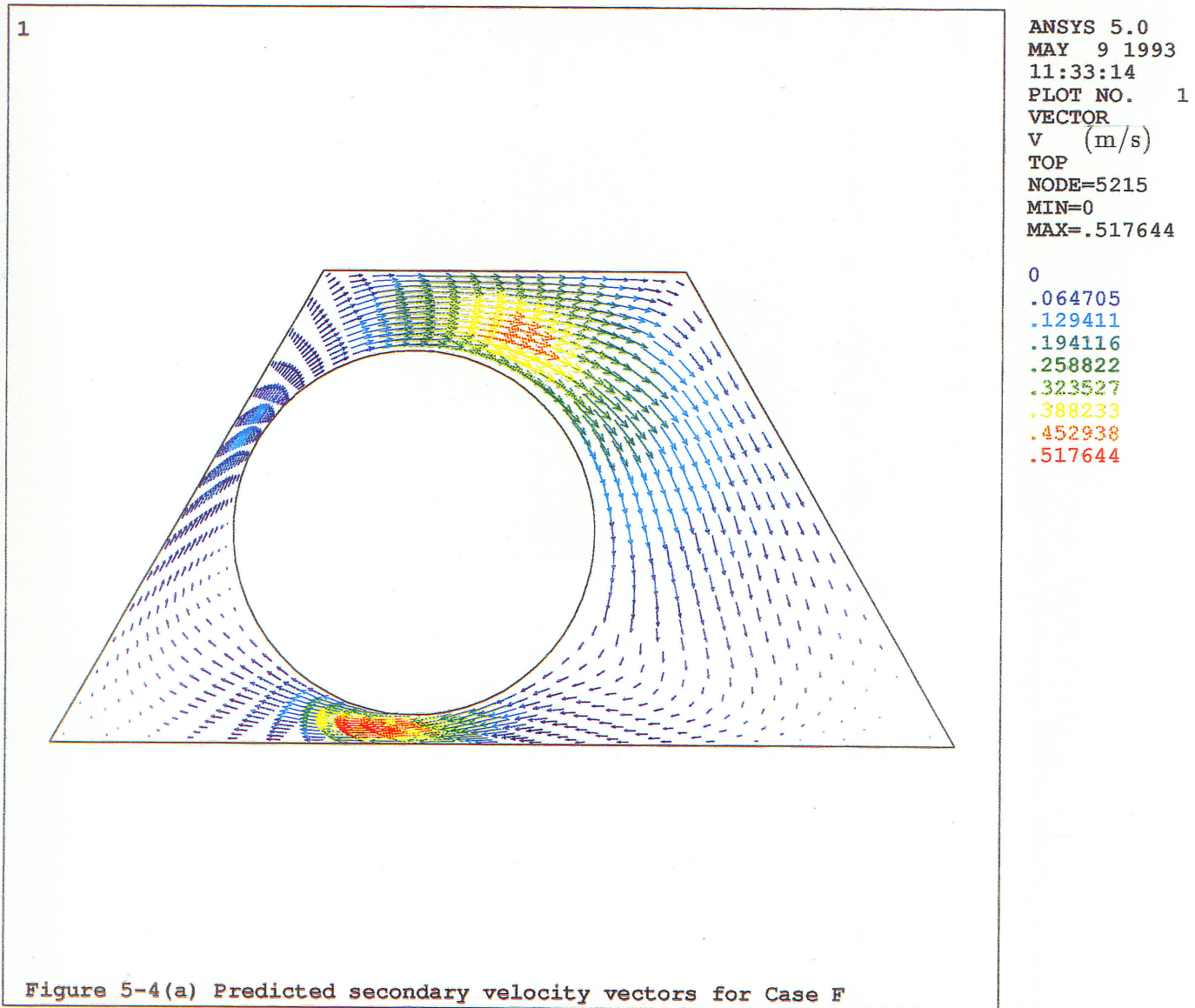
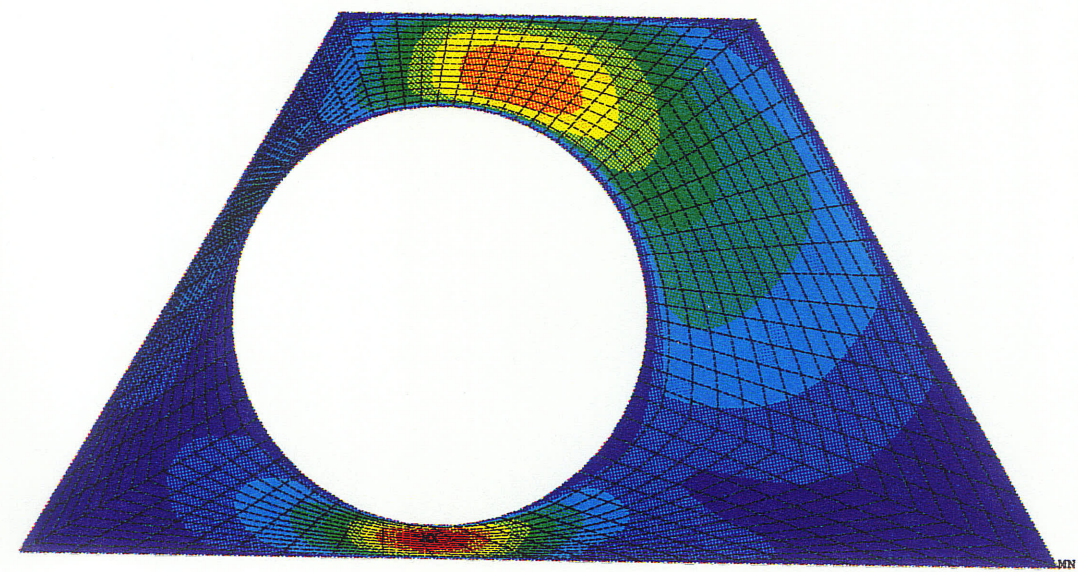


Figure 5-3 Comparison between predicted and measured axial velocity for Case F  
 (b) measurement



1



ANSYS 5.0  
MAY 9 1993  
11:30:24  
PLOT NO. 1  
NODAL SOLUTION  
VSUM (m/s)  
TOP  
RSYS=0  
SMX =.517644  
0  
.057516  
.115032  
.172548  
.230064  
.28758  
.345096  
.402612  
.460128  
.517644

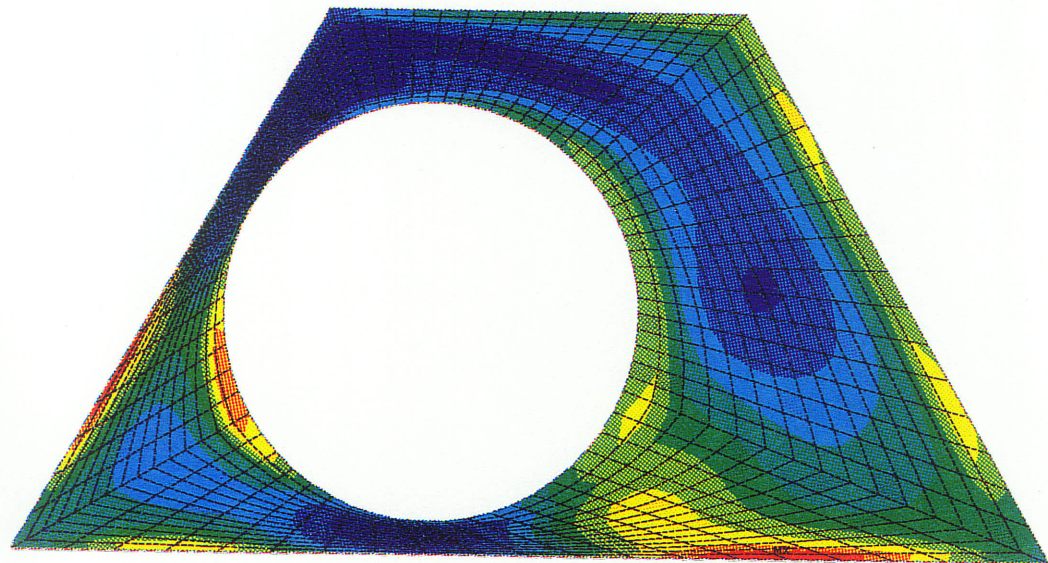
Figure 5-4(b) Predicted secondary velocity magnitude for Case F

modelled, is the message that transport between asymmetric rod bundle subchannels is strongly influenced by crossing-gap secondary velocity, supporting the apparent high mixing factors for asymmetric rod-to-wall gaps shown in Fig. 3-17. Fig. 5-4(b) gives the predicted secondary velocity magnitudes. The peak secondary velocity is  $3.9\% \bar{V}_b$ , similar to those in the symmetric gap cases.

### 5.3.3 Turbulence Kinetic Energy

The predicted turbulence kinetic energy contours ( $k$ ) for case F are given in Fig. 5-5. Comparison of the calculated  $k$  distribution with the experimental data shown in Figs. 3-9(f) only exhibits agreement in the large subchannel central area far away from gaps. This is due to the fact that the present standard  $k-\epsilon$  turbulence model does not account for the cross-gap eddy motion which modifies the  $k$  distribution significantly in the near gap regions. The predicted maximum  $k/v^2$  (4.4) is located near the large subchannel bottom area. It is emphasized that the present predicted secondary flow pattern is a very preliminary result which should be treated with caution. In addition to further numerical study, because of the far-reaching consequences, attempts should also be made to experimentally confirm the recirculation.

1



ANSYS 5.0  
MAY 9 1993  
11:20:21  
PLOT NO. 1  
NODAL SOLUTION  
ENKE  
TOP  
SMN = .112062  
SMX = 1.813

Color	Value	$k/v^{*2}$
Dark Blue	.112062	
Blue	.301086	1.66
Light Blue	.490109	2.12
Green	.679132	2.58
Dark Green	.868155	3.04
Light Green	1.057	3.50
Yellow	1.246	3.96
Orange	1.435	4.42
Red	1.624	
Dark Red	1.813	

Figure 5-5 Predicted turbulence kinetic energy for Case F

# Chapter 6

## Concluding Remarks

### 6.1 Experimental Studies

Extensive hot-wire, Preston tube and Pitot tube measurements were performed over a Reynolds number range of 25,000 to 55,000, in simulated rod bundle subchannels (rod-trapezoidal duct cross-section) for which the tube positions were varied to provide  $s/d$  ratios from 1.220 down to 1.020, including asymmetric tube orientations. As a result of these experiments, spatial distributions of the mean axial velocity, local wall shear stress, five of the six Reynolds stresses and the distributions of turbulence kinetic energy are obtained, as well as secondary velocities for the setting of  $s/d = 1.220$ . Measurements on power spectra of the axial and azimuthal Reynolds stress components in the near gap regions were also made. Examination of the presented experimental data leads to the following conclusions:

1. The Reynolds number dependence of friction factor in the simulated rod bundle subchannel with  $s/d = 1.220$  can be described by  $f = 0.152Re^{-0.192}$ . Based on the equivalent hydraulic diameter, friction factors in rod-noncircular duct are generally lower than smooth pipe flow values.
2. Maximum axial velocity in the present rod-trapezoidal duct is typically about

twenty per cent higher than the subchannel averaged value. Contours of normalized axial velocity display bulges towards duct corners and indentations away from the lower part of the inclined duct wall due to the convection of momentum by secondary flow. There is no indication that the axial velocity distribution is affected to any significant extent by large scale cross-gap eddy motion.

3. The numerical integration based overall average wall shear stress  $\bar{\tau}_w$  is within two per cent of the duct average value from the measured axial pressure gradients. Global maxima of normalized local wall shear stress  $\tau_w/\bar{\tau}_w$  are consistently located on the rod surface where  $\theta \approx 60^\circ$  to  $80^\circ$  with the value of about  $1.3 \sim 1.4$ , while global minima are generally located in the  $60^\circ$  trapezoidal duct corner at a level of about 0.3. The local wall shear stress distributions are markedly modified by secondary flows, such as the dip on the inclined duct wall for case A. There are also signs that in the vicinity of small gaps, local wall shear stress can be modified by large scale cross-gap eddy motion.
4. The present experimental results uniquely confirm the existence of an unusual region near the rod-to-wall gap characterized by high magnitude axial turbulence intensity with a remarkably different type of distribution compared to a normal boundary layer. The quantitative level of this high-intensity region increases with decreasing  $s/d$  ratio. However, such increases do not extend to the case of extremely small gaps under which condition any cross-gap eddy motion becomes impossible. Azimuthal turbulence intensities reach peak values under conditions corresponding to when the aforementioned high-intensity region occurred. The disappearance of the peak normalized azimuthal turbulence intensity also coincides with the limiting case stated above. The quantitative level of the azimuthal turbulence intensity is larger than the axial component near

the small gap region. Based on the measurements of Reynolds normal stresses, turbulence kinetic energy was calculated and its distribution was found essentially similar to the axial turbulence intensity but it was strongly influenced by the azimuthal component right near the gap.

5. Secondary velocities on the symmetric rod setting  $s/d = 1.220$  were measured with X-probe; the magnitudes of secondary flow in most places were around the level of  $1\% \bar{V}_{z,b}$ , with a maximum of about  $3.4\% \bar{V}_{z,b}$ . The obtained flow pattern coincided well with the bulges of wall shear stress and turbulence kinetic energy distributions, suggesting that secondary flow is an important transport process within the present rod-trapezoidal subchannels, and possibly for other rod bundle subchannels as well. However, there is no apparent linkage between secondary flow and the abnormal turbulence intensity distribution.
6. The peak frequencies from the measured power spectra on axial and azimuthal Reynolds stress components strongly suggest the existence of strong periodic eddy movement; this characteristic frequency depends on the subchannel geometry and flow condition. The present data can be correlated with a linear correlation of Eq.(3-2). While the derived mixing factor from symmetric gap spectral data show good agreement with the Rehme's correlation Eq. (3-11), mixing factors from asymmetric gap spectral data are much higher than predicted by Eq. (3-11), suggesting that mixing between adjacent subchannels might be enhanced by cross-gap secondary flows.

## 6.2 Numerical Studies

Simulations of fully developed turbulent flow through the rod-trapezoidal duct

were made using the numerical methodology based on the combination of curvilinear non-orthogonal grids and primitive variables. As confirmed by a series of developmental test cases, the simple coordinate system transformation employed in the study applies to simulated and real rod bundle subchannels. Turbulence modelling was made possible by combining the existing algebraic Reynolds stress model and the experimentally determined empirical anisotropic eddy viscosity factor. This turbulence model was found to be capable of qualitatively reproducing major turbulence quantities such as turbulence kinetic energy and local wall shear stress in the presence of large scale cross-gap eddy motion. In parallel with the experimental studies, friction factor, local wall shear stress and distributions of axial velocity, turbulence kinetic energy and secondary velocities were predicted for selected rod settings. Specific conclusions can be drawn from the presented numerical results, as follows:

1. The predicted normalized isovels  $\bar{V}_z/\bar{V}_{z,b}$  were very similar to the experimental data with maximum difference of about 1.5% in the subchannel central region and 3.0% in the corner and gap regions. Evidences of secondary flow such as bulges towards duct corners and dip away from the inclined wall were reproduced but with somewhat reduced distortions compared to the experimental data.
2. Two counter rotating secondary flow cells were predicted with the current numerical model for each rod-to-wall gap, including a large central vortex and a small cell. There are also two pairs of counter-rotating cells coming from the subchannel central region towards the duct corners. The full picture of secondary flow consists of twelve counter-rotating cells for a symmetric half of the rod-trapezoidal duct. Variation of this pattern with changes of  $s/d$  ratio were obtained. In comparison with experimental secondary flow data, the predicted

pattern offers a more complete description of the secondary flow which encompasses two of the three measured cells. The predicted maximum secondary velocity was  $3.5\% \bar{V}_{b,z}$ , comparing to the measured maximum of  $3.4\% \bar{V}_{b,z}$ . Considering the difference between the predicted and measured secondary flow pattern, more experimental work on this regard is needed.

3. The predicted local wall shear stress distribution did not exhibit the interesting dip that was measured along the inclined duct wall for the symmetric case of  $s/d = 1.220$ ; associated with this, the prediction was about 10% lower than the experimental data in the bottom gap area. These differences aside, the numerically calculated local wall shear stress was generally within 6% of the experimental values, with the exception of the gap region where the present turbulence model provided inadequate description of the cross-gap eddy motion.
4. The experimentally obtained high turbulence kinetic energy ( $k/v^2$ ) patches were correctly predicted by the present numerical scheme. The migration of the patch from bottom gap region for case A to the top gap region for case C was achieved by empirical input of anisotropic eddy viscosity factor in the turbulence model. Quantitative differences between prediction and measurement were generally within 10%. Distortions in the predicted contours due to secondary flows resembled those from measurements with somewhat lesser degree of bulging and dipping.

### 6.3 Recommendations

The ultimate aim of the enormous efforts devoted so far to the area of rod bundle subchannel flow is to facilitate the design and safe operation of nuclear reactor fuel

channels. Consistent with this aim, recommendations for future work in the present research area are noted below in order to priority.

1. Measurements of temperature fluctuation for fully developed turbulent flow in simulated rod bundle subchannels with  $g/d = 0.10$  to  $0.02$ .
2. Flow visualization of large scale cross-gap eddy motion in simulated and triangular array rod bundles.
3. Development of a turbulence model with minimum possible empirical input to simulate rod bundle subchannel flows, including the flow regions which consist of coherent cross-gap eddy motion and the regions which only consist of ordinary boundary layer behavior.

## References

- Aly, A.M.M., Turbulent Flows in Equilateral Triangular Ducts and Rod Bundle Subchannels, *Ph.D Thesis*, Univ. Manitoba, 1977.
- Aly, A.M.M., Trupp, A.C., and Gerrard, A.D., Measurements and Prediction of Fully Developed Turbulent Flow in an Equilateral Triangular Duct, *J. Fluid Mech.*, **85**, 57-83, 1978.
- Antonopoulos, K.A., The Prediction of Turbulent Inclined Flow in Rod Bundles, *Computer and Fluids*, **14**, 361-378, 1986
- Bartzis, J.G. and Todreas, N.E., Turbulence Modelling of Axial Flow in a Bare Rod Bundle, *J. Heat Transfer*, **101**, 628-634, 1979.
- Bender, D.J. and Switick, D.M., Turbulent Velocity Distribution in a Rod Bundle, *ASME Paper 68-WA/HT-36*, 1968.
- Benodeker, R.W. and Date, A.E., Prediction of Turbulent Flow in Finite Rod Clusters, *2nd Symp. Turb. Shear Flows*, Imperial College, London, 1979.
- Bremhorst, K. and Walker, T.B., Spectral Measurements of Turbulent Momentum Transfer in Fully Developed Pipe Flow, *J. Fluid Mech.*, **61**, 173-186, 1973.
- Carajilescov, P. and Todreas, N.E., Experimental and Analytical Study of Axial Turbulent Flows in an Interior Subchannel of a Bare Rod Bundle, *J. Heat Transfer*, **98**, 262-268, 1976.
- Chieng, C.C. and Lin, C., Velocity Distribution in the Peripheral Subchannels of the

- CANDU Type 19 Rod Bundle, *Nucl. Engrg. Des.*, **55**, 389-394, 1979.
- Demuren, A.O., Calculation of Turbulence-Driven Secondary Motion in Ducts with Arbitrary Cross Section, *AIAA Journal*, **29**, 531-537, 1991.
- Eichhorn, R., Kao, H.C. and Neti, S., Measurements of Shear Stress in a Square Array Rod Bundle, *Nucl. Engrg. Des.*, **56**, 385-391, 1980.
- Eifler, W. and Nijsing, R., Experimental Investigation of Velocity Distribution and Flow Resistance in a Triangular Array of Parallel Rods, *Nucl. Engrg. Des.*, **5**, 22-42, 1967.
- Fakory, M. and Todreas, N., Experimental Investigation of Flow Resistance and Wall Shear Stress in the Interior Subchannel of a Triangular Array of Parallel Rods, *J. Fluids Engineering*, **101**, 429-435, 1979.
- Galbraith, K.P. and Knudsen, J.G., Turbulent Mixing Between Adjacent Channels for Single Phase Flow in a Rod Bundle, *American Institute of Chemical Engineer*, Preprint, 1971.
- Gerrard, A.D., Turbulent Flow in an Equilateral Triangular Duct, *M.Sc. Thesis*, Univ. of Manitoba, 1976.
- Hejna, J. and Mantilk, F., Turbulent Flow in Rod Bundles with Geometrical Disturbances, *Nuclear Tech.*, **59**, 509-525, 1982.
- Hinze, J.O., *Turbulence*, 2nd Ed., McGraw-Hill, New York, 1975.
- Hooper, J.D., Developed Single Phase Turbulent Flow Through a Square-pitch Rod Cluster, *Nucl. Engrg. Des.*, **60**, 365-379, 1980.
- Hooper, J.D. and Wood, D.H., Fully Developed Rod Bundle Flow over a Large Range of Reynolds Number, *Nucl. Engrg. Des.*, **83**, 31-46, 1984.
- Hooper, J.D. and Rehme, K., Large-scale Structural Effects in Developed Turbulent Flow through Closely-spaced Rod Arrays, *J. Fluids Mech.*, **145**, 305-337, 1984.

- Ingesson, L. and Hedberg, S., Heat Transfer between Subchannels in a Rod Bundle, *Heat Transfer*, 1970, Paris III, FC. 7.11, Elsevier, Amsterdam, (1970)
- Khalifa, M.M.A. and Trupp, A.C., Measurements of Fully Developed Turbulent Flow in a Trapezoidal Duct, *Experiments in Fluids*, **6**, 344-352, 1988.
- Kjellström, B., Studies of Turbulent Flow Parallel to a Rod Bundle of Triangular Arrays, *AB Atomenergi, Sweden*, Rep. AE-RV-16, 1971.
- Kohav, Y., Hetsroni, G. and Solan, A., Velocity Distribution in Semiopen Channels, *J. Fluids Engineering*, **98**, 746-766, 1976.
- Lauder, B.E. and Ying, W.M., Prediction of Flow and Heat Transfer in Ducts of Square-section, *The Institution of Mechanical Engineers, Proceedings 1973*, **187**, No.37/73, 455-461, 1973.
- Lawn, C.J., Turbulence Measurements with Hot Wires, *RD/B/M 1277*, Berkeley Nuclear Laboratories, 1969.
- Lei, Q.M., Numerical and Experimental Study of Laminar Mixed Convection in a Horizontal Semicircular Duct, *Ph.D Thesis*, University of Manitoba, 1990
- Lemos, de M.J.S., Anisotropic Turbulent Transport Modelling for Rod-bundle, *Heat and Technology*, **6**, 27-37, 1988.
- Markatos, N.C.G., Spalding, D.B., Tatchell, D.C. and Vlachos, N., A Solution Method for Three-Dimensional Turbulent Boundary Layers on Bodies of Arbitrary Shapes, *Computer Methods in Applied Mechanics and Engineering*, **15**, 161-174, 1978.
- Melaen, M.C., Calculation of Fluid Flows with Staggered and Nonstaggered Curvilinear Nonorthogonal Grids – The Theory, *Numerical Heat Transfer, Part B*, **21**, 1-19, 1992.
- Möller, S.V., On Phenomena of Turbulent Flow Through Rod Bundles, *Experimental Thermal and Fluid Science*, **4**, 25-35, 1991.

- Möller, S.V., Single-Phase Turbulent Mixing in Rod Bundles, *Experimental Thermal and Fluid Sciences*, **5**, 26-33, 1992.
- Nakayama, A., Chow, W.L., and Sharma, D., Calculation of Fully Developed Turbulent Flows in Ducts of Arbitrary Cross-Section, *J. Fluids Mech.*, **128**, 199-217, 1983.
- Palmer, L.D. and Swanson, L.L., Measurements of Heat Transfer Coefficients, Friction Factors and Velocity Profiles for Air Flowing Parallel to Closely Spaced Rods, *Int. Dev. in Heat Transfer*, (ASME, New York, 1961/1962), 535-542.
- Patel, V.C., Calibration of the Preston Tube and Limitations on its Use in Pressure Gradients, *J. Fluid Mech.*, **23**, Part I, 185-208, 1965.
- Rapley, C.W. and Gosman, A.D., The Prediction of Fully Developed Axial Turbulent Flow in Rod Bundles, *Nuclear Engineering and Design*, **97**, 313-325, 1986.
- Rehme, K., The Structure of Turbulent Flow Through a Wall Subchannel of a Rod Bundle, *Nuclear Engineering and Design*, **45**, 311-323, 1978.
- Rehme, K., Turbulent Momentum Transfer in Rod Bundles, *Nuclear Engineering and Design*, **62**, 137-146, 1980.
- Rehme, K., Distribution of Velocity and Turbulence in a Parallel Flow Along an Asymmetric Rod Bundle, *Nuclear Technology*, **59**, 148-159, 1982.
- Rehme, K., The Structure of Turbulent Flow Through Rod Bundles, *Nuclear Engineering and Design*, **99**, 141-154, 1987.
- Rehme, K., Turbulent Flow Through Two Asymmetric Rod Bundles, *Heat and Technology*, **5**, 19-37, 1987.
- Rehme, K., The Structure of Turbulence in Rod Bundles and the Implications on Natural Mixing between the Subchannels, *Int. J. Heat Mass Transfer*, **35**, 567-581, 1992.
- Renkizbulut, M. and Hadaller, G.I., An Experimental Study of Turbulent Flow Through

- A Square-Array Rod Bundle, *Nuclear Engineering and Design*, **91**, 41-45, 1986.
- Rowe, D.S., Johnson, B.M., and Knudsen, J.G., Implications Concerning Rod Bundle Crossflow Mixing Based on Measurements of Turbulent Flow Structure, *Int. J. Heat Mass Transfer*, **17**, 407-419, 1974.
- Seale, W.J., Measurements and Predictions of Fully Developed Turbulent Flow in a Simulated Rod Bundle, *J. Fluid Mech.*, **123**, 399-423, 1982.
- Shah, R.K. and London, A.J., Laminar Flow Forced Convection in Ducts, *Advances in Heat Transfer*, Academic, New York, 1978
- Subbotin, V.I. and Ushakov, P.A., Levchenko, Yu.D. and Aleksandrov, A.M., Velocity Fields in Turbulent Flow Past Rod Bundles, *Heat Transfer - Soviet Research*, **3**, 9-35, 1971.
- Tahir, A. and Rogers, J.T., The Mechanism of Secondary Flows in Turbulent Interchange in Rod Bundles, *Proc. 7th Canadian Congress App. Mech.*, 773-774, 1979.
- Trupp, A.C., The Structure of Turbulent Flow in Triangular Array Rod Bundles, *Ph.D Thesis*, Univ. of Manitoba, 1973.
- Trupp, A.C., and Azad, R.S., The Structure of Turbulent Flow in Triangular Array Rod Bundles, *Nuclear Engineering and Design*, **32**, 47-84, 1975.
- Trupp, A.C. and Aly, A.M.M., Predicted Secondary Flows in Triangular Array Rod Bundles, *J. Fluids Engineering*, **101**, 354-363, 1979.
- Vagt, J.D., Hot-wire Probes in Low Speed Flow, *Prog. Aerospace Sci.*, **18**, 271-323, 1979.
- Vonka, V., Measurement of Secondary Flow Vortices in a Rod Bundle, *Nucl. Engng. Des.*, **106**, 191-207, 1988.
- Wu, X. and Trupp, A.C., Experimental Study on the Unusual Turbulence Intensity Distributions in Rod-to-wall Gap Regions, *Experimental Thermal and Fluid Science*,

6, 360-370, 1993.

Wu,X. and Trupp,A.C., Prediction of Fully Developed Turbulent Flow in Simulated Rod Bundle Subchannels, *14th Canadian Congress of Applied Mechanics*, 1993

Yavuzkurt,S., A Guide to Uncertainty Analysis of Hot-Wire Data, *J. Fluids Engineering*, **106**, 181-186, 1984.

## Appendix A

# Error Analysis of Secondary Velocity Measurements

Given the fact that hot wire measurement is such a sensitive and intricate technique, it is natural to understand that one inherent problem always associated with the application of hot wire anemometry is the estimation of experimental error. Certain scientific sense can only be reached if a competent error analysis has been conducted. This is particularly true when the direction-sensitivity of the hot wire anemometry is used to extract the extreme weak information of non-zero mean transversal velocity.

Before analysing the experimental error, we will first go over the basic classification of measurement errors, because this will certainly benefit the following discussions. Systematic measurement errors (bias) can be caused by the use of imperfect measurement devices, measurement procedures, by environmental influences (influence quantities) existing during measurement, as well as by the influence of the measuring person. Systematic errors can be determined and eliminated according to a principle and are, in theory, predictable on a single measurement basis. Random measurement errors can occur in sensitive measurements conducted under repetitional conditions. Repetitional conditions exist when the measuring person is repeatedly measuring the same quantity, using the same measuring device and the same mea-

surement procedure. The scatter of the measured value is caused by temporally and locally non-constant error sources. Random measurement errors cannot be individually eliminated because it is not possible to predict the error magnitude at a given time.

The standard approach to estimate the systematic error involves three steps: applying partial differentiation to the original response equation with respect to virtually every variable which may cause deviation from the real value; evaluating the magnitude of influence resulting from the differential change of each individual variable in terms of percentage; finally making use of root-sum-square method to get the overall deviation which is the systematic error. To put this into mathematical language, assume we have

$$y = f(x_1, x_2, \dots, x_n)$$

according to linear error-propagation law,

$$\Delta y = \sum_{i=1}^n \frac{\partial y}{\partial x_i} \Delta x_i$$

For relative measurement errors in terms of percentage,

$$\frac{\Delta y}{y} = \sum_{i=1}^n \frac{\partial y}{\partial x_i} \frac{\Delta x_i}{y}$$

making use of the root-sum-square method to get the maximum systematic error estimation

$$\frac{\Delta y}{y} \leq \sqrt{\sum_{i=1}^n \left[ \frac{\partial y}{\partial x_i} \frac{\Delta x_i}{y} \right]^2}$$

Several prerequisites have to be met if the above illustrated principle is to practically make sense. An explicit expression of the desired quantity  $y$  in terms of every influencing factor is indispensable if a theoretically strict estimation is to be achieved. Unfortunately in some cases the derived expression  $y = f(x_1, x_2, \dots, x_n)$  only holds true

provided certain assumptions have been made which implies some error-causing factors  $x_{n+1}, \dots, x_{n+k}$  have been implicitly omitted and hence do not appear in the final equation. Lengthy mathematical derivation of partial derivation  $\partial y / \partial x_i$  often adds significant trouble, if not making it impossible, to the implementation of the error estimation process. Apart from these, perhaps the most perplexing problem associated with the above process is to quantify the magnitude of  $\Delta x_i / y$  because some variables are themselves quantities dependent on other variables, i.e.  $x_i = f'(x_1', x_2', \dots, x_n')$ , which means that a chain estimation is needed to reach a strict error estimation, and this is not always practically possible. In this regard, generally two approaches are available, i.e. theoretical analysis which in essence is by virtue of series expansion and omission of terms of high order smallness; and sensitivity analysis which involves altering some error dominating factors experimentally step by step and examining the relative changes of outputs. The former was adopted by Lawn (1969) in low Reynolds number smooth pipe flow whereas the latter was employed by Seale (1982) in simulated rod bundle subchannel flow over a wide Reynolds number range. Although these two methods seem to differ from each other significantly, they are virtually the same in the sense that both of them start from the cooling response equation and proceed following the differentiation procedure.

Compared with the estimation of systematic error, random error analysis is a relatively simple matter in the sense it mainly involves arithmetic calculation on a repetitional measurement basis. Suppose we have,

$$y = f(x)$$

and  $x$  is the measured quantity. After  $n$  times tests, a random sample with size  $n$  is obtained which can be denoted by  $x_i, i = 1, 2, \dots, n$ . Mathematically, the random error of the measurement of  $x$  is characterized by the following parameters,

- mean deviation

$$M.D. = \frac{1}{n} \sum_{i=1}^n |x_i - \bar{x}|$$

where  $\bar{x} = 1/n \sum_{i=1}^n x_i$

- standard deviation

$$s = \sqrt{\sum_{i=1}^n (x_i - \bar{x})^2 / (n - 1)}$$

- variance

$$v = s^2$$

The random property of the desired quantity  $y$  can be calculated using the variables in the sample size of  $x_i, i = 1, 2, \dots, n$ , assuming the random property is preserved through the calculation process, notwithstanding some additional error may be introduced from this simplification.

Assuming  $\alpha$  is the angle between the normal to the wire and the  $z$ -axis and  $\gamma_w$  the rotation angle of the wire around the  $z$ -axis, the response equation of instantaneous effective cooling velocity, according to Vagt (1979), reads

$$V_{eff}^2 = V_z^2 + V_x^2 + V_y^2 - (1 - k)^2 [V_z \sin \alpha + V_x \cos \alpha \cos \gamma_w + V_y \cos \alpha \sin \gamma_w]^2 \quad [1]$$

where  $\gamma_w = 0^\circ$  and  $\gamma_w = 90^\circ$  correspond to the cases that the wire lies in the Z-X plane and Z-Y plane, respectively. For the sake of simplicity, let's restrict ourselves to the Z-X plane, and write the response equation for the two wire orientations,

$$\begin{aligned} \text{orientation one } \gamma_w = 0^\circ \quad \alpha_1 = \alpha \\ \text{orientation two } \gamma_w = 90^\circ \quad \alpha_2 = \alpha + \pi/2 \end{aligned}$$

Assuming the relative turbulence intensity is small, after separating mean average terms on both sides from the instantaneous terms and some simple algebra derivation,

$$\bar{V}_{eff,I}^2 = (\bar{V}_z \cos \alpha - \bar{V}_x \sin \alpha)^2 + k^2 (\bar{V}_z \sin \alpha + \bar{V}_x \cos \alpha)^2 + \bar{V}_y^2 = A \quad [2]$$

$$\overline{V}_{eff,II}^2 = (\overline{V}_z \sin \alpha + \overline{V}_x \cos \alpha)^2 + k^2(\overline{V}_z \cos \alpha - \overline{V}_x \sin \alpha)^2 + \overline{V}_z^2 = A' \quad [3]$$

The contribution to  $\overline{V}_{eff}^2$  by the time average of turbulence correlations  $\overline{v_i^m v_j^n}$  are omitted owing to the assumption made above. Certain systematic error would be introduced in this respect, we will come back to this point later on.

Subtraction of Eq. [2] from Eq.[3] yields,

$$\overline{V}_{eff,II}^2 - \overline{V}_{eff,I}^2 = 4 \sin \alpha \cos \alpha (1 - k^2) \overline{V}_z \overline{V}_x$$

The linearized outputs of the anemometers are

$$\begin{aligned} E_I &= K_I V_{eff,I} \\ E_{II} &= K_{II} V_{eff,II} \end{aligned}$$

assuming  $K_I = K_{II} = K$ , substitution yields

$$\overline{V}_x = \frac{E_{II}^2 - E_I^2}{2K^2(1 - k^2)\overline{V}_z \sin 2\alpha}$$

and similarly, for

$$\begin{aligned} \text{orientation one } \gamma_w = 90^\circ \quad \alpha_1 &= \alpha \\ \text{orientation two } \gamma_w = 90^\circ \quad \alpha_2 &= \alpha + \pi/2 \end{aligned}$$

we have

$$\overline{V}_y = \frac{E_{II}^2 - E_I^2}{2K^2(1 - k^2)\overline{V}_z \sin 2\alpha}$$

The relative wire orientations gives the direction of the above evaluated transversal velocity. A simple confirmatory test was performed on a calibrator in this regard. The conclusion is that negative (downward) mean transversal velocity  $\overline{V}_y$  causes higher voltage output registered by the wire which has acute angle  $\alpha \leq 90^\circ$  with positive main flow direction (counterclockwise), and similarly positive (outward) mean transversal velocity  $\overline{V}_x$  is registered by the wire which also has acute angle  $\alpha \leq 90^\circ$  with positive main flow direction (counterclockwise).

Experimentally, the most natural way to materialize the outcome of the above mathematical derivations is direct recourse to a X-wire probe with which the simultaneity of the outputs from two different  $\alpha$  settings can be absolutely guaranteed. Indeed this straightforward approach has been employed successfully by Aly et.al. (1978) and by Khalifa and Trupp (1988) in the secondary flow measurements in an equilateral triangular duct and trapezoidal duct, respectively. Nevertheless one prerequisite that must be met with this approach is that the instantaneous velocity distribution must be uniform in the region occupied by the element; this means that the detecting element must be smaller than the dimensions of the smallest eddies of the turbulence. Unfortunately, the separation of the two slanted wires, in the case of a miniature P61 DISA X-wire, is 1.0 mm which fails to work given the smallness of the present flow geometry and steep velocity gradients. One alternative is the rotation technique associated with a single slanted wire, which was reported by Seale (1982). A single slanted wire with  $\alpha = 45^\circ$  had been used in the present test in view that it minimizes the spatial difference in two  $\alpha$  cases. However, inherently the dependence on the rotation of a single slanted wire not only lose the signal simultaneity but also brings about extreme difficulty in relocating the wire due to possible the eccentricity of the probe support and the random scatter of the experimental data may swamp the tiny mean secondary velocity information. After a lot of repetitive trial tests, a compromise was made between the requirements of simultaneity and spatial accuracy, i.e. the compensation technique of the X-wire separation. For example, suppose we are again restricted to the Z-X plane. Once a X-wire probe output from one wire along one horizontal traverse has been collected, the position of the X-wire probe is changed according to a previously measured wire separation to bring the center of the second wire to the point where the former wire center rested, and the same

traverse was repeated to complete measurements along one horizontal traverse. Thus, the stringent requirement of precise relocation of wire can be easily met because the spatially imprecise rotation of wire is replaced by a line translation that can be easily handled.

One of the other problems associated with the implementation of the above principle is calibration. It would be ideal to have the hot wire calibrated in a perfect laminar flow with a calibrator. From the experience obtained in the Reynolds stress measurement carried out previously, it is almost impossible to remove the hot wire probe from a calibrator and install it to the actual test facility and at the same time maintain the calibration constants unchanged. The routine insitu calibration method can solve the above problem and this is indeed the procedure employed in the Reynolds stress measurement. As a rule of thumb, the calibration position is always chosen as the point where the maximum axial velocity is reached, i.e. the pipe centerline in pipe flow or the intersection of two symmetric lines, if symmetries exist, in noncircular duct flow. In the present test, this rule was also used to choose the insitu calibration position. Calibration conducted at such position yielded expected secondary velocity data along the symmetric line of the top gap. In order to maintain the consistency of the calibration constant, the hot wire was calibrated before and after several, (usually four), horizontal traverses.

Table A1: Calibration position for secondary  
velocity measurement ( $s/d = 1.220$ )

X (mm)	Y (mm)	$\bar{V}_z$ (m/sec)	$E_I$ (V)	$E_{II}$ (V)
35.56	12.12	30.90	6.49	6.49

Having illustrated the principles and some of the salient points of the experimental approach, let's come back to the theme of the text and derive the experimental systematic error associated with the X-wire secondary flow measurement. Before outlining the major sources of systematic error, it is appropriate to recapitulate as complete as possible the assumptions routinely made that are associated with the use of X-wire probe, although in most cases implicitly, because the influences from these factors are usually considered to be negligibly small so that they will not be included in the constituents of systematic error. On the other hand, these assumptions will not always hold true so certain additional systematic errors will be introduced again due to this neglect. To put into mathematical form, these factors can be grouped into  $x_{n+1}, x_{n+2}, \dots, x_{n+k}$  which has been discussed previously. They are,

1. that the hot wires are perfectly linearized so that all frequencies occurring in the flow are correctly transmitted,
2. that the hot wires are straight so that the angle between the main flow direction and wire axis is known exactly,
3. that no vibrations of the various elements of the probe are present so that aerodynamic disturbances can be neglected,
4. that fluctuations present in the flow are uniform over the whole length of the sensing element,

5. that steady state relations are assumed to be equally valid for instantaneous values,
6. that hot-wake effects for multi-wire probes can not be detected,
7. that the influence of the wall on the hot-wire signal can be disregarded.
8. that the cooling effects of the wire supports can be neglected.

Excluding the aforementioned impacts, notwithstanding certain amount of deviation will inevitably be introduced resulting from this, two major categories of systematic error sources in the secondary flow measurement can be singled out and examined, i.e. errors linked to hot wire anemometer responses  $E_I, E_{II}$  and those related to repeatability which are pertinent to the secondary flow measurement. Sources belonging to the first group are, for example, yaw parameter precision, exponent of linearization, precision of mean main flow velocity. These are common in the application of hot wire technique while those peculiar to this test and hence belonging to the other group are unprecise relocation of wire by translation, drifts in mean tunnel velocity and in calibration constants during a traverse.

Table A2: Systematic error constituents in secondary flow measurement

No.	variable $x_i$	$\Delta x_i (\pm)$	$\Delta x_i/x_i (\pm\%)$	typical value
1	rotation angle $\gamma_w$	$1.0^\circ$	1.1	$0^\circ, 90^\circ$
2	wire slanting angle $\alpha$	$0.25^\circ$	0.56	$\pm 45^\circ$
3	calibration constant $K^*$	0.001	0.36	0.276
4	yaw parameter $k$	0.005	2.0	0.23
5	mean axial velocity $\bar{V}_z^{***}$	0.2 m/sec	1.0	25 m/sec
6	turbulence correlation $\overline{u_i^m u_j^n}^{****}$			

\* Variation in  $K$  includes calibration uncertainty, mismatch between two wires and channel drift.

\* Variation in  $\bar{U}$  includes uncertainty in  $\bar{U}$ , drift of the wind tunnel velocity and

uncertainty caused by space relocation.

$$** \quad m + n = 2.$$

### Systematic error associated with rotation angle $\gamma_w$

Apply linearity assumption on the wire instantaneous response equation [1], separating time mean items from the instantaneous terms and omitting the terms of turbulence correlation, leads to:

$$\begin{aligned} \bar{V}_{eff}^2 &= \bar{V}_z^2 + \bar{V}_x^2 + \bar{V}_y^2 \\ &\quad - (1 - k^2) [\bar{V}_z^2 \sin^2 \alpha + \bar{V}_x^2 \cos^2 \alpha \cos^2 \gamma_w + \bar{V}_y^2 \cos^2 \alpha \sin^2 \gamma_w \\ &\quad + 2\bar{V}_z \bar{V}_x \sin \alpha \cos \alpha \cos \gamma_w + 2\bar{V}_z \bar{V}_y \sin \alpha \cos \alpha \sin \gamma_w + 2\bar{V}_x \bar{V}_y \cos^2 \alpha \sin \gamma_w \cos \gamma_w] \end{aligned}$$

Consider the case  $\gamma_w = \bar{\gamma}_w + \Delta\gamma = 0^\circ + \Delta\gamma_w$ , in which  $\Delta\gamma \ll \bar{\gamma}_w$

$$\begin{aligned} \bar{V}_{eff}^2 &= \bar{V}_z^2 + \bar{V}_x^2 + \bar{V}_y^2 \\ &\quad - (1 - k^2) [\bar{V}_z^2 \sin^2 \alpha + \bar{V}_x^2 \cos^2 \alpha \cos^2 \Delta\gamma + \bar{V}_y^2 \cos^2 \alpha \sin^2 \Delta\gamma \\ &\quad + 2\bar{V}_z \bar{V}_x \sin \alpha \cos \alpha \cos \Delta\gamma + 2\bar{V}_z \bar{V}_y \sin \alpha \cos \alpha \sin \Delta\gamma + 2\bar{V}_x \bar{V}_y \cos^2 \alpha \sin \Delta\gamma \cos \Delta\gamma] \end{aligned}$$

Recall the rules of series expansion,

$$\begin{aligned} \cos^2 \Delta\gamma &= \frac{1}{2}(1 + \cos 2\Delta\gamma) = \frac{1}{2}(1 + 1 - \frac{(2\Delta\gamma)^2}{2} + \dots) = 1 - \Delta\gamma^2 \\ \sin^2 \Delta\gamma &= \frac{1}{2}(1 - \cos 2\Delta\gamma) = \frac{1}{2}(1 - 1 + \frac{(2\Delta\gamma)^2}{2} + \dots) = \Delta\gamma^2 \\ \cos \Delta\gamma &= 1 - \frac{\Delta\gamma^2}{2} + \dots \\ \sin \Delta\gamma &= \Delta\gamma + \dots \end{aligned}$$

Substitution yields

$$\begin{aligned} \bar{V}_{eff}^2 &= A - (1 - k^2) [-\bar{V}_x^2 \cos^2 \alpha \Delta\gamma^2 + \bar{V}_y^2 \cos^2 \alpha \Delta\gamma^2 \\ &\quad - \bar{V}_z \bar{V}_x \sin \alpha \cos \alpha \Delta\gamma^2 + 2\bar{V}_z \bar{V}_y \sin \alpha \cos \alpha \Delta\gamma + 2\bar{V}_x \bar{V}_y \cos^2 \alpha \Delta\gamma (1 - \frac{\Delta\gamma^2}{2})] \\ &= A - (1 - k^2) [\cos^2 \alpha \Delta\gamma^2 (\bar{V}_y^2 - \bar{V}_x^2) - \bar{V}_z \bar{V}_x \sin \alpha \cos \alpha \Delta\gamma^2 \\ &\quad + 2\bar{V}_z \bar{V}_y \sin \alpha \cos \alpha \Delta\gamma + 2\bar{V}_x \bar{V}_y \cos^2 \alpha \Delta\gamma - \dots] \\ &= A - B \end{aligned}$$

Assuming no error is introduced in the location of the rotation angle associated with the orientation two, we have

$$\begin{aligned}\bar{V}_{eff,I}^2 &= A - B \\ \bar{V}_{eff,II}^2 &= A'\end{aligned}$$

where  $A$  and  $A'$  are defined by the righthand sides of Eq.[2] and Eq.[3], respectively.

$$\bar{V}_{eff,II}^2 - \bar{V}_{eff,I}^2 = A' - A + B = 2 \sin 2\alpha(1 - k^2)\bar{V}_z\bar{V}_x + B$$

$$\begin{aligned}\bar{V}_x &= \frac{E_{II}^2 - E_I^2}{2K^2(1 - k^2)\bar{V}_z \sin 2\alpha} - \frac{B}{2(1 - k^2)\bar{V}_z \sin 2\alpha} \\ &= \bar{V}_{x,measure} - \frac{B}{2(1 - k^2)\bar{V}_z \sin 2\alpha}\end{aligned}$$

Assume  $\bar{V}_y = 0.01\bar{V}_z$ ,  $\Delta\gamma = 1.0^\circ = 0.017$ ,  $\bar{V}_x = 0.01\bar{U}$ ,  $\alpha = 45^\circ$ ,

$$B = 0.00016\bar{V}_z^2$$

$$\bar{V}_x = \bar{V}_{x,measure} - 0.01\%\bar{V}_z$$

### Systematic error associated with wire slanting angle $\alpha$

After applying the small signal assumption, taking time-average leads to:

$$\begin{aligned}\bar{V}_{eff}^2 &= \bar{V}_z^2 + \bar{V}_x^2 + \bar{V}_y^2 - (1 - k^2)[\bar{V}_z^2 \sin^2 \alpha + \bar{V}_x^2 \cos^2 \alpha \cos^2 \gamma_w + \bar{V}_y^2 \cos^2 \alpha \sin^2 \gamma_w \\ &\quad + 2\bar{V}_z\bar{V}_x \sin \alpha \cos \alpha \cos \gamma_w + 2\bar{V}_z\bar{V}_y \sin \alpha \cos \alpha \sin \gamma_w + 2\bar{V}_x\bar{V}_y \cos^2 \alpha \sin \gamma_w \cos \gamma_w]\end{aligned}$$

Consider the case  $\gamma_w = 0^\circ$ ,

$$\bar{V}_{eff}^2 = \bar{V}_z^2 + \bar{V}_x^2 + \bar{V}_y^2 - (1 - k^2)[\bar{V}_z^2 \sin^2 \alpha + \bar{V}_x^2 \cos^2 \alpha + 2\bar{V}_z\bar{V}_x \sin \alpha \cos \alpha]$$

Assume  $\alpha = \bar{\alpha} + \Delta\alpha$  where  $\Delta\alpha \ll \bar{\alpha}$ ,

$$\begin{aligned}f(x + h) &= f(x) + hf'(x) + \frac{h^2}{2}f''(x) + \dots \\ \sin^2(\alpha + \Delta\alpha) &= \sin^2 \alpha + 2\Delta\alpha \sin \alpha \cos \alpha + \dots \\ \cos^2(\alpha + \Delta\alpha) &= \cos^2 \alpha + 2\Delta\alpha \cos \alpha(-\sin \alpha) + \dots \\ \sin(\alpha + \Delta\alpha) &= \sin \alpha + \Delta\alpha \cos \alpha + \dots \\ \cos(\alpha + \Delta\alpha) &= \cos \alpha - \Delta\alpha \sin \alpha + \dots\end{aligned}$$

Substitution yields,

$$\begin{aligned}\bar{V}_{eff}^2 = & A - (1 - k^2)[\bar{V}_z^2 \Delta\alpha \sin 2\alpha - \bar{V}_x^2 \Delta\alpha \sin 2\alpha - 2\bar{V}_z \bar{V}_x \Delta\alpha \sin^2 \alpha \\ & + 2\bar{V}_z \bar{V}_x \Delta\alpha \cos^2 \alpha - 2\bar{V}_z \bar{V}_x \Delta\alpha^2 \sin \alpha \cos \alpha]\end{aligned}$$

With  $\alpha = 45^\circ$ ,

$$\begin{aligned}\bar{V}_{eff}^2 = & A - (1 - k^2)[\bar{V}_z^2 \Delta\alpha - \bar{V}_x^2 \Delta\alpha - \bar{V}_z \bar{V}_x \Delta\alpha + \bar{V}_z \bar{V}_x \Delta\alpha] \\ = & A - (1 - k^2)[\bar{V}_z^2 - \bar{V}_x^2] \Delta\alpha \\ = & A - C\end{aligned}$$

$$\bar{V}_{eff,II}^2 - \bar{V}_{eff,I}^2 = A' - A + C$$

$$\begin{aligned}\bar{V}_x = & \bar{V}_{x,measure} - \frac{C}{2(1 - k^2)\bar{V}_z} \\ = & \bar{V}_{x,measure} - \frac{(\bar{V}_z^2 - \bar{V}_x^2)\Delta\alpha}{2\bar{V}_z}\end{aligned}$$

Assuming  $\Delta\alpha = 0.25^\circ = 0.0044$ ,  $\bar{V}_x = 0.01\bar{U}$ ,

$$\bar{V}_x = \bar{V}_{x,measure} - 0.22\% \bar{V}_z$$

**Systematic error associated with calibration constant  $K$**

$$E_I = K_I V_{eff,I}$$

$$E_{II} = K_{II} V_{eff,II}$$

If  $K_I = \bar{K}_I + \Delta K_I$  where  $\Delta K_I \ll \bar{K}_I = K_{II} = K$ , substitution yields,

$$\begin{aligned}\frac{E_I^2}{(\bar{K}_I + \Delta K_I)^2} - \frac{E_{II}^2}{K_{II}^2} = & 2 \sin 2\alpha \bar{V}_z \bar{V}_x \\ \bar{V}_x = & \frac{E_{II}^2 - E_I^2}{2K^2 \sin 2\alpha (1 - k^2) \bar{V}_z} + \frac{E_I^2 [1/K^2 - 1/(K + \Delta K)^2]}{2 \sin 2\alpha (1 - k^2) \bar{V}_z}\end{aligned}$$

$$= \bar{V}_{x,measure} + \frac{\bar{V}_z[1 - K^2/K^2 + 2\Delta K K]}{2(1 - k^2) \sin 2\alpha}$$

with  $\alpha = 45^\circ$ ,  $K = 0.276$  and  $\Delta K = 0.001$ ,

$$\bar{V}_x = \bar{V}_{x,measure} + \frac{\bar{V}_z[1 - 1/(1 - 2\Delta K/K)]}{2(1 - k^2)} = \bar{V}_{x,measure} - 0.38\% \bar{V}_z$$

**Systematic error associated with Yaw parameter  $k$**

$$\bar{V}_{eff,I}^2 = (\bar{V}_z \cos \alpha - \bar{V}_x \sin \alpha)^2 + k^2(\bar{V}_z \sin \alpha + \bar{V}_x \cos \alpha)^2 + \bar{V}_y^2$$

Assume  $k = \bar{k} + \Delta k$ ,

$$\begin{aligned} \bar{V}_{eff,I}^2 &= (\bar{V}_z \cos \alpha - \bar{V}_x \sin \alpha)^2 + (\bar{k} + \Delta k)^2(\bar{V}_z \sin \alpha + \bar{V}_x \cos \alpha)^2 + \bar{V}_y^2 \\ &= A + 2k\Delta k(\bar{V}_z \sin \alpha + \bar{V}_x \cos \alpha)^2 \end{aligned}$$

With  $\alpha = 45^\circ$ ,

$$\begin{aligned} \bar{V}_{eff,I}^2 &= A + k\Delta k(\bar{V}_z + \bar{V}_x)^2 \\ \bar{V}_{eff,II}^2 - \bar{V}_{eff,I}^2 &= A' - A - k\Delta k(\bar{V}_z + \bar{V}_x)^2 \\ \bar{V}_x &= \bar{V}_{x,measure} + \frac{k\Delta k(\bar{V}_z + \bar{V}_x)^2}{2(1 - k^2)\bar{V}_z} \end{aligned}$$

Assume  $\bar{V}_x = 0.01\bar{V}_z$ ,  $k = 0.23$ ,  $\Delta k = 0.005$ ,

$$= \bar{V}_{x,measure} + 0.06\% \bar{V}_z$$

**Systematic error associated with mean axial velocity  $\bar{V}_z$**

$$\bar{V}_x = \frac{E_{II}^2 - E_I^2}{2K^2(1 - k^2)\bar{V}_z \sin 2\alpha}$$

The contribution of the variation of mean axial velocity  $\bar{V}_z$  to the systematic error can be evaluated more straightforwardly by

$$\Delta \bar{V}_x = \frac{\partial \bar{V}_x}{\partial \bar{V}_z} \Delta \bar{V}_z$$

$$= -\bar{V}_x \frac{\Delta \bar{V}_z}{\bar{V}_z}$$

Assume  $\Delta \bar{V}_z = 0.2m/sec$ ,  $\bar{V}_z = 25m/sec$ ,  $\bar{V}_x = 0.01\bar{V}_z$ ,

$$\Delta \bar{V}_x = 0.08\% \bar{V}_z$$

### Systematic error associated with large turbulence fluctuation

In view of the strong turbulence intensity present in the rod-wall gap region, intuitively one would consider the time-mean voltage output be more or less distorted. To appreciate the degree of distortion, let's start from the instantaneous wire response equation [1]

$$V_{eff} = \{V_z^2 + V_x^2 + V_y^2 - (1 - k^2)[V_z \sin \alpha + V_x \cos \alpha \cos \gamma_w + V_y \cos \alpha \sin \gamma_w]^2\}^{1/2}$$

$$V_z = \bar{V}_z + v_z$$

$$V_x = \bar{V}_x + v_x$$

$$V_y = \bar{V}_y + v_y$$

$$V_{eff} = \bar{V}_{eff} + v_{eff}$$

After substituting into the instantaneous response equation, the individual terms read

$$\begin{aligned} V_z^2 &= \bar{V}_z^2 + 2\bar{V}_z v_z + v_z^2 \\ V_x^2 &= \bar{V}_x^2 + 2\bar{V}_x v_x + v_x^2 \\ V_y^2 &= \bar{V}_y^2 + 2\bar{V}_y v_y + v_y^2 \\ V_z^2 \sin^2 \alpha &= \bar{V}_z^2 \sin^2 \alpha + 2\bar{V}_z v_z \sin^2 \alpha + v_z^2 \sin^2 \alpha \\ V_x^2 \cos^2 \alpha \cos^2 \gamma_w &= \bar{V}_x^2 \cos^2 \alpha \cos^2 \gamma_w + 2\bar{V}_x v_x \cos^2 \alpha \cos^2 \gamma_w + v_x^2 \cos^2 \alpha \cos^2 \gamma_w \\ V_y^2 \cos^2 \alpha \sin^2 \gamma_w &= \dots (\text{similar}) \\ 2V_z V_x \sin \alpha \cos \alpha \cos \gamma_w &= 2(\bar{V}_z + v_z)(\bar{V}_x + v_x) \sin \alpha \cos \alpha \cos \gamma_w = \dots \\ 2V_z V_y \cos \alpha \sin \alpha \sin \gamma_w &= \dots \\ 2V_x V_y \cos^2 \alpha \sin \gamma_w \cos \gamma_w &= \dots \end{aligned}$$

thus

$$V_{eff} = \{A + f(v_i^m v_j^n) + g(v_i \bar{V}_j)\}^{1/2}$$

where  $m + n = 2$  and  $A$  is the instantaneous value.

$$(x + y)^n = x^n + nx^{n-1}y + \dots$$

$$\overline{V}_{eff} = \overline{A} + \frac{1}{2} \frac{f(v_i^m v_j^n)}{\sqrt{A}} + \dots$$

$$\overline{V}_{eff}^2 = A + \sqrt{A}f(v_i^m v_j^n) + \dots$$

Finally we have

$$\overline{V}_{eff,I}^2 = A + \sqrt{A}f(v_i^m v_j^n)$$

$$\overline{V}_{eff,II}^2 = A' + \sqrt{A'}f'(v_i^m v_j^n)$$

With  $\gamma_w = 0^\circ$ ,  $\alpha = \pm 45^\circ$ ,

$$f = (3/2 - k^2)\overline{v_z^2} + (3/2 - k^2)\overline{v_x^2} + \overline{v_y^2} + (1 - k^2)(\overline{v_z v_x} + \overline{v_z v_y})$$

$$f' = (3/2 - k^2)\overline{v_z^2} + (3/2 - k^2)\overline{v_x^2} + \overline{v_y^2} - (1 - k^2)(\overline{v_z v_x} + \overline{v_z v_y})$$

It is hardly possible to draw a quantitative estimation out of these two expressions. Accordingly, it is assumed that after subtraction these two influences tend to cancel, leaving negligible impact on secondary velocity data.

Table A3: Recapitulation of systematic errors

No.	variable	$\Delta V_x (\% \overline{V}_z)$
1	$\gamma_w$	0.01
2	$\alpha$	0.22
3	$K$	0.38
4	$k$	0.06
5	$\overline{V}_z$	0.08
6	$\overline{v_i^m v_j^n}$	cancel

The overall estimation of the systematic error associated with the X-wire probe secondary velocity measurement can be deduced according to the root-mean-square method,

$$\Delta V_x = 0.45\% \overline{V}_z \leq 0.5\% \overline{V}_z$$

Another question which is more or less related to the systematic error estimation is that how strong the magnitude of the secondary flow velocity should be in order to be sensed by the present measurement technique. Intuitively one would think that if the secondary velocity is larger than the systematic error in terms of the mean axial velocity, then this method makes sense. This is not wrong. But there is another experimental means by which this minimum magnitude can be estimated. To this end, a simple test was performed on a calibrator and the results are summarized as follows,

Table A4: Directional response of X-wire via calibrator

$\theta^\circ$	$\bar{V}_z$	$\tan \theta$	$E_I(\text{V})$	$E_{II}(\text{V})$	$E_{II}^2 - E_I^2$	$\bar{V}_x/\bar{V}_z$ Eq.[4]
0	30.90	0.0	6.47	6.47	0.0	
0.3	30.90	0.0052	6.45	6.49	0.52	0.0036
1	30.90	0.0174	6.37	6.56	2.46	0.0170
2	30.90	0.0349	6.28	6.65	4.78	0.0331
3	30.90	0.0524	6.17	6.76	7.62	0.0527
4	30.90	0.0699	6.06	6.85	10.0	0.0705
5	30.90	0.0874	5.98	6.94	12.4	0.0857
0	23.16	0.0	4.91	4.91	0.0	
0.3	23.16	0.0052	4.89	4.92	0.29	0.0060
1	23.16	0.0174	4.84	4.97	1.27	0.0157
2	23.16	0.0349	4.78	5.06	2.75	0.0340
3	23.16	0.0524	4.71	5.13	4.13	0.0508
4	23.16	0.0699	4.63	5.20	5.60	0.0689
5	23.16	0.0874	4.56	5.27	6.97	0.0859
0	20.94	0.0	4.43	4.43	0.0	
0.3	20.94	0.0052	4.41	4.45	0.35	0.0053
1	20.94	0.0174	4.38	4.49	0.97	0.0147
2	20.94	0.0349	4.32	4.55	2.04	0.0307
3	20.94	0.0524	4.25	4.62	3.28	0.0494
4	20.94	0.0699	4.19	4.67	4.25	0.0640
5	20.94	0.0874	4.13	4.72	5.22	0.0786

The derived secondary velocity expression

$$\frac{\bar{V}_x}{\bar{V}_z} = \frac{E_{II}^2 - E_I^2}{2K^2(1 - k^2)\bar{V}_z^2} \quad [4]$$

has been verified in the above test, and a quick comparison between  $\tan \theta$  and the calculated secondary velocity ratio  $\bar{V}_x/\bar{V}_z$  confirms the reliability of this equation. From the above table, it is also concluded that the present technique is able to extract secondary velocity with magnitude down to  $0.5\% \bar{V}_z$ .

## Appendix B

### Computer Code To Predict Real and Simulated Rod Bundle Subchannel Flows

```

1. //XWU JOB ',, ,T=1999,I=10,L=90,', 'XWU',NOTIFY=XWU
2. // EXEC FORT7CLG,SIZE=1200K,P=D,PARM='LC(88) '
3. //FORT.SYSIN DD *
4. CCCCCCCCCCCCCCCCCCCCCCCCCCCCCCCCCCCCCCCCCCCCCCCCCCCCCCCCCC
5. C          FULLY DEVELOPED TURBULENT FLOW IN
6. C          REAL OR SIMULATED ROD BUNDLE SUBCHANNELS
7. CCCCCCCCCCCCCCCCCCCCCCCCCCCCCCCCCCCCCCCCCCCCCCCCCCCCCCCCCC
8. C          DEFINITION OF ARRAYS AND VARIABLES
9. C-----
10. C      1. CON(I,J),AE(I,J),AW(I,J),AN(I,J),AP(I,J),
11. C         PT(I),QT(I): COEFFICIENTS OF THE DISCRETIZED
12. C         LINEARIZED EQ. (4.33)
13. C         F(I,J,K): GENERAL VARIABLE IN EQ. (4.33)
14. C      2. GAMR(I,J),GAMT(I,J): RADIAL AND PERIPHERAL
15. C         EFFECTIVE TRANSPORT COEFFICIENTS OF THE
16. C         EQ.(4.24)
17. C         P(I,J): NODAL STATIC PRESSURE, EQ.(4.1),
18. C         EQ.(4.2) AND EQ.(4.3)
19. C         DU(I,J),DV(I,J): VELOCITY CORRECTIONS
20. C         TAU(I): LOCAL WALL SHEAR STRESS
21. C         TAUA: AVERAGED WALL SHEAR STRESS
22. C         DH: HYDRAULIC DIAMETER
23. C         RE: REYNOLDS NUMBER
24. C      3. R(I,J),RU(I,J),RV(I,J),RC(I,J): RADIUS FOR MAIN AND
25. C         STAGGERED NODES
26. C         GC(I,J),G(I,J),GU(I,J),GV(I,J): GEOMETRIC GROUP
27. C         = ETA*DRB/DTHETA FOR MAIN AND STAGGERED NODES
28. C         THETA(I), THETAU(I), THETAC(I) : ANGLE IN CYLINDRICAL
29. C         COORDINATES FOR MAIN AND STAGGERED NODES
30. C         ETA(I),XI(I),ETAV(I),XIU(I),ETAC(I): TRANSFORMED
31. C         COORDINATES FOR MAIN AND STAGGERED NODES
32. C         RB(I),RBU(I),RBC(I): RADIUS OF OUTER BOUNDARY FOR
33. C         MAIN AND STAGGERED NODES
34. C         RA: RADIUS OF INNER ROD, MAY BE ZERO
35. C         TB,TA: STARTING AND ENDING ANGLES OF THE DOMAIN
36. C         DX,DE: INCREMENT OF TRANSFORMED COORDINATES
37. C         RELAX(I): RELAXATION NUMBERS
38. C         RHO: DENSITY OF FLUID
39. C         AMU: DYNAMIC VISCOSITY OF FLUID
40. C         SMAX: MAXIMUM LOCAL RESIDUE OF PRESSURE CORRECTION
41. C         EQUATION
42. C         SSUM: SUMMATION OF LOCAL RESIDUE OF PRESSURE
43. C         CORRECTION EQUATION.
44. C      4. NF: IDENTITY NUMBER OF EQUATIONS TO BE SOLVED
45. C         L1,M1: NUMBER OF NODES IN RADIAL AND PERIPHERAL
46. C         DIRECTIONS
47. C         LSOLVE(I): LOGICAL VARIABLE CONTROLLING WHETHER
48. C         AN EQUATION IS TO BE SOLVED
49. C         IST,JST: INTERNAL VARIABLES
50. C         ITER: NUMBER OF ITERATIONS
51. C         LAST: MAXIMUM NUMBER OF ITERATIONS
52. C         NTIMES(I): NUMBER OF TDMA SWEEP ACROSS THE DOMAIN
53. C         NFMAX: MAXIMUM NUMBER OF EQUATIONS TO BE SOLVED
54. C         IREF,JREF: INTERNAL VARIABLES
55. C      5. FLOW: FLOW RATES DEFINED IN EQ.(4.30)
56. C         DIFF: CONDUCTANCE DEFINED IN EQ.(4.35)
57. C         ACOF: EQ(4.36)
58. C      6. U(I,J),V(I,J),W(I,J): NODAL VELOCITIES
59. C         PC(I,J): NODAL PRESSURE CORRECTIONS
60. C         AK(I,J),E(I,J): TURBULENCE KINETIC ENERGY AND
61. C         DISSIPATION
62. CCCCCCCCCCCCCCCCCCCCCCCCCCCCCCCCCCCCCCCCCCCCCCCCCCCCCCCCCC
63. C          MAIN PROGRAM
64. C-----

```

```

65. C   THIS IS THE MAIN PROGRAM WHICH CALLS
66. C   SUBROUTINES TO SOLVE THE FLOW PROBLEM
67. C-----
68.     IMPLICIT REAL*8 (A-H,O-Z)
69.     LOGICAL LSOLVE,LSTOP
70.     COMMON/VV1/F(52,52,10),CON(52,52),
71.     &AE(52,52),AW(52,52),AN(52,52),AS(52,52),AP(52,52),
72.     &PT(52),QT(52)
73.     COMMON/VV2/GAMR(52,52),GAMT(52,52),
74.     & P(52,52),DU(52,52),DV(52,52),
75.     & TAU0,TAU(52),TAUA,DH,RE
76.     COMMON/GRIDS/R(52,52),RU(52,52),RV(52,52),GC(52,52),
77.     & G(52,52),GU(52,52),THETA(52),ETA(52),XI(52),RB(52),
78.     & GV(52,52),RBU(52),RA,TB,TA,THETAU(52),T1,T2,
79.     & ETAV(52),XIU(52),THETAC(52),ETAC(52),RC(52,52),
80.     & RBC(52),DX,DE,RELAX(13),RHO,AMU,SMAX,SSUM
81.     COMMON/INDX/NF,L1,L2,L3,M1,M2,M3,LSOLVE(10),
82.     & IST,JST,ITER,LAST,NTIMES(10),NFMAX,
83.     & IREF,JREF
84.     COMMON/COEF/FLOW,DIFF,ACOF
85.     DIMENSION U(52,52),V(52,52),W(52,52),PC(52,52)
86.     DIMENSION AK(52,52),E(52,52)
87.     EQUIVALENCE(F(1,1,1),V(1,1)),(F(1,1,2),U(1,1)),
88.     & (F(1,1,3),PC(1,1)),(F(1,1,4),W(1,1)),
89.     & (F(1,1,5),AK(1,1)),(F(1,1,6),E(1,1))
90. CCCCCCCCCCCCCCCCCCCCCCCCCCCCCCCCCCCCCCCCCCCCCCCCCCCCCCCCCC
91.     CALL USER(1)
92.     CALL USER(2)
93. 10    CALL USER(3)
94.     CALL USER(4)
95.     CALL USER(5)
96.     IF(ITER.GE.LAST) GOTO 20
97.     CALL SETUP
98.     GOTO 10
99. C-----
100. 20   STOP
101.     END
102. CCCCCCCCCCCCCCCCCCCCCCCCCCCCCCCCCCCCCCCCCCCCCCCCCCCCCCCCCC
103.     SUBROUTINE USER(KENTRY)
104. CCCCCCCCCCCCCCCCCCCCCCCCCCCCCCCCCCCCCCCCCCCCCCCCCCCCCCCCCC
105. C     THIS IS A SUBROUTINE TO INPUT DATA, CALLS MESH
106. C     SUBROUTINE, INITIALIZE ARRAYS, IMPOSE BOUNDARY
107. C     CONDITIONS, UPDATE VARIABLES INCLUDING WALL SHEAR
108. C     AND UPDATE SOURCE TERMS
109. C-----
110.     IMPLICIT REAL*8 (A-H,O-Z)
111.     LOGICAL LSOLVE,LSTOP
112.     COMMON/VV1/F(52,52,10),CON(52,52),
113.     &AE(52,52),AW(52,52),AN(52,52),AS(52,52),AP(52,52),
114.     &PT(52),QT(52)
115.     COMMON/VV2/GAMR(52,52),GAMT(52,52),
116.     & P(52,52),DU(52,52),DV(52,52),
117.     & TAU0,TAU(52),TAUA,DH,RE
118.     COMMON/GRIDS/R(52,52),RU(52,52),RV(52,52),GC(52,52),
119.     & G(52,52),GU(52,52),THETA(52),ETA(52),XI(52),RB(52),
120.     & GV(52,52),RBU(52),RA,TB,TA,THETAU(52),T1,T2,
121.     & ETAV(52),XIU(52),THETAC(52),ETAC(52),RC(52,52),
122.     & RBC(52),DX,DE,RELAX(13),RHO,AMU,SMAX,SSUM
123.     COMMON/INDX/NF,L1,L2,L3,M1,M2,M3,LSOLVE(10),
124.     & IST,JST,ITER,LAST,NTIMES(10),NFMAX,
125.     & IREF,JREF
126.     COMMON/COEF/FLOW,DIFF,ACOF
127.     DIMENSION U(52,52),V(52,52),W(52,52),PC(52,52)
128.     DIMENSION AK(52,52),E(52,52)

```

```

129.     DIMENSION SRZ(52,52),STZ(52,52),SR2(52,52),ST2(52,52),
130.     & SRT(52,52)
131.     EQUIVALENCE(F(1,1,1),V(1,1)),(F(1,1,2),U(1,1)),
132.     & (F(1,1,3),PC(1,1)),(F(1,1,4),W(1,1)),
133.     & (F(1,1,5),AK(1,1)),(F(1,1,6),E(1,1))
134.     DIMENSION WOLD(52,52),TAUO(52),DN(52,52),WEIGHT(52)
135.     CCCCCCCCCCCCCCCCCCCCCCCCCCCCCCCCCCCCCCCCCCCCCCCCCCCCCCCCCC
136.     GO TO(1111,2222,3333,4444,5555,6666) KENTRY
137.     CCCCCCCCCCCCCCCCCCCCCCCCCCCCCCCCCCCCCCCCCCCCCCCCCCCCCCCCCC
138.     1111 CONTINUE
139. C-----
140. C     INPUT CONSTANTS HERE
141. C-----
142.     NFMAX=6
143.     LSTOP=.FALSE.
144.     ITER=0
145.     LAST=2000
146.     RHO=1.205D0
147.     AMU=18.17D-6
148.     PI=3.1415926535897932D0
149.     SMAX=0.0D0
150.     SSUM=0.0D0
151.     DO 1000 I=1,6
152.     NTIMES(I)=1
153. 1000 CONTINUE
154.     RELAX(1)=0.1D0
155.     RELAX(2)=0.1D0
156.     RELAX(3)=0.1D0
157.     RELAX(4)=0.1D0
158.     RELAX(5)=0.1D0
159.     RELAX(6)=0.1D0
160.     DO 1002 I=1,3
161.     LSOLVE(I)=.FALSE.
162. 1002 CONTINUE
163.     LSOLVE(4)=.TRUE.
164.     LSOLVE(5)=.TRUE.
165.     LSOLVE(6)=.TRUE.
166.     L1=48
167.     M1=20
168.     L2=L1-1
169.     L3=L2-1
170.     M2=M1-1
171.     M3=M2-1
172. C-----
173.     C2=0.013D0
174.     C3=0.562D0
175.     C4=0.085D0
176.     SIGK=1.0D0
177.     SIGE=1.34D0
178.     CE1=1.55D0
179.     CE2=2.0D0
180. C-----
181.     RETURN
182.     CCCCCCCCCCCCCCCCCCCCCCCCCCCCCCCCCCCCCCCCCCCCCCCCCCCCCCCCCC
183.     2222 CONTINUE
184. C-----
185. C     GENERATE MESH HERE
186. C-----
187.     CALL GRID
188. C-----
189.     DH=31.4D-3
190.     RE=55200.0D0
191.     WAV=RE*AMU/(DH*RHO)
192. C-----

```

```

193. C      INITIALIZING ARRAYS
194. C-----
195.      DO 2000 I=1,L1
196.      DO 2000 J=1,M1
197.      GAMR(I,J)=AMU
198.      GAMT(I,J)=AMU
199.      U(I,J)=0.0D0
200.      V(I,J)=0.0D0
201.      W(I,J)=WAV
202.      PC(I,J)=0.0D0
203.      AK(I,J)=0.1D0
204.      E(I,J)=10.0D0
205.      SRZ(I,J)=0.0D0
206.      STZ(I,J)=0.0D0
207.      SR2(I,J)=0.0D0
208.      ST2(I,J)=0.0D0
209.      SRT(I,J)=0.0D0
210.      DU(I,J)=0.0D0
211.      DV(I,J)=0.0D0
212.      AP(I,J)=0.0D0
213.      CON(I,J)=0.0D0
214.      AN(I,J)=0.0D0
215.      AS(I,J)=0.0D0
216.      AE(I,J)=0.0D0
217.      AW(I,J)=0.0D0
218.      DN(I,J)=1.0D0
219. 2000 CONTINUE
220. C-----
221. C      INPUT ANISOTROPY FACTOR DN(I,J) HERE
222. C-----
223.      READ(11,999) ((DN(I,J),I=1,L1),J=1,M1)
224. C-----
225.      TAU0=1.90D0
226.      DO 2001 I=1,L1
227.      TAU(I)=TAU0
228. 2001 CONTINUE
229.      RETURN
230. CCCCCCCCCCCCCCCCCCCCCCCCCCCCCCCCCCCCCCCCCCCCCCCCCCCCCCCCCC
231. 3333 CONTINUE
232. C-----
233.      IF(ITER.GT.1) THEN
234.      DO 2999 I=1,3
235.      LSOLVE(I)=.TRUE.
236. 2999 CONTINUE
237.      ELSE
238.      END IF
239. C-----
240. C      BOUNDARY CONDITIONS (NON-SLIP ONLY)
241. C      SYMMETRIY CONDITIONS ARE IMPOSED IN SOLVE
242. C-----
243.      DO 5200 I=1,L1
244. C-----
245.      W(I,M1)=0.0D0
246.      U(I,M1)=U(I,M2)
247.      V(I,M1)=V(I,M2)
248. C-----
249.      W(I,1)=0.0D0
250.      U(I,1)=U(I,2)
251.      V(I,1)=0.0D0
252. C-----
253. 5200 CONTINUE
254.      DO 3456 I=2,L1
255.      IF(THETA(I).LE.T1) THEN
256.      V(I,M2)=0.5D0*(U(I,M2)+U(I-1,M2))*DSIN(THETA(I))/

```

```

257.      & DCOS(THETA(I))
258.      ELSE IF(THETA(I).GT.T1.AND.THETA(I).LE.T2) THEN
259.          V(I,M2)=0.5D0*(U(I,M2)+U(I-1,M2))*DSIN(THETA(I)-2.D0*PI/3.D0)/
260.      & DCOS(THETA(I)-2.D0*PI/3.D0)
261.      ELSE IF(THETA(I).GT.T2) THEN
262.          V(I,M2)=-0.5D0*(U(I,M2)+U(I-1,M2))*DSIN(PI-THETA(I))/
263.      & DCOS(PI-THETA(I))
264.      ELSE
265.      END IF
266.      3456 CONTINUE
267.      CCCCCCCCCCCCCCCCCCCCCCCCCCCCCCCCCCCCCCCCCCCCCCCCCCCCCCCCCC
268.      C      CALCULATE AVERAGED AXIAL VELOCITY AND REYNOLDS NUMBER
269.      C-----
270.          WV=0.0D0
271.          AREA=0.0D0
272.          DO 5201 I=2,L2
273.          DO 5201 J=2,M2
274.              WV=WV+W(I,J)*R(I,J)*(TB-TA)*DX*((RB(I)-RA)*DE+
275.      & G(I,J)*R(I,J)*(TB-TA)*DX)
276.              AREA=AREA+R(I,J)*(TB-TA)*DX*((RB(I)-RA)*DE+
277.      & G(I,J)*R(I,J)*(TB-TA)*DX)
278.      5201 CONTINUE
279.          DO 5202 J=2,M2
280.              WV=WV+W(1,J)*R(1,J)*(TB-TA)*DX/2.D0*((RB(1)-RA)*DE+
281.      & G(1,J)*R(1,J)*(TB-TA)*DX/2.D0)
282.              AREA=AREA+R(1,J)*(TB-TA)*DX/2.D0*((RB(1)-RA)*DE+
283.      & G(1,J)*R(1,J)*(TB-TA)*DX/2.D0)
284.      5202 CONTINUE
285.          DO 5203 J=2,M2
286.              WV=WV+W(L1,J)*R(L1,J)*(TB-TA)*DX/2.D0*((RB(L1)-RA)*DE+
287.      & G(L1,J)*R(L1,J)*(TB-TA)*DX/2.D0)
288.              AREA=AREA+R(L1,J)*(TB-TA)*DX/2.D0*((RB(L1)-RA)*DE+
289.      & G(L1,J)*R(L1,J)*(TB-TA)*DX/2.D0)
290.      5203 CONTINUE
291.          WV=WV/AREA
292.          RE=WV*DH/(AMU/RHO)
293.      C-----
294.      C      CALCULATE LOCAL WALL SHEAR STRESS
295.      C-----
296.          IF(ITER.LE.1) THEN
297.              READ(12,999) (WEIGHT(I),I=1,L1)
298.          ELSE
299.          END IF
300.      C-----
301.          TAU0=0.0D0
302.          DO 5205 I=1,L1
303.              YPT1=DABS(R(I,3)-RA)
304.      C-----
305.          IF(THETA(I).LE.T1) THEN
306.              YP=DABS((RB(I)-R(I,M2))*DCOS(THETA(I)))
307.              YPT=DABS((RB(I)-R(I,M3))*DCOS(THETA(I)))
308.          ELSE IF(THETA(I).GT.T1.AND.THETA(I).LE.T2) THEN
309.              YP=DABS((RB(I)-R(I,M2))*DCOS(THETA(I)-2.D0*PI/3.D0))
310.              YPT=DABS((RB(I)-R(I,M3))*DCOS(THETA(I)-2.D0*PI/3.D0))
311.          ELSE IF(THETA(I).GT.T2) THEN
312.              YP=DABS((RB(I)-R(I,M2))*DCOS(PI-THETA(I)))
313.              YPT=DABS((RB(I)-R(I,M3))*DCOS(PI-THETA(I)))
314.          ELSE
315.          END IF
316.      C-----
317.          IF(ITER.LE.0) THEN
318.              TAU(I)=TAU0
319.              TAUO(I)=TAU0
320.          ELSE

```

```

321.      YYP=RHO*C4**0.25D0*DSQRT(AK(I,M3))*YPT/AMU
322.      YYYP=RHO*C4**0.25D0*DSQRT(AK(I,3))*YPT1/AMU
323.      IF(YYP.GT.11.63D0) THEN
324.      TAU(I)=W(I,M3)*RHO*C4**0.25D0*DSQRT(AK(I,M3))/
325.      & (5.50D0*DLOG10(9.77D0*YPT*C4**0.25D0*DSQRT(AK(I,M3))/AMU*RHO))
326.      ELSE
327.      TAU(I)=AMU*(W(I,M3)-W(I,M2))/YPT/2.D0
328.      END IF
329.      IF(YYYP.GT.11.63D0) THEN
330.      TAUO(I)=W(I,3)*RHO*C4**0.25D0*DSQRT(AK(I,3))/
331.      & (5.50D0*DLOG10(9.77D0*YPT1*C4**0.25D0*DSQRT(AK(I,3))/AMU*RHO))
332.      ELSE
333.      TAUO(I)=AMU*(W(I,3)-W(I,2))/YPT1/2.D0
334.      END IF
335.      END IF
336.      TAU=TAU(I)+TAUA*WEIGHT(I)+TAUO(I)*PI*RA/L1
337. 5205 CONTINUE
338.      TAUAB=TAUA/(PI*RA+127.0D-3)
339. C-----
340.      TAU=0.0D0
341.      DO 5207 I=1,L1
342.      TAU(I)=TAU(I)*TAU0/TAUAB
343.      TAUO(I)=TAUO(I)*TAU0/TAUAB
344.      TAU=TAUA+TAU(I)*WEIGHT(I)+TAUO(I)*PI*RA/L1
345. 5207 CONTINUE
346.      TAU=TAUA/(PI*RA+127.0D-3)
347. CCCCCCCCCCCCCCCCCCCCCCCCCCCCCCCCCCCCCCCCCCCCCCCCCCCCCCCCCC
348.      DO 5206 I=1,L1
349.      IF(THETA(I).LE.T1) THEN
350.      YP=DABS((RB(I)-R(I,M2))*DCOS(THETA(I)))
351.      ELSE IF(THETA(I).GT.T1.AND.THETA(I).LE.T2) THEN
352.      YP=DABS((RB(I)-R(I,M2))*DCOS(THETA(I)-2.D0*PI/3.D0))
353.      ELSE IF(THETA(I).GT.T2) THEN
354.      YP=DABS((RB(I)-R(I,M2))*DCOS(PI-THETA(I)))
355.      ELSE
356.      END IF
357.      YP1=DABS(R(I,2)-RA)
358.      YPLUS1=YP1*DSQRT(TAUO(I)/RHO)/(AMU/RHO)
359.      YPLUS=YP*DSQRT(TAU(I)/RHO)/(AMU/RHO)
360.      W(I,M2)=DSQRT(TAU(I)/RHO)*(5.5D0*DLOG10(9.77D0*YPLUS))
361.      W(I,2)=DSQRT(TAUO(I)/RHO)*(5.5D0*DLOG10(9.77D0*YPLUS1))
362. C-----
363.      AK(I,M2)=TAU(I)/DSQRT(RHO**2*C4)
364.      AK(I,2)=TAUO(I)/DSQRT(RHO**2*C4)
365.      E(I,M2)=C4**0.75D0*AK(I,M2)**1.5D0/YP/5.50D0
366.      E(I,2)=C4**0.75D0*AK(I,2)**1.5D0/YP1/5.50D0
367. C-----
368. 5206 CONTINUE
369.      RETURN
370. CCCCCCCCCCCCCCCCCCCCCCCCCCCCCCCCCCCCCCCCCCCCCCCCCCCCCCCCCC
371. 4444 CONTINUE
372. C-----
373. C      TURBULENCE SHEAR STRESS
374. C-----
375.      DO 4001 I=1,L1
376.      DO 4001 J=2,M2
377.      DWDE=0.0D0
378.      IF(J.NE.M2.AND.J.NE.2) THEN
379.      DWDE=0.5D0*(W(I,J+1)-W(I,J-1))/DE
380.      ELSE IF(J.EQ.M2) THEN
381.      DWDE=(W(I,J)-W(I,J-1))/DE
382.      ELSE IF(J.EQ.2) THEN
383.      DWDE=(W(I,J+1)-W(I,J))/DE
384.      ELSE

```

```

385.     END IF
386.     DWDR=1.D0/(RB(I)-RA)*DWDE
387. C-----
388.     SRZ(I,J)=-C4*AK(I,J)**2/E(I,J)*DWDR
389. C-----
390.     CC4=C3*AK(I,J)-
391.     & C2*C4*AK(I,J)**3/E(I,J)**2*DWDR**2
392.     SR2(I,J)=0.05D0*CC4+(1.0D0-0.05D0)*SR2(I,J)
393. C-----
394.     4001 CONTINUE
395. C-----
396.     DO 4002 J=2,M2
397.     DO 4002 I=1,L2
398.     DWDX=0.0D0
399.     DWDX=(W(I+1,J)-W(I,J))/DX
400.     DWDE=0.5D0*(0.5D0*(W(I,J+1)+W(I+1,J+1))-0.5D0*
401.     & (W(I,J-1)+W(I+1,J-1)))/DE
402.     DWDT=1.D0/(TB-TA)*DWDX-1.D0/(RBU(I)-RA)*GU(I,J)*RU(I,J)*DWDE
403.     DWDR=1.D0/(RBU(I)-RA)*DWDE
404. C-----
405.     CC1=(-C4*(0.5D0*(AK(I,J)+AK(I+1,J)))**2/(0.5D0*
406.     & (E(I,J)+E(I+1,J)))*1.D0/RU(I,J)*DWDT)
407.     STZ(I,J)=0.05D0*CC1+(1.0D0-0.05D0)*STZ(I,J)
408.     STZ(I,M2)=STZ(I,M3)
409. C-----
410.     CC2=C3*(0.5D0*(AK(I,J)+AK(I+1,J)))-C2*C4*
411.     & (0.5D0*(AK(I,J)+AK(I+1,J)))**3/(0.5D0*
412.     & (E(I,J)+E(I+1,J)))**2*(DWDT/RU(I,J))**2
413.     ST2(I,J)=0.05D0*CC2+(1.0D0-0.05D0)*ST2(I,J)
414.     ST2(I,M2)=ST2(I,M3)
415. C-----
416.     CC3=-C2*C4*(0.5D0*(AK(I,J)+AK(I+1,J)))**3/
417.     & (0.5D0*(E(I,J)+E(I+1,J)))**2*DWDR*DWDT/RU(I,J)
418.     SRT(I,J)=0.05D0*CC3+(1.0D0-0.05D0)*SRT(I,J)
419.     SRT(I,M2)=SRT(I,M3)
420. C-----
421.     4002 CONTINUE
422. C-----
423.     RETURN
424. CCCCCCCCCCCCCCCCCCCCCCCCCCCCCCCCCCCCCCCCCCCCCCCCCCCCCCCCCC
425.     5555 CONTINUE
426. C-----
427.     WRITE(6,998) ITER,SMAX,V(1,8),V(L1,8),TAUA,WV,WAV
428.     IF(ITER.EQ.LAST-1) THEN
429.     DO 5000 I=2,L2
430.     DO 5000 J=2,M2
431.     WOLD(I,J)=W(I,J)
432.     5000 CONTINUE
433.     ELSE
434.     END IF
435. C-----
436.     IF(ITER.EQ.LAST) THEN
437.     CH=0.0D0
438.     WC=0.0D0
439.     DO 4999 I=2,L2
440.     DO 4999 J=2,M2
441.     WC=DABS((WOLD(I,J)-W(I,J))/W(I,J))
442.     IF(WC.GE.CH) CH=WC
443.     4999 CONTINUE
444.     WRITE(10,999) ((W(I,J),AK(I,J),E(I,J),U(I,J),V(I,J)),
445.     & SRZ(I,J),STZ(I,J),SR2(I,J),ST2(I,J),SRT(I,J),R(I,J)),
446.     & THETA(I),TAU(I),TAUO(I),I=1,L1),J=1,M1)
447.     ELSE
448.     END IF

```

```

449. 999 FORMAT(1X,6(1PE10.3))
450. 998 FORMAT(1X,I4,4X,6(1PD10.3))
451. C-----
452. RETURN
453. CCCCCCCCCCCCCCCCCCCCCCCCCCCCCCCCCCCCCCCCCCCCCCCCCCCCCCCCC
454. 6666 CONTINUE
455. IF(NF.NE.1) GOTO 600
456. C-----
457. C DIFFUSION COEFFICIENT FOR V
458. C-----
459. DO 5231 I=1,L1
460. DO 5231 J=1,M1
461. GAMT(I,J)=AMU
462. GAMR(I,J)=AMU
463. 5231 CONTINUE
464. C-----
465. C SOURCE TERM OF RADIAL VELOCITY
466. C-----
467. DO 6000 I=2,L2
468. DO 6000 J=2,M3
469. CON(I,J)=0.0D0
470. C-----
471. DEDX=0.5D0*(0.5D0*(GAMT(I,J+2)+GAMT(I,J+1))*
472. & 0.5D0*(V(I+1,J+1)-V(I-1,J+1))/DX-
473. & 0.5D0*(GAMT(I,J-1)+GAMT(I,J))*
474. & 0.5D0*(V(I+1,J-1)-V(I-1,J-1))/DX)/DE
475. CON(I,J)=CON(I,J)-1.D0/RV(I,J)*1.D0/(TB-TA)*1.D0/(RB(I)-RA)*
476. & GV(I,J)*DEDX
477. C-----
478. DXDE=0.5D0*(0.5D0*(GAMT(I+1,J+1)+GAMT(I+1,J))*
479. & 1.D0/(RB(I+1)-RA)*GV(I+1,J)*RV(I+1,J)*
480. & 0.5D0*(V(I+1,J+1)-V(I+1,J-1))/DE-
481. & 0.5D0*(GAMT(I-1,J+1)+GAMT(I-1,J))*
482. & 1.D0/(RB(I-1)-RA)*GV(I-1,J)*RV(I-1,J)*
483. & 0.5D0*(V(I-1,J+1)-V(I-1,J-1))/DE)/DX
484. CON(I,J)=CON(I,J)-1.D0/RV(I,J)**2*1.D0/(TB-TA)*
485. & DXDE
486. C-----
487. DVDE=0.5D0*(V(I,J+1)-V(I,J-1))/DE
488. DGDE=0.5D0*(GV(I,J+1)-GV(I,J-1))/DE
489. CON(I,J)=CON(I,J)-1.D0/(RB(I)-RA)**2*
490. & 0.5D0*(GAMT(I,J+1)+GAMT(I,J))*GV(I,J)*
491. & DVDE*DGDE
492. C-----
493. IF(I.NE.2) THEN
494. DUDX=0.5D0*((U(I+1,J)+U(I+1,J+1)+U(I,J+1)+U(I,J))/4.D0-
495. & (U(I-1,J)+U(I-1,J+1)+U(I-2,J+1)+U(I-2,J))/4.D0)/DX
496. ELSE
497. DUDX=0.5D0*((U(I+1,J)+U(I+1,J+1)+U(I,J+1)+U(I,J))/4.D0-
498. & (U(I-1,J)+U(I-1,J+1))/2.D0)/DX
499. END IF
500. DUDE=0.5D0*((U(I,J+1)+U(I,J+2)+U(I-1,J+2)+U(I-1,J+1))/4.D0-
501. & (U(I,J)+U(I,J-1)+U(I-1,J-1)+U(I-1,J))/4.D0)/DE
502. CON(I,J)=CON(I,J)-AMU*(V(I,J)/RV(I,J)**2+2.D0/RV(I,J)*
503. & (1.D0/RV(I,J)*1.D0/(TB-TA)*DUDX-1.D0/(RB(I)-RA)*GV(I,J)*
504. & DUDE))
505. CON(I,J)=CON(I,J)+RHO*((U(I,J)+U(I,J+1)+U(I-1,J+1))+
506. & U(I-1,J))/4.D0)**2/RV(I,J)
507. CCCCCCCCCCCCCCCCCCCCCCCCCCCCCCCCCCCCCCCCCCCCCCCCCCCCCCCCC
508. C TURBULENCE SOURCE PART
509. C-----
510. IF(J.NE.M3) THEN
511. DR2DE=0.5D0*(0.5D0*RV(I,J+1)*(SR2(I,J+2)+SR2(I,J+1))-
512. & 0.5D0*RV(I,J-1)*(SR2(I,J)+SR2(I,J-1)))/DE

```

```

513.     ELSE IF(J.EQ.M3) THEN
514.     DR2DE=0.5D0*(RV(I,J+1)*SR2(I,J+1)-0.5D0*RV(I,J-1)*
515.     & (SR2(I,J)+SR2(I,J-1)))/DE
516.     ELSE
517.     END IF
518.     DR2DR=1.D0/(RB(I)-RA)*DR2DE
519. C-----
520.     IF(J.NE.M3) THEN
521.     DRTDE=0.5D0*((SRT(I-1,J+1)+SRT(I,J+1)+SRT(I,J+2)+
522.     & SRT(I-1,J+2))/4.D0-(SRT(I-1,J)+SRT(I,J)+SRT(I,J-1)+
523.     & SRT(I-1,J-1))/4.D0)/DE
524.     ELSE IF(J.EQ.M3) THEN
525.     DRTDE=0.5D0*((SRT(I-1,J+1)+SRT(I,J+1))/2.D0-
526.     & (SRT(I-1,J)+SRT(I,J)+SRT(I,J-1)+SRT(I-1,J-1))/4.D0)/DE
527.     ELSE
528.     END IF
529.     DRTDR=1.D0/(RB(I)-RA)*DRTDE
530. C-----
531.     IF(I.NE.2.AND.I.NE.L2) THEN
532.     DRTDX=0.5D0*((SRT(I,J)+SRT(I+1,J)+SRT(I+1,J+1)+
533.     & SRT(I,J+1))/4.D0-(SRT(I-1,J)+SRT(I-2,J)+SRT(I-2,J+1)+
534.     & SRT(I-1,J+1))/4.D0)/DX
535.     ELSE IF(I.EQ.2) THEN
536.     DRTDX=0.5D0*((SRT(I,J)+SRT(I+1,J)+SRT(I+1,J+1)+
537.     & SRT(I,J+1))/4.D0-(SRT(I-1,J)+SRT(I-1,J+1))/2.D0)/DX
538.     ELSE IF(I.EQ.L2) THEN
539.     DRTDX=0.5D0*((SRT(I,J)+SRT(I,J+1))/2.D0-(SRT(I-1,J)+
540.     & SRT(I-2,J)+SRT(I-2,J+1)+SRT(I-1,J+1))/4.D0)/DX
541.     ELSE
542.     END IF
543. C-----
544.     DRTDT=1.D0/(TB-TA)*DRTDX-1.D0/(RB(I)-RA)*GV(I,J)*RV(I,J)*
545.     & DRTDE
546. C-----
547.     CON(I,J)=CON(I,J)-RHO/RV(I,J)*(DR2DR+DRTDT-
548.     & (ST2(I,J)+ST2(I-1,J)+ST2(I-1,J+1)+ST2(I,J+1))/4.D0)
549. C-----
550.     CON(I,J)=CON(I,J)*DE*DX
551. 6000 CONTINUE
552. RETURN
553. CCCCCCCCCCCCCCCCCCCCCCCCCCCCCCCCCCCCCCCCCCCCCCCCCCCCCCCCCC
554. 600 IF(NF.NE.2) GOTO 601
555. C-----
556. C    DIFFUSION COEFFICIENT FOR U
557. C-----
558.     DO 5232 I=1,L1
559.     DO 5232 J=1,M1
560.     GAMT(I,J)=AMU
561.     GAMR(I,J)=AMU
562. 5232 CONTINUE
563. C-----
564. C    SOURCE TERM OF PERIPHERAL VELOCITY
565. C-----
566.     DO 6001 I=2,L3
567.     DO 6001 J=2,M2
568.     CON(I,J)=0.0D0
569. C-----
570.     DEDX=0.5D0*(2.D00*GAMT(I+1,J+1)*GAMT(I,J+1)/(GAMT(I+1,J+1)+
571.     & GAMT(I,J+1))*0.5D0*(U(I+1,J+1)-U(I-1,J+1))/DX-
572.     & 2.D00*GAMT(I+1,J-1)*GAMT(I,J-1)/(GAMT(I+1,J-1)+
573.     & GAMT(I,J-1))*0.5D0*(U(I+1,J-1)-U(I-1,J-1))/DX)/DE
574.     CON(I,J)=CON(I,J)-1.D0/RU(I,J)*1.D0/(TB-TA)*1.D0/(RBU(I)-RA)*
575.     & GU(I,J)*DEDX
576. C-----

```

```

577.      DXDE=0.5D0*(2.D0*GAMT(I+2,J)*GAMT(I+1,J)/
578.      & (GAMT(I+2,J)+GAMT(I+1,J))*
579.      & 1.D0/(RBU(I+1)-RA)*GU(I+1,J)*RU(I+1,J)*
580.      & 0.5D0*(U(I+1,J+1)-U(I+1,J-1))/DE-
581.      & 2.D0*GAMT(I-1,J)*GAMT(I,J)/(GAMT(I-1,J)+GAMT(I,J))*
582.      & 1.D0/(RBU(I-1)-RA)*GU(I-1,J)*RU(I-1,J)*
583.      & 0.5D0*(U(I-1,J+1)-U(I-1,J-1))/DE)/DX
584.      CON(I,J)=CON(I,J)-1.D0/RU(I,J)**2*1.D0/(TB-TA)*
585.      & DXDE
586. C-----
587.      DUDE=0.5D0*(U(I,J+1)-U(I,J-1))/DE
588.      DGDE=0.5D0*(GU(I,J+1)-GU(I,J-1))/DE
589.      CON(I,J)=CON(I,J)-1.D0/(RBU(I)-RA)**2*
590.      & 2.D0*GAMT(I+1,J)*GAMT(I,J)/(GAMT(I+1,J)+GAMT(I,J))*
591.      & GU(I,J)*DUDE*DGDE
592. C-----
593.      DVDX=0.5D0*((V(I+1,J)+V(I+1,J-1)+V(I+2,J-1)+V(I+2,J))/4.D0-
594.      & (V(I-1,J)+V(I-1,J-1)+V(I,J-1)+V(I,J))/4.D0)/DX
595.      IF(J.NE.2) THEN
596.      DVDE=0.5D0*((V(I,J+1)+V(I,J)+V(I+1,J)+V(I+1,J+1))/4.D0-
597.      & (V(I,J-1)+V(I,J-2)+V(I+1,J-2)+V(I+1,J-1))/4.D0)/DE
598.      ELSE
599.      DVDE=0.5D0*((V(I,J+1)+V(I,J)+V(I+1,J)+V(I+1,J+1))/4.D0-
600.      & (V(I,J-1)+V(I+1,J-1))/2.D0)/DE
601.      END IF
602.      CON(I,J)=CON(I,J)+AMU*(2.D0/RU(I,J)*
603.      & (1.D0/RU(I,J)*1.D0/(TB-TA)*DVDX-1.D0/(RBU(I)-RA)*GU(I,J)*
604.      & DVDE)-U(I,J)/RU(I,J)**2)
605.      CON(I,J)=CON(I,J)+RHO*((V(I,J)+V(I+1,J)+V(I+1,J-1)+
606.      & V(I,J-1))/4.D0)*U(I,J)/RU(I,J)
607. C-----
608.      IF(J.NE.2.AND.J.NE.M2) THEN
609.      DPDE=0.5D0*((P(I,J+1)+P(I+1,J+1))/2.D0-(P(I,J-1)+
610.      & P(I+1,J-1))/2.D0)/DE
611.      ELSE IF(J.EQ.2) THEN
612.      DPDE=((P(I,J+1)+P(I+1,J+1))/2.D0-(P(I,J)+
613.      & P(I+1,J))/2.D0)/DE
614.      ELSE IF(J.EQ.M2) THEN
615.      DPDE=((P(I,J)+P(I+1,J))/2.D0-(P(I,J-1)+
616.      & P(I+1,J-1))/2.D0)/DE
617.      ELSE
618.      END IF
619.      CON(I,J)=CON(I,J)+1.D0/(RBU(I)-RA)*GU(I,J)*DPDE
620. CCCCCCCCCCCCCCCCCCCCCCCCCCCCCCCCCCCCCCCCCCCCCCCCCCCCCCCCCC
621. C      TURBULENCE SOURCE PART
622. C-----
623.      IF(J.NE.M2) THEN
624.      DRTDE=0.5D0*(SRT(I,J+1)-SRT(I,J-1))/DE
625.      DT2DE=0.5D0*(ST2(I,J+1)-ST2(I,J-1))/DE
626.      ELSE IF(J.EQ.M2) THEN
627.      DRTDE=(SRT(I,J)-SRT(I,J-1))/DE
628.      DT2DE=(ST2(I,J)-ST2(I,J-1))/DE
629.      END IF
630.      IF(I.NE.L2) THEN
631.      DRTDX=0.5D0*(SRT(I+1,J)-SRT(I-1,J))/DX
632.      DT2DX=0.5D0*(ST2(I+1,J)-ST2(I-1,J))/DX
633.      ELSE IF(I.EQ.L2) THEN
634.      DRTDX=(SRT(I,J)-SRT(I-1,J))/DX
635.      DT2DX=(ST2(I,J)-ST2(I-1,J))/DX
636.      ELSE
637.      END IF
638. C-----
639.      DRTDR=1.D0/(RBU(I)-RA)*DRTDE
640.      DT2DT=1.D0/(TB-TA)*DT2DX-1.D0/(RBU(I)-RA)*GU(I,J)*RU(I,J)*

```

```

641.      & DT2DE
642. C-----
643.      CON(I,J)=CON(I,J)-RHO*(DRTDR+1.D0/RU(I,J)*DT2DT+
644.      & 2.D0*SRT(I,J)/RU(I,J))
645. C-----
646.      CON(I,J)=CON(I,J)*DE*DX
647. 6001 CONTINUE
648.      RETURN
649. CCCCCCCCCCCCCCCCCCCCCCCCCCCCCCCCCCCCCCCCCCCCCCCCCCCCCCCCCC
650. 601 IF(NF.NE.3) GOTO 602
651. C-----
652. C      SOURCE TERM FOR PRESSURE CORRECTION
653. C-----
654.      DO 6002 I=2,L2
655.      DO 6002 J=2,M2
656.      CON(I,J)=0.0D0
657. C-----
658.      CON(I,J)=CON(I,J)+1.D0/R(I,J)*1.D0/(RB(I)-RA)*RHO*RV(I,J-1)*
659.      & (V(I,J-1)-(U(I,J)+U(I,J-1)+U(I-1,J-1)+U(I-1,J)))/4.D0*
660.      & GV(I,J-1))*DX
661. C-----
662.      CON(I,J)=CON(I,J)-1.D0/R(I,J)*1.D0/(RB(I)-RA)*RHO*RV(I,J)*
663.      & (V(I,J)-(U(I,J)+U(I,J+1)+U(I-1,J+1)+U(I-1,J)))/4.D0*
664.      & GV(I,J))*DX
665. C-----
666.      CON(I,J)=CON(I,J)+1.D0/R(I,J)*1.D0/(TB-TA)*RHO*
667.      & U(I-1,J)*DE
668. C-----
669.      CON(I,J)=CON(I,J)-1.D0/R(I,J)*1.D0/(TB-TA)*RHO*
670.      & U(I,J)*DE
671. C-----
672.      CON(I,J)=CON(I,J)-1.D0/(RB(I)-RA)*G(I,J)/ETA(J)*
673.      & RHO*(U(I,J)+U(I-1,J))/2.D0*DX*DE
674. C-----
675. 6002 CONTINUE
676.      RETURN
677. CCCCCCCCCCCCCCCCCCCCCCCCCCCCCCCCCCCCCCCCCCCCCCCCCCCCCCCCCC
678. 602 IF(NF.NE.4) GOTO 603
679. C-----
680.      DO 6669 I=1,L1
681.      DO 6669 J=1,M1
682.      GAMT(I,J)=AMU
683.      GAMR(I,J)=AMU
684. 6669 CONTINUE
685. C-----
686. C      SOURCE TERM OF AXIAL VELOCITY
687. C-----
688.      DO 6003 I=2,L2
689.      DO 6003 J=3,M3
690.      CON(I,J)=0.0D0
691. C-----
692.      DEDX=0.5D0*(GAMT(I,J+1)*
693.      & 0.5D0*(W(I+1,J+1)-W(I-1,J+1))/DX-GAMT(I,J-1)*
694.      & 0.5D0*(W(I+1,J-1)-W(I-1,J-1))/DX)/DE
695.      CON(I,J)=CON(I,J)-1.D0/R(I,J)*1.D0/(TB-TA)*1.D0/(RB(I)-RA)*
696.      & G(I,J)*DEDX
697. C-----
698.      DXDE=0.5D0*(GAMT(I+1,J)*
699.      & 1.D0/(RB(I+1)-RA)*G(I+1,J)*R(I+1,J)*
700.      & 0.5D0*(W(I+1,J+1)-W(I+1,J-1))/DE-
701.      & GAMT(I-1,J)*
702.      & 1.D0/(RB(I-1)-RA)*G(I-1,J)*R(I-1,J)*
703.      & 0.5D0*(W(I-1,J+1)-W(I-1,J-1))/DE)/DX
704.      CON(I,J)=CON(I,J)-1.D0/R(I,J)**2*1.D0/(TB-TA)*

```

```

705.      & DXDE
706. C-----
707.      DWDE=0.5D0*(W(I,J+1)-W(I,J-1))/DE
708.      DGDE=0.5D0*(G(I,J+1)-G(I,J-1))/DE
709.      CON(I,J)=CON(I,J)-1.D0/(RB(I)-RA)**2*
710.      & GAMT(I,J)*G(I,J)*DWDE*DGDE
711. C-----
712.      CON(I,J)=CON(I,J)+4.D0*TAUA/DH
713. C-----
714. C      TURBULENCE SOURCE PART
715. C-----
716.      DRZDE=0.5D0*(R(I,J+1)*SRZ(I,J+1)-R(I,J-1)*SRZ(I,J-1))/DE
717.      DRZDR=1.D0/(RB(I)-RA)*DRZDE
718.      CON(I,J)=CON(I,J)-RHO/R(I,J)*DRZDR
719. C-----
720.      DTZDE=0.5D0*(0.5D0*(STZ(I-1,J+1)+STZ(I,J+1))-0.5D0*
721.      & (STZ(I-1,J-1)+STZ(I,J-1)))/DE
722.      DTZDX=(STZ(I,J)-STZ(I-1,J))/DX
723.      DTZDT=1.D0/(TB-TA)*DTZDX-1.D0/(RB(I)-RA)*G(I,J)*R(I,J)*DTZDE
724.      CON(I,J)=CON(I,J)-RHO/R(I,J)*DTZDT
725. C-----
726.      CON(I,J)=CON(I,J)*DE*DX
727. 6003 CONTINUE
728.      RETURN
729. CCCCCCCCCCCCCCCCCCCCCCCCCCCCCCCCCCCCCCCCCCCCCCCCCCCCCCCCCC
730. 603  IF(NF.NE.5) GOTO 604
731. C-----
732. C      DIFFUSION COEFFICIENT FOR AK
733. C-----
734.      DO 6525 I=1,L1
735.      DO 6525 J=2,M2
736.      GAMT(I,J)=C4*AK(I,J)**2/E(I,J)/SIGK+AMU
737.      GAMR(I,J)=C4*AK(I,J)**2/E(I,J)/SIGK+AMU
738. 6525 CONTINUE
739. C-----
740. C      SOURCE TERM FOR AK
741. C-----
742.      DO 6005 I=2,L2
743.      DO 6005 J=3,M3
744.      CON(I,J)=0.0D0
745. C-----
746.      DWDE=0.5D0*(W(I,J+1)-W(I,J-1))/DE
747.      DWDR=1.D0/(RB(I)-RA)*DWDE
748.      DWDX=0.5D0*(W(I+1,J)-W(I-1,J))/DX
749.      DWDT=1.D0/(TB-TA)*DWDX-1.D0/(RB(I)-RA)*G(I,J)*R(I,J)*DWDE
750.      GAK=-RHO*(SRZ(I,J)*DWDR+
751.      & 0.5D0*(STZ(I,J)+STZ(I-1,J))/R(I,J)*DWDT)
752. C-----
753.      CON(I,J)=CON(I,J)+GAK*DN(I,J)-RHO*E(I,J)
754.      CON(I,J)=CON(I,J)*DE*DX
755. C-----
756. 6005 CONTINUE
757.      RETURN
758. C-----
759. 604  IF(NF.NE.6) GOTO 605
760. C-----
761.      DO 6526 I=1,L1
762.      DO 6526 J=2,M2
763.      GAMT(I,J)=C4*AK(I,J)**2/E(I,J)/SIGE+AMU
764.      GAMR(I,J)=C4*AK(I,J)**2/E(I,J)/SIGE+AMU
765. 6526 CONTINUE
766. C-----
767. C      SOURCE TERM FOR E
768. C-----

```

```

769.      DO 6006 I=2,L2
770.      DO 6006 J=3,M3
771.      CON(I,J)=0.0D0
772. C-----
773.      DWDE=0.5D0*(W(I,J+1)-W(I,J-1))/DE
774.      DWDR=1.D0/(RB(I)-RA)*DWDE
775.      DWDX=0.5D0*(W(I+1,J)-W(I-1,J))/DX
776.      DWDT=1.D0/(TB-TA)*DWDX-1.D0/(RB(I)-RA)*G(I,J)*R(I,J)*DWDE
777.      GAK=-RHO*(SRZ(I,J)*DWDR+
778.      & 0.5D0*(STZ(I,J)+STZ(I-1,J))/R(I,J)*DWDT)
779. C-----
780.      CON(I,J)=CON(I,J)+E(I,J)*(CE1*GAK*DN(I,J)-CE2*RHO*E(I,J))/AK(I,J)
781. C-----
782.      CON(I,J)=CON(I,J)*DX*DE
783.      6006 CONTINUE
784. C-----
785.      605  CONTINUE
786. C-----
787.      RETURN
788.      END
789. CCCCCCCCCCCCCCCCCCCCCCCCCCCCCCCCCCCCCCCCCCCCCCCCCCCCCCCCCCCCC
790.      SUBROUTINE SETUP
791. C-----
792.      IMPLICIT REAL*8 (A-H,O-Z)
793.      LOGICAL LSOLVE,LSTOP
794.      COMMON/VV1/F(52,52,10),CON(52,52),
795.      &AE(52,52),AW(52,52),AN(52,52),AS(52,52),AP(52,52),
796.      &PT(52),QT(52)
797.      COMMON/VV2/GAMR(52,52),GAMT(52,52),
798.      & P(52,52),DU(52,52),DV(52,52),
799.      & TAU0,TAU(52),TAUA,DH,RE
800.      COMMON/GRIDS/R(52,52),RU(52,52),RV(52,52),GC(52,52),
801.      & G(52,52),GU(52,52),THETA(52),ETA(52),XI(52),RB(52),
802.      & GV(52,52),RBU(52),RA,TB,TA,THETAU(52),T1,T2,
803.      & ETAV(52),XIU(52),THETAC(52),ETAC(52),RC(52,52),
804.      & RBC(52),DX,DE,RELAX(13),RHO,AMU,SMAX,SSUM
805.      COMMON/INDX/NF,L1,L2,L3,M1,M2,M3,LSOLVE(10),
806.      & IST,JST,ITER,LAST,NTIMES(10),NFMAX,
807.      & IREF,JREF
808.      COMMON/COEF/FLOW,DIFF,ACOF
809.      DIMENSION U(52,52),V(52,52),W(52,52),PC(52,52)
810.      DIMENSION AK(52,52),E(52,52)
811.      EQUIVALENCE(F(1,1,1),V(1,1)),(F(1,1,2),U(1,1)),
812.      & (F(1,1,3),PC(1,1)),(F(1,1,4),W(1,1)),
813.      & (F(1,1,5),AK(1,1)),(F(1,1,6),E(1,1))
814.      DIMENSION PC1(52,52)
815. CCCCCCCCCCCCCCCCCCCCCCCCCCCCCCCCCCCCCCCCCCCCCCCCCCCCCCCCCCCCC
816. C      RADIAL VELOCITY
817. C-----
818.      NF=1
819.      IF(.NOT.LSOLVE(NF)) GOTO 1000
820. C-----
821.      IST=2
822.      JST=2
823.      CALL USER(6)
824. C-----
825.      DO 100 I=2,L2
826.      DO 100 J=2,M3
827.      FLOW=1.D0/RV(I,J)*1.D0/(RB(I)-RA)*(RHO*R(I,J+1)*
828.      & (0.5D0*(V(I,J)+V(I,J+1))-0.5D0*(U(I,J+1)+U(I-1,J+1))*
829.      & G(I,J+1)))*DX
830.      DIFF=1.D0/RV(I,J)*1.D0/(RB(I)-RA)**2*
831.      & (R(I,J+1)*(GAMR(I,J+1)+GAMT(I,J+1)*G(I,J+1)*G(I,J+1)))*
832.      & DX/DE

```

```

833.      CALL DIFLOW
834.      AN(I,J)=ACOF+DMAX1(0.0D0,-FLOW)
835. C-----
836.      FLOW=1.D0/RV(I,J)*1.D0/(RB(I)-RA)*(RHO*R(I,J)*
837.      & (0.5D0*(V(I,J)+V(I,J-1))-0.5D0*(U(I,J)+U(I-1,J))*
838.      & G(I,J))*DX
839.      DIFF=1.D0/RV(I,J)*1.D0/(RB(I)-RA)**2*
840.      & (R(I,J)*(GAMR(I,J)+GAMT(I,J)*G(I,J)*G(I,J))*
841.      & DX/DE
842.      CALL DIFLOW
843.      AS(I,J)=ACOF+DMAX1(0.0D0,FLOW)
844. C-----
845.      FLOW=1.D0/RV(I,J)*1.D0/(TB-TA)*(RHO*
846.      & 0.5D0*(U(I,J)+U(I,J+1)))*DE
847.      DIFF=1.D0/RV(I,J)**2*1.D0/(TB-TA)**2*
848.      & GAMT(I,J)*DE/DX
849.      CALL DIFLOW
850.      AE(I,J)=ACOF+DMAX1(0.0D0,-FLOW)
851. C-----
852.      FLOW=1.D0/RV(I,J)*1.D0/(TB-TA)*(RHO*
853.      & 0.5D0*(U(I-1,J)+U(I-1,J+1)))*DE
854.      DIFF=1.D0/RV(I,J)**2*1.D0/(TB-TA)**2*
855.      & GAMT(I,J)*DE/DX
856.      CALL DIFLOW
857.      AW(I,J)=ACOF+DMAX1(0.0D0,FLOW)
858. C-----
859.      AP(I,J)=AN(I,J)+AS(I,J)+AE(I,J)+AW(I,J)
860. C-----
861. C      UNDER RELAXATION HERE
862. C-----
863.      AP(I,J)=AP(I,J)/RELAX(NF)
864.      CON(I,J)=CON(I,J)+(1.D0-RELAX(NF))*AP(I,J)*V(I,J)
865. C-----
866.      DV(I,J)=1.D0/(RB(I)-RA)*DX
867.      CON(I,J)=CON(I,J)+DV(I,J)*(P(I,J)-P(I,J+1))
868.      DV(I,J)=DV(I,J)/AP(I,J)
869. 100  CONTINUE
870. C-----
871.      DO 681 I=2,L2
872.      CON(I,M2)=1.0D20*F(I,M2,NF)
873.      AP(I,M2)=1.0D20
874.      AN(I,M2)=0.D0
875.      AS(I,M2)=0.0D0
876.      AE(I,M2)=0.0D0
877.      AW(I,M2)=0.0D0
878. 681  CONTINUE
879. C-----
880.      CALL SOLVE
881. 1000 CONTINUE
882. C-----
883. C      PERIPHERAL VELOCITY
884. C-----
885.      NF=2
886.      IF(.NOT.LSOLVE(NF)) GOTO 1001
887. C-----
888.      IST=2
889.      JST=2
890.      CALL USER(6)
891. C-----
892.      DO 101 I=2,L3
893.      DO 101 J=2,M2
894.      FLOW=1.D0/RU(I,J)*1.D0/(RBU(I)-RA)*(RHO*RC(I,J)*
895.      & (0.5D0*(V(I,J)+V(I+1,J))-0.5D0*(U(I,J)+U(I,J+1))*
896.      & GC(I,J))*DX

```

```

897.      DIFF=1.D0/RU(I,J)*1.D0/(RBU(I)-RA)**2*(RC(I,J)*
898.      & (GAMR(I,J)+GAMT(I,J)*GC(I,J)**2))*DX/DE
899.      CALL DIFLOW
900.      AN(I,J)=ACOF+DMAX1(0.0D0,-FLOW)
901. C-----
902.      FLOW=1.D0/RU(I,J)*1.D0/(RBU(I)-RA)*(RHO*RC(I,J-1)*
903.      & (0.5D0*(V(I,J-1)+V(I+1,J-1))-0.5D0*(U(I,J)+U(I,J-1))*
904.      & GC(I,J-1))*DX
905.      DIFF=1.D0/RU(I,J)*1.D0/(RBU(I)-RA)**2*(RC(I,J-1)*
906.      & (GAMR(I,J)+GAMT(I,J)*GC(I,J-1)**2))*DX/DE
907.      CALL DIFLOW
908.      AS(I,J)=ACOF+DMAX1(0.0D0, FLOW)
909. C-----
910.      FLOW=1.D0/RU(I,J)*1.D0/(TB-TA)*(RHO*
911.      & 0.5D0*(U(I,J)+U(I+1,J)))*DE
912.      DIFF=1.D0/RU(I,J)**2*1.D0/(TB-TA)**2*
913.      & GAMT(I+1,J)*DE/DX
914.      CALL DIFLOW
915.      AE(I,J)=ACOF+DMAX1(0.0D0,-FLOW)
916. C-----
917.      FLOW=1.D0/RU(I,J)*1.D0/(TB-TA)*(RHO*
918.      & 0.5D0*(U(I,J)+U(I-1,J)))*DE
919.      DIFF=1.D0/RU(I,J)**2*1.D0/(TB-TA)**2*
920.      & GAMT(I,J)*DE/DX
921.      CALL DIFLOW
922.      AW(I,J)=ACOF+DMAX1(0.0D0, FLOW)
923. C-----
924.      AP(I,J)=AN(I,J)+AS(I,J)+AE(I,J)+AW(I,J)
925. C-----
926. C      UNDER RELAXATION HERE
927. C-----
928.      AP(I,J)=AP(I,J)/RELAX(NF)
929.      CON(I,J)=CON(I,J)+(1.D0-RELAX(NF))*AP(I,J)*U(I,J)
930. C-----
931.      DU(I,J)=1.D0/RU(I,J)*1.D0/(TB-TA)*DE
932.      CON(I,J)=CON(I,J)+DU(I,J)*(P(I,J)-P(I+1,J))
933.      DU(I,J)=DU(I,J)/AP(I,J)
934. 101  CONTINUE
935. C-----
936.      DO 682 J=2,M2
937.      CON(L2,J)=1.0D20*F(L2,J,NF)
938.      AE(L2,J)=0.D0
939.      AP(L2,J)=1.0D20
940.      AN(L2,J)=0.0D0
941.      AS(L2,J)=0.0D0
942.      AW(L2,J)=0.0D0
943. 682  CONTINUE
944. C-----
945.      CALL SOLVE
946. 1001 CONTINUE
947. CCCCCCCCCCCCCCCCCCCCCCCCCCCCCCCCCCCCCCCCCCCCCCCCCCCCCCCCCC
948. C      PRESSURE CORRECTION
949. C-----
950.      NF=3
951.      IF(.NOT.LSOLVE(NF)) GOTO 1002
952. C-----
953.      IST=2
954.      JST=2
955.      CALL USER(6)
956.      SMAX=0.0D0
957.      SSUM=0.0D0
958. C-----
959.      DO 102 I=2,L2
960.      DO 102 J=2,M2

```

```

961.      IF(J.NE.M2) THEN
962.      AN(I,J)=RV(I,J)*DV(I,J)
963.      AN(I,J)=AN(I,J)*1.D0/R(I,J)*1.D0/(RB(I)-RA)*DX*RHO
964.      ELSE
965.      AN(I,J)=0.0D0
966.      END IF
967. C-----
968.      IF(J.NE.2) THEN
969.      AS(I,J)=RV(I,J-1)*DV(I,J-1)
970.      AS(I,J)=AS(I,J)*1.D0/R(I,J)*1.D0/(RB(I)-RA)*DX*RHO
971.      ELSE
972.      AS(I,J)=0.0D0
973.      END IF
974. C-----
975.      IF(I.NE.L2) THEN
976.      AE(I,J)=1.D0/R(I,J)*1.D0/(TB-TA)*RHO*DE*DU(I,J)
977.      ELSE
978.      AE(I,J)=0.0D0
979.      END IF
980. C-----
981.      IF(I.NE.2) THEN
982.      AW(I,J)=1.D0/R(I,J)*1.D0/(TB-TA)*RHO*DE*DU(I-1,J)
983.      ELSE
984.      AW(I,J)=0.0D0
985.      END IF
986. C-----
987.      AP(I,J)=AN(I,J)+AS(I,J)+AE(I,J)+AW(I,J)
988. C-----
989.      PC(I,J)=0.0D0
990.      SMAX=DMAX1(SMAX,ABS(CON(I,J)))
991.      SSUM=SSUM+CON(I,J)
992. 102  CONTINUE
993. C-----
994.      DO 902 I=1,L1
995.      DO 902 J=1,M1
996.      PC(I,J)=0.0D0
997.      PC1(I,J)=PC(I,J)
998. 902  CONTINUE
999. CCCCCCCCCCCCCCCCCCCCCCCCCCCCCCCCCCCCCCCCCCCCCCCCCCCCCCCCCCCCC
1000.      DO 901 K=1,52
1001.      DO 900 I=2,L2
1002.      DO 900 J=2,M2
1003.      PC(I,J)=AN(I,J)*PC1(I,J+1)+AS(I,J)*PC1(I,J-1)+
1004.      & AE(I,J)*PC1(I+1,J)+AW(I,J)*PC1(I-1,J)+CON(I,J)
1005.      PC(I,J)=PC(I,J)/AP(I,J)
1006. 900  CONTINUE
1007.      DO 903 I=2,L2
1008.      DO 903 J=2,M2
1009.      PC1(I,J)=PC(I,J)
1010. 903  CONTINUE
1011. 901  CONTINUE
1012. CCCCCCCCCCCCCCCCCCCCCCCCCCCCCCCCCCCCCCCCCCCCCCCCCCCCCCCCCCCCC
1013. C    CORRECT PRESSURE AND VELOCITIES
1014. C-----
1015.      DO 1003 I=2,L2
1016.      DO 1003 J=2,M2
1017.      P(I,J)=P(I,J)+PC(I,J)*RELAX(NF)
1018.      IF(J.NE.M2) V(I,J)=V(I,J)+DV(I,J)*(PC(I,J)-PC(I,J+1))
1019.      IF(I.NE.L2) U(I,J)=U(I,J)+DU(I,J)*(PC(I,J)-PC(I+1,J))
1020. 1003 CONTINUE
1021.      PREF=P(2,2)
1022.      DO 889 I=2,L2
1023.      DO 889 J=2,M2
1024.      P(I,J)=P(I,J)-PREF

```

```

1025. 889 CONTINUE
1026. 1002 CONTINUE
1027. CCCCCCCCCCCCCCCCCCCCCCCCCCCCCCCCCCCCCCCCCCCCCCCCCCCCCCCCCC
1028. DO 1004 N=4,NFMAX
1029. NF=N
1030. IF(.NOT.LSOLVE(NF)) GOTO 1004
1031. C-----
1032. IST=2
1033. JST=3
1034. CALL USER(6)
1035. C-----
1036. DO 104 I=2,L2
1037. DO 104 J=3,M3
1038. FLOW=1.D0/R(I,J)*1.D0/(RB(I)-RA)*(RHO*RV(I,J)*
1039. & (V(I,J)-(U(I,J)+U(I,J+1)+U(I-1,J+1)+U(I-1,J))/4.D0*
1040. & GV(I,J))*DX
1041. DIFF=1.D0/R(I,J)*1.D0/(RB(I)-RA)**2*(RV(I,J)*
1042. & (2.D0*GAMR(I,J+1)*GAMR(I,J)/(GAMR(I,J+1)+GAMR(I,J))
1043. & +2.D0*GAMT(I,J+1)*GAMT(I,J)/(GAMT(I,J+1)+GAMT(I,J))
1044. & *GV(I,J)*GV(I,J))*DX/DE
1045. CALL DIFLOW
1046. AN(I,J)=ACOF+DMAX1(0.0D0,-FLOW)*0.5D0
1047. C-----
1048. FLOW=1.D0/R(I,J)*1.D0/(RB(I)-RA)*(RHO*RV(I,J-1)*
1049. & (V(I,J-1)-(U(I,J)+U(I,J-1)+U(I-1,J-1)+U(I-1,J))/4.D0*
1050. & GV(I,J-1))*DX
1051. DIFF=1.D0/R(I,J)*1.D0/(RB(I)-RA)**2*(RV(I,J-1)*
1052. & (2.D0*GAMR(I,J-1)*GAMR(I,J)/(GAMR(I,J-1)+GAMR(I,J))
1053. & +2.D0*GAMT(I,J-1)*GAMT(I,J)/(GAMT(I,J-1)+GAMT(I,J))
1054. & *GV(I,J-1)*GV(I,J-1))*DX/DE
1055. CALL DIFLOW
1056. AS(I,J)=ACOF+DMAX1(0.0D0,FLOW)*0.5D0
1057. C-----
1058. FLOW=1.D0/R(I,J)*1.D0/(TB-TA)*(RHO*U(I,J))*DE
1059. DIFF=1.D0/R(I,J)**2.D0*1.D0/(TB-TA)**2*
1060. & 2.D0*GAMT(I+1,J)*GAMT(I,J)/(GAMT(I,J)+GAMT(I+1,J))
1061. & *DE/DX
1062. CALL DIFLOW
1063. AE(I,J)=ACOF+DMAX1(0.0D0,-FLOW)*0.5D0
1064. C-----
1065. FLOW=1.D0/R(I,J)*1.D0/(TB-TA)*(RHO*U(I-1,J))*DE
1066. DIFF=1.D0/R(I,J)**2.D0*1.D0/(TB-TA)**2*
1067. & 2.D0*GAMT(I-1,J)*GAMT(I,J)/(GAMT(I-1,J)+GAMT(I,J))
1068. & *DE/DX
1069. CALL DIFLOW
1070. AW(I,J)=ACOF+DMAX1(0.0D0,FLOW)*0.5D0
1071. C-----
1072. AP(I,J)=AN(I,J)+AS(I,J)+AE(I,J)+AW(I,J)
1073. C-----
1074. C UNDER RELAXATION HERE
1075. C-----
1076. AP(I,J)=AP(I,J)/RELAX(NF)
1077. CON(I,J)=CON(I,J)+(1.D0-RELAX(NF))*AP(I,J)*F(I,J,NF)
1078. C-----
1079. 104 CONTINUE
1080. C-----
1081. DO 7001 I=2,L2
1082. CON(I,M2)=1.0D20*F(I,M2,NF)
1083. AP(I,M2)=1.0D20
1084. AN(I,M2)=0.0D0
1085. AS(I,M2)=0.0D0
1086. AE(I,M2)=0.0D0
1087. AW(I,M2)=0.0D0
1088. 7001 CONTINUE

```

```

1089. C-----
1090.     CALL SOLVE
1091.     1004 CONTINUE
1092. CCCCCCCCCCCCCCCCCCCCCCCCCCCCCCCCCCCCCCCCCCCCCCCCCCCCCCCCC
1093.     ITER=ITER+1
1094.     IF(ITER.GE.LAST) LSTOP=.TRUE.
1095. C-----
1096.     RETURN
1097.     END
1098. CCCCCCCCCCCCCCCCCCCCCCCCCCCCCCCCCCCCCCCCCCCCCCCCCCCCCCCCC
1099.     SUBROUTINE SOLVE
1100. C-----
1101.     IMPLICIT REAL*8 (A-H,O-Z)
1102.     LOGICAL LSOLVE,LSTOP
1103.     COMMON/VV1/F(52,52,10),CON(52,52),
1104.     &AE(52,52),AW(52,52),AN(52,52),AS(52,52),AP(52,52),
1105.     &PT(52),QT(52)
1106.     COMMON/VV2/GAMR(52,52),GAMT(52,52),
1107.     & P(52,52),DU(52,52),DV(52,52),
1108.     & TAU0,TAU(52),TAUA,DH,RE
1109.     COMMON/GRIDS/R(52,52),RU(52,52),RV(52,52),GC(52,52),
1110.     & G(52,52),GU(52,52),THETA(52),ETA(52),XI(52),RB(52),
1111.     & GV(52,52),RBU(52),RA,TB,TA,THETAU(52),T1,T2,
1112.     & ETAV(52),XIU(52),THETAC(52),ETAC(52),RC(52,52),
1113.     & RBC(52),DX,DE,RELAX(13),RHO,AMU,SMAX,SSUM
1114.     COMMON/INDX/NF,L1,L2,L3,M1,M2,M3,LSOLVE(10),
1115.     & IST,JST,ITER,LAST,NTIMES(10),NFMAX,
1116.     & IREF,JREF
1117.     COMMON/COEF/FLOW,DIFF,ACOF
1118.     DIMENSION U(52,52),V(52,52),W(52,52),PC(52,52)
1119.     DIMENSION AK(52,52),E(52,52)
1120.     EQUIVALENCE(F(1,1,1),V(1,1)),(F(1,1,2),U(1,1)),
1121.     & (F(1,1,3),PC(1,1)),(F(1,1,4),W(1,1)),
1122.     & (F(1,1,5),AK(1,1)),(F(1,1,6),E(1,1))
1123. CCCCCCCCCCCCCCCCCCCCCCCCCCCCCCCCCCCCCCCCCCCCCCCCCCCCCCCCC
1124.     ISTF=IST-1
1125.     JSTF=JST-1
1126.     IT1=L2+IST
1127.     IT2=L3+IST
1128.     JT1=M2+JST
1129.     JT2=M3+JST
1130. C-----
1131.     DO 1000 NT=1,NTIMES(NF)
1132.     DO 1000 N=NF,NF
1133. C-----
1134. C     IMPOSE SYMMETRY BOUNDARY CONDITIONS HERE
1135. C-----
1136.     DO 272 J=1,M1
1137.     U(1,J)=0.0D0
1138.     U(L2,J)=0.0D0
1139.     U(L1,J)=0.0D0
1140.     272 CONTINUE
1141.     DO 273 J=3,M3
1142.     V(1,J)=1.D0/(TB-TA)*1.D0/DX*V(2,J)+1.D0/(RB(1)-RA)*
1143.     & GV(1,J)*RV(1,J)*1.D0/DE*V(1,J-1)
1144.     V(1,J)=V(1,J)/(1.D0/(TB-TA)*1.D0/DX+1.D0/(RB(1)-RA)*
1145.     & GV(1,J)*RV(1,J)*1.D0/DE)
1146.     V(L1,J)=1.D0/(TB-TA)*1.D0/DX*V(L2,J)-1.D0/(RB(L1)-RA)*
1147.     & GV(L1,J)*RV(L1,J)*1.D0/DE*V(L1,J-1)
1148.     V(L1,J)=V(L1,J)/(1.D0/(TB-TA)*1.D0/DX-1.D0/(RB(L1)-RA)*
1149.     & GV(L1,J)*RV(L1,J)*1.D0/DE)
1150.     V(L1,J)=V(L2,J)
1151.     & +(TB-TA)/(RB(I)-RA)*DX/DE*GV(L1,J)*
1152.     & RV(L1,J)*0.5D0*(V(L1,J+1)-V(L1,J-1))

```

```

1153. 273 CONTINUE
1154. DO 274 J=3,M3
1155. W(1,J)=1.D0/(TB-TA)*1.D0/DX*W(2,J)+1.D0/(RB(1)-RA)*
1156. & G(1,J)*R(1,J)*1.D0/DE*W(1,J-1)
1157. W(1,J)=W(1,J)/(1.D0/(TB-TA)*1.D0/DX+1.D0/(RB(1)-RA)*
1158. & G(1,J)*R(1,J)*1.D0/DE)
1159. W(L1,J)=1.D0/(TB-TA)*1.D0/DX*W(L2,J)-1.D0/(RB(L1)-RA)*
1160. & G(L1,J)*R(L1,J)*1.D0/DE*W(L1,J-1)
1161. W(L1,J)=W(L1,J)/(1.D0/(TB-TA)*1.D0/DX-1.D0/(RB(L1)-RA)*
1162. & G(L1,J)*R(L1,J)*1.D0/DE)
1163. C-----
1164. AK(1,J)=1.D0/(TB-TA)*1.D0/DX*AK(2,J)+1.D0/(RB(1)-RA)*
1165. & G(1,J)*R(1,J)*1.D0/DE*AK(1,J-1)
1166. AK(1,J)=AK(1,J)/(1.D0/(TB-TA)*1.D0/DX+1.D0/(RB(1)-RA)*
1167. & G(1,J)*R(1,J)*1.D0/DE)
1168. AK(L1,J)=1.D0/(TB-TA)*1.D0/DX*AK(L2,J)-1.D0/(RB(L1)-RA)*
1169. & G(L1,J)*R(L1,J)*1.D0/DE*AK(L1,J-1)
1170. AK(L1,J)=AK(L1,J)/(1.D0/(TB-TA)*1.D0/DX-1.D0/(RB(L1)-RA)*
1171. & G(L1,J)*R(L1,J)*1.D0/DE)
1172. C-----
1173. E(1,J)=1.D0/(TB-TA)*1.D0/DX*E(2,J)+1.D0/(RB(1)-RA)*
1174. & G(1,J)*R(1,J)*1.D0/DE*E(1,J-1)
1175. E(1,J)=E(1,J)/(1.D0/(TB-TA)*1.D0/DX+1.D0/(RB(1)-RA)*
1176. & G(1,J)*R(1,J)*1.D0/DE)
1177. E(L1,J)=1.D0/(TB-TA)*1.D0/DX*E(L2,J)-1.D0/(RB(L1)-RA)*
1178. & G(L1,J)*R(L1,J)*1.D0/DE*E(L1,J-1)
1179. E(L1,J)=E(L1,J)/(1.D0/(TB-TA)*1.D0/DX-1.D0/(RB(L1)-RA)*
1180. & G(L1,J)*R(L1,J)*1.D0/DE)
1181. C-----
1182. F(L1,J,NF)=F(L2,J,NF)
1183. & +(TB-TA)/(RB(I)-RA)*DX/DE*G(L1,J)*
1184. & R(L1,J)*0.5D0*(F(L1,J+1,NF)-F(L1,J-1,NF))
1185. 274 CONTINUE
1186. CCCCCCCCCCCCCCCCCCCCCCCCCCCCCCCCCCCCCCCCCCCCCCCCCCCCCCCCCC
1187. JM=M2
1188. IL=L2
1189. DO 90 J=JST,JM
1190. PT(ISTF)=0.D0
1191. QT(ISTF)=F(ISTF,J,N)
1192. DO 70 I=IST,IL
1193. DENOM=AP(I,J)-PT(I-1)*AW(I,J)
1194. PT(I)=AE(I,J)/DENOM
1195. TEMP=CON(I,J)+AN(I,J)*F(I,J+1,N)+
1196. & AS(I,J)*F(I,J-1,N)
1197. QT(I)=(TEMP+AW(I,J)*QT(I-1))/DENOM
1198. 70 CONTINUE
1199. DO 80 II=IST,IL
1200. I=IT1-II
1201. 80 F(I,J,N)=F(I+1,J,N)*PT(I)+QT(I)
1202. 90 CONTINUE
1203. C-----
1204. DO 190 JJ=JST,JM-1
1205. J=JT2-JJ
1206. PT(ISTF)=0.D0
1207. QT(ISTF)=F(ISTF,J,N)
1208. DO 170 I=IST,IL
1209. DENOM=AP(I,J)-PT(I-1)*AW(I,J)
1210. PT(I)=AE(I,J)/DENOM
1211. TEMP=CON(I,J)+AN(I,J)*F(I,J+1,N)+AS(I,J)*F(I,J-1,N)
1212. QT(I)=(TEMP+AW(I,J)*QT(I-1))/DENOM
1213. 170 CONTINUE
1214. DO 180 II=IST,IL
1215. I=IT1-II
1216. 180 F(I,J,N)=F(I+1,J,N)*PT(I)+QT(I)

```

```

1217. 190 CONTINUE
1218. C-----
1219.     DO 290 I=IST,IL
1220.     PT(JSTF)=0.D0
1221.     QT(JSTF)=F(I,JSTF,N)
1222.     DO 270 J=JST,JM
1223.     DENOM=AP(I,J)-PT(J-1)*AS(I,J)
1224.     PT(J)=AN(I,J)/DENOM
1225.     TEMP=CON(I,J)+AE(I,J)*F(I+1,J,N)+AW(I,J)*F(I-1,J,N)
1226.     QT(J)=(TEMP+AS(I,J)*QT(J-1))/DENOM
1227. 270 CONTINUE
1228.     DO 280 JJ=JST,JM
1229.     J=JT1-JJ
1230. 280 F(I,J,N)=F(I,J+1,N)*PT(J)+QT(J)
1231. 290 CONTINUE
1232. C-----
1233.     DO 390 II=IST,IL-1
1234.     I=IT2-II
1235.     PT(JSTF)=0.D0
1236.     QT(JSTF)=F(I,JSTF,N)
1237.     DO 370 J=JST,JM
1238.     DENOM=AP(I,J)-PT(J-1)*AS(I,J)
1239.     PT(J)=AN(I,J)/DENOM
1240.     TEMP=CON(I,J)+AE(I,J)*F(I+1,J,N)+AW(I,J)*F(I-1,J,N)
1241.     QT(J)=(TEMP+AS(I,J)*QT(J-1))/DENOM
1242. 370 CONTINUE
1243.     DO 380 JJ=JST,JM
1244.     J=JT1-JJ
1245. 380 F(I,J,N)=F(I,J+1,N)*PT(J)+QT(J)
1246. 390 CONTINUE
1247. C-----
1248. 1000 CONTINUE
1249. C-----
1250.     DO 400 J=2,M2
1251.     DO 400 I=2,L2
1252.     CON(I,J)=0.0D0
1253.     AP(I,J)=0.0D0
1254.     AN(I,J)=0.0D0
1255.     AS(I,J)=0.0D0
1256.     AE(I,J)=0.0D0
1257.     AW(I,J)=0.0D0
1258. 400 CONTINUE
1259. C-----
1260.     RETURN
1261.     END
1262. CCCCCCCCCCCCCCCCCCCCCCCCCCCCCCCCCCCCCCCCCCCCCCCCCCCCCCCCCC
1263.     SUBROUTINE DIFLOW
1264. C-----
1265.     IMPLICIT REAL*8 (A-H,O-Z)
1266.     COMMON/COEF/FLOW,DIFF,ACOF
1267. C-----
1268.     IF(DABS(FLOW/DIFF).LE.1.D-5) THEN
1269.     ACOF=1.0D0
1270.     GOTO 10
1271.     ELSE
1272.     END IF
1273.     ACOF=DMAX1(0.0D0,(1.0D0-0.1D0*DABS(FLOW/DIFF))**5)
1274. 10 ACOF=DIFF*ACOF
1275.     RETURN
1276.     END
1277. CCCCCCCCCCCCCCCCCCCCCCCCCCCCCCCCCCCCCCCCCCCCCCCCCCCCCCCCCC
1278.     SUBROUTINE GRID
1279. C-----
1280. C     GENERATE CURVILINEAR NON-ORTHOGONAL GRIDS

```

```

1281. C-----
1282.     IMPLICIT REAL*8 (A-H,O-Z)
1283.     LOGICAL LSOLVE,LSTOP
1284.     COMMON/VV1/F(52,52,10),CON(52,52),
1285.     &AE(52,52),AW(52,52),AN(52,52),AS(52,52),AP(52,52),
1286.     &PT(52),QT(52)
1287.     COMMON/VV2/GAMR(52,52),GAMT(52,52),
1288.     & P(52,52),DU(52,52),DV(52,52),
1289.     & TAU0,TAU(52),TAUA,DH,RE
1290.     COMMON/GRIDS/R(52,52),RU(52,52),RV(52,52),GC(52,52),
1291.     & G(52,52),GU(52,52),THETA(52),ETA(52),XI(52),RB(52),
1292.     & GV(52,52),RBU(52),RA,TB,TA,THETAU(52),T1,T2,
1293.     & ETAV(52),XIU(52),THETAC(52),ETAC(52),RC(52,52),
1294.     & RBC(52),DX,DE,RELAX(13),RHO,AMU,SMAX,SSUM
1295.     COMMON/INDX/NF,L1,L2,L3,M1,M2,M3,LSOLVE(10),
1296.     & IST,JST,ITER,LAST,NTIMES(10),NFMAX,
1297.     & IREF,JREF
1298.     COMMON/COEF/FLOW,DIFF,ACOF
1299.     DIMENSION U(52,52),V(52,52),W(52,52),PC(52,52)
1300.     DIMENSION AK(52,52),E(52,52)
1301.     EQUIVALENCE(F(1,1,1),V(1,1)),(F(1,1,2),U(1,1)),
1302.     & (F(1,1,3),PC(1,1)),(F(1,1,4),W(1,1)),
1303.     & (F(1,1,5),AK(1,1)),(F(1,1,6),E(1,1))
1304. C-----
1305.     D=25.4D-3
1306.     PI=3.1415926535897932D0
1307.     TA=0.0D0
1308.     TB=PI
1309.     AG=14.2D-3
1310.     A=AG+25.4D-3
1311.     AL=DSQRT(63.5D-3**2+A**2)
1312.     T1=DARSIN(63.5D-3/AL)
1313.     B=AL*DCOS(2.D0*PI/3.D0-T1)
1314.     C=66.0D-3-A
1315.     T2=PI-DARSIN(25.4D-3/DSQRT(C**2+25.4D-3**2))
1316. C-----
1317.     XI(1)=0.0D0
1318.     DX=1.D00/FLOAT(L1-1)
1319.     DO 1001 I=2,L1
1320.     XI(I)=XI(I-1)+DX
1321. 1001 CONTINUE
1322. C-----
1323.     ETA(1)=0.0D0
1324.     DE=1.D00/FLOAT(M1-1)
1325.     DO 1002 J=2,M1
1326.     ETA(J)=ETA(J-1)+DE
1327. 1002 CONTINUE
1328. C-----
1329.     DO 1000 I=1,L1
1330.     THETA(I)=XI(I)*(TB-TA)+TA
1331. 1000 CONTINUE
1332. C-----
1333.     RA=D
1334. C-----
1335.     DO 1003 I=1,L1
1336.     DT1=THETA(I)-T1
1337.     DT2=THETA(I)-T2
1338.     IF(DT1.LE.0.0D0) THEN
1339.     RB(I)=A/DCOS(THETA(I))
1340.     ELSE IF(DT1.GT.0.0D0.AND.DT2.LE.0.0D0) THEN
1341.     RB(I)=B/DCOS(2.D0*PI/3.D0-THETA(I))
1342.     ELSE IF(DT2.GT.0.0D0) THEN
1343.     RB(I)=C/DCOS(PI-THETA(I))
1344.     ELSE

```

```

1345.      END IF
1346.      1003 CONTINUE
1347. C-----
1348.      DO 1004 I=1,L1
1349.      DO 1004 J=1,M1
1350.      R(I,J)=ETA(J)*(RB(I)-RA)+RA
1351.      DT1=THETA(I)-T1
1352.      DT2=THETA(I)-T2
1353.      IF(DT1.LE.0.0D0) THEN
1354.      DRBDT=A*DSIN(THETA(I))/DCOS(THETA(I))**2
1355.      ELSE IF(DT1.GT.0.0D0.AND.DT2.LE.0.0D0) THEN
1356.      DRBDT=-B*DSIN(2.D0*PI/3.D0-THETA(I))/
1357.      & DCOS(2.D0*PI/3.D0-THETA(I))**2
1358.      ELSE IF(DT2.GT.0.0D0) THEN
1359.      DRBDT=-C*DSIN(PI-THETA(I))/DCOS(PI-THETA(I))**2
1360.      ELSE
1361.      END IF
1362.      G(I,J)=ETA(J)/R(I,J)*DRBDT
1363.      1004 CONTINUE
1364. C-----
1365.      ETAV(1)=DE/2.D0
1366.      DO 2002 J=2,M2
1367.      ETAV(J)=ETAV(J-1)+DE
1368.      2002 CONTINUE
1369. C-----
1370.      DO 2004 I=1,L1
1371.      DO 2004 J=1,M2
1372.      RV(I,J)=ETAV(J)*(RB(I)-RA)+RA
1373.      DT1=THETA(I)-T1
1374.      DT2=THETA(I)-T2
1375.      IF(DT1.LE.0.0D0) THEN
1376.      DRBDT=A*DSIN(THETA(I))/DCOS(THETA(I))**2
1377.      ELSE IF(DT1.GT.0.0D0.AND.DT2.LE.0.0D0) THEN
1378.      DRBDT=-B*DSIN(2.D0*PI/3.D0-THETA(I))/
1379.      & DCOS(2.D0*PI/3.D0-THETA(I))**2
1380.      ELSE IF(DT2.GT.0.0D0) THEN
1381.      DRBDT=-C*DSIN(PI-THETA(I))/DCOS(PI-THETA(I))**2
1382.      ELSE
1383.      END IF
1384.      GV(I,J)=ETAV(J)/RV(I,J)*DRBDT
1385.      2004 CONTINUE
1386. CCCCCCCCCCCCCCCCCCCCCCCCCCCCCCCCCCCCCCCCCCCCCCCCCCCCCC
1387.      XIU(1)=DX/2.D0
1388.      DO 2999 I=2,L2
1389.      XIU(I)=XIU(I-1)+DX
1390.      2999 CONTINUE
1391.      DO 5200 I=1,L2
1392.      THETAU(I)=XIU(I)*(TB-TA)+TA
1393.      5200 CONTINUE
1394. C-----
1395.      DO 5203 I=1,L2
1396.      DT1=THETAU(I)-T1
1397.      DT2=THETAU(I)-T2
1398.      IF(DT1.LE.0.0D0) THEN
1399.      RBU(I)=A/DCOS(THETAU(I))
1400.      ELSE IF(DT1.GT.0.0D0.AND.DT2.LE.0.0D0) THEN
1401.      RBU(I)=B/DCOS(2.D0*PI/3.D0-THETAU(I))
1402.      ELSE IF(DT2.GT.0.0D0) THEN
1403.      RBU(I)=C/DCOS(PI-THETAU(I))
1404.      ELSE
1405.      END IF
1406.      5203 CONTINUE
1407. C-----
1408.      DO 5204 I=1,L2

```

```

1409.      DO 5204 J=1,M1
1410.      RU(I,J)=ETA(J)*(RBU(I)-RA)+RA
1411.      DT1=THETAU(I)-T1
1412.      DT2=THETAU(I)-T2
1413.      IF(DT1.LE.0.0D0) THEN
1414.      DRBDT=A*DSIN(THETAU(I))/DCOS(THETAU(I))**2
1415.      ELSE IF(DT1.GT.0.0D0.AND.DT2.LE.0.0D0) THEN
1416.      DRBDT=-B*DSIN(2.D0*PI/3.D0-THETAU(I))/
1417.      & DCOS(2.D0*PI/3.D0-THETAU(I))**2
1418.      ELSE IF(DT2.GT.0.0D0) THEN
1419.      DRBDT=-C*DSIN(PI-THETAU(I))/DCOS(PI-THETAU(I))**2
1420.      ELSE
1421.      END IF
1422.      GU(I,J)=ETA(J)/RU(I,J)*DRBDT
1423.      5204 CONTINUE
1424. C-----
1425.      DO 4000 I=1,L2
1426.      THETAC(I)=THETAU(I)
1427.      4000 CONTINUE
1428. C-----
1429.      ETAC(1)=DE/2.D0
1430.      DO 4002 J=2,M2
1431.      ETAC(J)=ETAC(J-1)+DE
1432.      4002 CONTINUE
1433. C-----
1434.      DO 4003 I=1,L2
1435.      DT1=THETAC(I)-T1
1436.      DT2=THETAC(I)-T2
1437.      IF(DT1.LE.0.0D0) THEN
1438.      RBC(I)=A/DCOS(THETAC(I))
1439.      ELSE IF(DT1.GT.0.0D0.AND.DT2.LE.0.0D0) THEN
1440.      RBC(I)=B/DCOS(2.D0*PI/3.D0-THETAC(I))
1441.      ELSE IF(DT2.GT.0.0D0) THEN
1442.      RBC(I)=C/DCOS(PI-THETAC(I))
1443.      ELSE
1444.      END IF
1445.      4003 CONTINUE
1446. C-----
1447.      DO 4004 I=1,L2
1448.      DO 4004 J=1,M2
1449.      RC(I,J)=ETAC(J)*(RBC(I)-RA)+RA
1450.      DT1=THETAC(I)-T1
1451.      DT2=THETAC(I)-T2
1452.      IF(DT1.LE.0.0D0) THEN
1453.      DRBDT=A*DSIN(THETAC(I))/DCOS(THETAC(I))**2
1454.      ELSE IF(DT1.GT.0.0D0.AND.DT2.LE.0.0D0) THEN
1455.      DRBDT=-B*DSIN(2.D0*PI/3.D0-THETAC(I))/
1456.      & DCOS(2.D0*PI/3.D0-THETAC(I))**2
1457.      ELSE IF(DT2.GT.0.0D0) THEN
1458.      DRBDT=-C*DSIN(PI-THETAC(I))/DCOS(PI-THETAC(I))**2
1459.      ELSE
1460.      END IF
1461.      GC(I,J)=ETAC(J)/RC(I,J)*DRBDT
1462.      4004 CONTINUE
1463.      CCCCCCCCCCCCCCCCCCCCCCCCCCCCCCCCCCCCCCCCCCCCCCCCCCCCCCCCC
1464.      RETURN
1465.      END
1466.      CCCCCCCCCCCCCCCCCCCCCCCCCCCCCCCCCCCCCCCCCCCCCCCCCCCCCCCCC
1467.      //GO.FT10F001 DD DSN=XWU.RESULT,DISP=SHR
1468.      //GO.FT11F001 DD DSN=XWU.DNFILE,DISP=SHR
1469.      //GO.FT12F001 DD DSN=XWU.WEIGHT,DISP=SHR
1470.      //GO.SYDSIN DD *
1471.      //

```